University of Tennessee, Knoxville
TRACE: Tennessee Research and Creative Exchange

Doctoral Dissertations | Graduate School

8-1995

ATEC: The Aerodyanmic Turbine Engine Code for the Analysis of Transient and Dynamic Gas Turbine Engine System Operations

Glenn Douglas Garrard
University of Tennessee - Knoxville

Follow this and additional works at: https://trace.tennessee.edu/utk_graddiss

 Part of the Mechanical Engineering Commons

Recommended Citation

Garrard, Glenn Douglas, "ATEC: The Aerodyanmic Turbine Engine Code for the Analysis of Transient and Dynamic Gas Turbine Engine System Operations. " PhD diss., University of Tennessee, 1995.
https://trace.tennessee.edu/utk_graddiss/1605

This Dissertation is brought to you for free and open access by the Graduate School at TRACE: Tennessee Research and Creative Exchange. It has been accepted for inclusion in Doctoral Dissertations by an authorized administrator of TRACE: Tennessee Research and Creative Exchange. For more information, please contact trace@utk.edu.

To the Graduate Council:

I am submitting herewith a dissertation written by Glenn Douglas Garrard entitled "ATEC: The Aerodyanmic Turbine Engine Code for the Analysis of Transient and Dynamic Gas Turbine Engine System Operations." I have examined the final electronic copy of this dissertation for form and content and recommend that it be accepted in partial fulfillment of the requirements for the degree of Doctor of Philosophy, with a major in Mechanical Engineering.

Roy J. Schulz, Major Professor

We have read this dissertation and recommend its acceptance:

Milton W. Davis, Frank S. Collins, Roger Crawford, Baril Amin

Accepted for the Council:

Carolyn R. Hodges

Vice Provost and Dean of the Graduate School

(Original signatures are on file with official student records.)

To the Graduate Council:

I am submitting herewith a dissertation written by Glenn Douglas Garrard entitled "ATEC: The Aerodynamic Turbine Engine Code for the Analysis of Transient and Dynamic Gas Turbine Engine System Operations." I have examined the final copy of this dissertation for form and content and recommend that it be accepted in partial fulfillment of the requirements for the degree of Doctor of Philosophy, with a major in Mechanical Engineering.

Roy J. Schulz, Major Professor

We have read this dissertation
and recommend its acceptance:

Accepted for the Council:

Associate Vice Chancellor and
Dean of The Graduate School

ATEC: THE AERODYNAMIC TURBINE ENGINE CODE FOR THE ANALYSIS OF TRANSIENT AND DYNAMIC GAS TURBINE ENGINE SYSTEM OPERATIONS

A Dissertation
Presented for the
Doctor of Philosophy
Degree
The University of Tennessee, Knoxville

Glenn Douglas Garrard
August, 1995

DEDICATION

This dissertation is dedicated to my wife, Angelia Gail Garrard, and children, Justin Matthew Garrard and Rachel Marie Garrard. Their unwavering support and complete faith in my dream during the five years that this effort has taken is what made it possible. They made sacrifices beyond what they expected, but they contributed more to this effort than they could ever have imagined.

ACKNOWLEDGMENTS

I would like to acknowledge the United States Air Force and Sverdrup Technology, Inc. for support provided at the Arnold Engineering Development Center (AEDC) and during my year of off-site study as recipient of the Resident Graduate Study Program scholarship. I would also like to express my appreciation to the many individuals who have assisted and supported me throughout my studies. Dr. Milton W. Davis, Jr. is due a very special thanks as he was the one who introduced me to dynamic gas turbine engine modeling. His leadership and encouragement has been my guiding light during this dissertation effort. Mr. Alan A. Hale has made this dissertation possible with his efforts on the implicit solver. Alan was willing to put aside his own dissertation efforts during this work and for that I am extremely appreciative. The assistance of Mr. Stephen Savelle during the model development and calibration efforts is also acknowledged. The support of the Joint Dynamic Airbreathing Propulsion Simulations (JDAPS) partnership is recognized. Major non-AEDC funding for the development of ATEC was provided by NASA Lewis Research Center in Cleveland, Ohio. Additional indirect funding was provided by other JDAPS partners such as Allied-Signal and the Army Vehicle Propulsion Directorate located at NASA Lewis Research Center.

Appreciation is also extended to Dr. Roy J. Schulz for his guidance and technical support and to the entire review committee for their constructive review comments. Additionally, the guidance and motivational assistance provided by Dr. Virgil K. Smith, III, of Sverdrup Technology is greatly appreciated.

Finally, two close friends and coworkers, Mr. L. Brent Bates and Mr. C. Scott Bartlett, have made this effort possible by providing both help and, at times, a shoulder to cry on during the class work and exams. They have been my biggest supporters and I doubt this goal would be possible without their friendship.

The work reported herein was conducted at the Arnold Engineering Development Center (AEDC), Air Force Materiel Command (AFMC). The results were obtained by Sverdrup Technology, Inc., AEDC Group, operating contractor for the propulsion test facilities at AEDC, AFMC, Arnold Air Station, Tennessee, under Job 0091 and Job 2383. The Air Force Project Manager was Mr. James D. Mitchell. The manuscript was submitted for publication on August 5, 1995.

ABSTRACT

A new one-dimensional, time dependent aerothermodynamic mathematical model and computer simulation of the gas turbine engine has been developed and is introduced herein. The Aerodynamic Turbine Engine Code (ATEC) simulates the operation of the gas turbine engine by solving conservation equations, expressed as one dimensional, time dependent Euler equations, with turbomachinery source terms. By incorporating both implicit and explicit equation solvers, transient simulations of the gas turbine engine can be conducted efficiently while maintaining the capability of simulating dynamic events such as compressor stall. ATEC can also be used to address dynamic events or steady-state processes to model both on- and off-design engine operation.

The dissertation is presented in seven chapters. The first chapter introduces the gas turbine engine and discusses its operation. Out of this discussion falls the reason for striving for a mathematical model and computer simulation of the gas turbine engine. Previous efforts at providing a mathematical model and computer simulation of the gas turbine engine are summarized in the second chapter, with particular focus given to their contribution to the advancement of the state-of-the-art in gas turbine engine modeling. It is shown that the current state-of-the-art is advanced by the development of the ATEC model and simulation. The third chapter of the dissertation provides an overview of the mathematical approach taken within ATEC. The general philosophy of the ATEC mathematical model is discussed, and the method of solving the governing equations using both an explicit and implicit equation solver is presented. The third chapter of the

dissertation also describes the various component mathematical models which provide the turbomachinery source terms to the Euler equations. The fourth chapter of the dissertation provides operational verification of the ATEC simulation. The various component models are exercised for representative test cases to demonstrate the functionality of each model and that the results provided by the models are appropriate. The fifth chapter of the dissertation presents the results of calibration efforts. It is here that the ATEC simulation results are compared to pertinent data sets. It is shown that with the proper tuning of the various component models, simulation results can be obtained that match the engine test data over the entire engine system to within three percent during a transient event. During a dynamic event, it is shown that ATEC will predict the overall frequency and magnitude of the engine response. The ATEC simulation was also shown to match the overall trends of a engine start sequence. The dissertation concludes with two chapters that summarize the previous five chapters and present recommendations for future efforts.

TABLE OF CONTENTS

SECTION Page

LIST OF FIGURES

LIST OF TABLES

LIST OF SYMBOLS

Symbol	Definition
a	Speed of sound
A, **A**	Surface area, Coefficient matrix in Appendix C
B, **B**	Gritzer's B parameter, Coefficient matrix in Appendix C
c, C, **C**	Specific heat, Coefficient matrix in Appendix C
CALF	Combined air loading factor
Cd	Combustor pressure loss coefficient
CFL	Courant-Fredricks-Lewey stability limit
D	Fuel droplet diameter
E	Total Energy
F, **F**	Force, Coefficient matrix in Appendix C
F	Flux term variable matrix
G	Source term variable matrix
$\bar{h}$	Average convective heat transfer coefficient
H	Total enthalpy
I	Rotor polar moment of interia
I	Identity Matrix
k	Thermal conductivity
L	Length
m	Mass

Symbol	Definition
Mn	Mach number
MW	Molecular weight
n	Coefficient in Equation 3.34
p, P	Pressure
PR	Pressure ratio
$\dot{q}$	Heat transfer rate
Q	Heat transfer rate, Eigenrow matrix
R	Gas constant
$\mathcal{R}$	Universal gas constant
S	Cross-sectional area
SW	Shaft work
t	Time
T	Temperature
TFF	Turbine flow function
TR	Temperature ratio
u	Axial velocity
U	Circumferential wheel speed at mean radius
U	Dependent variable matrix
V	Volume

Symbol	Definition
W	Work
WDF	Turbine work done factor
x	Axial distance

Greek

α	Coefficient used in exponential grid spacing
β	Fuel droplet evaporation coefficient
Δ	Delta
ϕ	Compressor flow coefficient
	Equivalence Ratio
γ	Ratio of specific heats
Γ	Torque
η	Efficiency
Λ	Eigenvalue matrix
λ	Eigenvalue
ρ	Density
τ	Time Constant
ω	Helmholtz resonator frequency, Rotor rotational speed
Ψ	Compressor characteristic coefficients
ζ	Equidistant value of n^{th} grid point

Symbol	Definition
	Subscripts
3	Station 3 - Inlet to combustor
4	Station 4 - Turbine inlet
B	Bleed
b	Blade
b-a	Blade to air
b-b	Blade to base
base	Blade base
blade	Blade
c	Compressor, Combustor
check	Check value
comb	Combustor
comp	Compressor
cor	corrected
e	Efficiency of fuel evaporation
eff	Effective
gas	Gas
i	Inlet
L	Lean
limit	Limit of value
max	Maximum

Symbol	Definition
N	Current time step
N+1	Next time step
new	New value
o	Exit, Reference
p	At constant pressure, Customer power
PZ	Primary zone in the combustor
R	Rich
r	reaction efficiency
ref	Reference conditions
rotor	Rotor
s	Starter, Surface
ss	Steady state
stator	Stator
t	Total, Turbine
v	At constant volume, Viscous Loss
x	per unit length

Superscripts

n	Current time step
n-1	Previous time step

Symbol	Definition
P	Pressure
T	Temperature
**	Referenced to sonic conditions

1. INTRODUCTION

The gas turbine engine has played a significant role in the advancement of the flight capabilities of modern day aircraft. A sketch of a gas turbine engine with its various components is shown in Fig. 1[1]. Because aircraft performance is tied directly and inseparably to the performance of the propulsion device, efforts are continually underway to increase both the thrust generation and fuel efficiency of gas turbine engines. The continuing demands for increased performance, however, have resulted in engine designs which operate near the aerodynamic, thermal, and structural limits of the engine system components.

In order for a gas turbine engine to achieve the performance levels and durability for which it was designed, stable operation of the engine must be ensured [1][2]. Even during normal operation, a gas turbine engine will be exposed to time variant, or transient, events. A transient event is said to occur when an aerodynamic or mechanical change occurs in the engine that is a function of time without undesirable changes in the engine operating characteristics. An example of a transient event is a change in an engine operating condition due to a fuel flow rate change. If not carefully made, a transient event can potentially force the engine into unstable operation, which can be dynamic in nature. Dynamic engine operation is defined as engine behavior occurring when aerodynamic or mechanical changes in the engine occur very quickly (cyclic frequencies

---

[1] All tables and figures may be found in the Appendices.

[2] Numbers in brackets refer to similarly numbered references in the bibliography.

measured in tenth's of seconds or less) and are usually undesirable. Dynamic events, which lead to dynamic engine operation, include, but are certainly not limited to, gun gas ingestion and inlet distortion [2]. These transient events and the resulting dynamic operation of the engine could result in loss of thrust, loss of engine control, or possible engine damage due to high heat loads and high cyclic stresses [3]. The operating characteristics of a given engine during transient and dynamic events must be quantified in order to ensure that the engine will perform as desired over the range of conditions it will experience during normal operation.

Because of the open flow paths and mostly subsonic flow throughout the engine, each of the various components in the engine are aerodynamically and, in some cases, mechanically coupled to the other components. It is this coupling that permits the gas turbine engine to operate as a propulsion device. An insignificant problem in one component, however, can lead to significant problems in other components. For example, a transient increase in fuel flow rate to the combustor can cause the engine compression system to stall [4]. It is important for the engine designer to be able to predict when an engine will encounter a dynamic event such as compressor stall due to transient phenomena, and to understand how the engine will react once a dynamic event occurs.

Because of the coupling of the various individual engine components, the entire gas turbine engine system is engineered to ensure that the desired operational characteristics are achieved. One method available to analyze an engine system is to

model the system components mathematically (create a component model) and then tie the component models together with a computer simulation (the simulation). The computer simulation can permit the study of integrated engine performance and behavior, reducing or eliminating costly and time consuming testing of the physical hardware. As will be noted in the next chapter, many gas turbine engine models and simulations have been developed and reported in the open literature. Few, however, have addressed the integration of all of the various components of a gas turbine engine in a system model that can handle both transient and dynamic events in an efficient manner.

The Aerodynamic Turbine Engine Code, or ATEC, has been developed in the present research to address this issue. ATEC is a one-dimensional mathematical model of a gas turbine engine solving the equations of conservation of mass, momentum, and energy expressed as the compressible Euler equations with turbomachinery source terms. The resulting model equations have been implemented in a computer simulation. Operational verification and calibration of the ATEC model and simulation have been conducted for a representative data set obtained during the testing of a small turboshaft engine.

This dissertation is organized such that the operational characteristics of a gas turbine engine during transient and dynamic events are reviewed in the next section. A complete statement of the problem is given in Section 1.2. In Chapter 2, a review of the pertinent literature that addresses the modeling of gas turbine engines is presented. The overall mathematical model and the individual models for turbomachinery source terms

are presented in Chapter 3. The operational verification of the model and simulation is presented in Chapter 4, and calibration of the mathematical model and simulation with test data is presented in Chapter 5. Conclusions and recommendations for future work are presented in Chapters 6 and 7, respectively.

1.1. Background

The primary function of an aircraft gas turbine engine is to convert the energy stored in the fuel to increased kinetic energy of the flow through the engine (or of a stream of air passing through an external propeller). This task is accomplished by mixing the fuel with air and burning the resulting mixture. Some of the added flow energy is then extracted from the combustion products by a turbine and used to drive a compressor. The compressor pumps the air flow through the engine. The compressor utilizes the work extracted by the turbine to increase the pressure of the air flow before it enters the combustor. This increase in pressure of the incoming air stream increases the net amount of energy (or energy density) that can be obtained from the system. Energy that is remaining in the flow downstream of the turbine is either converted to shaft work by another turbine (to drive a propeller), or expanded to a high velocity by placing a nozzle downstream of the gas generator turbine.

The basics of the thermodynamic steady-state operation of a gas turbine engine (the overall pressures, temperatures and flow velocities) can be determined through ideal as well as non-ideal cycle analysis for both on-design and off-design operating conditions. Numerous undergraduate and graduate level text books (such as [5-8]) give all of the

details necessary to adequately define the thermodynamics of flow properties inside the gas turbine engine. Transient and dynamic analysis techniques, however, have not typically been taught at either the undergraduate or graduate level. For this reason, this section of the dissertation will briefly discuss the transient and dynamic operation of the gas turbine engine in order to provide the necessary background to the reader.

During steady-state operation, the various components of a gas turbine engine each operate at some nominal condition as given by a point on their respective component performance maps. A representative compressor performance map is sketched in Fig. 2. The compressor pressure ratio is plotted against inlet corrected air flow rate for selected rotor speeds. The actual compressor operating point is a function of a number of variables such as the air mass flow rate, the compressor efficiency, compressor pressure ratio and rotor speed as controlled by the turbine mass flow and work balance. For on-design engine operation, each point on a given speed line represents a different engine design. The designer selects the particular location of the design point depending on the proposed application of the engine, optimizing the requirement for thrust generation or power output with the desire to maximize the specific fuel consumption [9].

Operating off the design point for a given engine drives the compressor pressure ratio and bypass ratio to values other than the design values. Determination of the engine performance for off-design operation follows the same basic calculation process as for on-design operation; however, the variation of component efficiency with varying conditions must be accounted for in the analysis. For example, compressor efficiency

varies as a function of pressure ratio and corrected inlet mass flow rate. Lines of constant efficiency are plotted on the compressor performance map shown in Fig. 2. As the relationship of compressor pressure ratio to corrected inlet mass flow rate changes, so too does the compressor efficiency. To analyze a given system during off-design operation, the component efficiency variation can either be estimated analytically or obtained experimentally [10].

Steady-state engine operation is characterized by one fact: the engine system is balanced relative to its component energy requirements. That is, the power extracted from the flow by the turbine is exactly equal to what is required by the compressor, plus any associated losses. During a transient event, however, this is not the case. Because of varying flow conditions and the finite reaction time required by the system, the power balance is lost. This in turn results in either an acceleration or deceleration of the rotor, depending on which direction the power balance is pushed.

Fortunately, experience has shown that during transient events, the engine operational characteristics can by described by the use of "instantaneous" steady-state component characteristics. For example, the compressor performance characteristics determined from steady-state tests also adequately describe the system behavior during transient events. This results from the observation that transient events typically occur over time periods measured in seconds, whereas a nominal residence time of a fluid element inside the engine is on the order of 0.01 seconds [11]. It is critical to note that if the transient event forces the engine into dynamic operation, such as compressor surge,

then the use of steady-state characteristics for describing engine performance is no longer applicable.

For the purposes of describing the engine operation during a transient event, consider a fuel flow rate increase that occurs over some finite time period. Other commonly occurring phenomena, such as inlet total pressure and total temperature distortion, will have essentially the same basic effect. From a steady-state perspective, the increased fuel flow rate will increase the combustor exit temperature by increasing the fuel-to-air ratio in the primary zone of the combustor. The higher exit temperature will in turn increase the power extraction by the turbine. Because of the additional energy extraction in the turbine, an increase in the rotor speed occurs. The increased speed of the rotor causes the compressor pressure ratio to increase along with the mass flow rate through the system. Eventually, the air mass flow rate increases to the point that the fuel-to-air ratio provides a turbine inlet temperature such that the power is again balanced through the system. The path taken by the compressor during the "ideal" transient operation is shown on the map sketched in Fig. 3 and is called the normal operating line.

In reality, the increased fuel flow rate causes all of the events described above, but the rotational moment of inertia of the rotor must be factored in. Even though the turbine extracts excess power, the rotor speed does not immediately increase. The time dependent characteristics of the rotor system are such that the aerodynamic response is much faster, causing the system to follow a different path than if the rotor speed responded immediately. Instead of following the normal operating line to the new

operating point, the actual compressor pressure ratio is forced higher due to the increased combustor exit gas temperature. The compressor pressure ratio is increased by the increased combustor exit temperature due to the fact that the higher gas temperature requires a higher pressure in the combustor for the given mass flow rate to pass through the turbine nozzles (assuming they are choked). As the rotor speed gradually increases, the pressure ratio moves to the right, increasing the mass flow rate through the system. Finally, as the entire system reaches equilibrium, the engine returns to the normal operating line at the new operation point.

During the initial portion of the transient, the compressor pressure ratio increases along a given speed line. This can not continue indefinitely. Eventually, a point is reached at which the compressor operation becomes unstable and the boundary layer separates from the compressor blading [12]. The unstable event can occur as one of two phenomena. Surge, which occurs as a fully planar disturbance in which the entire compressor annulus reverses flow, empties the volume downstream of the compressor until the back pressure is relieved and the correct pumping action is reestablished. This phenomena is shown in Fig. 4. The filling and then emptying cycles are repeated until the cause of the surge event is removed. The frequency of the oscillations is determined by the elasticity present in the system. For the gas turbine engine, it is the compressibility of the air and the system volume that provides the elasticity [13]. Frequencies on the order of 10 Hertz are typical, although smaller engines with smaller volumes can have oscillations on the order of 20 - 30 Hertz.

Rotating stall, another type of compression system instability, occurs when a portion of the blading circumference is locally stalled by some destabilizing event such as a low-pressure region in the engine inlet. The region of reverse flow causes an increased angle of attack on adjacent blades, thus stalling them. The stalled region propagates from one blade passage to the next giving the impression that the stalled region rotates in the direction of the rotor rotation [14]. The frequency of the resulting pressure oscillations typically lies in the 50 - 100 Hertz range. This phenomena is shown in Fig. 5. The rotating stall event can be removed by opening up the flow area behind the compressor in order to increase the mass flow rate through the system. In a compressor rig, this can be accomplished by opening a valve. On an engine, however, there is typically no valve available to open. In fact, the combustion process has the effect of reducing flow through the turbine nozzles. Thus, rotating stall in a gas turbine engine is sometimes termed "nonrecoverable stall" [15]. Recovery from rotating stall is usually possible in an engine by stopping the fuel flow rate and restarting the engine.

Either event is an undesirable instability, which if not properly accounted for during the design process, can destroy an engine [16, 17]. Because the highest compressor efficiency and hence the compressor design point typically lie near the surge boundary (as shown in Fig. 2), even minor transients can result in the compressor system entering into surge or rotating stall. These excursions into the unstable operating regime can result in an undesirable reduction of the engine life [18].

Surge and rotating stall are not the only dynamic events that can occur in a gas turbine engine. A great deal of analysis effort has been spent in trying to develop an understanding of combustion processes and their effect on gas turbine engine operation. Ignition and extinction of the flame in the combustor has been researched extensively [19-20]. Highly cyclic combustion instabilities and the resulting acoustic interactions with the rest of the engine have also been dealt with in the literature [21-23].

1.2. Transient And Dynamic Engine Modeling Requirements

Given the complexity of the gas turbine engine's operation during both transient and dynamic events, it is important to ensure that the mathematical equations used to model the internal engine flow field include all of the necessary physics. It has been found that only the time-dependent equations for the conservation of mass and energy must be satisfied to model a transient event. The time-dependent compressibility of the gases and the dynamics of the system volumes (as represented by the equation for the conservation of momentum) can typically be neglected during a transient event. This is because of the large time scale involved in a transient event relative to the residence time of a particle of mass in the engine. The effects of volume dynamics and flow compressibility are simply not key players. It is also because of the relatively large time scale during transient events that specification of the various components can be in an overall sense. For example, the compressor performance characteristics can be given for the whole compression system, rather than considering or modeling each stage or rotor

behavior. Rotor rotational dynamics must be included, however, since rotor speed can change significantly during a transient event.

The number of dimensions modeled by the equations is entirely dependent on the type of problem being considered. Quantification of the engine performance during a transient event can be obtained with a one-dimensional model. Problems which are multi-dimensional in nature require multi-dimensional models to adequately simulate the system operation. For example, a study to look at the influence of the combustor pattern factor on the turbine power extraction as it changes during a throttle transient, would require at least a two dimensional, axisymmetric combustor model to predict the temperature profiles of the flow leaving the combustor.

On the other hand, for analysis of dynamic events, such as surge and rotating stall, the requirements for successfully modeling the engine system are much more analytically and computationally demanding. With the time scale of a dynamic event approaching the residence time of a fluid particle in the engine, the compressibility of the fluid and the volume dynamics of the system play a critical function in the resulting engine operation. The equations used to describe the system must therefore address the fluid compressibility and volume dynamics. That means that as a minimum, the mathematical model used to specify the dynamic problem must solve the compressible equations for conservation of mass, momentum, and energy. The small time scale of the dynamic model also means that component performance must be broken down to a level smaller than that of an overall component. Using the example from above, a dynamic model

must break the compressor performance down to at least a stage-by-stage level to ensure that the effects of a dynamic event are adequately resolved [2].

Considering the relatively small time scales of a dynamic event, however, rotor rotational dynamics can typically be neglected in a dynamic model. Because of the large rotor mass and the resulting large rotor polar moment of inertia, the rotor speed does not have time to change significantly during a dynamic event. For the same reason, a control system is typically not required for a dynamic model. An exception to this, however, is for models and simulations being developed to investigate active control schemes, an area of current day research [e.g., 24 - 26].

As with a transient model, the number of dimensions required for solving the problem under consideration is dictated by the problem itself. Since the axial direction is dominant in the gas turbine engine, one-dimensional models can solve a broad class of dynamic problems. As will be shown in Chapter 2, the bulk of the available literature on modeling gas turbine engines presents the results of one-dimensional models and simulations. There are occurrences, however, when a one-dimensional model is not sufficient. For example, inlet distortion requires some sort of modification to the one-dimensional model to appropriately handle the problem. Shahrohki [27] utilized a modified one-dimensional compression system model for addressing the effects of inlet distortion on a low aspect ratio fan. The influences of the radial and circumferential flow were considered using multiple one-dimensional grids with algebraically specified mass flow adjustments between the grids. This type of model provided acceptable results for

circumferential distortion patterns. For radial distortion, it was recommended that a two dimensional, axisymmetric model and simulation such as given by Hale, et. al. [28], be applied.

A requirement for both types of models and simulations is that they be usable and be able to withstand the rigors of the operational verification and calibration process. The concept of "usable" means that the simulation can be used in a timely fashion to obtain an entire engine aerothermodynamic solution. Solution times provided by workstation type computer resources should be measured in minutes, not days. The model also must not depend on data that is unobtainable for the operational verification and calibration process. No model and simulation will build the necessary credibility without proper calibration [29].

1.3. Statement Of Problem

The present research was undertaken to provide a usable mathematical model and simulation of a gas turbine engine, capable of simulating dynamic, post-stall events, which can also provide an efficient transient simulation capability, including these features:

- The mathematical model must be specified using the time-dependent, compressible, one-dimensional equations of conservation for mass, momentum, and energy.
- The compressor and turbine components in the gas turbine engine will be represented in a stage-by-stage manner. The combustor and other ducting will

be broken down into multiple control volumes to ensure adequate dynamic resolution.

- Models for the various systems in a gas turbine engine will be necessary, and they must function correctly over the full range of engine operation. These include the compression system, the combustor, the turbine, and rotor dynamics.
- For efficient transient solutions, an implicit numerical solver must be used. For dynamic events, with the resulting small time increment, an explicit flow solver would be more efficient. The numerical simulation should provide both types of solvers and the logic to know when to switch between them.

The ATEC model and simulation developed herein were focused on a turboshaft engine, such as is used in power generation or in helicopter propulsion units. Component models were developed for the compressor, combustor, turbine, and rotor dynamics. The operational fidelity of the model and simulation were addressed by operational verification and through calibrating the model and simulation to data.

2. LITERATURE SURVEY

With the introduction of the electronic computer to the engineering community, many mathematical models and computer simulations of the gas turbine engine have been developed. The models and simulations have been classified into three major categories, depending on the engine operational regime addressed by the model and simulation. The first category of model and simulation that has been developed addressed the steady-state engine operation at both on-design and off-design conditions. The second category of models and simulations addressed the transient operation of the gas turbine engine. The third category of models and simulations have addressed the operation of the gas turbine engine during dynamic events such as compressor surge. Several examples of these types of computer programs will be examined in this chapter.

The models and simulations developed for the gas turbine engine have varied from simple algebraic solutions to simulations that solve the fully three dimensional, viscous, time accurate Navier-Stokes equations. Computational capabilities have limited the latter type of model and simulation to steady-state analyses of the overall gas turbine engine. Future computer developments, such as massively parallel computers, may make the solution of the Navier-Stokes equations for transient and dynamic flow fields inside a complete gas turbine engine possible, but at present this is not feasible [32].

2.1. Steady-State Models

Steady-state models and simulations of the gas turbine engine have been developed and used since the initial development of the gas turbine engine. The early

steady-state models were typically algebraic in nature and required nothing more complex than the solution of a set of simultaneous equations that ensured that the conservation of mass and energy were maintained. As the power of the electronic computer has increased, the steady-state models and the computer simulations developed using these models have grown more complex. The growth in the complexity of the models and simulations have occurred not only in the algebraic equations used to describe the various components of the gas turbine engine, but also in the mathematical and numerical techniques used to solve the given model equations. The models and simulations developed by Fishbach and Caddy [29] and Mattingly [30] are excellent examples of steady-state computer programs.

2.2. Transient Models

Transient models and simulations of the gas turbine engine should not be considered simply an extension of a steady-state model to the time dependent domain. Two significant operational characteristics of the gas turbine engine must be addressed in a transient model and simulation that can be ignored in a steady-state model and simulation. First, an energy balance between the turbines and compressors of the gas turbine engine can not be assumed. The shaft rotation inertia must also be considered. Neither of these parameters must be considered in a steady-state model and simulation as the engine is by definition operating with a power balance across the various components. An example of a gas turbine engine transient model and simulation is provided by the work of Chappell and McLaughlin [31].

2.3. Dynamic Models

The survey of the available literature for this effort has focused on models that solve the time dependent conservation equations that have the capability of resolving the gas turbine engine system response during a dynamic event. As noted in Chapter 1, a dedicated transient model can not handle dynamic events, but a dynamic model may handle transient events. Large amounts of computer time, however, may be required to apply a dynamic model to study a transient event. The intent of this survey is to quickly show that the development of an integrated gas turbine engine model and simulation that can efficiently handle both transient and dynamic events and their interactions has not occurred to date and, as such, the development of such a model and simulation would be an advance in the state-of-the-art.

Gas turbine engine mathematical models and simulations reported in the open literature that address dynamic engine operation are listed in Table 1. Detailed references are included in the bibliography. It should be noted that not every piece of literature that uses a gas turbine engine model and simulation for the purpose of some analytical study is listed here. Only those works that discuss the development and calibration of the respective models are given.

Dynamic modeling and simulation of gas turbine engines received considerable attention during the 1970's from NASA. Seldner, et. al. [33] provided a nonlinear analog simulation technique for use in dynamics and controls research. The simulation addressed turbojet engine operation from idle to rated speed with dynamic events of up to

50 hertz. No post-stall capability was included. The J85-13 engine was the specific calibration data source. Each of the eight stages of the J85 compressor were modeled using individual stage pressure and temperature characteristic maps to solve the conservation of mass, momentum, and energy equations. The combustor was modeled using a lumped parameter approach, wherein the entire combustor section was modeled as one volume. Combustion dynamics were modeled by controlling fuel flow and, hence, heat release. The two stage turbine was modeled using overall characteristic maps due to a lack of individual stage characteristic maps. The modeling technique provided the foundation for later compressor modeling efforts (such as [34]), but there were shortfalls in the work. For example, compressibility effects were neglected due to the complexity of solving for flow Mach number (an iterative process) using an analog computer.

Szuch [34] provided a model and computer simulation (HYDES) that while building on the work presented in Seldner, et. al. [33], also took a few steps backwards. On the positive side, Szuch provided the user with multiple engine configuration options. The options varied from a single spool turbojet to a two spool, mixed flow turbofan with fan characteristic maps given for both the hub and tip sections of the blading. A schematic representation of the types of configurations that can be studied with the Szuch model and simulation is shown in Fig. 6. Unfortunately, the hybrid computer equipment on which the simulation was developed limited the complexity of the model. Unlike Seldner, et. al. [33], where the individual compressor stage characteristic maps were used, Szuch lumped all of the compressor stages together to use overall characteristic maps.

The lack of gas dynamic effects in the individual stages limited the application of the computer simulation to transient events measured in terms of seconds, not milliseconds (less than 10 Hertz). As in Seldner, et. al. [33], compressibility effects were neglected. No comparison to test data was made, and the results presented are for steady-state, off design solutions. The work by Szuch is noteworthy, however, because he demonstrated the feasibility of making the code structure modular, allowing the user to pick and choose the various parts to build up the entire engine under consideration.

Sellers and Daniele [35] provided an all digital simulation of the gas turbine engine model. The DYNGEN program, like the HYDES program in Szuch [34], provided the user with the capability to simulate many different engine configurations without rewriting the computer code. DYNGEN used a modified Euler method to solve the differential equations used to describe the flow processes occurring in the engine. The modified Euler method, which is substantially different from the forward-difference integration techniques typically used in digital simulations of this time period, provided a robust solution scheme with time step size large enough to provide reasonable run times. The method did, however, have numerical stability problems with time step sizes less than one millisecond. This limited the applicability of the program to steady-state and low frequency transient events. No comparison was found in the literature of the simulation results to test data.

Schuerman, et. al. [36], developed a high frequency model and computer simulation of a turbofan engine (the TF30). The objective of their study was to achieve a

frequency response up to 100 Hertz, but successful comparison to data was only obtained up to 10 Hertz. At 15 Hertz the simulation required twice the inlet pressure amplitude variation to stall the compressor as compared to the data. A comparison of the frequency response of the engine model to the actual engine is shown in Fig. 7. The comparison between the two sources is reasonable for frequencies up to about 10 Hertz. Beyond the 10 Hertz limit, however, the engine simulation fails to adequately match the test data. The equations of conservation of mass, momentum, and energy were solved implicitly through a relaxation method. The authors investigated the sensitivity of the results to the size of grid used. Stage by stage modeling of the fan and compressor systems was available, but the sensitivity study indicated that satisfactory results could be obtained at the lower dynamic frequencies with multiple stages being included in a given model element. The discretization of the fan and compressor region is shown in Fig. 8. No post-stall capability was included in the model and simulation. The results obtained indicated that the modeling of the fan bypass/core flow dynamic coupling and the transient aerodynamics of the flow splitter needed to be improved.

Mason, et. al. [37], took the basic model presented in Schuerman, et. al. [36] and enhanced the high frequency response of the simulation by including a radial term in the fan and splitter duct elements. Separate volumes were provided for the hub and tip regions at a given axial location. The radial term was provided to account for any flow exchange between the hub and tip region control volumes. The radial flow was calculated by solving the basic unsteady flow equations in the radial direction. The radial

term provided a means to handle radial total pressure distortion at the exit of the fan which occurs in the majority of turbofan operations. The initially calculated flow per unit area was held constant in both the core and bypass control volumes during the simulation run. This was accomplished by changing the radial location of the separating boundary between the two control volumes. This concept is sketched in Fig. 9. The model and simulation results compared favorably with test data for both the TF30 and F100 engines. Agreement was obtained up to a dynamic limit of 100 hertz, with the simulation matching resonant frequencies in the fan core and bypass streams with a slight error in the absolute magnitude. A comparison of the simulation results with measured F100 fan exit pressure is shown in Fig. 10 for a 52 Hertz augmentor rumble. The phase angle of the simulation system response in the bypass duct was too high by 55 degrees as compared to the data, but the magnitude variation was within 25 percent. A better match was obtained in the core volume, with the phase angle matching very closely and the magnitude variation was within 10 percent. This model and simulation was promisingly headed in the right direction, but there is no discussion concerning how efficient the solution process would be for a problem that was transient in nature.

Sadler and Melcher discuss the turbofan engine model and simulation DEAN (Dynamic Engine ANanysis) in [38]. Based on the description of the program given in the reference, DEAN is a interactive program which allows the user to simulate both engine subsystems as well as full gas turbine engine systems. Through the proper selection of inputs, the user can construct multi-variable performance maps for the

turbine and compressor systems. Models for the additional subsystems in the turbine engine are also provided. Four numerical schemes are available to solve the nonlinear ordinary differential equations that are used to describe the various systems. Unfortunately, the authors mostly report the details of the graphical interface to the program and not the details of the workings of the model and simulation. The only sample results given in the reference are of a simple compressor rig test. The simulation output shown is not compared to any test data, nor is a time scale given on the plots. No complete engine simulation results are shown.

The General Electric Company developed a turbofan engine model and simulation that was reported in [39]. K. Chung et. al. modeled a high bypass turbofan engine (6:1 bypass ratio) with both axial and radial flow possible in selected control volumes. Radial flow was permitted in the control volumes upstream and downstream of the single stage fan. All of the other control volumes assumed one-dimensional flow. The discretization of the flow domain is shown in Fig. 11. The characteristics for the fan were divided between the hub and tip region. Compressor characteristics were given in the form of pressure and work coefficients as shown in Fig. 12. The fourteen stage high pressure compressor was modeled by three one-dimensional control volumes, not with a stage-by-stage representation. Bleed ports were located at the exit of the three control volumes. The model was used to demonstrate control options for removing nonrecoverable stall. Comparison of the model results to actual test data was not directly made by the authors; model trends were shown to agree with the test data trends. The simulation utilized an

explicit solver, implying that transient event calculations would not be computationally feasible.

French [40] reports on the modeling work performed by Pratt & Whitney Aircraft. Because of the proprietary nature of the work, little is said about the actual model and simulation formulation in the paper. It is mentioned that the program uses a variable time step implicit formulation in order to provide computational efficiency. Large time step sizes are taken until a limit on the derivatives is exceeded. The time step size is then reduced until the limit is not exceeded. This computational scheme permits efficient solution of both transient and dynamic events during the same test case run. To demonstrate the capabilities of the scheme, a bodie transient is presented, in which the compression system enters into a rotating stall. The resulting combustor inlet pressure is plotted versus time in Fig. 13. The locations are identified at which the simulation works in the low frequency mode and then switches into a high frequency mode (smaller time step size).

The various components of the simulated gas turbine engine were broken down into individual control volumes, where the multi-stage fan was modeled as a single control volume, as was the high pressure compressor. French stated that this was acceptable due to the fact that surge and stall events have a fundamental frequency of less than 100 hertz. The momentum of the flow was conserved only in the compression system control volumes. One observation made by French that will have bearing on the current effort is that because of the very rapid nature in which the internal flow can

change direction during post stall events, careful accounting of the energy balances must be maintained for both forward and reverse flow. It is also noted that low frequency dynamics and rotor speed transients must also be included for the model and simulation to be a usable design tool. The model and simulation results are compared to compressor rig results and data from a moderate bypass ratio turbofan engine. In both cases, the model and simulation compared favorably to the test data, both in terms of frequency and magnitude of the system oscillations.

Hosney, et. al., [41] likewise provided a turbofan model and simulation similar to Chung, et. al., and French. The individual components of an engine were modeled as single control volumes, with interconnecting ducting control volumes separating each of the component control volumes. Two dimensional flow volumes were provided just upstream and downstream of the fan control volume. Stage-by-stage representation of the compressor was not provided. The simulation used an implicit numerical scheme to solve the model equations. Results of the model were compared to test data obtained from an F101X augmented turbofan engine. The comparison indicated a significant degree of similarity between the test data and the simulation results relative to the shape and character of key parameters. However, no quantitative comparison of the simulation predictions and the test data was given.

A model and simulation of a J85 turbojet engine is reported in [42]. Sugiyama, et. al., developed a one-dimensional, lumped volume model of the J85 turbojet engine to conduct a parametric study of the compressor stage characteristics during surge. Eleven

parameters were used to describe the pressure ratio, efficiency, and time constants of the compressor system during post-stall operation. These parameters are shown and defined in Table 2. The parameters were used to tune the model results to match the available test data. The location and range of influence of each of the tuning parameters on the stage characteristic curves are shown in Fig. 14. Each stage of the eight stage axial compressor was treated as a separate control volume. The blade forces of the rotor and stator blades were applied to the flow using actuator disk theory [43]. An actuator disk was located at the inlet of each compressor control volume. The two stage turbine was modeled using one control volume due to lack of interstage performance data. A turbine actuator disk used to account for the forces acting on the gas flow in the turbine was added at the control volume exit. A fourth-order predictor-corrector explicit integration method is used to solve the differential equations. The model did not include components necessary for transient modeling such as rotor dynamics and engine controls.

The work reported by Schobeiri, et. al., [44-46] documented the development of a multispool turbojet engine model that can be configured to handle several engine types. This model also breaks the engine domain down into control volumes and solves the Euler flow equations. An implicit flow solver is used which uses variable time step sizes. Rather than represent the compressor and turbine stages using experimentally derived stage characteristics, this model and simulation used row-by-row geometry data and the flow loss and efficiency characteristics. While this approach can provide a more fundamental understanding of the processes going on in the compressor and turbine

stages, it can not be used to simulate post-stall operation. The method, further developed in [47], does provide a capability to perform non-stalled analyses for compressors where experimental data is not available. Calibration of the model was limited in the report to transient events, and included a single shaft turbojet shut down, a power turbine adverse load change, and fuel flow variation. The only comparisons to experimental data are made for power output and rotor speed, as shown in Fig. 15.

Badmus, et. al., [48] presents a general one-dimensional model for a gas turbine engine and the various components. No simulation has been developed using the model equations, however, for a full gas turbine engine. Application of the model equations to a single stage compression system is presented in the work by Badmus, Chowdhury, et. al. [49]. The model equations were set up to be solved using an explicit ordinary differential equation solver and, as such, would not provide an efficient transient capability. The primary focus of the model was on control algorithm development. One interesting aspect of the model is the use of effective lengths for the rotating flows. Axial lengths are extended to account for the rotation of the flow inside the engine. It is shown in Badmus, Chowdhury, et. al. [49] that the need for empirical, first order linear time lags is removed for compression system models.

2.4. Current State-of-the-Art

With this brief review of the literature, it can be argued that the current state of the art in gas turbine engine modeling does not satisfy the requirements for a gas turbine engine model and simulation capable of simulating dynamic, post-stall events while also

providing an efficient transient simulation capability as was specified in Section 1.3 above. The general capabilities of each of the above referenced models and simulations are tabulated against the given requirements in Table 3. The current state-of-the-art in the time-dependent modeling of the complete gas turbine engine is limited to one- and two-dimensional models and simulations that solve the equations for the conservation of mass, momentum, and energy as given by the Euler equations for fluid motion in the compressor section. Downstream of the compressor, the current state-of-the-art is limited to a control volume type approach wherein the effects of flow momentum are neglected. A more efficient approach to simulating both transient and dynamic events can be obtained as the current state-of-the-art in gas turbine engine modeling uses an implicit flow solver for both flow regimes. A strong foundation has been laid by previous efforts, and will provide significant guidance in the development of a mathematical model and computer simulation capable of providing the transient and dynamic simulation capabilities as given in Section 1.3.

3. MODEL DEVELOPMENT

The point of origin for the development of ATEC was provided by the Dynamic Turbine Engine Compressor Code (DYNTECC) ([50] and [2]). The Advanced Turbine Engine Simulation Technique (ATEST) code [31] was also used as a stepping stone to the ATEC simulation. DYNTECC is a stage-by-stage, one-dimensional compression system model and simulation. It was chosen as one of the foundations for this effort for two reasons. First, DYNTECC has been in use throughout the country for approximately 5 years, and has been established as a useful tool by numerous researchers [27, 51-59]. It provides a fast and efficient simulation for analyzing dynamic compressor operation during both pre- and post-stall operation. Secondly, most of the DYNTECC development activities have been conducted at the Arnold Engineering Development Center (AEDC). The people most familiar with DYNTECC were available to the author for consultations on the development of ATEC. The ATEST simulation provided guidance and "lessons learned" on how to transiently model a complete gas turbine engine. ATEST also provided the form of expression for the turbine performance characteristics used in ATEC.

To reach the point of a full gas turbine engine transient model and simulation with dynamic capabilities that satisfy the requirements specified in Section 1.3, several fundamental enhancements to the DYNTECC model and simulation were required. These enhancements were added by the author to construct the ATEC model and simulation from DYNTECC, and included adding the necessary models required to

describe a full gas turbine engine during both transient and dynamic events. Modifications to the flow solver was also required to improve the efficiency of the code during transient events while maintaining the already efficient solver capabilities for the dynamic events. Component models added by the author included descriptions of the combustor and turbine performance. Additional models were provided for the rotor dynamics and heat transfer` effects in the axial compressor. Finally, a variable time step routine was added to ATEC by the author that permits relatively large time step sizes during steady-state and transient events but reduces the time step size to an appropriate level during dynamic events.

3.1. Governing Equations

The ATEC simulation uses a finite difference numerical technique to simultaneously solve the mass, momentum, and energy equations with or without turbomachinery source terms (mass bleed, blade forces, heat transfer, and shaft work). The compression system source terms are determined from a complete set of stage pressure and temperature characteristics. The combustion system source terms are determined from a complete specification of the fuel energy content, flammability limits, and combustion efficiency. Turbine system source terms are determined from a complete set of the mass flow function, work done factor, and efficiency characteristics. A representative, single-spool, gas turbine engine is illustrated in Fig. 16.

The engine systems are modeled by an overall control volume as shown in Fig. 17. The overall control volume is subdivided into a set of elemental control volumes as

shown in Fig. 18. Typically, the compressor section is subdivided such that the axial length of each control volume is defined by the individual compressor stages. The compressor stages are defined as either rotor-stator or stator-rotor combinations, depending on how the experimental stage characteristics are obtained. All other duct control volume axial lengths are selected to maintain approximately the same average length as was used in the compressor section. Using the same approximate length for the control volume axial lengths in regions other than the compressor section helps to ensure that a common frequency response limit is obtainable throughout the entire grid.

The governing equations are derived from the application of mass, momentum, and energy conservation principles to each elemental control volume as sketched in Fig. 19. These equations can be expressed as:

$$\frac{\partial \mathbf{U}}{\partial t} + \frac{\partial \mathbf{F}}{\partial x} = \mathbf{G} \qquad [3.1]$$

where

$$\mathbf{U} = \begin{Bmatrix} S\rho \\ \rho Su \\ SE \end{Bmatrix} \qquad [3.2]$$

$$\mathbf{F} = \begin{Bmatrix} \rho Su \\ \rho Su^2 + SP \\ u(SE + SP) \end{Bmatrix} \qquad [3.3]$$

$$\mathbf{G} = \begin{Bmatrix} -W_{Bx} \\ F_x \\ Q_x + SW_x - H_{Bx} \end{Bmatrix} \qquad [3.4]$$

The specific flow variables are density ρ, static pressure P, total energy per unit volume E, and the axial flow velocity, u. The cross-sectional area of the flow path is defined as S. The turbomachinery source term for the conservation of mass equation is the bleed flow rate distribution w_{Bx}. The conservation of momentum equation turbomachinery source term is F_x, which is the axial force distribution acting on the control volume. This term can be broken down further into axial components for blade forces and wall forces:

$$F_x = F_b + P\frac{\partial S}{\partial x} \qquad [3.5]$$

The blade and wall forces are lumped together in the ATEC model formulation due to the difficulty of separately distilling the effects of each from experimental data [60].

The conservation of energy equation turbomachinery source terms include the heat transfer rate into the control volume fluid Q_x, the shaft work distribution applied to the control volume SW_x, and the enthalpy change due to the bleed flow distribution H_{Bx}.

Several other equations are required to obtain closure of the equation set. These include the ideal gas equation of state:

$$P = \rho RT \qquad [3.6]$$

A constant ratio of specific heats is also assumed:

$$\gamma = \frac{c_p}{c_v} = \text{constant} \qquad [3.7]$$

Mach number is defined as the ratio of the flow velocity divided by the speed of sound in the fluid:

$$Mn = \frac{u}{a} \qquad [3.8]$$

where

$$a = \sqrt{\gamma RT} \qquad [3.9]$$

and

$$R = \frac{\mathcal{R}}{MW} \qquad [3.10]$$

where $\mathcal{R}$ is the universal gas constant and MW is the flow molecular weight. The definition of total temperature is given as:

$$T_t = T\left(1 + \frac{\gamma + 1}{2} Mn^2\right) \qquad [3.11]$$

and the definition of total pressure is given as:

$$P_t = P\left(1 + \frac{\gamma + 1}{2} Mn^2\right)^{\frac{\gamma}{\gamma - 1}} \qquad [3.12]$$

To provide compressor and turbine stage force (F_X) and shaft work (SW_X) inputs to the momentum and energy equations, sets of steady-state stage characteristics must be available for closure. Likewise, providing the combustor heat addition (Q_X) to the energy equation requires a set of steady-state flammability limits and combustion efficiency maps. The models used to provide this information to the flow solver will be discussed in the following sections.

The model and simulation are formulated as an initial condition boundary value problem. Initial conditions for the dependent variables ($\rho S, \rho Su, ES$) are provided by an internal steady-state calculation routine. Major inputs include the corrected rotational speed of the rotor, the initial airflow rate, and the boundary condition type and magnitude. A set of initial conditions for each control volume entrance is calculated using steady-state flow physics and pre-stall compressor stage characteristics. This develops a steady-state initial conditions set of data from which the time dependent model solution is initiated. Upon specification of boundary conditions, the simulation is ready for execution.

Time dependent boundary conditions can be specified at the entrance and the exit of the overall control volume. Inlet total pressure or temperature time history may be linearly ramped, varied cyclically, or remain constant. The same is true during a given simulation for the overall control volume exit pressure, Mach number, or airflow rate. At the entrance, both total pressure and total temperature must be specified. At the exit, however, only static pressure, Mach number, or mass flow rate is specified. All other parameters are obtained from reference plane characteristic theory. Details of the flow solution technique, including a description of how boundary conditions are applied are discussed in Section 3.3.3 and in Appendix C.

3.2. Component Models

Given the overall specification of the governing equations, models of the various components of the gas turbine engine are used to provide closure to the equations. These models are discussed in the following paragraphs.

3.2.1 Compressor Model: Traditionally, steady-state compressor stage characteristics are presented in the form of pressure ratio across the given stage versus the corrected mass flow rate entering the stage along lines of constant rotor speed. Lines of constant efficiency are also typically plotted on the compressor map, as is shown in Fig. 2. An alternate form of presenting compressor stage characteristics was shown in [39], where a compressor pressure coefficient and work coefficient were plotted against a flow coefficient. In whatever form the compressor characteristics are presented, they can be used to provide the governing equations of the subject model and simulation with the total pressure and total temperature rise across the compressor stage.

Using the compressor model from the DYNTECC simulation [2], the ATEC model and simulation currently utilizes the compressor stage characteristics presented as a pressure and temperature coefficient plotted versus a flow coefficient for lines of constant rotor speed. The exact form of the pressure, temperature, and flow coefficients can vary, depending on which form gives the smoothest surface in the operational space (a subjective decision on the part of the user). A smooth surface is desirable in order to ensure accurate reading of the compressor characteristic maps by the simulation.

The simulation can handle the coefficients specified in one of four manners. The first approach classically defines the stage flow coefficient, ϕ, as

$$\phi = u / U \qquad [3.13]$$

where u is the axial flow velocity and U is the circumferential wheel speed at the mean-blade radius. Pressure and temperature coefficients, Ψ^P and Ψ^T respectively are defined as:

$$\Psi^P = PR \qquad [3.14]$$

$$\Psi^T = TR - 1 \qquad [3.15]$$

The form of the flow coefficient defined above does not lend itself to terms that are easily measured. By using the concepts of Mach number, flow function, and critical reference state, stage characteristics can be manipulated to produce the following form, which differs from the classical definition by a constant.

$$\phi = \frac{W_{cor} NR_{cor}}{W_{cor}^{**}} \qquad [3.16]$$

where

$$W_{cor} = \frac{W\sqrt{T_t}}{P_t S} \qquad [3.17]$$

and W is the actual physical airflow entering the compressor stage, T_t is the total temperature of the air flow entering the compressor stage, and P_t is the total pressure entering the compressor stage. The corrected rotor speed is defined as:

$$NR_{cor} = \frac{\text{Design Corrected Speed}}{\text{Actual Corrected Speed}} \quad [3.18]$$

The term in the denominator of Equation 3.16 references the compressor inlet conditions to sonic conditions and is given by:

$$W_{cor}^{**} = \text{Constant} = 0.5318 \quad [3.19]$$

The pressure and temperature characteristic coefficients are given by:

$$\Psi^{P} = (PR^{\frac{\gamma-1}{\gamma}} - 1)NR_{cor}^{2} \quad [3.20]$$

$$\Psi^{T} = (TR - 1)NR_{cor}^{2} \quad [3.21]$$

A third form of the characteristic coefficients take the second type of characteristic coefficients and corrects the pressure and temperature of the flow to standard day conditions. It is given by:

$$\phi = W_{cor}^{'} NR_{cor} \quad [3.22]$$

where

$$W_{cor}^{'} = \frac{W\sqrt{TR_{ref}}}{PR_{ref}} \quad [3.23]$$

$$TR_{ref} = \frac{T_t}{T_{ref}} \quad [3.24]$$

$$PR_{ref} = \frac{P_t}{P_{ref}} \quad [3.25]$$

and NR_{cor} is as shown in Equation 3.18. The pressure and temperature characteristic coefficients are given by:

$$\Psi^P = (PR - 1)NR_{cor}^2 \quad [3.26]$$

$$\Psi^T = (TR - 1)NR_{cor}^2 \quad [3.27]$$

A fourth form of the characteristic coefficients is a variation of the third type and is defined by ignoring the influence of speed:

$$\phi = W_{cor}^{'} \quad [3.28]$$

where $W_{cor}^{'}$ is given in Equation 3.23. The pressure and temperature characteristic coefficients are given by:

$$\Psi^P = (PR - 1) \quad [3.29]$$

$$\Psi^T = (TR - 1) \quad [3.30]$$

After the stage characteristic definition has been chosen and the characteristics have been specified in the proper form , the simulation will automatically return steady-state total pressure ratio, PR , and total temperature ratio, TR , as a function of any airflow rate, W .

A typical set of steady-state characteristics for both pre-and post-stall operation is presented in Fig. 20. Although only one speed line is shown for purposes of clarity, a complete set of compressor characteristics would include lines for each stage and the selected speeds. The stage characteristics are divided into three distinct regions: pre-stall, rotating stall, and reversed flow. The pre-stall characteristic represents the performance of a blade row in normal operation. The transition to a rotating stall characteristic is approximated as a continuous characteristic along a postulated throttle

line. The performance in the rotating stall region is based upon flow-weighted averages of the pressures and temperatures in a fully-developed rotating stall cell. The pressure and temperature ratios in this region represent the average pressure and temperature rise across the stage for both stalled flow and unstalled flow. The reversed-flow characteristic region represents the pressure loss and temperature rise associated with full-annulus reversed flow. The discontinuity at zero flow has been experimentally shown to exist for a three-stage low-speed compressor [61]. This aspect of the quasi-steady flow characteristic has been incorporated into the modeling technique and can be implemented if so desired.

With the steady-state total pressure ratio and temperature ratio at an assumed steady flow rate, the simulation uses the steady-state version of the conservation equations to compute the appropriate steady-state control volume forces and shaft work. These values are then used in the dynamic equations (Equation 3.1) as the necessary values of the forces in the momentum equation and shaft work in the energy equation. A more detailed discussion of this technique will be given in Section 3.3.4.

The foregoing discussion of the stage characteristic has described the principal features of the pre-stall and reversed-flow steady-state performance, and the globally-steady rotating stall average performance. For pre-stall and post-stall reversed flow, steady characteristics can be used as they exist. However, for a dynamic event such as rotating stall or surge, the use of steady characteristics is not complete. In the post-stall region, the stall cell develops very rapidly and the globally steady characteristics are no

longer applicable. To provide a dynamic stage characteristic, a first order time lag on the stage forces has been incorporated into the modeling technique in the post-stall stall region only [50]. The first order lag equation used is:

$$\tau_{comp} \frac{dF_x}{dt} + F_x = (F_x)_{ss} \qquad [3.31]$$

where F_x is the blade force and pressure area force as given in Equation 3.5, τ_{comp} is a time constant used to define the compressor response time, and $(F_x)_{ss}$ is the steady-state value of the blade force and pressure area force obtained from the steady-state compressor characteristics.

Time constants are provided for two portions of the compressor stage operation during the dynamic event. As shown in Fig. 21, a time constant is provided for the time period that the compressor is just starting to reverse flow (pressure is high and flow rate derivative as a function of time is negative). After the flow reaches its maximum negative value and the pressure has been relieved, a separate time constant is supplied to control the reacceleration process. The steady-state characteristics are used "as-is" during the reversed flow and repressurization processes.

The use of time constants in describing the performance of the system volume dynamics during post-stall operation is similar to the use of the B parameter as given by Greitzer [12].

$$B = \frac{U}{2\omega L_c} \qquad [3.32]$$

where U is the rotor speed, L_c is an effective length of the compressor volume, and ω is the Helmholtz resonator frequency of the system. Depending on a value of B, the compression system responds differently during post-stall operation. A critical value of B can be determined that defines the operational point at which the compression system either enters into surge cycles or rotating stall. The value of the B parameter, however, is difficult to determine for a realistic compression system due to the difficulty of defining L_c and ω. On the other hand, the time constant τ_{comp} is readily determined by matching simulation results to experimental data for a given system. In this sense, the transient and dynamic model is calibrated by experimental data.

The above discussion focuses on using experimental data to define the compression system characteristics. There are also numerous analytical techniques for defining the characteristics. Examples include the row-by-row diffusion factor and loss correlation technique [47] or a streamline curvature approach [28]. It must be noted, however, that any analytical method used must be correlated to actual test data to ensure the accuracy and consistency of its predictions. An analytical approach could require the calculation of the compressor characteristics at each time step. Using the characteristic maps as discussed above is much more computationally efficient since the characteristics can be determined from a simple table search. The analytical methods are not without merit, however, since they can be used to build the compressor characteristics before test data are available.

3.2.2 Combustor Model: The combustor provides an environment in the gas turbine engine in which stable and efficient combustion occurs. A typical annular-type combustor cross-section is sketched in Fig. 22. The primary zone in the combustor provides a near-stoichiometric region of recirculating flow which provides the incoming fuel and air mixture sufficient time to react and burn. As shown in the figure, not all of the air flow exiting the compressor is used in the primary zone combustion process. Some percentage of the air flows around the internal liner and is mixed with the hot combustion products downstream of the primary zone. This bypass or dilution flow provides three benefits. First, the reduced air flow into the recirculating primary zone increases the fuel-to-air ratio to near stoichiometric proportions. This moves the combustion process away from the lower, or lean, limit of combustion. Second, the bypass air also cools the hot combustion products to below the maximum temperature limit of the turbine nozzle materials, and third, the bypass air cools the combustor walls and liner.

The dynamic combustor model used in the gas turbine engine model and simulation is a one-dimensional heat release model. Given the flow conditions in the control volumes that define the combustor, the amount of energy generated by the combustion of the fuel is calculated and input to the overall flow solver. The overall cross-sectional area of the combustor is specified for the geometry. Because of the one-dimensional formulation of the model, the liner is neglected.

The energy added to the flow is treated as a source term just as heat transfer is treated in the compressor model. The amount of heat released is a function of five primary variables: the combustor primary zone equivalence ratio, the combustion efficiency, the upper and lower flammability limits, and the lower heating value of the fuel. As with the compressor, the overall combustor volume is divided into individual control volumes as shown in Fig. 23.

The equivalence ratio of the flow in the combustor is a function of the airflow rate, the fuel flow rate, and the stoichiometric fuel-to-air ratio of the fuel. The percentage of the air entering the combustor which is used in the actual combustion process is accounted for in the equivalence ratio calculations. As occurs in a physical combustor, the model and simulation has the option of mixing the fuel with only part of the incoming airflow. To model the effect of the bypass flow in the combustor, the fraction of the overall airflow involved in the combustion process can be specified. For example, if the actual engine has a combustor where 50 percent of the air flow enters the primary zone and 50 percent goes into the liner, the equivalence ratio calculation will use only 1/2 of the airflow rate. The one dimensional nature of the combustor model, however, results in the temperatures calculated in the combustor be mass averaged values between the temperature of the primary zone and the temperature of the bypass flow.

The combustor flammability limits are determined by using steady-state engineering correlations developed by Herbert [62]. In order for stable combustion to

occur, the primary zone equivalence ratio (ϕ_{PZ}) must fall within a rich limit and a lean limit:

$$\phi_L \leq \phi_{PZ} \leq \phi_R \qquad [3.33]$$

Based on experimental data, Herbert defined a Combined Air Loading Factor to calibrate the lightoff and blowout data.

$$CALF = \frac{W_{PZ}}{V_{pz} P_{t3}^2 e^{\left(\frac{T_3}{n}\right)}} \qquad [3.34]$$

where W_{PZ} is the mass flow rate of the air entering the combustor primary zone, V_{PZ} is the volume of the combustor primary zone, P_{t3} is the total pressure of the flow entering the combustor, T_3 is the temperature of the flow entering the combustor, and:

$$n = 220\left[\sqrt{2} \pm \ln\left(\frac{\phi_{PZ}}{1.03}\right)\right] \qquad [3.35]$$

The plus sign corresponds to $\phi_{PZ} \geq 1.03$. A typical data set as given in [62] is shown in Fig. 24. A polynomial curve fit of Herbert's flammability data for a generic can type combustor is used in the simulation model.

Combustion efficiency is determined by using steady-state engineering correlations developed by Lefebvre [63]. Lefebvre assumed that the overall combustion efficiency is limited by the efficiency of fuel evaporation and the reaction efficiency.

$$\eta_c = \eta_e * \eta_r \qquad [3.36]$$

where

$$\eta_e = 1 - \exp\left[\frac{-36*10^6 P_3 V_c \beta}{W_{PZ} D_0^2 T_c}\right] \qquad [3.37]$$

and

$$\eta_r = 1 - \exp\left[\frac{-0.022 P_3^{1.3} V_c \exp(T_c/400)}{W_{PZ}}\right] \qquad [3.38]$$

A plot of the data used by Lefebvre to develop these correlations is shown in Fig. 25. Further modification to the Lefebvre work following Derr and Mellor [64] is made such that $V_c = V_{PZ}$ and $T_c = T_{PZ}$. In turn, T_{PZ} is estimated by averaging the temperatures at the interfaces of the primary zone control volumes.

During the dynamic operation of the combustor, it is possible for the combustion process (and hence the heat release) to occur for a short period of time even though the combustor equivalence ratio may lie outside the steady-state flammability limits. Likewise, the combustion process may not resume immediately after the combustor equivalence ratio reenters the flammability bounds due to ignition time delays [65]. To account for these effects, Davis [14] proposed using a first order lag on the heat release rate similar to the one used in the compressor model which is incorporated in the present combustor model as:

$$\tau_{comb} \frac{dQ_x}{dt} + Q_x = (Q_x)_{ss} \qquad [3.39]$$

where Q_x is the heat release rate in the control volume as is used in the governing equations (Equation 3.1), $(Q_x)_{ss}$ is the steady-state value of the heat release rate

calculated in the combustor model at the current time step, and τ_{comb} is a time constant used to model the combustor heat release response time.

Time constants are provided to lag both the flame extinction process and the ignition process. A typical value of both time constants is 0.005 seconds. The use of the first order time lag functions provides a model to account for such variables as radiation losses, finite chemical reaction times, and fuel diffusion effects. During reversed flow operation, it is assumed that the combustion process is extinguished, and the steady-state value of heat release is set to zero.

Pressure loss in the combustor is based on a one-dimensional, constant cross-sectional area analysis of the combustor stagnation pressure loss due to the energy release, as given by Oates [66]. The model assumes that the combustion gases generated are calorically perfect at the inlet and exit of the combustor, and that the mass addition rate of fuel is small relative to the air flow rate. The total pressure ratio across the combustor is given by:

$$\frac{P_{t4}}{P_{t3}} = \frac{\left(1+\frac{\gamma_4-1}{2}Mn_4^2\right)^{\gamma_4/(\gamma_4-1)}}{\left(1+\frac{\gamma_3-1}{2}Mn_3^2\right)^{\gamma_3/(\gamma_3-1)}}\frac{P_4}{P_3} \qquad [3.40]$$

where

$$\frac{P_4}{P_3} = \frac{1+\gamma_3 Mn_3^2\left[1-(Cd/2)\right]}{1+\gamma_4 Mn_4^2} \qquad [3.41]$$

Station 3 is assumed to be at the inlet to the combustor and Station 4 is at the combustor exit. The influence of the pressure loss coefficient Cd and the combustor inlet Mach number Mn_3 is shown in the plot presented in Fig. 26.

3.2.3 Turbine Model: Consistent with the approach taken to formulate and construct the compressor model, turbine performance characteristics are defined which have a particular format, and in which they are typically presented. A generic plot of a turbine performance characteristic is sketched in Fig. 27. The turbine flow function is based entirely on upstream total flow conditions:

$$TFF = \frac{W_4\sqrt{T_{t_4}}}{P_{t_4}} \qquad [3.42]$$

Once the turbine flow function is calculated, the total pressure ratio across the turbine stage and its adiabatic efficiency can be found from curves similar to those shown in Fig. 27 for a given engine speed. The total temperature ratio across the turbine stage is then calculated based on the total pressure ratio and the turbine adiabatic efficiency.

In practice, however, for the model and simulation presented herein, a minor change was made to the above procedure to increase computational efficiency and stability for modeling an engine starting process. The plot of turbine flow function versus total pressure ratio was replaced with two curves, which are shown in Fig. 28. Using the same definition for the turbine flow function, the turbine work done factor WDF is found from the first plot for a given rotor speed and turbine flow function (Equation 3.42). The turbine work done factor is defined as:

$$WDF = \frac{h_4 - h_5}{T_{t4}} \qquad [3.43]$$

Knowing the total specific enthalpy of the flow entering the turbine and the inlet total temperature, the exit total specific enthalpy can be calculated. The turbine inlet specific enthalpy h_4 is calculated accounting for the combustion processes occurring in the combustor. The value of h_4 (and the effects of combustion on the flow properties) is not used in the flow solver, since the flow solver was formulated assuming constant values of the specific heats of the flow. The correction to the turbine inlet flow enthalpy must be made in order to obtain the correct work extraction from the turbine. Once the turbine work done factor is known for the given inlet flow conditions and rotor speed, the turbine stage exit temperature is found. Given the total temperature ratio across the turbine, the second plot shown in Fig. 28 is used to obtain the total pressure ratio across the turbine stage. At this point, sufficient information has been obtained about the turbine to move on to the next component in the simulation

The choking line shown in Figs. 27 and 28 is a result of the actual flow restriction inside the engine caused by the turbine nozzles (or stators). In the one-dimensional representation of the engine by the model and simulation, the physical blockage afforded by the nozzles is not provided. The engine is typically modeled using the overall flow passage geometry with no reduction in area made for blading. The mass flow through the turbine, however, can not exceed the limit given by the turbine flow function. To account for this effect in the model, the flow is restricted to the maximum value of the turbine flow function for a given speed. In an actual engine, although the nozzle geometry does

not change as a function of speed, the location of the choking point (and hence the nozzle throat area) does change slightly due to boundary layer differences.

The plot of total temperature ratio versus total pressure ratio for given rotor speeds is obtained from information such as shown in Fig. 28. The use of total temperature ratio versus total pressure ratio is desirable for this type of model and simulation since for zero flow, the respective ratios collapse to unity. The efficiency, however, converges to zero, which creates a singularity in the calculated turbine work when related to an isentropic value [31].

3.2.4 Rotor Dynamics Model: Although not directly tied to a source term calculation, the rotor dynamics play an important function in the transient operation of a gas turbine engine. For both the compressor and turbine models, the rotor rotational speed determines where, on the given operational maps, the operating condition is located.

As noted above, the rotor rotational speed is given as part of the initial conditions. Once the time integration process is started, the change in rotational speed is given by:

$$\frac{d\omega}{dt} = \frac{1}{I}\left(\Gamma_t - \Gamma_c - \Gamma_v - \Gamma_p + \Gamma_s\right) \qquad [3.44]$$

where I is the rotor polar moment of inertia, ω is the shaft rotational speed, Γ_t is the torque produced by the turbine, Γ_c is the torque required by the compressor, Γ_v is the torque required to account for viscous losses, Γ_p is the torque required to satisfy any

customer power requirements, and Γ_s is the net torque produced by the starter and delivered to the rotor.

The rotor dynamics model is integrated into the overall simulation at the end of the time marching routine. To begin a new time step, it is assumed that the rotor rotational speed is known either from the initial conditions or from the previous time step. During the calculation of source terms for the current time step, the rotor rotational speed is held constant. Given the changes in source terms that occur during the current time step, a new flow field solution is determined by the flow solver routine. With the new flow field variables, the change in rotor speed is determined by using Equation 3.44. With the new value for rotor rotational speed, the simulation moves on to the next time step. The inclusion of the rotor dynamics model in the ATEC simulation is discussed further in Section 3.3.4.

The rotor dynamics model works with torque rather than power due to the requirements at zero speed. If power, which is the torque divided by the rotor speed, is used during an engine starting process, the initial rotor speed of zero will result in power requirements being indeterminate. Rather than basing the change in rotor speed on a power balance, the rotor dynamics model tracks the torque level as given by the starter motor and other interacting components.

3.2.5 Heat Transfer Model: During normal engine operation, heat transfer processes occur throughout the engine. Heat transfer from the air to the compressor blading and through the liner of the combustor are just two examples of where large

quantities of energy are exchanged continuously. The effects of this heat transfer on the gas turbine engine operation can be significant [67]. During steady-state operation, however, the heat transfer effects are implicitly built into the component performance maps. Since the simulation is based upon steady-state performance maps, the heat transfer does not have to be considered and modeled to match the steady state operation.

Frequently, however, the engine is not operated at the conditions for which the steady-state performance maps were developed. For example, if the engine is started shortly after it has been shut down, the metal temperatures inside the engine will not have had a chance to reach thermal equilibrium with the ambient environment. The higher-than-normal metal temperatures and the resulting heat transfer to the air decreases the density of the air as it passes through the compressor. This in turn reduces the performance of the compression system by decreasing the corrected air flow rate through the system. Likewise, if an engine is started with the metal temperature being colder than ambient, the reduced energy of the air due to the heat transfer will increase the corrected air flow rate through the system. If the heat transfer rate to the air is high enough, the reduced corrected air flow rate can raise the pressure across the system to the point of stall [68].

The ATEC model and simulation will consider only the effects of the heat transfer in the axial compressor. This limitation is based on the fact that the heat transfer in the compressor has a large aerodynamic influence on the performance of the system. The heat transfer that occurs in the other components, such as the combustor and turbine, is

important, but mainly from a structural point-of-view. The ATEC simulation is certainly capable of providing heat transfer models for the other components, but for the purposes of this dissertation, only the compression system will be modeled. The heat transfer model will also only consider the heat transfer occurring inside the engine. It will be assumed that the overall engine operates adiabatically with the surroundings.

Two paths for the heat transfer are available in the compressor as shown in Fig. 29. In a stator row, the heat can be convected from the air to the stator blades and then conducted to the outer engine casing. In a rotor row, the heat is likewise convected from the air to the rotor blading and then conducted to the rotor. To represent the convective and conductive flow paths, a simple representation of the system will be used. The heat transfer model will track four temperatures. They are the rotor and stator blade temperatures, and the base metal for the respective blades. The temperatures will be determined using standard engineering textbook equations [69]. The convective heat transfer rate from the blade to the air is given by:

$$\dot{q}_{b-a} = \bar{h} A_s \left(T_{blade} - T_{gas} \right) \qquad [3.45]$$

where T_{gas} is the average total temperature of the air flow through the compressor stage. The conductive heat transfer rate from the blade to the base is given by:

$$\dot{q}_{b-b} = (kL)_{eff} \left(T_{base} - T_{blade} \right) \qquad [3.46]$$

where $(kL)_{eff}$ is a measure of the potential for conduction heat transfer. It is a combination of the thermal conductivity of the blade material and the overall all length

across which the conduction occurs. Given these two heat transfer rates, the metal temperatures are calculated using:

$$T_{blade}^{n} = T_{blade}^{n-1} + \frac{\left(\dot{q}_{b-b} - \dot{q}_{b-a}\right)}{m_{blade} C_{blade}} \Delta t \qquad [3.47]$$

$$T_{base}^{n} = T_{base}^{n-1} - \frac{\dot{q}_{b-b}}{m_{base} C_{base}} \Delta t \qquad [3.48]$$

It will be assumed in the model that the Biot modulus of the respective metal parts is sufficiently small to warrant the assumption of equal temperature throughout the metal mass. The average convective heat transfer coefficient ($\bar{h}$) will be provided as a user input, rather than calculated. This is due to the complexities of the flow field around the blade and the resulting complexities of determining an average convective heat transfer coefficient. For the conduction that occurs in the metal, only heat transfer in the radial direction will be considered. Heat transfer in the axial direction, while present, is small relative to the radial heat transfer due to the high contact resistance's in the compressor assemblage. The model input to the numerical solver occurs in the energy equation source term (Equation 3.4), where:

$$Q_x = \left[\left(\dot{q}_{b-a}\right)_{stator} + \left(\dot{q}_{b-a}\right)_{rotor}\right] \qquad [3.49]$$

3.3. Solution Technique

The above discussions in this chapter have focused on the governing equations and the individual models for the various components of the gas turbine engine. This section of the dissertation will focus on how these mathematical equations that make up the individual models have been incorporated in the ATEC computer simulation. First, the variable time step routine that significantly enhances the efficiency of the flow solution during transient events will be discussed. Second, the solution technique will be discussed, addressing both the explicit and implicit numerical solvers. Third, the types of boundary conditions that can be specified at the inflow and exit of the grid will be discussed. Fourth, the overall layout and flow of the computer simulation will be considered.

3.3.1 Variable Time Step Routine: In order to provide efficient flow solutions for transient problems, the simulation uses a combination of an explicitly formulated numerical solver and an implicitly formulated numerical solver. Both of these numerical solvers are discussed in detail in Appendix C. Through the combination of the two different solvers, efficient flow solutions using large time step sizes were obtained for all non-dynamic simulations while maintaining the capability of using only the explicit flow solver (with the resulting small time step size) during dynamic events. The approach used to provide this capability will now be developed.

A common measure of the stability of a given explicit numerical solution is given by the stability criteria of Courant, Friedricks, and Lewey (CFL) [71]. The CFL stability

criteria states that for a stable numerical solution of a linear system, a sound wave should not propagate farther than one elemental control volume length during a time step. In other words, the CFL criteria is a measure of how far a sound wave travels during a given time step on the grid:

$$\frac{(|u| + a)\Delta t}{\Delta x} \leq CFL_{limit} \leq 1.0 \qquad [3.50]$$

where a is the speed of sound in the flow as given by Equation 3.9. For a linear system, the CFL is limited to 1.0. Due to the nonlinear nature of the turbomachinery simulation, particularly when simulating a choked turbine, experience has shown that a more realistic limit is 0.6. If the CFL limit is exceeded, the explicit method becomes numerically unstable and the resulting flow solution meaningless. For a given grid and flow, the maximum time step size that can be taken is given by rearranging Equation 3.50 to the following form:

$$\Delta t_{max} = \frac{CFL_{limit}\Delta x}{a + |u|_{max}} \qquad [3.51]$$

The implicitly formulated numerical solver is not restricted by the CFL limit since the solution is obtained by solving all equations simultaneously at the current time step. For a purely linear system, a CFL approaching infinity is possible using an implicit numerical solver. Experience has shown, however, that with the nonlinear turbomachinery source terms, stable, steady-state solutions with a CFL on the order of 500 are possible. This means that the implicit numerical solver can use a time step size 500 times larger than the explicit numerical solver during steady-state solutions.

Because the implicit flow solver used in the present work solves for the flow field solution simultaneously across the entire computational domain at the current time step, it takes more computational effort than an explicit solver that is also used. The implicit numerical solver used in ATEC and described in Appendix C takes four times the amount of solution time than the explicit numerical solver requires for the same overall time step size. Greater efficiency in calculating a flow solution can therefore be obtained by using the explicit numerical solver whenever the CFL criteria for the implicit numerical solver is less than four times the maximum CFL limit using the explicit numerical solver.

During transient events, the use of the implicit numerical solver reduces the accuracy of the flow field solution because the value of the CFL criteria is greater than one. In other words, because a sonic wave can propagate farther than one elemental control volume length during a given time step, certain characteristics of the flow solution may be missed by the implicit numerical solver. To minimize the computational errors when implementing the implicit numerical solver, a unique variable time step routine was developed in the present research study and implemented into the ATEC simulation. The technique, discussed in detail in the following paragraphs, sets the time step size based on a user defined rate-of-change limit in the dependent variable time derivatives. The technique also takes advantage of the greater efficiency of the explicit solver at small time step sizes.

The following variable time step routine has been developed and implemented into the ATEC simulation:

- After the initial conditions and boundary conditions have been specified, the first time step is integrated using the explicit numerical solver. The time step size is calculated using the formulation given in Equation 3.51 based upon the flow field velocities calculated in the initial conditions routine and a user provided explicit numerical solver CFL limit.
- Based upon the solution obtained by the explicit numerical solver, the time derivatives of the dependent variables are linearly extrapolated to the maximum time step size as provided by the user.
- If the extrapolated values of the time derivatives do not exceed a user defined limit (expressed as a percentage of the dependent variable), the next time integration is taken using the maximum time step size with the implicit numerical solver.
- If one or more of the time derivatives of the dependent variables changes more than allowed, the time step size is reduced to keep the time derivative change equal to the limit:

$$\Delta t_{new} = \frac{(\text{Derivative Change Limit})(\text{Time Step Size from Explicit Solution})}{\text{Maximum Derivative Change Extrapolated from Explicit Solution}} \qquad [3.52]$$

- For each implicit numerical solver time step, the variable time step routine checks to see if using the explicit numerical solver would be more efficient than using the implicit numerical solver. First, a maximum CFL for the next time integration of the flow field solution, based upon the current flow field solution and the time step size determined in Equation 3.52, is calculated:

$$CFL_{check} = \frac{(\text{Maximum CFL from Explicit Solution})\Delta t_{new}}{(\text{Time Step Size from Explicit Solution})} \qquad [3.53]$$

If CFL_{check} is greater than or equal to four times the maximum CFL allowed by the explicit numerical solver, the implicit solver is used. Otherwise, the explicit solver is used.

- If the implicit numerical solver is used, the next time step integration uses the explicit solver to again calculate the time derivatives for the flow field solution. If the explicit numerical solver is used, the technique re-enters the procedure at the second bullet above. This process is repeated until an imposed simulation time limit is reached.

The variable time step routine is graphically depicted in Fig. 30. The line identified as Case 1 represents a solution wherein the maximum rate of change of the dependent variables do not exceed the user imposed limit. Therefore, the full implicit time step size would be used for the next time integration. The line identified as Case 2, on the other hand, does exceed the derivative limit when linearly extrapolated. For this case, the implicit time step size would be limited to keep the derivatives from exceeding the imposed limit. A case where the implicit time step size is restricted sufficiently enough to warrant using the explicit solver is not shown in Fig. 30.

3.3.2 Simulation Solution Procedure: For a given integration of the flow solution in time, the conservation equations as presented in Equation 3.1 are used to define the fluxes and conservation variables on the faces of the individual control

volumes interior to the boundaries. The source terms, provided by the various component models developed in Section 3.2 and shown in Equation 3.4, are known on the control volume interval. The time rate of change of the dependent variables (Equation 3.2) represents a change at some point within the control volume interval (assumed to be the center). In order to obtain a flow solution, the change in the dependent variables across the control volume interval must be converted into a change in the dependent variables on the control volume faces (or grid points) [2]. To achieve this redistribution, both the explicit and implicit numerical solvers split the change over the control volume interval to the control volume faces by using a flux difference splitting algorithm [71]. A finite difference representation of Equation 3.1, given in Equation 14 in Appendix C, provides the foundation for each algorithm. Both algorithms are based upon characteristic theory with modifications to maintain strong conservation properties. The algorithms were developed by Mr. K. R. Kneile and Mr. A. A. Hale, both with Sverdrup Technology, Inc, AEDC Group, Arnold Air Station, Tennessee. The algorithms are robust and efficient, and can handle large changes in cross sectional area and nonuniform axial spacing with minimal numerical losses. Only a brief introduction to the methods are given here; a more detailed discussion of the solvers is given in Appendix C.

Explicit Numerical Solver: Consider a grid point at location j at the current time step n. As noted above, the fluxes are known at the current time (n) at j. The source terms, however, are known for the current time step at the center of the interval between nodes j-1 and j and the interval between nodes j and j+1. The explicit numerical solver

transposes the appropriate contribution of the fluxes and sources at the j-1/2 and j+1/2 positions to j by using a characteristic weighting term (Equation 18 in Appendix C) based upon the positive and negative running characteristics, respectively. With the fluxes and sources redefined on the nodes, the dependent variables are determined for the next time step (line n+1) using a first order Euler time integration method [72].

Implicit Numerical Solver: The implicit numerical solver was developed following a path similar to that used to develop the explicit numerical solver. The conservation equations as expressed in Equation 3.1 are approximated by the finite difference representation of Equation 14 in Appendix C. The characteristic weighting terms are developed differently, however, resulting in an implicit formulation of the finite difference representation of the conservation equations. Once the implicitly formulated system of equations are defined for the given time step, a tri-diagonal matrix solver [73] is used to determine the time derivatives at the nodes. A first-order Runge-Kutta scheme [72] is then used to integrate the solution from the current time step to the next time step.

3.3.3 Boundary Conditions: Since ATEC has been formulated as a boundary value problem, the type of specification used to define the boundary conditions at both the inlet and exit of the computational domain must be chosen. As noted by Davis [50], boundary specifications can influence both the stability and accuracy of the solution. Taking advantage of the research performed by Davis [50] and the successful techniques developed for DYNTECC [2], ATEC has been formulated using a method of characteristics (MOC) approach at the boundary points. A detailed discussion of the

implementation of the boundary conditions in both the explicit and implicit numerical solvers is given in Appendix C. This section will discuss the information that must be provided by the user to completely define the flow variables at the inflow and outflow boundaries.

Inlet Boundary Conditions: For flow in the positive direction (entering the grid from the left), the inlet boundary thermodynamic properties for a given time step are determined by the specification of two parameters. These parameters are total pressure and total temperature. As outlined in Appendix C, specification of these two parameters along with the knowledge of the internal grid values for the dependent variables permits the determination of the dependent variables at the inflow boundary for the next time step. Algebraically, different approaches are taken depending on whether the explicit numerical solver or the implicit numerical solver is being used, but both of the solvers' inflow boundary conditions are based on a common framework. Both the total pressure and total temperature can be varied as a function of time.

The flow rate at the inlet of the computational domain may reverse for certain flow situations, such as compressor stall. The above specification of the inlet boundary condition is inappropriate for this case. Therefore, when reverse flow is sensed at the inlet boundary, the boundary condition specification changes and the inlet boundary is treated as an exit boundary with constant static pressure, which is discussed below.

Exit Boundary Conditions: Subsonic exit boundary conditions are assumed in the development of the exit boundary condition specifications. Either static pressure or

Mach number can be specified and varied as a function of time. The scheme discussed for the inlet boundary conditions can then be used to determine the appropriate exit boundary thermodynamic properties as outlined in Appendix C. The static pressure exit boundary condition is used when the static pressure variation with time is known, or for the reversed flow inlet boundary condition case. The Mach number exit boundary condition is used when there is a sonic flow restriction downstream of the grid geometry, such as a choked exhaust nozzle or turbine nozzle.

3.3.4 Simulation Process: The solution procedure used during the simulation is dependent upon which numerical flow solver is being used for the given time step. At a high level, however, the flow solution follows the path shown in Fig. 31. The simulation first reads in the necessary data files that describe the details of the case under consideration (Step 1), such as the geometry, the types and initial values for the boundary conditions, and the various operational characteristics of the engine components. The dependent variables are calculated for every control volume by computationally marching from the inlet of the grid to the exit (Step 2). Steady-state flow conditions are assumed. Once the dependent variables are determined, all thermodynamic variables are calculated for each of the control volumes (Step 3). After this step, the time integration begins. The first step during the time integration is to select the appropriate numerical solver and determine the time step size (Step 4). The criteria for choosing a particular numerical solver and time step size are given in Section 3.2.1. Next, the boundary conditions are updated for the next time step using either the method of characteristics technique or the

sonic nozzle technique (Step 5). The simulation then calculates the turbomachinery source terms based on the performance of the individual components selected for the simulation (Step 6) based on the inlet conditions to the source term control volumes from the previous time step (or initial conditions if it is the first time step). Source terms for the compressor and combustor characteristics are lagged if appropriate (Step 7). After the source terms are determined using the component models described above in Section 3.2, the flow solution is obtained (Step 8). The actual process followed during Steps 6 to 8 vary depending upon which numerical solver is used. The respective differences will be discussed below. Once the solution for the dependent variables are determined, the remaining thermodynamic properties are calculated for each control volume (Step 9). Then, the rotor rotational velocity is updated for the next time step (Step 10). The path returns to Step 4 at this point unless the end of the simulation is reached, at which point files are closed out and the simulation stops.

The explicit and implicit numerical solvers follow the processes for Steps 6 to 8 sketched out in Figs. 32 and 33. For the explicit numerical solver, the path of which is shown if Fig. 32, calculation of the source terms (Step 6) and the appropriate lagging (Step 7) occurs only once for each time step. Once the source terms are determined, the fluxes as given in Equation 3.3 are split from the control volume interval to the control volume interfaces following the procedure given in Appendix C. The solution of the dependent variables at the next time step is then obtained using an explicit Euler time integration technique (Step 8).

The implicit numerical solver follows the process for Steps 6 to 8 as sketched out in Fig. 33. As with the explicit numerical solver, the source terms are calculated and appropriate lagging terms are applied (Steps 6 and 7). The implicit numerical solver, however, calculates the source terms four times for each time step. The source terms are calculated for the given flow field solution first. Then, the source terms are recalculated with each of the three dependent variables perturbed individually. After perturbing each dependent variable, the thermodynamic properties are recalculated, and then the source terms are recalculated. Once the derivatives of the source terms are defined for use in Equation 51 in Appendix C, the implicit solver uses a block tri-diagonal matrix solver as discussed in Appendix C to arrive at the time derivatives. A first order Runge-Kutta scheme is then used to move the flow field solution to the next time step.

4. OPERATIONAL VERIFICATION

With the mathematical models presented in Chapter 3, the ATEC computer simulation has been constructed. This chapter will present the results of the effort to operationally verify the models and the resulting simulation. The goal of the operational verification is to first ensure that the models as stated are appropriate for the problem under consideration, and secondly, to ensure that the translation of the models to lines of computer coding have been completed successfully and with no errors.

The approach taken for the operational verification of ATEC will be as follows. First, the general Euler flow solver (both explicit and implicit) will be exercised for a generic, textbook type problem for which there is an exact, analytical solution. This will provide confidence in the foundation of the simulation for the latter efforts when the turbomachinery source terms are added. After the Euler flow solver is shown to be functional, the source term models will be added one at a time. Each engine component model will be added to the simulation until all the components of a gas turbine engine are included. Finally, the model for heat transfer will be added and verified. With the full turbine engine model operationally verified, the effort will focus on the calibration of the model and simulation to representative data sets, to be presented in Chapter 5.

The results presented herein were obtained running the simulation on an IBM-compatible Personal Computer (PC). The computer was a 90 MHz Pentium^{tm} system using 32 Mbytes of memory. The computer language used for the simulation was

FORTRAN 77 and was compiled using the Microsoft® Powerstation™ Version 1.0a FORTRAN compiler.

4.1. Euler Flow Solver

The test case which was used to operationally verify the Euler flow solver was the flow inside a convergent / divergent duct. This was used to verify that the flow model adequately predicts accelerating and decelerating subsonic flow in variable area ducts using a grid that has nonuniform spacing in the axial direction. Comparisons were made to isentropic subsonic flow [74]. The test case also demonstrated the functionality of the explicit numerical solver, the implicit numerical solver, and the variable time step routine that alternately used both solvers.

The geometry for the problem is shown in Fig. 34. The cross-sectional area of the duct first converges, then diverges as the flow moves along the axial direction. The axial coordinates and the outer wall radius of the ducting at each grid point location are given in Table 4. The grid was constructed by packing the points about the minimum area location (axial location of 0.0) using exponential packing. The equation used for determining the spacing of the grid is given by:

$$x = \frac{\exp[\alpha\zeta] - 1}{\exp\alpha - 1} \qquad [4.1]$$

where, for this particular grid, α was chosen to equal two. The value of ζ used in the above equation is the equidistant value of the n^{th} grid point divided over a range from zero to one. Since the subject grid is applied over the range from zero to one, no

additional conversion is necessary the x-coordinate location. The points located on the negative side of the grid are a mirror reflection of the positive side.

The initial conditions were specified based on isentropic flow relations. The flow predicted by the solver should remain constant, equal to the initial conditions until some perturbing event occurs, such as a boundary condition change. For the operational verification, the exit Mach number of the duct flow was perturbed as shown in Fig. 35. After 0.5 seconds, the Mach number was increased linearly over a 0.01 second interval to a level twenty five percent higher than the initial value. After an additional 0.5 seconds, the exit Mach number was linearly raised again over a 0.01 second interval by an additional twenty five percent. The simulation was completed at 1.5 seconds.

First, the explicit flow solver was exercised. A non-varying time step size of 0.15×10^{-4} seconds was used, resulting in an average maximum CFL in the flow domain of approximately 0.8. The total time required to run the simulation was seven minutes, twenty four seconds. The total pressure through the duct during the first 0.5 seconds, which ideally should be constant, is shown for both the initial conditions and at 0.5 seconds in Fig. 36. No variation is noted between the two time periods. Static pressure in the flow domain is also plotted in Fig. 36 for the same time period. No discernible differences exist for either pressure. The simulation values of static pressure are compared to the values calculated using isentropic flow relationships as given in [71] at selected times in Fig. 37. Simulation values for mass flow rate are likewise compared to

isentropic values in Fig. 38. Agreement between the values are within the numerical error of the computer.

The implicit solver utilized a non-varying time step size of 0.01 seconds, limited by the rate of change of the exit Mach number. This time step size resulted in an average maximum CFL of 460 during the simulation. The run time for this simulation was twelve seconds. The total pressure and static pressure in the duct are compared for both the initial conditions and at 0.5 seconds as above in Fig. 39. As with the explicit solver, there were no discernible differences between the respective values. The comparison of the simulation values for static pressure and mass flow rate are compared to isentropic values in Figs. 40 and 41, respectively. Again, no discernible differences were detected.

For one final comparison, values of Mach number at the minimum area throat (at the zero axial location) for both the explicit solver and the implicit solver as a function of time are compared in Fig. 42. During the steady state portions of the simulation, there is no discernible difference between the two simulations. There is, however, a slight difference during the transient portion of the test case (less than three percent). The region of time surrounding the first exit Mach number transient is plotted in Fig. 43. The differences are not unexpected since the explicit solution provides the time resolution to pick up the flow dynamics during the change in Mach number. The implicit solution, on the other hand, does not provide this capability due to the larger time step size, and the dynamics of the flow are missed in the solution of the flow field.

To provide support for this conclusion, the implicit test case was rerun using the variable time step size routine. The maximum time step size limit was 0.01 seconds as above, but the explicit solver was used to correct the time step during the transients. This approach does take longer to obtain a solution (the run time was twice as long at twenty four seconds), but it does show the effect of the variable time step size routine. The throat Mach number is plotted as a function of time for both the explicit and variable time step cases in Fig. 44 during the time period around the first exit Mach number transient. As is shown, the two solutions lie nearly on top of each other. During the simulation run, the time step size was reduced such that the implicit solver ran with a CFL of approximately 15, rather than the original 460. Once the flow reached the new steady-state conditions, the time step size was quickly increased back to the original 0.01 seconds. This test case demonstrates that ATEC can seamlessly adjust the time step size to match the flow field requirements and provides an efficient flow solution capability for transient problems.

The differences in the amount of computational time required to run each of the three simulations were significant. As noted in Chapter 3, the purpose of the variable time step routine was to increase the efficiency of the model for transient events. This simple test case demonstrated dramatically the potential improvement in efficiency that can be obtained with the new routine. The explicit solution required seven minutes, twenty four seconds to simulate the test case. The implicit solution, using the much larger time step size, required only twelve seconds. As noted above, however, some

accuracy was sacrificed during the exit Mach number perturbations. The variable time step routine, using the implicit solver and large time step sizes during the near steady-state parts of the problem, but using the explicit solver during the dynamic parts of the solution, required only twenty four seconds to simulate the test case. As shown in Fig. 44, accuracy was not sacrificed during the dynamic portions of the run. For this particular case, the variable time step routine provided an accurate solution with a run time more than eighteen times faster. For test cases where the time period of interest is much longer than 1.5 seconds, such as a starting simulation that may take thirty seconds or more, this level of efficiency improvement could greatly enhance the feasibility of using the model and simulation.

4.2. Compressor Model

As noted in Chapter 2, the foundation for the ATEC mathematical model and numerical simulation is the DYNTECC simulation [2]. As such, the operational verification of the model has been well established and is reported in the literature [47-56]. Several changes to the simulation have been made, however, to incorporate the remaining components of the gas turbine engine. For this reason, operational verification is required to ensure that the simulation was not inflicted with an error during the simulation development effort.

To operationally verify the compressor model, the results presented in [55] will be used. The material in [55] discusses the application of the DYNTECC model and simulation to a seven stage axial and a single stage centrifugal compression system. The

data was collected on a compressor test rig. The compression system, obtained from a Lycoming T55-L-712 turboshaft engine, was run at several constant rotor speeds during both steady state, transient, and dynamic, post-stall events. A cutaway view of the engine is shown in Fig. 45. The reader is referenced to [55] for a complete description of the test goals, instrumentation, and results, including compressor stage characteristics.

The engine compression system consists of a seven stage axial compressor and a single stage centrifugal compressor. A graphical representation of the geometry inputs for the simulation are shown in Fig. 46. A total of 39 control volumes were used. The calculation domain spanned from the inlet of the bellmouth to the throttle valve. Each control volume inside the compressor represents a combination rotor/stator pair. One control volume is provided at the exit of the axial compression system to account for the ducting between the axial compressor and the centrifugal compressor. The centrifugal compressor was represented by four control volumes. This minimized the system control volume length. All work done by the centrifugal compressor was assumed to occur in the first control volume, with the other control volumes providing only the correct compression system volumetric geometry.

The simulation used the same stage characteristics as reported in [55]. The constant eighty percent rotor speed case was duplicated. For comparison purposes, the DYNTECC model and simulation results were recreated in order to provide a basis for the following discussion. Two runs were made with the ATEC simulation. The first run was similar to the explicit solution provided by the DYNTECC simulation except for the

time step size. Since the ATEC simulation bases its time step size on the CFL, the time step size does not remain constant even when using only the explicit solver. The CFL was set equal to 0.8 for the current case, which gave a slightly larger time step size than was used in DYNTECC (0.000043 seconds on average versus 0.00004 seconds). The second run used the implicit solver with the variable time step size routine. For most of the simulation, the explicit solver was required due to the dynamic nature of the flow field. When near steady-state conditions were reached, however, the implicit solver took over the numerical integrations and significantly increased the time step size, while reducing the overall simulation computation time.

In order to force the compression system into multiple surge cycles, the exit boundary condition of specified Mach number was varied as shown in Fig. 47. By reducing the exit Mach number, the simulation modeled the closing of the exit throttle valve on the actual test rig. The reduced Mach number translates into a reduced mass flow rate through the system. Since the system is operating at constant rotor speed, the compressor performance moves up the speed line until the point of instability (stall) is reached. Surge cycles then begin until the flow restriction is reduced and the compression system can maintain a stable operating condition.

The resulting relative compressor pressure ratio of the three simulation runs are compared in Fig. 48. The results are identical during the steady-state portion of the simulation and are closely matched during the dynamic portion of the simulation. There are slight differences between the three runs during the surge cycles, but these differences

were expected due the different time step size being used during each run. By solving for the flow field at a different instant in time, the source terms for the compressor stages were read at different locations on the characteristic maps. This propagated slight differences in system performance as functions of time. As discussed in the introduction, once the flow restriction was removed, the compression system re-established steady state operation.

A more in-depth discussion and analysis of this data set and simulation results will be given in Chapter 5. This preliminary discussion has presented the operational verification of the compressor model. Operational verification of the combustor model will now be considered.

4.3. Combustor Model

To operationally verify the combustor model and the resulting portion of the simulation, a test case built upon the foundation of the compressor operational verification test case will be shown. The test case will present the integration of and the interaction of the combustor and compressor models, by adding a combustor onto the T55-L-712 compression system model discussed in Section 4.2. The operational verification procedure presents the effects of the equivalence ratio in the combustor and the resulting heat release rate on model predictions of the simulation. The time lagging procedure for the heat release rate is exercised to ensure that the first order lagging equation has been implemented successfully.

The test case geometry is sketched in Fig. 49. The same geometry is used in the compressor section as in Section 4.2. Only downstream of the centrifugal compressor is there any differences in geometry. A close-up view of the combustor geometry is shown in Fig. 50. The combustor consisted of 8 control volumes, with the first four control volumes being specified as the primary zone control volumes. The exit boundary condition was specified to be constant Mach number.

The first test case run was to establish steady state operation. Once that was obtained, the fuel flow rate to the combustor was ramped as shown in Fig. 51. As noted earlier, the excess fuel flow raises the temperature of the flow exiting the combustor. Since the exit boundary condition holds the Mach number constant, the mass flow rate exiting the system is reduced. As discussed in Section 3.3.3, the constant Mach number exit boundary condition places an imaginary isentropic, converging nozzle operating with the exit plane Mach number equal to one, attached downstream of the exit of the grid. This is used to approximate the choked turbine nozzles that would normally be located downstream of the combustor. As with the compressor operational verification test case, the reduced flow through the system forces the compressor into multiple surge cycles.

The relative compressor pressure ratio as a function of time is shown in Fig. 52. The results shown in Fig. 52 are similar to the results presented for the compressor operational verification in Fig. 48. The system response frequency is greater with the combustor modeled (approximately 18 Hertz with the combustor versus 10 Hertz for the compression system only). The response frequency is inversely related to the system

volume. Comparing the geometry of the compression system simulation shown in Fig. 46 with that of the combustor geometry shown in Fig. 50, it is apparent that the combustor geometry provided less volume downstream of the compressor. This difference in volume accounted for the difference in the response frequency.

During the surge cycles, the air flow rate entering the combustor is reduced as the system back pressure (which is the combustor inlet pressure) reduces. The air mass flow rate entering the combustor is plotted as a function of time in Fig. 53. During the surge cycles, the air flow rate is reduced enough to force the fuel-to-air equivalence ratio in the combustor above the upper flammability limit. This in turn results in the extinguishment of the flame in the combustor and a reduction in the calculated heat release rate in the combustor. The equivalence ratio in the primary zone is plotted as a function of time in Fig. 54.

The upper and lower limits of flammability as bounded by the correlations of Herbert's data [51], are plotted as a function of time in Figs. 55 and 56, respectively. As noted in Chapter 3, the flammability limits are correlated as a function of the Combined Air Loading Parameter (CALF). The CALF is determined from the mass flow rate, total pressure, and total temperature at the combustor inlet. Since these parameters vary during the compressor surge cycles, the flammability limits also vary.

The variation in instantaneous value of the heat release rate during the surge cycles is shown in Fig. 57. As noted in the discussion of the combustor model in Chapter 3, the actual physical process of flame ignition and extinction and the resulting heat

release rate does not occur instantaneously as is shown in Fig. 57. Rather, there is a lag in the heat release rate due to the chemical and heat transfer processes that are occurring. These effects are modeled with a first-order lagging in time (Equation 3.39), which results in a heat release rate provided to the flow solver as shown in Fig. 58. Because of the exponential lagging of the heat release rate, the combustion process was completely extinguished for only a short period of time during each surge cycle.

To investigate the effects of lagging the combustion processes, the time constants for the ignition and extinction events were increased by an order of magnitude and the simulation repeated. The new time lagged heat release rate is plotted in Fig. 59. Comparing to Fig. 58, it is apparent that the approach can modify and control the frequency of cyclic events. The influence on the overall system behavior was not dramatic, but the higher lagging rates did reduce the system response frequency. The relative compressor pressure ratio as a function of time for this simulation run is shown in Fig. 60. Comparing to Fig. 53, the additional lagging of the heat release rate forced the system volume dynamics to a reduction in system response frequency of 16 Hertz. This reduction in response frequency was expected since the average energy content in the combustor was higher for the second test case. The higher energy content tended to damp the system response due to the higher volumetric flow rate in the system.

4.4. Turbine Model

A compressor and combustor model were formulated, implemented, and operationally verified. By adding a turbine component model, a complete turbojet engine

model can be constructed. The turbine model added was based on the characteristics of the T55-L-712 engine turbine, consistent with what was done to model the compressor and combustor. The goal of the operational verification of the turbine model will be to ensure that the turbine performance simulation matches the actual turbine performance, as given by its operational characteristics. The operational characteristics are generically plotted in Fig. 28. The test case will operate with constant rotor speed; rotor dynamics will be operationally verified in a following section.

The geometry of the test case is shown in Fig. 61. The T55-L-712 engine uses two two-stage turbines. The first turbine is attached to the compression system and is called the gas generator turbine. The second turbine is used to power a shaft (to drive a helicopter rotor) and is called the power turbine. As is shown in Fig. 61, the gas generator turbine geometry was broken into four control volumes. As is typical of most engine performance data sets, interstage turbine data is not available for the T55-L-712 engine. Only overall turbine performance is available. The limited dynamic aspects of the turbine operation are accounted for by linearly dividing the overall gas generator turbine performance across the four control volumes. The power turbine geometry was divided into three control volumes. A constant static pressure boundary condition at the last control volume of the grid was specified for this test case, rather than constant Mach number. The constant static pressure boundary condition closely approximates an actual engine exhaust environment.

To operationally verify the turbine model and simulation, the T55-L-712 engine simulation was subjected to a fuel flow increase as shown in Fig. 62. A total transient simulation run time of three seconds was chosen. The engine was simulated at design rotor speed. The ten percent increase in fuel flow rate forced the calculated flow through the choked turbine nozzles to be reduced due to the increase in volumetric flow rate. Once the reduced flow rate propagated back upstream to the compressor, the engine compression system entered into multiple surge cycles. Once the fuel flow rate was reduced back to the original level, the engine system returned to steady state operation.

The relative total pressures at four locations in the engine as functions of time for the current test case are shown in Figs. 63 through 66. The locations at which the pressures were obtained were at the axial compressor exit, the centrifugal compressor exit, the combustor exit, and the engine exit downstream of the turbines. All total pressure levels were referenced to the centrifugal compressor exit total pressure. The engine surge cycles occurred at a frequency of approximately 16 Hertz. The relative total temperature of the flow at the same four locations in the engine as a function of time are shown in Figs. 67 through 70. All total temperature levels were referenced to the centrifugal compressor exit total temperature. The relative temperature increased significantly during the surge cycles before the flame in the combustor was extinguished. Once the volume downstream of the compressor was emptied and then refilled, the combustor heat release was reestablished. This process was repeated for each of the surge cycles.

The relative mass flow rate in the engine at the same four selected locations is plotted as a function of time in Figs. 71 through 74. All mass flow rate levels were referenced to the engine inlet mass flow rate. It is interesting to note that although the axial compressor exit mass flow rate reverses during the surge cycle, the mass flow rate in the combustor and turbine control volumes does not completely reverse.

For a more detailed look at the turbine performance, the relative turbine flow function and the relative work done factor are plotted as functions of time for the gas generator turbine in Figs. 75 and 76, respectively. The relative total pressure and total temperature ratios across the gas generator turbine as functions of time are shown in Figs. 77 and 78, respectively. As expected, the reduction in turbine flow function caused by the surge cycles translates into reduced work output from the turbine and a reduction in the pressure and temperature ratio across the turbine.

The performance ratios across the turbine indicate that the simulation successfully incorporated the turbine characteristic maps shown in Fig. 28. The relative turbine flow function as a function of relative work done factor for the gas generator turbine is shown in Fig. 79. The surge cycles generate sufficient variation in flow conditions that the full range of turbine performance was exercised during this one test case. The relative total pressure ratio across the gas generator turbine is plotted as a function of relative total temperature ratio in Fig. 80. The turbine model and simulation followed the performance data given in the maps (with some variation caused by the constraint of constant rotor

speed with varying inlet temperature), which indicates that the turbine model and simulation has been operationally verified.

4.5. Rotor Dynamics Model

To operationally verify the rotor dynamics model, a transient test case was considered. A transient rather than dynamic test case is more appropriate for the operational verification of the rotor dynamics model since the shaft rotational moment of inertia prevents a dynamic event from significantly affecting the rotational speed of the rotor. The test case considered and simulated a transient throttle movement, that resulted in the gas generator portion of the engine changing from a 100 percent speed case to an 85 percent speed case. The influence of the shaft rotational moment of inertia on transient system behavior was demonstrated by repeating the test case simulation with a different rotor rotational moment of inertia. It should be noted that the rotor dynamics model was applied only to the gas generator rotor. It was assumed that the power turbine shaft was held as constant rotational speed.

The total time period simulated was five seconds. The fuel flow rate was reduced by 30 percent in a one second time period beginning 0.5 second into the test case, to reduce the engine shaft speed from 100 percent of design to 85 percent of design. After a one second delay, the fuel flow rate was ramped back up to the original level in a one second time period. The relative fuel flow rate as a function of time is shown in Fig. 81.

The relative overall total pressure ratio across the compressor system is shown as a function of relative compressor inlet mass flow rate in Fig. 82. Also shown in Fig. 82 is

the steady-state operational line which was determined by carrying out steady-state simulation runs wherein the fuel flow rate was reduced five, ten, fifteen, twenty, and twenty five percent of the nominal value. As noted in Chapter 1, the deceleration of the gas generator rotor takes longer than the aerodynamic deceleration of the flow field. This causes the operational path of the compressor to follow a route below the steady-state operational line. Once the fuel transient was started, the maximum pressure of the compression system (compressor outlet) was reduced. From the rotor dynamics model, the relative gas generator shaft speed was obtained as a function of time and is shown in Fig. 83. The shaft speed fell off from the 100 percent level shortly after the fuel flow was reduced, but it took approximately 0.1 seconds longer to reach the new steady state level.

The influence of the shaft rotational moment of inertia was verified by increasing it by 65 percent and repeating the test case. Any additional increase in the rotor moment of inertia caused the acceleration of the rotor to be delayed to the point that the compressor entered the post-stall regime for the given transient. The expected result was that the rotor would be less responsive to the fuel flow rate transient, and that was exactly what was obtained. The relative compressor pressure ratio plotted as a function of relative compressor inlet mass flow rate for both cases is shown in Fig. 84. The relative gas generator shaft speed predicted as a function of time for the increased rotational moment of inertia is compared to the original level speed variation in Fig. 85. Clearly, the gas generator rotor speed was affected by the higher rotor moment of inertia, as the rotor with

the lower rotor rotational moment of interia reached the new steady-state speed more quickly than did the rotor connected to the rotor with the higher moment of inertia.

4.6. Heat Transfer Model

All of the results presented above considered adiabatic engine operation. To operationally verify the compressor heat transfer model, a simulation was run that incorporated a change in the inlet flow temperature. Simulation results with and without the heat transfer model activated will be shown. The same test case geometry as Section 4.5 was used.

The operational verification was conducted with a five second simulation. The inlet total temperature variation during the simulation is shown in Fig. 86. The temperature was initially set to 518 °R. After 0.5 seconds, the temperature was linearly ramped downward twenty percent over a 0.5 second interval. After a 1.5 second time period, the inlet air total temperature was ramped back to the original level over 0.5 second time interval. Metal mass in the compressor that was used in the heat transfer model was estimated from T55-L-712 design drawings. The effective, overall convective heat transfer coefficient was established at 800 BTU/sec-ft^2-°R for the design flow conditions based on private communications with compressor heat transfer experts at a major gas turbine engine manufacturer. The thermophysical properties of the metal were assumed to be equal to the properties of mild steel to demonstrate the effects of the heat transfer model on the ATEC calculations.

The results of the adiabatic simulation are presented first. The overall axial compressor relative total temperature ratio as a function of time is shown in Fig. 87. The relative total temperature ratio changed only slightly due to the variation in inlet temperature. The relative overall axial compressor pressure ratio is shown in Fig. 88 as a function of time. The reduction in inlet temperature increases the corrected mass flow rate, which forces the compressor to move to a lower point on the compressor performance map (i.e., the pressure ratio is lowered). Once the original inlet temperature is restored, the compressor pressure ratio returns to the initial level.

The results obtained with the heat transfer model activated are now presented. As with the adiabatic case, the relative total temperature ratio across the axial compressor and the relative total pressure ratio across the compressor are shown. The relative total temperature ratio, shown in Fig. 89, is considerably different with the heat transfer model activated. Because of the stored energy in the metal blades, the reduced inlet temperature does not immediately lower the compressor exit temperature as happens in the adiabatic case shown in Fig. 87. Rather, the energy is transferred from the blades to the air stream. The effect of the heat transfer is also apparent in the relative compressor pressure ratio plot shown in Fig. 90.

Looking at the heat transfer model in more detail, the total heat transfer rate from the compressor blading to the air stream is plotted in Fig. 91 as a function of time. When the inlet air stream total temperature is reduced, the heat transfer rate quickly becomes significant. Once the inlet air total temperature stabilizes, the heat transfer rate falls back

towards zero as the temperature difference between the air stream and the metal comes to an equilibrium. When the inlet air total temperature is ramped back to it's original level, the heat transfer rate response in the reverse direction as expected. The relative temperature of the seventh stage rotor and stator blades as a function of time are shown in Fig. 92. Also shown in Fig. 92 is the average relative static temperature of the air flow across the seventh stage, since this is the temperature that drives the heat transfer. As the air flow static temperature changes, so does the metal temperatures. It should be noted that the seventh stage results were presented because the seventh stage experienced the largest effects caused by the heat transfer. The other stages behaved in a similar fashion, but with changes smaller in magnitude.

5. ATEC CALIBRATION

One of the most difficult tasks in the development of any mathematical model is ensuring that the actual system has been represented in sufficient detail, i.e., whether the model is valid. If a model is not sufficiently detailed, then any conclusions made about the actual system based on the model results will most likely be incorrect [29]. As such, the calibration of Computational Fluid Dynamics (CFD) programs has been a very active research topic in the recent past. As more and more dependence is placed on CFD calculations, the sources of errors in the computational algorithms must be fully understood. It is of extreme importance that CFD programs be tested by comparing them to appropriate data sets to ensure their validity and to define their applicable range. Any shortfalls in the CFD model must be fully understood before it can be applied with confidence.

The terminology used in the present discussion will be based on the definitions for calibration and validation as given in [75]. This work has received considerable attention in the CFD community literature ([76] and [77], for example), and was based on the work of a National Aeronautics and Space Administration (NASA) ad hoc Committee on Validation. The pertinent definitions are:

CFD Program Validation: Validation provides detailed surface and flow field comparisons with experimental data. The purpose of the comparison is to verify the program's ability to correctly model the critical physics of the flow. It is required that the

accuracy and limitations of both the experimental data and the program be thoroughly known and understood over a range of specified parameters.

CFD Program Calibration: Calibration provides a comparison of a program's ability to accurately predict certain aspects of the flow field by comparing the program output to experimental data obtained from geometry's that are similar to the one under consideration. It is important to ensure that the parameters of interest are acceptably predicted, however, not all aspects of the flow are necessarily correctly modeled.

As a general observation, in the purest sense the concept of a fully validated CFD program is presently an unachievable goal. The current state-of-the-art of many aspects of CFD modeling dictates that proper modeling of the critical flow physics can not occur. For large, multi-dimensional CFD programs, the most obvious shortfall is in the area of turbulence modeling. Although just one of many sources of error in CFD [78], turbulence modeling as it currently stands, with empirically based models, has a long way to go before an accurate reproduction of the flow physics is obtained [79]. Significant progress has been made in recent years, however, and while there are not any CFD simulations that can claim full validation, many simulations can make restricted declarations of being validated [80].

The ATEC model and simulation, based on the one-dimensional, inviscid Euler equations, is a CFD program. The one-dimensionality of the program, however, means that it can not be validated based on the definitions given above. Strict validation of ATEC is not required for the model to be considered credible, however, since ATEC will

never be used to predict the surface and detailed flow field properties inside the complex geometry that makes up a gas turbine engine. That, of course, is not the purpose of the ATEC simulation. Rather, ATEC provides a "moderately" detailed simulation that can be used to identify the important factors which influence the bulk flow within the overall gas turbine engine, and hence its operation. The development of detailed, component and sub-component level simulations can then be focused on the critical parameters.

The purpose of the calibration effort and hence this chapter in the dissertation, is to demonstrate that the ATEC model and simulation can match representative test cases, over the full range of operational conditions. Since the art of calibration involves the "tuning" of the simulation to match a given data set, it is not strictly required that the data set be tied directly to an experimental effort. For example, other computer simulations can be used as a source for calibration data. Care must be exercised, of course, to make sure that the calibration data set is representative of actual engine performance to ensure that the conclusions drawn from the simulation are reasonable. The calibration effort that is discussed in the following sections used both engine simulation output from other codes and actual test data.

Calibration of the ATEC model and simulation was conducted for three data sets. All data sets focused on the T55-L-712 engine. Because of the limited scope of the data sets, a full and complete calibration of the various components of the ATEC simulation was not made. For example, no data were identified that would permit the calibration of the heat transfer model. Sufficient data were collected, however, to demonstrate the

process of calibration and that the ATEC simulation can be matched to representative data sets.

The first data set addressed the transient operation of the simulation with the engine operating near design rotational speed. Comparison is shown between ATEC model results and results from a T55-L-712 component level model. A change in the engine operation was affected by reducing the load on the power turbine, which in actual operation of the engine causes a reduction in the fuel flow rate to the combustor. The reduced fuel flow rate schedule was used as input to ATEC for the simulation. The second calibration comparison was a more in-depth comparison of the compression system operation during a dynamic event, as was shown in Section 4.2. The simulation results were compared to actual compressor rig test data. Finally, the full engine simulation was compared to test data obtained from a T55-L-712 engine going through a start cycle.

5.1. Transient Calibration

The ATEC model and simulation was calibrated to a transient component level model and simulation called the Advanced Turbine Engine Simulation Technique, or ATEST [31]. In a fashion similar to ATEC, ATEST solves the inviscid Euler equations. ATEST does not break the engine systems down into a stage-by-stage representation, but rather considers the engine components on an overall or global component basis. While this precludes the use of ATEST for dynamic events, it is applicable to transient simulations.

The T55-L-712 version of ATEST breaks the engine down into various component volumes as shown in Fig. 93. The compressor representation combines both the axial and centrifugal compressors into one overall block. Likewise, the combustor and gas generator and power turbines are described using overall characteristics. The ducting connecting the various components of the engine are neglected. The ATEST model does provide a control system representation of the actual T55-L-712 hydromechanical control system. The primary output of the ATEST control simulation is fuel flow rate, so, as mentioned earlier, during the calibration effort, the ATEST calculated fuel flow rate was used as an input to the ATEC simulation since the ATEC simulation does not include a control system model.

The T55-L-712 turboshaft engine control system is configured for helicopter operation. Simply put, what this means is that the operation of the gas generator portion of the engine is determined by the power required by the helicopter rotor system. During normal flight operation, the throttle for the gas generator is set to full open. The lift provided by the rotors is then set by the pilot using a second throttle. Changes in the amount of lift requested by the pilot do not change the speed of the power turbine since it operates as a constant speed device. Rather, the change in the amount of lift is affected by changing the fuel flow rate to the gas generator portion of the engine. The modified fuel flow rate results in the inlet conditions to the power turbine changing, which changes the power level produced by the power turbine for its given operational speed.

The calibration effort was accomplished as follows. First, the ATEST simulation was exercised for two steady-state operating conditions. Next, the ATEC simulation output was tuned to match the ATEST predicted levels of performance as defined by the steady-state temperatures, flow rates, and pressures throughout the engine. Once the steady-state engine performance calculations were acceptably close, a transient test case was executed. The gas generator speed was reduced by lowering the fuel flow rate. Values of the calculated engine operational parameters for both ATEST and ATEC were compared.

Calibrating the results of the ATEC model and simulation to the ATEST output utilized various scalar multipliers on the component performance levels. These scalar multipliers were required due to differences in the component performance specifications incorporated in ATEST and ATEC. For example, the compressor performance maps used by ATEC and ATEST were from two different sources. The ATEC stage-by-stage compressor maps were based on the compressor rig data discussed in Section 4.2. The ATEST overall compressor map, however, was obtained from the engine manufacturer's steady-state model and represented a "nominal" engine compressor. As such, for a given inlet flow rate and rotor speed, the calculated values of total pressure ratio and total temperature ratio across the compressor were somewhat different for the two simulations. In this particular case, the ATEC maps described a compressor system with a larger rise in pressure and temperature across the compression system than ATEST simulation, for the same rotational speed. Both simulations provide scalars that can be used to adjust the

values, but for this effort the ATEST results were taken as "truth", that is, defined the benchmarks for the ATEC simulation. Only the ATEC results were modified for the calibration effort.

The two steady-state test cases selected for the calibration effort were based on the power conditions that occur when the throttle for the requested lift was set at sixty five degrees, and at sixty degrees. This provided a difference in the fuel flow rate delivered to the gas generator combustor of approximately twenty percent. The engine inlet conditions were set to sea level static conditions.

The calibration of the ATEC simulation results to the ATEST steady-state values was accomplished by matching pressures, temperatures, and flow rates along the engine flow path, one component at a time. Initial conditions were determined such that the values of the parameters closely matched the ATEST values after some amount of time integration. The compressor outlet total pressure and total temperature were adjusted to match the ATEST results by applying a single scalar multiplier to all seven stages of the axial compression system and then making a final adjustment using the scalars for the centrifugal compressor. For both calibration data points, some reduction was required in the axial compressor performance in order to keep the compression system out of the post-stall regime. By reducing the temperature across each axial stage, the corrected flow rate for the next stage was increased, which moved the operating point away from the surge line. Values for the total pressure and total temperature scalar multipliers that best matched the test data are shown in Table 5.

For the combustor, sufficient tuning of the ATEC total temperature results was obtained by increasing the lower heating value of the fuel to obtain a higher heat release rate. Initially, ATEC calculated a combustor exit temperature lower than ATEST due to a lower calculated level of combustion efficiency. Both test cases required a value of the lower heating value of 18,425 BTU/lbm versus the nominal value of 18,400 BTU/lbm as used by ATEST. The correct pressure drop across the combustor was obtained by adjusting the loss coefficient. The values of the loss coefficient used for both test cases are shown in Table 6.

The turbine maps used by ATEC were extracted directly from the ATEST simulation. There was therefore very limited adjustment needed. Some correction in the inlet turbine flow function was needed, however, since a very slight difference can have a dramatic impact on the amount of work obtained from the turbine. As shown in Fig. 28, once the turbine flow function reaches the choking limit in the turbine, small perturbations in the mass flow rate result in large changes in the turbine work done factor. The calculated value of turbine flow function was therefore adjusted to provide the proper level of work across the turbine. The mass flow function scalar multipliers for both turbines for the two test cases are shown in Table. 7.

The overall steady-state calibration results for the sixty five degree throttle test case are graphically depicted in Fig. 94 through Fig. 96. The total pressure through the engine system are shown in Fig. 94. The total temperature in the engine system is shown in Fig. 95. Finally, the mass flow rate through the engine system is shown in Fig. 96. On

the scale used for the figures, there is no noticeable differences between the ATEC and ATEST results. For a more specific comparison, the relative values of total pressure, total temperature, and mass flow rate at the locations where the ATEST were defined are shown in Table 8 through 10, respectively. The relative values were based on dividing the actual values of the parameters by the highest values given by the ATEST simulation. For example, the relative total pressure levels were obtained by dividing the actual total pressure by the total pressure just downstream of the centrifugal compressor. Careful selection of the scalar multipliers resulted in ATEC values falling within 0.2 percent of the ATEST levels for this steady-state test case.

The overall steady-state calibration results for the sixty degree throttle test case are graphically depicted in Fig. 97 through Fig. 99. The total pressure through the engine system are shown in Fig. 97. The total temperature in the engine system is shown in Fig. 98. Finally, the mass flow rate through the engine system is shown in Fig. 99. As with the sixty five degree test case, there is no noticeable differences between the ATEC and ATEST results. Specific comparison of the relative values of total pressure, total temperature, and mass flow rate at the locations where the ATEST were defined are shown in Table 11 through 13, respectively. Again, careful selection of the scalar multipliers resulted in ATEC values falling within 0.2 percent of the ATEST levels for this steady-state test case.

Comparing the values of the scalar multipliers in Tables 5 through 7 for the two test cases, indicates that using the values of the scalars for one test case will not provide

reasonable results at the second test case. In fact, using the sixty five degree throttle test case scalar values as component performance corrections to simulate the sixty degree throttle test case do not work, since they force the compressor operation beyond the surge limit. To do a full calibration of the ATEC model and simulation to match the ATEST results throughout the entire range of engine operation, a more intelligent technique would be required than used here (manually making the fit) where the component performance correction scalars are fit with functions, such as polynomial functions. The values of the scalars at each operating point would be collected into an array and correlated as functions of some primary variable such as rotor speed. For the purposes of this dissertation, however, only the simple, manual tuning technique was applied. This limits the exercise to only a couple of engine operational points since the level of effort required to completely manually tune the maps is beyond the scope of this research. It should be noted that as the simulation operation moves away from the point of tuning, differences between the ATEC results and the ATEST results (the "truth") will increase.

To check the performance of the ATEC simulation for a transient operation, the ATEST simulation was run through a two second simulation at the sixty five degree throttle test case. The transient was initiated by a change in the rotor power throttle position. The change in rotor power throttle position occurred over a 0.05 second time period. The change in throttle position resulted in a gas generator fuel flow rate reduction of approximately ten percent. The relative ATEST fuel flow rate to the combustor as a function of time is shown in Fig. 100. This variation in the fuel flow rate was

implemented in ATEC by approximating the curve as a series of straight line segments. The straight line segment representation as used by ATEC is shown in Fig. 101.

The results from ATEST were obtained by integrating using a time step size of 0.025 seconds. ATEST can use larger time steps, but the simulation was limited by the sampling frequency of the control system model. Although the actual T55-L-712 engine uses a hydromechanical control system (which is analog), the ATEST representation of the control system is digital and requires some reasonable sampling rate. The 0.025 second time step size was selected based on experiences with other digital engine control systems and their sampling frequencies. The maximum time step size used to obtain the ATEC simulation results, at 0.0001 seconds, was much smaller. The time step size was driven by the turbine model. Operation of the turbine with the mass flow function at or near the choking limit results in a small perturbation in mass flow rate having a large effect on the turbine work done factor. The time step size was kept to a minimum in order to keep the changes in the primary variable derivatives below a reasonable level.

The relative compressor pressure ratios, as functions of time, are compared in Fig. 102 for both simulations, while those as functions of compressor inlet mass flow rate are compared in Fig. 103. While there are some differences between the two data sets, actual differences between the numbers are small, with a maximum difference between the ATEC and ATEST results of 0.1 percent occurring at the end of the simulation (the percent differences given on the figures and noted in the text are based on actual differences, not relative differences). As noted in the discussion on the steady-state

calibration, the differences increase as the flow conditions move away from the point at which the steady-state calibration occurred. However, in general, ATEC results closely follow the ATEST results.

The relative combustor exit temperatures as functions of time are compared in Fig. 104 for both simulations. The relative temperature ratios across the gas generator turbine as functions of time are compared in Fig. 105. The relative pressure ratios across the gas generator turbine as functions of time are compared in Fig. 106. The power turbine relative temperature ratios and pressure ratios are compared in Figs. 107 and 108, respectively. Since the transient is not large enough to unchoke the turbine nozzles, variation of the total temperature and total pressure ratios were small. For all of the compared parameters, the observed differences in the simulation results are small. The largest difference occurred between the power turbine total pressure ratios, with a 1.5 percent difference occurring at the end of the simulation.

Looking at the relative rotor speeds for the two simulations, which are shown in Fig. 109, it is apparent that the differences between the response rates of the two simulations also carry over to the rotor speed calculation. The differences in the simulations of the rotor dynamics were traced to two causes. First, as the ATEC flow field solution changed from the initial, steady-state operating point, the scalar multipliers used to tune the model to ATEST became less valid. Another reason for the differences was attributed to the fact that the methods of calculating the rotor speed are different in ATEST and ATEC. ATEC performs the rotor dynamics calculations sequentially with

the time integration of the flow field. The acceleration rate of the rotor at a given time step is not calculated until after the flow field solution is obtained from the flow solver. ATEST, however, solves for the rotor speed as part of the overall flow field solution. It is one of the independent variables of an overall, error-term-minimization technique that ATEST uses to obtain the flow field solution. Because of the different techniques that are used to calculate rotor dynamics between the two simulations, some differences in the final answers should be expected.

The above comparisons resulted from simulations of an engine deceleration mode. To complete the transient calibration effort, an engine acceleration case was also considered. As was done above, the sample case started at the sixty five degree throttle test case. The transient was initiated by an increase in the rotor power throttle position over a 0.25 second time period. Since, during an acceleration, the compressor moves closer to the surge limit, the throttle rate of change was less than that used for the deceleration study. Using ATEST, the change in throttle position was input to the ATEST control system model and the gas generator fuel flow rate was observed to increase by approximately six percent. The observed change in the relative ATEST fuel flow rate to the combustor is shown in Fig. 110. As was done in the deceleration transient simulation, this variation in the fuel flow rate was implemented in an ATEC simulation by approximating the curve as a series of straight line segments. The straight line segment representation used by ATEC is shown in Fig. 111.

The results of running the ATEC and ATEST simulations agreed closely. The relative compressor pressure ratios as functions of time for both simulations, shown in Fig. 112, agreed to within 0.2 percent. Again, as the flow conditions move farther away from the engine operation point of steady-state calibration, the differences increase. For the range of the imposed transient, however, the differences are small. Mapping of the relative compressor pressure ratios as functions of relative compressor inlet mass flow rates is displayed in Fig. 113. The ATEC simulation results take a wider path than the ATEST simulation to reach the final, steady-state answer.

The relative combustor exit temperatures as functions of time for both simulations are compared in Fig. 114. The relative temperature ratios across the gas generator turbine as functions of time are compared in Fig. 115. The relative pressure ratios across the gas generator turbine as functions of time are compared in Fig. 116. The power turbine relative temperature ratios and pressure ratios are compared in Figs. 117 and 118, respectively. As with the deceleration calibration case, since the transient is not large enough to unchoke the turbine nozzles, variation of the total temperature and total pressure ratios were small. There are some differences between the two predicted data sets, however, but the differences are small. The largest difference occurs with the power turbine total pressure ratio, with a 0.7 percent difference occurring at the end of the simulation. In all instances, the ATEC simulation responded at a slower rate than the ATEST simulation. Looking at the relative rotor speeds for the two simulations, which are shown in Fig. 119, it is apparent that the differences between the response rates of the

two simulations also carry over to the rotor speed calculation. The gas generator rotor speed as calculated by ATEC was 0.2 percent slower than the ATEST speed.

This part of the dissertation research has shown that the ATEC model and simulation can be calibrated to give accurate results for both steady-state and transient engine operation. Care should be utilized, however, to ensure that adequate calibration data is available for the range of operation that is to be simulated. The accuracy of the ATEC calculations depends on the thoroughness of the calibration procedures and the details of the calibration data.

5.2. Dynamic Calibration

In Section 4.2 of Chapter 4, it was shown that ATEC closely matched calculated results given by DYNTECC for a T55-L-712 Turboshaft engine compressor rig as reported in [57]. This was done to ensure that the compressor model had been successfully transferred between the two simulations without any errors being introduced. For the calibration of ATEC for dynamic events, the comparison will be repeated and studied at a more in-depth level than was presented in Section 4.2. In this section of the dissertation, ATEC calculated results will be compared to actual compressor rig test data.

The ATEC simulation has been compared to compressor rig test data rather than a full engine system for one reason. A data set of sufficient detail was not found for a full engine system, that would have made such a calibration effort feasible. Since the compressor rig data was available, it was used as the foundation for the calibration effort. The operational characteristics of a full engine during a dynamic event were discussed in

Section 4.4. Various engine parameters are plotted as functions of time for the simulated full engine going through multiple compressor surge cycles, in Figs. 63 through 74.

Rig testing of the Lycoming T55-L-712 Turboshaft Engine compression system was conducted at Lycoming's compressor test facility at Stratford, CT in June of 1993. The testing was conducted at sea level, static conditions with unconditioned ambient air. The data were corrected to sea level standard dry air conditions. Steady-state and dynamic data were acquired at compressor rotational speeds between 20 and 100 percent of design rotational speed. Specific details of the test program are reported in [81].

High frequency instrumentation were included in the compressor hardware for the data acquisition. The instrumentation utilized in the calibration effort were fast response pressure transducers, flush mounted on the shroud flow path. The transducers were located just in front of the leading edge of each stator row in the axial compressor system in an axial line. Three transducers were circumferentially located at the centrifugal compressor impeller exit.

The geometry for the calibration test case is the same used during the operational verification in Chapter 4 and is shown in Fig. 46. A total of 39 control volumes were used. The calculation domain was selected to simulate the path from the inlet of the bellmouth to the throttle valve. The region upstream of the bellmouth was assumed to be open to the atmosphere. Each control volume the compressor model represents a combination rotor/stator pair. One control volume is provided at the exit of the axial compression system to account for the ducting between the axial compressor and the

centrifugal compressor. The centrifugal compressor was represented by four control volumes. This minimized the system control volume length. All work done by the centrifugal compressor was assumed to occur in the first control volume, with the other control volumes providing only the correct compression system volumetric geometry. The control volumes located downstream of the centrifugal compressor were sized to duplicate the volume of the T55-L-712 combustor and associated ducting. This also matched the geometry of the compressor test rig. A throttle valve was located where the choked turbine nozzles would be located, based on equivalent volumes along the flow path.

As discussed in Chapter 3, compressor stage pressure and temperature characteristics must be used to provide proper closure of the governing equations. The stage characteristics can be broken down into three distinct regions, as shown in Fig. 20:

1. the normal, pre-stall operating region
2. the region between the onset of stall and reverse flow
3. the reverse flow region

The steady-state Lycoming compressor rig test data were used to provide the pre-stall pressure and temperature characteristics. The stage characteristics are shown in Fig. 120 for an 80 percent rotor speed case. The characteristics shown are typical of those obtained for other high speed compression systems.

Steady-state data for compressor operation in the post-stall regions were not acquired during the Lycoming compressor rig test. Estimates for the post-stall

characteristics were synthesized using insight gained from low-speed compressor rigs and from test data acquired at the Compressor Research Facility at the Wright-Patterson Air Force Base in Dayton, Ohio. These data were acquired on a high-speed, ten stage axial compressor system [51,56,58]. The complete compressor characteristics for the 80 percent speed case are shown in Fig. 121. The post-stall temperature characteristics were generated by extrapolating the steady-state, pre-stall characteristic on the same slope until the flow coefficient was zero. A positive slope was then applied in the reverse flow region. The discontinuity in the characteristic at zero flow which is highlighted in Fig. 20 is accounted for logically within the ATEC coding and does not show up in the characteristics. Post-stall pressure characteristics were developed with a nearly smooth transition between the point of stall initiation and zero flow. This provided the correct operational response from the compression system during post-stall operation for the given speed case.

To demonstrate the ability of ATEC to simulate the characteristics of a compression system during post-stall operation, two areas of interest were investigated using the Lycoming compressor rig test data. First, the prediction of the critical stage as a function of compressor operational speed was studied. The critical stage is defined as the compressor stage that initiates the system instability (such as a pressure perturbation) which leads to the post-stall operation. Secondly, the calculation of the compression system characteristics during post-stall operation were addressed.

5.2.1 Critical Stage Determination: When building the compressor prestall characteristics for each stage, as shown in Fig. 120, the specific pressure coefficient, temperature coefficient, and flow coefficient at the stall operating point were not known. The prestall data set included only the operation points at which stable operation of the compressor was obtained. While it was assumed that the data point with the highest pressure rise and lowest mass flow rate was close to the stall point, it did not define the stall point. For this reason, the individual stage stall point pressure and temperature coefficients as functions of the flow functions must be defined to ensure the proper system response. To ensure that the proper critical stage is defined, the relative location of the stall point in relation to the other stages can be adjusted to match the experimental data. The determination of the critical stage in the T55-L-712 compression system was addressed by studying test data for rotor speeds of 70, 80, 85, and 100 percent of design. The ATEC representation of the T55-L-712 compression system was exercised at the 80 percent speed and the results compared to the data.

The data were obtained from the axially arrayed string of high response static pressure transducers located at the leading edge of each stator row. The pressure data taken that identified a post-stall event occurred for the 70 percent speed case, and is shown in Fig. 122. The data are presented as inlet static pressure traces as functions of time. At the time noted on the figure, a blockage seems to occur in the first stage. This blockage results in an increase in the static pressure just ahead of the stage, and is reported as caused by flow separation from the first stage rotor blade [82] . There does

not appear to be any other event which would force the compression system into post-stall operation. The pressure data for the 80 percent speed case are shown in Fig. 123. As with the 70 percent speed case, there is a distinct pressure pulse indicating a blockage on the first stage rotor. A closer look at the 80 percent speed case is shown in Fig. 124. The data shown are for the first, second, and third stage pressure transducers at the time of the pressure pulse. The effect of the blockage, which shows itself as an increase in the first stage inlet static pressure and a decrease in the second and third stage inlet static pressure, is easier to see in this magnified view.

At higher compressor operational speeds, the determination of the critical stage is not as straight forward. The stage inlet static pressure data for the compressor system operating at 85 percent speed are shown in Fig. 125. Although there is a definite pulse in the inlet static pressure just before the onset of system post-stall operation, the increase in the first stage inlet static pressure is not followed by a decrease in the second stage inlet static pressure. Since the critical stage normally moves aft as compressor speed increases, the 85 percent speed case may mark the beginning of the critical stage moving rearward to downstream stages in the compressor.

The stage inlet static pressure data for the compressor system operating at 100 percent speed are shown in Fig. 126. The nature of the surge initiation event is unclear from the data. There appears to be a low-frequency unsteadiness at the centrifugal compressor impeller exit, but because it exists throughout the data time frame, it is not clearly related to the surge event.

For comparison to the data, ATEC was exercised for a total simulation time length of 0.12 seconds at the 80 percent speed case. The simulation was allowed to stabilize at the nominal operating conditions for 0.05 seconds, and then the exit Mach number was reduced by 25 percent as shown in Fig. 127. The reduction in the exit Mach number boundary condition was used to represent the closing of the throttle valve. Both processes result in a reduction in the mass flow rate exiting the system.

The compressor system was fully involved in a stall event by the end of the 0.12 second duration. The overall relative compressor pressure ratio as a function of time is shown in Fig. 128. At the beginning of the throttle transient (exit boundary condition transient), the pressure ratio begins to increase. Because of the time lagged response caused by the volume in the system, the actual surge cycle does not begin until approximately four milliseconds after the exit Mach number transient is completed.

The relative static pressures at the inlet of first three stages for the 80 percent speed case are shown in Fig. 129. The time slice shown was selected based on the information presented in Fig. 128. As was present in the test data shown in Fig. 125, the first stage inlet static pressure does indeed indicate a pulse, or blockage, at approximately 0.115 seconds into the simulation. The blockage propagates to the second and third stages as a reduction in the inlet static pressure. Although not shown, the remainder of the stages of the axial compression system follow the same basic trend as the second and third stages.

Comparing the simulation results to the experimental data, it has been shown that the location of the stall point has been appropriately set for the 80 percent speed case. The remainder of the calibration effort will focus on the nature of the simulated response of the compression system during surge cycles.

5.2.2 Post-Stall Operation: To force the simulated T55-L-712 compression system into surge cycles, the same exit Mach number transient shown in Fig. 127 was used. The transient was extended such that at between 0.5 and 0.55 seconds, the exit Mach number boundary condition was returned to its original value. The simulation was allowed to run for one second. This allowed the system to stabilize and return to normal operation. The exit Mach number boundary condition variation is depicted graphically in Fig. 130.

The relative overall pressure ratio as a function of inlet corrected air flow rate, normalized by the design air flow rate, is shown in Fig. 131. The compressor operation is characterized by a relatively slow pressurization of the system due to the throttle (or exit Mach number boundary condition) closure. Once the system enters stall, the system volume quickly depressurizes by blowdown to the reversed flow region. The system continues to operate in stall until the compressor pressure ratio drops to nearly unity. At that point, the system repressurizes by a rapid reacceleration to positive flow. Once the flow reaches the normal compressor operational speed line, a slow pressurization is resumed until the process is then repeated. The process of stall and recovery at constant rotor speed continues until the throttle is returned to its on-design position. The relative

air flow rate is plotted as a function of time in Fig. 132. The relative pressure ratio across the compressor is plotted in Fig. 133, likewise as a function of time. The rapid drop and then sudden increase in mass flow through the compressor is apparent in Fig. 133. During part of the stall recovery process, the mass flow rate remains nearly constant. Comparing the results shown in Fig. 132 to those shown in Fig. 133, it is seen that the pressure ratio falls off on the same time scale as the mass flow rate, but the pressurization process takes longer relative to the time it takes for the flow to return to its original value.

Values for selected stage inlet static pressures are compared to test data in Figs. 134 through 137. The first stage inlet static pressure variation during the surge cycles, shown as a delta from the original, steady-state value, is compared to the test data in Fig. 134. The test data plot does not include static pressure difference (delta-static pressure) magnitude on it due to questions concerning the values given in the same figure by Owen and Davis [57]. The delta-static pressure scales used by Owen and Davis [57] indicated that the surge cycles produced negative pressure. It is interesting to note that the ATEC predicted surge cycle frequency was approximately 9.5 Hz, which is very near the measured frequency of 8.5 Hz. There is also a distinct similarity between the shapes and envelopes of the two data sets.

The change in the third stage inlet delta-static pressure during the surge cycle is shown and plotted against test data in Fig. 135. Given that the surge cycle frequency remains constant throughout the compressor and since the first stage matched the data, it is no surprise that the third stage data also compares favorably. What is of interest is that

the shape of the surge cycles as given by the test data is somewhat different than given by the first stage, and ATEC matches that difference. Comparing the shape of the surge cycles for the sixth stage and centrifugal compressor impeller exit delta-static pressure plots to the test data, shown in Fig. 136 and 137, respectively, indicates that the trend is consistent through the compressor.

5.3. Engine Starting

The successful starting of a gas turbine engine is dependent upon many variables. The size of the starting system, the engine torque drag, the rotor(s) polar moment(s) of inertia, and the compressor design all are first order effects on the starting process [82]. Adding in other variables such as bleed flows, variable geometry, and fuel scheduling makes an already complicated problem much worse. ATEC, with its ability to quickly and easily simulate the operation of a gas turbine engine, can provide a means to analyze starting problems and search for optimized hardware and control system configurations.

The purpose of this section of the dissertation is to demonstrate the capabilities of ATEC in the start regime. A sample data set of a successful T55-L-712 engine start was obtained and will be shown. ATEC was used to simulate the start sequence indicated in the data set. It should be noted that this study was for demonstration purposes only, and no effort was made to provide a close match of the simulation to the test data. This is driven by the fact that the data set is limited in scope, and several key parameters that would be needed to successfully calibrate ATEC to the engine start data were not available.

The T55-L-712 engine uses a hydraulic starter to initiate the rotation of the gas generator shaft. As the gas generator system begins to rotate, the fuel flow to the combustor is started and injected through two starting nozzles. Ignition is provided by spark plugs. As the engine speed increases, the fuel pressure also increases. When the pressure in the combustor reaches a minimum level, the fuel flow is switched over to atomizing primary nozzles and the starting nozzles are turned off.

The relative gas generator rotational speed during a successful engine start is shown in Fig. 138. When the starter was turned on , the engine speed increased nearly linearly until idle speed was reached. Some time before the engine reached idle speed, the starter was disengaged, but the available data does not specify when this occurred.. The overall relative compressor pressure ratio as a function of time is shown in Fig. 139. The pressure ratio followed the rotor speed, although its relationship with time was not linear.

The relative fuel flow rate provided to the combustor as a function of time is shown in Fig. 140. Once the rotor speed reached approximately 3000 rpm, the fuel flow was initiated and quickly rose to a given lower limit. At that point, the fuel flow rate increased as a function of engine speed (as noted above) because the pressurization of the fuel system was controlled by a fuel pump driven off of the gas generator rotor. The influence of the rotor speed on the fuel flow rate is shown in Fig. 141. Once the fuel flow was initiated, the relative fuel flow rate was very nearly linear with speed until idle speed was reached. Ignition was obtained almost as soon as the fuel flow stabilized at the lower

limit. This can be inferred from the gas temperature measured downstream of the gas generator turbine. The relative total temperature downstream of the turbine is plotted as a function of time in Fig. 142.

The ATEC representation of the starting process assumed that the rotor speed was a linear function of time with constant slope until the ground idle speed was reached. A model of a starting system was not used, although implementing a starter model into ATEC would not be a major effort. Since information on how the starter operated, relative to the test data, was not available, it was judged that modeling the rotor acceleration as a constant was appropriate for this effort. Fuel flow rate, which on an actual engine is determined by the hydromechanical control system, was calculated as a function of rotor speed as shown in Fig. 141.

The simulation of the start process was conducted as follows. The ATEC grid was initialized with ambient total pressure and total temperature and zero mass flow rate. The rotor speed was also set to zero. At ten seconds into the simulation, the rotor began its acceleration until at forty seconds into the simulation, the ground idle speed was reached and the rotor speed was held constant. The system was allowed to stabilize for ten seconds before the simulation was ended.

Rotor rotational speed as a function of time was input into the simulation as shown in Fig. 143. The fuel flow rate provided to the combustor model was implemented as a function of rotor rotational speed as is shown in Fig. 144. The variable time step routine was used for the simulation, with a maximum time step of 0.01 seconds used

where possible. During the starting transient, the rates of change in the flow field restricted the time step size to approximately $1.0x10^{-4}$ seconds.

The relative pressure ratio of the compression system as a function of time is shown in Fig. 145. As with the actual test data, the pressure climbs to the ground idle level in a parabolic form. Since the ATEC compressor characteristics are based on a compressor rig and the start data was obtained from a different compressor, one-to-one comparisons are not possible. The trends and overall magnitude of the model results are correct, however. The final ATEC calculated pressure ratio was within three percent of the test data.

The relative gas total temperature exiting the gas generator turbine as a function of time is shown in Fig. 146. As with the test data, the conditions inside the combustor were favorable for the combustion process to occur at the time of fuel flow initiation. The total temperature increased faster in the simulation than it did in the test data. An attempt to tune the flame ignition lagging time constant in the combustor model so that the simulation results matched the test data was made, but with limited success. It was judged that the test data reflects the effects of the heat transfer from the exhaust gas stream to the metal mass in the turbine area.

6. SUMMARY AND CONCLUSIONS

The objective of this research was to develop a mathematical model and computer simulation of a single-spool gas turbine engine system including a free power turbine, that could simulate on- and off-design steady-state operation, as well as transient and dynamic engine responses to perturbations in operational and control conditions. The desired model and simulation was to be capable of simulating engine operation over a wide range of operating conditions. The objective was satisfied and the state-of-the-art in gas turbine engine modeling was advanced by developing a mathematical model and computer simulation called the Aerodynamic Turbine Engine Code, or ATEC. The development effort and results have been documented herein. The dissertation has provided a description of the various component models required to describe the workings of a gas turbine engine. The mathematical approach taken to solve for the flow field inside the gas turbine engine has also been documented. Each of the various component models have been operationally verified. Calibration of the overall model and simulation was conducted for available data sets obtained from the Lycoming T55-L-712 turboshaft engine.

The test cases used during the operational verification were selected based upon their availability and also their ability to demonstrate the capabilities and features of the respective models. A new Euler flow solver, using both an explicit and implicit flow solution technique, was operationally verified by studying transient and steady subsonic flow in a converging / diverging nozzle. The program results for steady flow were

compared to isentropic flow relationships. There were no differences between the ATEC results and the isentropic flow relationships. The simulation was exercised using the explicit solver, the implicit solver, and then with the new solver that uses a variable time step routine that implements either the explicit solver or the implicit solver, depending on allowable maximum rates of change in the dependent flow variables. The variable time step size routine was shown to permit large time steps when the system was operating in steady-state mode, or in transient modes near steady-state. Reduced time step sizes were used during time variant events where it was required in order to adequately resolve flow perturbations.

The compressor model used by ATEC was operationally verified using a test case that had been reported in the literature. The test case focused on the dynamic response of a compressor system during post-stall operation. The results were compared to the results obtained using the same test case from the Dynamic Turbine Engine Compressor Code, or DYNTECC. It was shown that the ATEC compressor model matched the DYNTECC model results for the given dynamic flow field simulation. This was appropriate since the ATEC compressor model was based upon the DYNTECC compressor model..

A combustor model was operationally verified by incorporating the model downstream of the simulated compressor system, and then forcing the compressor through multiple surge cycles. During the surge cycles, the combustion process occurring in the combustor was blown out and then re-lit to match the upper and lower steady-state flammability limits. The predicted combustion efficiency was shown to be appropriate,

in that as the combustor system approached the blow off and light off equivalence ratio limits, the combustion efficiency was reduced. The dynamic modeling of the heat release rate, based on a first order time-lagging equation, was operationally verified by comparing results from the simulation with the same inputs, but with different time lagging constants.

The turbine model was operationally verified by exercising the full engine simulation through a dynamic surge cycle event, for a constant rotor rotational speed, which was caused by an increase in the fuel flow rate. As desired, the increased fuel flow rate decreased the mass flow rate through the turbine nozzles and forced the compression system into multiple surge cycles. It was shown that the model operated smoothly and that the calculated work done factor, total temperature ratio, and total pressure ratio followed the proper trends.

The rotor dynamics model was operationally verified by simulating a fuel flow rate transient during both a deceleration and an acceleration transient of the engine. The effect of the rotor dynamics on the simulation was demonstrated by increasing the gas generator rotor polar moment of inertia. With the same inputs, except for the higher rotor polar moment of inertia, the engine system was less responsive to the transient.

Finally, the heat transfer model for the axial compressor system was operationally verified. The compression system simulation was exposed to a nearly step input in the inlet temperature, such as would occur during inlet temperature distortion. The heat

transfer model tracked the metal temperatures for both the rotor and stator blades and the supporting base metal. The metal temperatures tracked the air temperature as required.

Calibration of the ATEC model and simulation has been presented for three available data sets. The first calibration effort addressed the transient performance of the simulation. The calibration data was obtained from a lumped-component type transient model and simulation called ATEST. The use of experimental data for the calibration effort was not possible because a representative and complete set of test data could not be found in the available literature. The calibration effort was broken into two parts. Steady-state calibration of the ATEC simulation was conducted to match the overall component performance as given by the ATEST simulation for the same engine (there were differences in the compressor performance representation). ATEC was matched or tuned to ATEST at two steady-state operation points. At each point, it was possible to match ATEC results to ATEST results within a few tenths of a percent. However, the scalar multipliers used to tune ATEC at one steady-state point were not appropriate at the other point, limiting the perturbation range about which transients could be imposed for each calibration point.

Transient calibration of ATEC to the ATEST results was obtained for both an engine deceleration case and an engine acceleration case. The component performance parameters that were compared typically fell within a few tenths of a percent of one another throughout the range of the transients. One parameter, the power turbine total pressure ratio, reached a maximum difference of 1.5 percent

The second calibration effort focused on the compressor model. The ATEC simulation results were compared to data from a compressor running at constant speed on a compressor rig obtained at an engine manufacturer's compressor research facility. As with the transient calibration, the ATEC simulation was not compared to a full engine test data set due to the unavailability of such data. The ATEC calibration effort focused on predicting the critical stage for stall initiation in the compressor, and in the dynamic characteristics of the system during the post-stall operation. An analysis of the test data indicated that the first stage of the compressor rig was the critical stage. That is, the first stage was the earliest stage to indicate that the air flow had separated, or stalled, from the blade, causing a blockage in the flow path. ATEC also indicated that the first stage was the critical stage, indicated by the correct signature response of an increase in the static pressure in front of the stage and a decrease in the static pressure in the stages downstream.

During the post-stall event, the compression system rig entered into multiple surge cycles. ATEC also successfully simulated the surge cycles. The frequency of the surge cycles was predicted to be 9.5 Hz, while the test data indicated a system frequency response of 8.5 Hz. The relative shapes of the pressure traces at various locations were also calculated appropriately by ATEC. Although the experimental data showed significant differences in the shapes of the pressure traces from the front of the compressor rig to the rear, and at each location, ATEC accurately calculated the shapes.

Because of potentially unquantifiable errors in the measured magnitudes of the pressure traces, no comparison was made with the ATEC predictions of magnitude.

The final comparison of ATEC calculations to representative data sets addressed the characteristics of a gas turbine engine during a starting process. A T55-L-712 turboshaft engine starting data set was presented and discussed. Because of the limited scope of the data set, a direct comparison of ATEC results to the test data was not possible. It was shown, however, that ATEC could accurately calculate the trends and responses of the engine system during the starting regime.

Based on these efforts and results, it is concluded that the ATEC model and simulation methodology represents a new capability in gas turbine engine modeling. Specific contributions to the advancement of the state-of-the-art include:

- Assembling a full model and simulation for a single shaft gas turbine engine that provides operational capabilities for steady-state, transient, and dynamic gas turbine engine operation, including post-stall compressor operation.
- A new variable time step integration routine that uses both an explicit and implicit numerical solver, selecting th appropriate solver by basing the allowable time step size (and, hence, CFL condition) on the time rate of change of the dependent variables.
- Operational verification and calibration of the model and simulation to appropriate data sets

- Providing a technique for determining the volumes and time constants that allow the one-dimensional model to be tuned to match an operational engine
- Developing a numerical modeling framework by which various parameters and their effects on gas turbine engine operation can be assessed, thereby extending the power of one-dimensional modeling of gas turbine engines. For example, the effect of blade-casing clearances on the overall engine operational characteristics can be evaluated by modifying the compressor stage characteristics as well as the appropriate time constants of the components.

Where previous researchers have focused their efforts on developing either a transient or a dynamic engine model, ATEC provides the capability to address both operational regimes with a one dimensional, stage-by-stage engine model with post-stall capability. With proper calibration of the simulation to the problem of interest, the ATEC model and simulation can supplement experimental efforts and provide a test bed for "what-if" studies that would not be economically affordable if done experimentally.

7. RECOMMENDATIONS FOR FUTURE WORK

The gas turbine engine model and simulation named ATEC has been created and calibrated against pertinent data sets obtained from both experimental efforts and other engine simulations. As with any software development effort, there were certain assumptions and limitations placed on the model and the resulting simulation that limit the applicability of ATEC. These limitations should be removed and further improvements made to facilitate applications to future gas turbine engines. The following recommendations for future work are therefore offered as a means to broaden the scope and viability of ATEC:

- **Additional Calibration:** As noted in an earlier section, the usefulness of a model and simulation is directly tied to the level of confidence that can be placed on the output. The only way a simulation can earn the trust of the user is to receive as much calibration and operational verification as possible. ATEC users should therefore continue to build upon its data base of calibration test cases.
- **Improved Numerical Solution Techniques:** One of the problems faced in the development effort was caused by the turbine model. When the turbine is operating in its normal operational regime, any small change in the mass flow function results in a large change in the work done factor. Since the work done factor defines the torque produced by the turbine for the rotor dynamics model, the sensitivity of the turbine model to changes in mass flow function

limits time step sizes below those desired for fast computations. Future efforts should focus on modifying the calculation of the relationship between the turbine work and turbine inlet mass flow, if possible. For example, the ATEST simulation model addresses this problem by including the rotor speed calculation in the implicit equation solver, whereas ATEC incorporates it determination sequentially outside the equation solver.

- **Stage Characteristics:** The compressor stage characteristics form the foundation for such gas turbine engine models. Future experimental efforts should be focused on obtaining accurate compression system characteristics on a stage-by-stage basis in both the pre- and post-stall regimes. The ability to obtain accurate stage characteristics using analytical methods should also receive the fullest attention to provide leverage to the experimental efforts.
- **Combustion Modeling:** The method used in ATEC to define the flammability limits and combustion efficiency are based on steady-state, engineering correlations developed for several generic type combustor configurations. For steady-state and transient operation, these correlations are adequate. To accurately model the combustion processes during dynamic events, where combustion can take place outside the combustor, a more fundamental approach should be used. It is recommended that the integration of a time dependent fuel injection, evaporation, and a simple combustion chemistry model be integrated into ATEC for dynamic combustion events.

- **Inlet Distortion Modeling:** In a real world environment, the gas turbine engine rarely gets exposed to a perfectly planar inflow boundary condition as is specified in ATEC. Rather, there more typically exists both radial and circumferential nonuniformities in the total pressure and temperature of the flow entering the engine. For this reason, it is recommended that the capability be included in ATEC to handle distorted inlet flow. There are several approaches to this problem, with the parallel compressor theory as discussed by Shahrokhi [27], and the more complex computational fluid dynamics approach as given by Hale, et. al. [28] being the most obvious choices.
- **Control System Modeling:** Because of the complexity of the modern gas turbine engine, the control system plays a major role in obtaining the desired performance over the range of engine operating conditions. Integrating a control system model into the ATEC simulation will permit check-out and optimization of control system architecture and time-constants before installed on a given engine.
- **Multiple Configurations:** ATEC currently is configured to handle a single spool turbojet or a turboshaft engine. While there are many engines that fall into these categories, the majority of the modern gas turbine engines are twin shaft turbofans. The necessary effort required to extend the ATEC model and

simulation to handle a turbofan configuration must be expended in order for ATEC to be fully applicable to the gas turbine engine community.

- **Additional Component Models:** Current efforts have focused on providing the fundamental building blocks of the gas turbine engine. Several "second-level" component models should be incorporated into ATEC to enhance its usability. For example, models of several different types of starters should be included. Models for friction and other parasitic losses should also be included in the rotor dynamics model. Heat transfer models for the centrifugal compressor, the combustor, and the turbines would also be of benefit.

Bibliography

Bibliography

1. Khalid, S. J., "Role of Dynamic Simulation in Fighter Engine Design and Development," AIAA Journal of Propulsion, Jan.-Feb. 1992, pp. 219-226.

2. Hale, A. A. and Davis, M. W., "DYNamic Turbine Engine Compressor Code DYNTECC - Theory and Capabilities," AIAA-92-3190, Presented at the AIAA/SAE/ASME/ASEE 28th Joint Propulsion Conference and Exhibit, Nashville, TN, July 6-8, 1992.

3. Montgomery, J. F., III, "The Need for Air Force Engine Stability Margin Testing for Inlet-Engine Interface Definition," AFAPL TR-71-84, December, 1971.

4. Thompson, H. A., Parallel Processing for Jet Engine Control, Springer-Verlag, New York, NY, © 1992.

5. Mattingly, J. D., Heiser, W. H., and Daley, D. H., Aircraft Engine Design, AIAA Education Series, J. S. Przemieniecki, Series Editor-in-Chief, American Institute of Aeronautics and Astronautics, Washington, DC, © 1987.

6. Oates, G. C., Aerothermodynamics of Gas Turbine and Rocket Propulsion, AIAA Education Series, J. S. Przemieniecki, Series Editor-in-Chief, American Institute of Aeronautics and Astronautics, Washington, DC, © 1988.

7. Zucrow, M. J., Aircraft and Missile Propulsion, Volume II, John Wiley & Sons, New York, NY, © 1958.

8. Hill, P. G., and Peterson, C. R., Mechanics and Thermodynamics of Propulsion, Addison-Wesley Publishing Company, Inc., Reading, MA, ©1965.

9. Mattingly, J. D., Heiser, W. H., and Daley, D. H., Aircraft Engine Design, AIAA Education Series, J. S. Przemieniecki, Series Editor-in-Chief, American Institute of Aeronautics and Astronautics, Washington, DC, © 1987, pp. 136-137.

10. Oates, G. C., "The Aerothermodynamics of Gas Turbine Engines," AFAPL TR 78-52, July, 1978, pg. 8-1.

11. Oates, G. C., Aerothermodynamics of Gas Turbine and Rocket Propulsion, AIAA Education Series, J. S. Przemieniecki, Series Editor-in-Chief, American Institute of Aeronautics and Astronautics, Washington, DC, © 1988, pg. 313.

12. Greitzer, E. M., "REVIEW-Axial Compressor Stall Phenomena," Transactions of the ASME, Journal of Fluids Engineering, Vol. 102, June, 1980, pp. 134 - 151.

13. Shepherd, D. G., Principles of Turbomachinery, The Macmillan Company, New York, © 1956.

14. Emmons, H. W., Pearson, C. E., and Grant, H. P., "Compressor Surge and Stall Propagation, " ASME Transactions, Vol. 27, April 1955, pp. 455-469.

15. Moore, F. K., and Greitzer, E. M., "A Theory of Post-Stall Transients in Multistage Axial Compression Systems," NASA CR 3878, March 1985.

16. Keenan, J. G., Elementary Theory of Gas Turbines and Jet Propulsion, Oxford University Press, London, UK, © 1946.

17. Sobey, A. J., and Suggs, A. M., Control of Aircraft and Missile Powerplants, John Wiley, New York, NY, © 1963.

18. Thompson, H. A., Parallel Processing for Jet Engine Control, Springer-Verlag, New York, NY, © 1992, pg. 10.

19. Lefebvre, A. H., Editor, Gas Turbine Design Problems, Hemisphere Publishing Corporation, New York, NY, © 1978.

20. Mellor, A. M., Editor, Design of Modern Turbine Combustors, Academic Press, Inc., San Diego, CA, © 1990.

21. Culick, F. E. C., "Some Recent Results for Nonlinear Acoustics in Combustion Chambers," AIAA Journal, Vol. 32, No. 1, January 1994, pp. 146 -169.

22. Bloxsidge, G. J., Dowling, A. P., Hooper, N., and Langhorne, P. J., "Active Control of Reheat Buzz," AIAA Journal, Vol. 26, No. 7, July 1988, pp. 783 - 790.

23. Jahnke, F. C. and Culick, F. E. C., "An Application of Dynamical Systems Theory to Nonlinear Combustion Instabilities," AIAA 93-0114, Presented at the 31st Aerospace Sciences Meeting and Exhibit, Reno, NV, January 11-14, 1993.

24. Simon, J. S., Valavani, L., Epstein, A. H., and Grietzer, E. M., "Evaluation of Approaches to Active Compressor Surge Stabilization," ASME 92-GT-182, Presented at the International Gas Turbine and Aeroengine Congress and Exposition, Cologne, Germany, June 1-4, 1992.

25. Day, I. J., "Active Suppression of Rotating Stall and Surge in Axial Compressors," ASME 91-GT-87, Presented at the International Gas Turbine and Aeroengine Congress and Exposition, Orlando, FL, June 3-6, 1991.

26. Badmus, O. O., Nett, C. N., and Schork, F. J., "An Integrated Full-Range Surge Control / Rotating Stall Avoidance Compressor Control System," in Proceedings of the 10th American Control Conference, Institute of Electrical and Electronics Engineers, Boston, MA, June 26-28, 1991, pp. 3173-3180.

27. Shahrohki, K. A., "Application of a Modified Dynamic Compression System Model to a Low-Aspect Ratio Fan: Effects of Inlet Distortion," Thesis submitted to Vanderbilt University, Nashville, TN, May, 1995.

28. Hale, A. A., Davis, M. W., Jr., and Kneile, K. R., "Turbine Engine Analysis Compressor Code: TEACC, Part I: Technical Approach and Steady State Results," Presented at the 32nd Aerospace Sciences Meeting, AIAA 94-0148, Reno, NV, January, 1994.

29. Fishbach, L. H. and Caddy, M. J., "NNEP: The Navy NASA Engine Program (NASA)," NASA TM-X-71857, December, 1975.

30. Mattingly, J. D., "ONX and OFFX User Guide, On-Design and Off-Design Cycle Analysis Computer Programs," American Institute of Aeronautics and Astronautics, Inc., New York, NY, © 1987.

31. Chappell, M. A., and McLaughlin, P. W., "Approach to Modeling Continuous Turbine Engine Operation from Startup to Shutdown," Journal of Propulsion and Power, Vol. 9, No. 3, May-June 1993, pp. 466 - 471.

32. Law, A. M., and Kelton, W. D., Simulation Modeling and Analysis, McGraw-Hill, Inc., New York, NY, © 1991, pp. 298 - 322.

33. Seldner, K., Mihaloew, J. R., and Blaha, R. J., "Generalized Simulation Technique for Turbojet Engine System Analysis," NASA TN D-6610, February, 1972.

34. Szuch, J. R., "HYDES - A Generalized Hybrid Computer Program for Studying Turbojet or Turbofan Engine Dynamics," NASA TM X-3014, April, 1974.

35. Sellers J. F., and Daniele, C. J., "DYNGEN - A Program for Calculating Steady-State and Transient Performance of Turbojet and Turbofan Engines," NASA TN D-7901, April, 1975.

36. Schuerman, J. A., Fischer, K. E., and McLaughlin, P. W., "High Frequency Dynamic Engine Simulation," NASA CR 135313, July, 1977.

37. Mason, J. R., Park, J. W., and Jaekel, R. F., "Extended frequency Turbofan Model," NASA CR-165261, December, 1980.

38. Sadler, G. G., and Melcher, K. J., "DEAN: A Program for Dynamic Engine Analysis," AIAA 85-1354, Presented at the AIAA/SAE/ASME/ASEE 21st Joint Propulsion Conference, Monterey, CA, July 8-10, 1985.

39. Chung, K., Leamy, K. R., and Collins, T. P., "A Turbine Engine Aerodynamic Model for In-Stall Transient Simulation," AIAA 85-1429, Presented at the AIAA/SAE/ASME/ASEE 21st Joint Propulsion Conference, Monterey, CA, July 8-10, 1985.

40. French, J. V., "Modeling Post-Stall Operation of Aircraft Gas Turbine Engines," AIAA 85-1431, Presented at the AIAA/SAE/ASME/ASEE 21st Joint Propulsion Conference, Monterey, CA, July 8-10, 1985.

41. Hosny, W. M., Bitter, S. B., and Steenken, W. G., "Turbofan Engine Nonrecoverable Stall Computer-Simulation Development and Validation," AIAA 85-1432, Presented at the AIAA/SAE/ASME/ASEE 21st Joint Propulsion Conference, Monterey, CA, July 8-10, 1985.

42. Sugiyama, Y., Tabakoff, W., and Hamed, A., "J-85 Surge Transient Simulation," Journal of Propulsion, Vol. 5, No. 3, May-June, 1989, pp. 375-381.

43. Marble, F. E., "Three Dimensional Flow in Turbomachines," Chapter C in Aerodynamics of Turbines and Compressors, W. R. Hawthorne, Editor, Volume X, High Speed Aerodynamics and Jet Propulsion, Princeton University Press, Princeton, NJ, © 1964, pp. 108-113.

44. Schobeiri, M. T., Attia, M., and Lippke, C., "GETRAN: A Generic, Modularly Structured Computer Code for Simulation of Dynamic Behavior of Aero- and Power Generation Gas Turbine Engines," Journal of Engineering for Gas Turbines and Power, Vol. 116, July, 1994, pp. 483 - 494.

45. Schobeiri, M. T., Attia, M., and Lippke, C., "Nonlinear Dynamic Simulation of Single- and Multispool Core Engines, Part I: Computational Method," Journal of Propulsion and Power, Vol. 10, No. 6, Nov. - Dec., 1994. pp. 855 - 862.

46. Schobeiri, M. T., Attia, M., and Lippke, C., "Nonlinear Dynamic Simulation of Single- and Multispool Core Engines, Part II: Simulation, Code Validation," Journal of Propulsion and Power, Vol. 10, No. 6, Nov. - Dec., 1994. pp. 863 - 867.

47. Attia, M. S., and Schobeiri, M. T., "A New Method for the Prediction of Compressor Performance Maps Using One-Dimensional Row-by-Row Analysis, with Application to Dynamic Simulations," ASME 95-GT-434, Presented at the International Gas Turbine and Aeroengine Congress and Exposition, Houston, TX, June 5-8, 1995.

48. Badmus, O. O., Eveker, K. M., and Nett, C. N., "Control-Oriented High Frequency Turbomachinery Modeling: General 1D Model Development," ASME 93-GT-385, presented at the International Gas Turbine and Aeroengine Congress and Exposition, Cincinnati, OH, May 24-27, 1993.

49. Badmus, O. O., Chowdhury, S., Eveker, K. M., and Nett, C. N., "Control-Oriented High-Frequency Turbomachinery Modeling: Single-Stage Compression System 1D

Model," ASME 93-GT-18, presented at the International Gas Turbine and Aeroengine Congress and Exposition, Cincinnati, OH, May 24-27, 1993.

50. Davis, M. W., Jr., "A Stage-by-Stage Post-Stall Compression System Modeling Technique: Methodology, Validation, and Application," Dissertation submitted to Virginia Polytechnic Institute and State University, Blacksburg, VA, December, 1986.

51. Davis, M. W., Jr., "Parametric Investigation into the Combined Effects of Pressure and Temperature Distortion on Compression System Stability". AIAA-91-1895, AIAA/SAE/ASME/ASEE 27th Joint Propulsion Conference, Sacramento, CA, June 1991.

52. Garrard, G. D., Davis, M. W., Jr., and Hale, A. A., "Recent Advances in Gas Turbine Engine Dynamic Models Developed Through JDAPS," ASME 95-GT-146, Presented at the International Gas Turbine and Aeroengine Congress and Exposition, Houston, TX, June 1995.

53. Davis, M. W., Jr., "A Stage-by-Stage Dual-Spool Compression System Modeling Technique". ASME 82-GT-189, International Gas Turbine and Aeroengine Conference and Exposition, London, England, March 1982.

54. Dowler, C., Boyer, K., and Poti, N., "Model Predictions of Fan Response to Inlet Temperature Transients and Spatial Temperature Distortion". AIAA-89-2686, AIAA/SAE/ASME/ASEE 25th Joint Propulsion Conference, Monterey, CA, July 1989.

55. Gorrell, S. E., and Davis, M. W., "Application of a Dynamic Compression System Model to a Low Aspect Ratio Fan: Casing Treatment and Distortion". AIAA-93-1871, AIAA/SAE/ASME/ASEE 29th Joint Propulsion Conference, Monterey, CA, July 1993.

56. O'Brien, W. F., "Dynamic Simulation of Compressor and Gas Turbine Performance". AGARD Lecture Series 183, Section 5, Steady and Transient Performance Prediction of Gas Turbine Engines, pp. 5-1 through 5-28.

57. O'Brien, W. F., and Boyer, K. M., "Stall and Recovery in Multistage Axial-Flow Compressors". Proceedings of the AGARD 74th Specialists' Meeting of the Propulsion and Energetics Panel, Luxembourg, August, 1989.

58. Owen, K. A., and Davis, M. W., Jr., "Modeling the Dynamic Behavior of an Axial-Centrifugal Compression System." AIAA 94-2802, 30th AIAA/ASME/SAE/ASEE Joint Propulsion Conference, Indianapolis, IN, June 27-29, 1994.

59. Russler, P. M., "An Investigation of the Surge Behavior of a High-Speed Ten-Stage Axial Flow Compressor". WL-TR-93-2076, May 1993.

60. Reddy, K. C., and Nayani, S. N., "Compressor and Turbine Models - Numerical Stability and Other Aspects," AEDC-TR-85-5, April, 1985.

61. Brent, J. A., "High-Stage Loading / Low Aspect Ratio Compressor (HSL/LARC)," AFWAL-TR-80-2075, September, 1980.

62. Herbert, M. V., "A Theoretical Analysis of Reaction Rate Controlled Systems - Part 1," Chapter 6 in *Combustion Research and Reviews, 1957*, Agardograph No. 15, Butterworths Scientific Publications, London, England, February, 1957.

63. Lefebvre, A. H., "Fuel Effects on Gas Turbine Combustion - Ignition, Stability, and Combustion Efficiency," Journal of Engineering for Gas Turbines and Power, Vol. 107, January 1985, pp. 24 - 37.

64. Derr, W. S., and Mellor, A. M., "Recent Developments," in Design of Modern Turbine Combustors, edited by A. M. Mellor, Academic Press, Harcourt Brace Jovanovich, New York, NY, © 1990.

65. Blazowski, W. S., "Fundamentals of Combustion," in "The Aerothermodynamics of Gas Turbine Engines," edited by G. C. Oates, AFAPL TR 78-52, July, 1978, pg. 15-16.

66. Oates, G. C., Aerothermodynamics of Gas Turbine and Rocket Propulsion, AIAA Education Series, J. S. Przemieniecki, Series Editor-in-Chief, American Institute of Aeronautics and Astronautics, Washington, DC, © 1988, pp. 218-220.

67. Crawford, R. A., and Burwell, A. E., "Quantitative Evaluation of Transient Heat Transfer on Axial Flow Compressor Stability," AIAA 85-1352, Presented at the 21st AIAA/SAE/ASME/ASEE Joint Propulsion Conference, Monterey, CA, July 8-10, 1985.

68. MacCallum, N. R. L., and Pilidis, P., "The Prediction of Surge Margins During Gas Turbine Engine Transients," ASME 85-GT-208, Presented at the Gas Turbine Conference and Exhibit, Houston, TX, March 18-21, 1985.

69. Sissom, L. E., and Pitts, D. R., Elements of Transport Phenomena, McGraw-Hill, Inc, New York, NY, © 1972, pp. 118-121.

70. Courant, R., Fredricks, K. O., and Levey, H.,(1928), translated from German to: "On the Partial Differential Equations on Mathematical Physics," IBM J. Res. Dev., Vol. II, pp. 215-234, 1967.

71. Varner, M. O., Martindale, W. J., Phares, W. J., Kneile, K. R., and Adams, J. C., Jr., "Large Perturbation Flow Field Analysis and Simulation for Supersonic Inlets," NASA CR-174676, September, 1984.

72. Hirsch, C. Numerical Computation of Internal and External Flows, Volume 1: Fundamentals of Numerical Discretization, John Wiley and Sons, New York, NY, ©1988, pp. 271-281.

73. Ibid, pp. 505-508.

74. Zucker, R. D., Fundamentals of Gas Dynamics, Matrix Publishers, Inc., Beaverton, OR, © 1977.

75. Bradley, R. G. "CFD Validation Philosophy," Paper No. 1, AGARD Symposium on Validation of Computational Fluid Dynamics, May 1988, Lisbon, Portugal.

76. Marvin, J. G., "Accuracy Requirements and Benchmark Experiments for CFD Validation," NASA TM 100087, May 1988.

77. Povinelli, L. A. "CFD Validation Experiments for Internal Flows," NASA TM 100797, May 1988.

78. Bobbitt, P. J., "The Pros and Cons of Code Validation," NASA TM 100657, July 1988.

79. Kutler, P., "A Perspective of Computational Fluid Dynamics," NASA TM 88246, May 1986.

80. AGARD Advisory Report, "A Selection of Experimental Test Cases for the Validation of CFD Codes," AGARD-AR-303, Vol. 1 and 2, August 1994.

81. Owen, A. K. and Bobula, G. A., "Analysis of Dynamic Rig Test Data for an Axial/Centrifugal Compressor Operating at Design Speed," Presented at the AKS 50th Annual Forum and Technology Display, May 11-13, 1994.

82. Cousins, W. T., Jones, M. G., and Belling, T. L., "Surge and Stall Characteristics of Axial-Centrifugal Compressors: The Enhancement to Engine Stability," Presented at the AGARD 85th Propulsion and Energetics Panel Meeting, Derby, England, May 8-12, 1995.

APPENDICES

APPENDIX A - Tables

Table 1. Survey of Gas Turbine Engine Mathematical Models and Simulations Reported in the Literature

Ref.	Author	Report Title	Source	Date
31	K. Seldner, J. R. Mihaloew, R. J. Blaha	Generalized Simulation Technique for Turbojet Engine System Analysis	NASA TN D-6610	02/01/72
32	J. R. Szuch	HYDES - A Generalized Hybrid Computer Program for Studying Turbojet or Turbofan Engine Dynamics	NASA TM X-3014	01/04/74
33	J. F. Sellers, C. J. Daniele	DYNGEN - A Program for Calculating Steady-State and Transient Performance of Turbojet and Turbofan Engines	NASA TN D-7901	04/01/75
34	J. A. Schuerman, K. E. Fischer, P. W. McLaughlin	High Frequency Dynamic Engine Simulation	NASA CR-135313	07/01/77
35	J. R. Mason, J. W. Park, R. F. Jaekel	Extended Frequency Turbofan Model	NASA CR-16526	12/15/80
36	G. G. Sadler, K. J. Melcher	DEAN: A Program for Dynamic Engine Analysis	AIAA-85-1354	06/06/85
37	K. Chung, K. R. Leamy, T. P. Collins	A Turbine Engine Aerodynamic Model for In-Stall Transient Simulation	AIAA-85-1429	07/08/85
40	J. V. French	Modeling Post-Stall Operation of Aircraft Gas Turbine Engines	AIAA-85-1431	07/08/85
41	W. M. Hosny, S. J. Bitter, W. G. Steenken	Turbofan Engine Nonrecoverable Stall Computer-Simulation Development and Validation	AIAA-85-1432	07/08/85
42	Y. Sugiyama, W. Tabakoff, A. Hamed	J85 Surge Transient Simulation	Journal of Propulsion, Vol. 5, No. 3	05/01/89
44	T. Schobeiri, C. Lippke, M. Abouelkheir	Nonlinear Dynamic Simulation of Single-and Multi-Spool Core Engines	AIAA 93-2580	06/28/93
48	O. O. Badmus, K. M. Eveker, C. N. Nett	Control-Oriented High Frequency Turbomachinery Modeling; General 1D Model Development	ASME 93-GT-385	05/24/93

Table 2. Definitions and Predicted Values of the Parameters for the J85 Surge Transient Simulation

Parameters**	Definitions	Predicted Values
PC	$(PR_c - 1)/(PR_a - 1)$	0.35 ~ 0.55
MC	CM_c/CM_a	0.0 ~ 0.2
MF	CM at $PR_f = PR_{ref}$	-0.3 ~ 0.2
PB	$(PR_b - 1)/(PR_a - 1)$	0.9*
MB	CM_b/CM_a	0.97*
τ_{RS}	τ at Point a	2 ms*
τ_{AC}	τ for $CM_c < CM < 0.9CM_a$	3 ~ 7 ms
τ_{NG}	τ for $CM < 0$	0.1 ms*
η_b	η at Point b	$0.9\eta_a$
η_{PS}	Lower Limitη for $CM > 0$	20 %*
η_{NG}	η for $CM < 0$	20 %*

*Indicates Assumed Values

**See Figure 14 for location of parameters on characteristic curves

Adapted from: Sugiyama, Y., Tabakoff, W., and Hamed, A., "J-85 Surge Transient Simulation," Journal of Propulsion, Vol. 5, No. 3, May-June, 1989, pp. 375-381.

Table 3. Survey of Model Capabilities and Features from the Literature

Ref.	First Author	Full Eqn. Set?	Post-Stall Compressor Model?	Transient Capabilities?	Calibrated?
31	Seldner	No	No	No	No
32	Szuch	No	No	Yes	No
33	Sellers	No	No	Yes	No
34	Schuerman	Yes	No	No	Attempted
35	Mason	Yes	No	No	Yes
36	Sadler	No	Yes	No	No
37	Chung	Yes	Yes	No	No
40	French	No	Yes	Yes	Yes
41	Hosny	No	Yes	Yes	Yes
42	Sugiyama	No	Yes	No	No
44	Schobeiri	Yes	No	Yes	Limited
48	Badmus	Yes	Yes	No	No

Table 4. Geometry for the Converging-Diverging Nozzle for the Flow Solver Check-Out

Node Indice	Axial Location (ft)	Outer Radius (ft)
1	-1	1
2	-0.790359	1
3	-0.618719	0.99
4	-0.478193	0.975
5	-0.363139	0.95
6	-0.268941	0.9
7	-0.191819	0.825
8	-0.128676	0.775
9	-0.0769792	0.75
10	-0.0346534	0.725
11	0	0.72
12	0.0346534	0.725
13	0.0769792	0.75
14	0.128676	0.775
15	0.191819	0.825
16	0.268941	0.9
17	0.363139	0.95
18	0.478193	0.975
19	0.618719	0.99
20	0.790359	1
21	1	1

Table 5. Scalar Multipliers Used to Adjust Compressor Total Pressure and Total Temperature Ratios for the Steady-State Calibration of ATEC

Parameter	Power Throttle Angle = 65° Degrees	Power Throttle Angle = 60° Degrees
Total Pressure Adjustment for Each Stage	Axial Stages: 0.992 Centrifugal: 0.9855	Axial Stages: 0.975 Centrifugal: 0.9855
Total Temperature Adjustment for Each Stage	Axial Stages: 1.000 Centrifugal: 1.0005	Axial Stages: 1.000 Centrifugal: 0.98

Table 6. Combustor Model Loss Coefficient (C_d) Used to Adjust Combustor Total Pressure Loss for the Steady-State Calibration of ATEC

	Power Throttle Angle = 65° Degrees	Power Throttle Angle = 60° Degrees
C_d	1.18	1.3

Table 7. Turbine Mass Flow Function Scalar Multiplier Used to Adjust Turbine Work Done Factor for the Steady-State Calibration of ATEC

	Power Throttle Angle = 65° Degrees	Power Throttle Angle = 60° Degrees
Gas Generator Turbine	0.99813	0.99891
Power Turbine	1.0005	0.9972

Table 8. Comparison of ATEC and ATEST Relative Total Pressure Values at Reference Stations in the Engine for the 65° Power Throttle Steady-State Calibration Test Case

Location	ATEST	ATEC	% Difference
Inlet	0.1321	0.1321	0.00
Compressor Inlet	0.1321	0.1321	0.00
Combustor Inlet	1.000	1.0008	0.08
Gas Generator Turbine Inlet	0.9601	0.9610	0.10
Power Turbine Inlet	0.3421	0.3422	0.04
Exit	0.1344	0.1342	-0.14

Table 9. Comparison of ATEC and ATEST Relative Total Temperature Values at Reference Stations in the Engine for the 65° Power Throttle Steady-State Calibration Test Case

Location	ATEST	ATEC	% Difference
Inlet	0.2341	0.2341	0.00
Compressor Inlet	0.2341	0.2341	0.00
Combustor Inlet	0.4515	0.4516	0.01
Gas Generator Turbine Inlet	1.0000	1.0002	0.02
Power Turbine Inlet	0.7981	0.7984	0.04
Exit	0.6567	0.6565	-0.03

Table 10. Comparison of ATEC and ATEST Relative Mass Flow Rate Values at Reference Stations in the Engine for the 65° Power Throttle Steady-State Calibration Test Case

Location	ATEST	ATEC	% Difference
Inlet	0.9965	0.9969	0.04
Compressor Inlet	0.9965	0.9969	0.04
Combustor Inlet	0.9465	0.9469	0.04
Gas Generator Turbine Inlet	0.9650	0.9654	0.04
Power Turbine Inlet	0.9970	0.9974	0.04
Exit	1.0000	1.0004	0.04

Table 11. Comparison of ATEC and ATEST Relative Total Pressure Values at Reference Stations in the Engine for the 60° Power Throttle Steady-State Calibration Test Case

Location	ATEST	ATEC	% Difference
Inlet	0.1496	0.1496	0.00
Compressor Inlet	0.1496	0.1497	0.03
Combustor Inlet	1.0000	1.0012	0.12
Gas Generator Turbine Inlet	0.9600	0.9593	-0.07
Power Turbine Inlet	0.3428	0.3441	0.38
Exit	0.1517	0.1514	-0.17

Table 12. Comparison of ATEC and ATEST Relative Total Temperature Values at Reference Stations in the Engine for the 60° Power Throttle Steady-State Calibration Test Case

Location	ATEST	ATEC	% Difference
Inlet	0.2543	0.2543	0.01
Compressor Inlet	0.2543	0.2543	0.01
Combustor Inlet	0.4703	0.4699	-0.09
Gas Generator Turbine Inlet	1.0000	1.0002	0.2
Power Turbine Inlet	0.7962	0.7979	0.21
Exit	0.6726	0.6727	0.02

Table 13. Comparison of ATEC and ATEST Relative Mass Flow Rate Values at Reference Stations in the Engine for the 60° Power Throttle Steady-State Calibration Test Case

Location	ATEST	ATEC	% Difference
Inlet	0.9988	0.9986	-0.02
Compressor Inlet	0.9988	0.9986	-0.02
Combustor Inlet	0.9487	0.9485	-0.02
Gas Generator Turbine Inlet	0.9649	0.9647	-0.02
Power Turbine Inlet	0.9970	0.9967	-0.03
Exit	1.0000	0.9997	-0.03

APPENDIX B. Figures

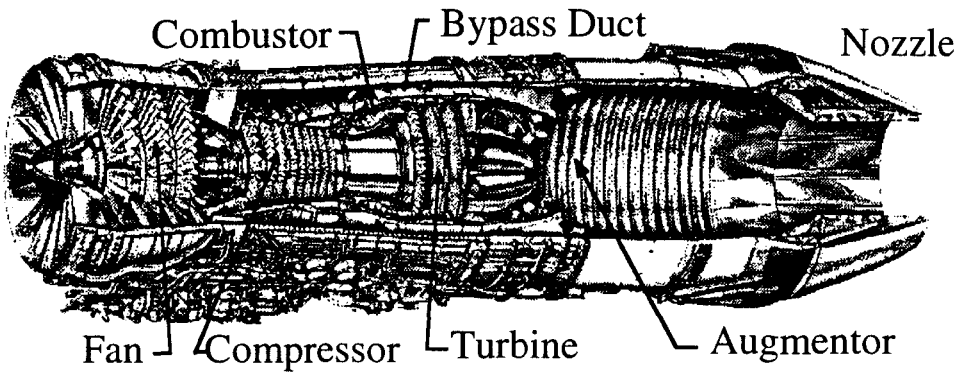

Figure 1. Cutaway View of a Gas Turbine Engine Showing its Various Components.

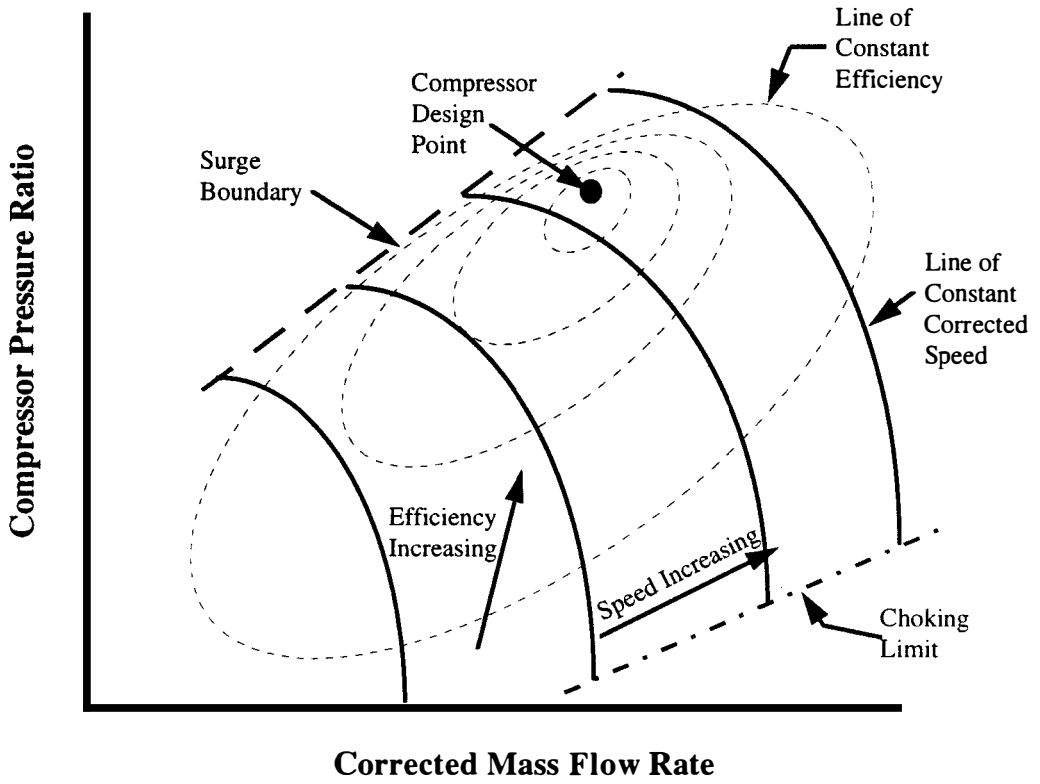

Figure 2. A Representative Compressor Performance Map Showing Lines of Constant Corrected Speed and Efficiency.

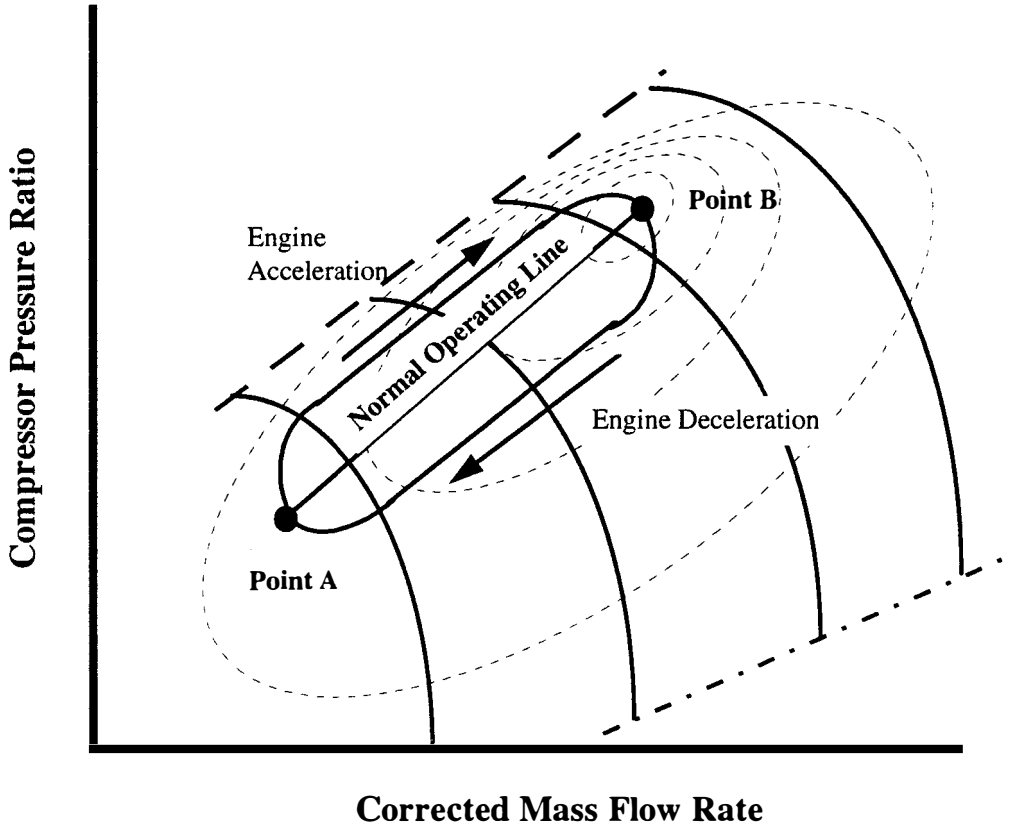

Figure 3. Path of Compressor Operation During Engine Transient Shown on Compressor Performance Map.

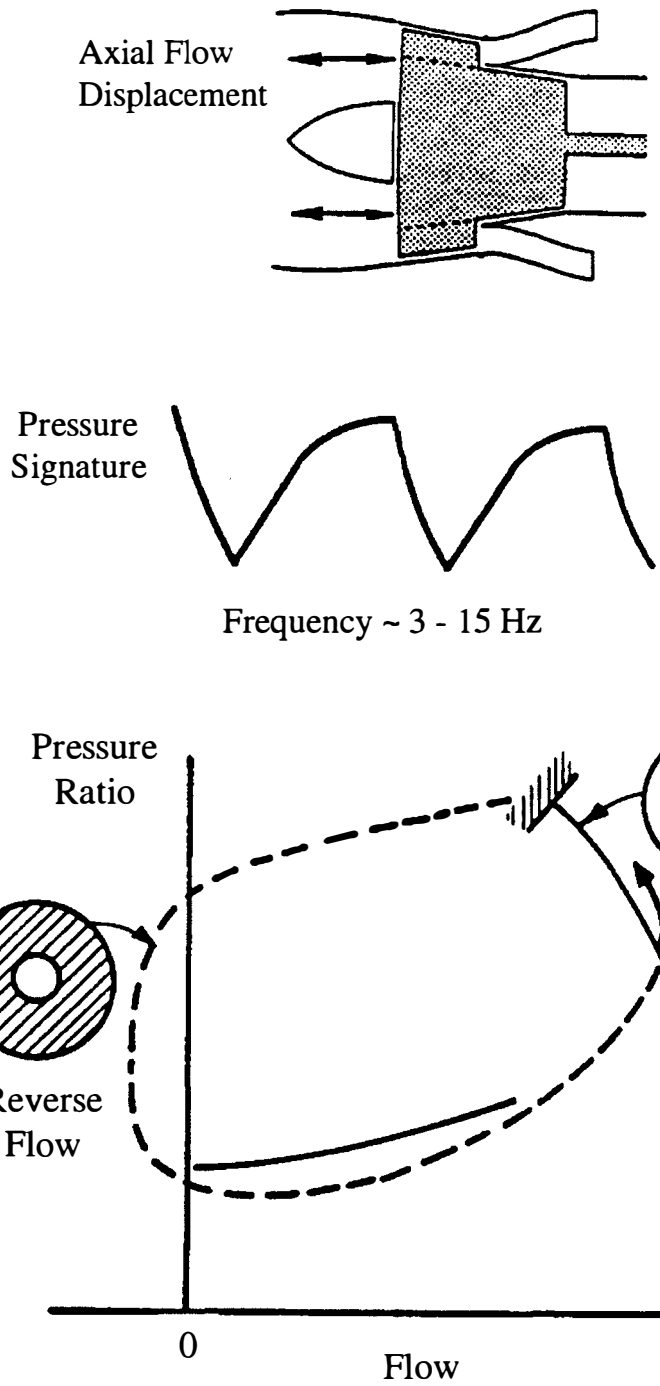

Figure 4. Compressor Surge - Axially Oscillating Flow.

Source: Davis, M. W., Jr., "A Stage-by-Stage Post-Stall Compression System Modeling Technique: Methodology, Validation, and Application," Dissertation submitted to Virginia Polytechnic Institute and State University, Blacksburg, VA, December, 1986

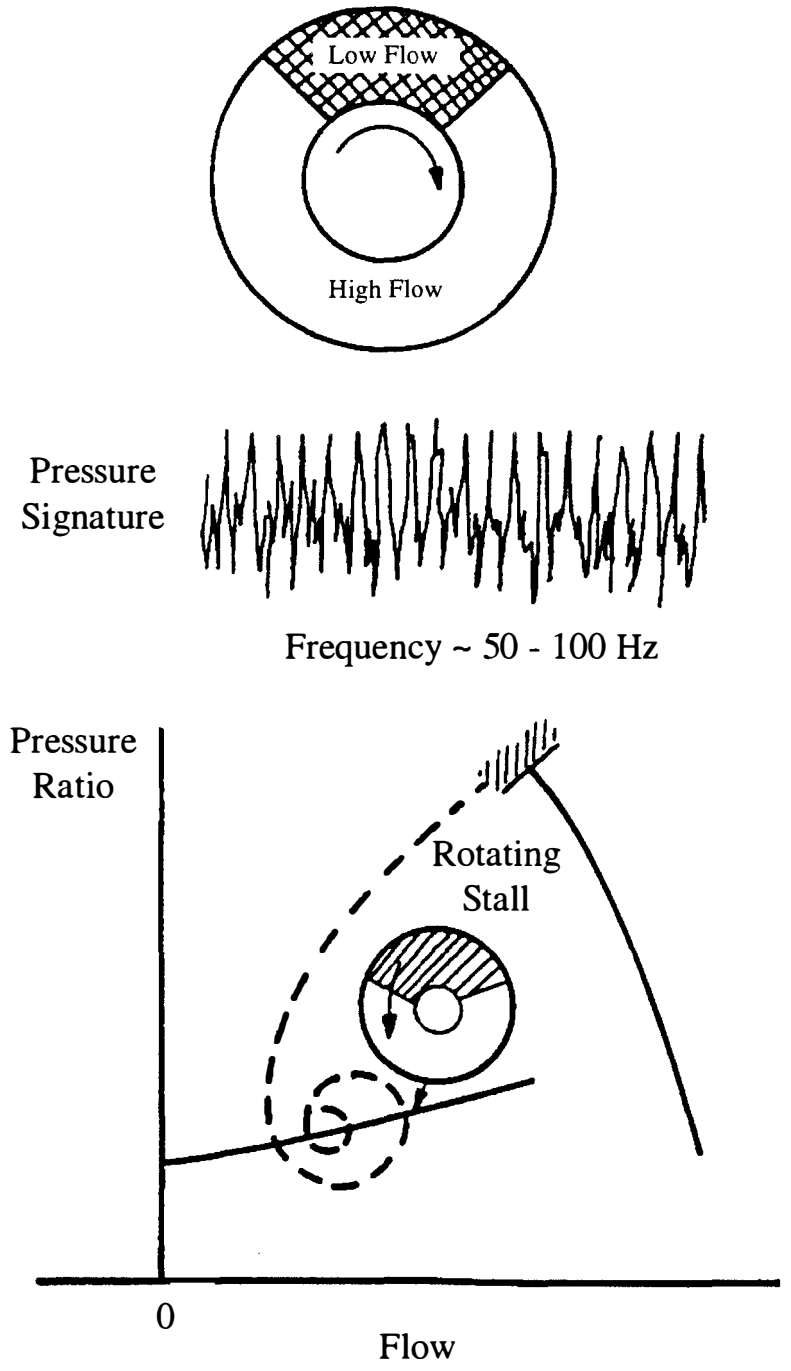

Figure 5. Compressor Rotating Stall - Circumferentially Nonuniform Flow

Source: Davis, M. W., Jr., "A Stage-by-Stage Post-Stall Compression System Modeling Technique: Methodology, Validation, and Application," Dissertation submitted to Virginia Polytechnic Institute and State University, Blacksburg, VA, December, 1986

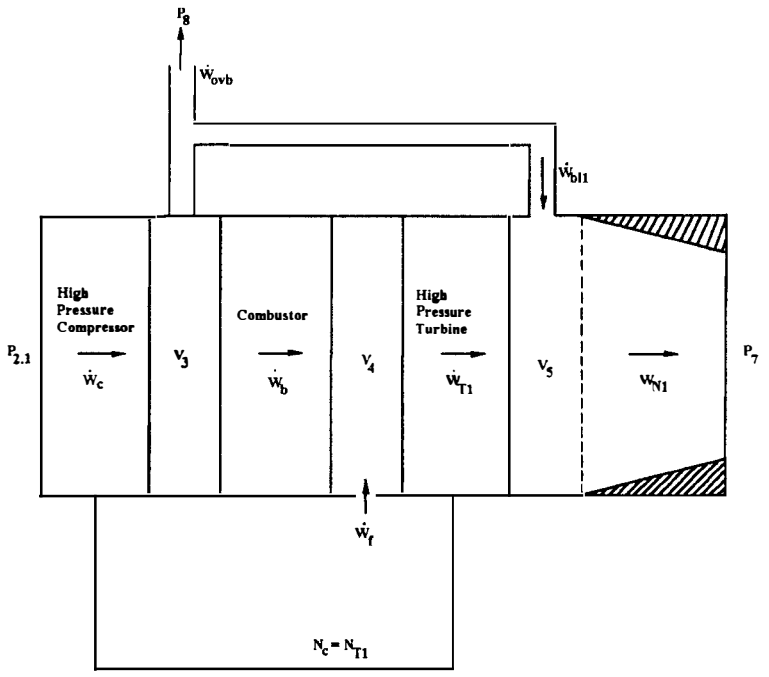

a. Single Spool Turbojet

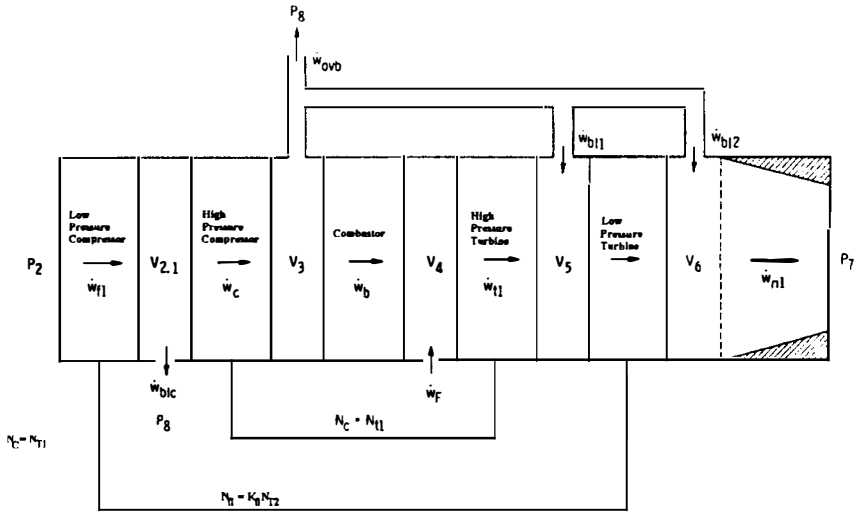

b. Two Spool Turbojet

Figure 6. Two Engine Configurations Modeled by Szuch

Source: Szuch, J. R., "HYDES - A Generalized Hybrid Computer Program for Studying Turbojet or Turbofan Engine Dynamics," NASA TM X-3014, April, 1974.

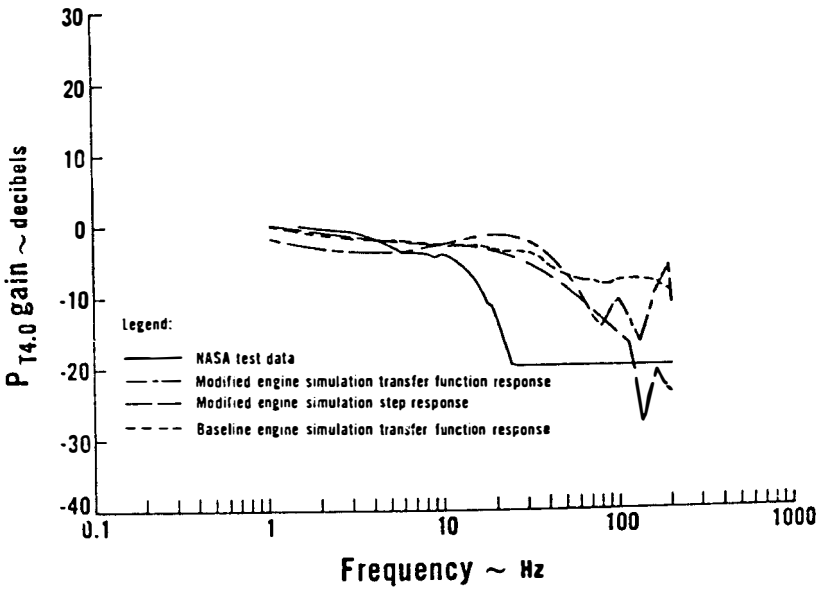

Figure 7. Comparison of Frequency Response of the Gas Turbine Engine Model Compared to Test Data by Schuerman, et. al.

Source: Schuerman, J. A., Fischer, K. E., and McLaughlin, P. W., "High Frequency Dynamic Engine Simulation," NASA CR 135313, July, 1977.

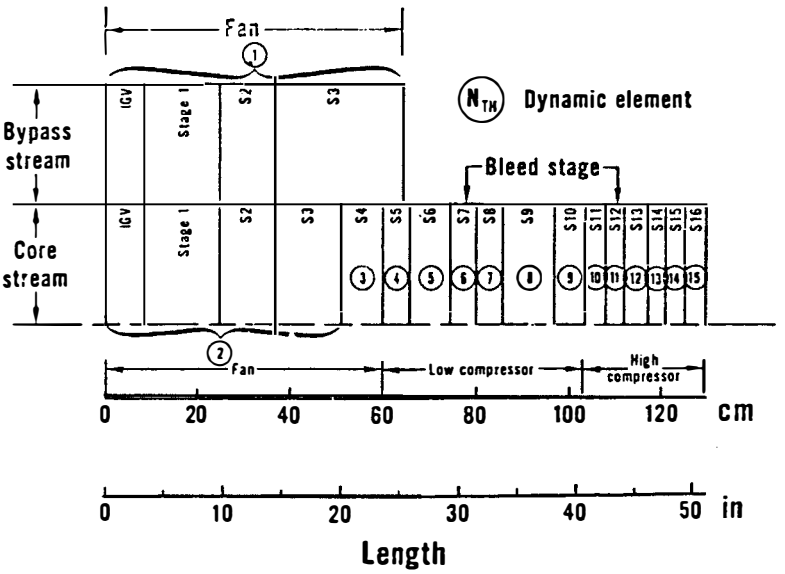

Figure 8. Discretization of the Fan and Compressor Region in Gas Turbine Engne Model by Schuerman, et. al.

Source: Schuerman, J. A., Fischer, K. E., and McLaughlin, P. W., "High Frequency Dynamic Engine Simulation," NASA CR 135313, July, 1977.

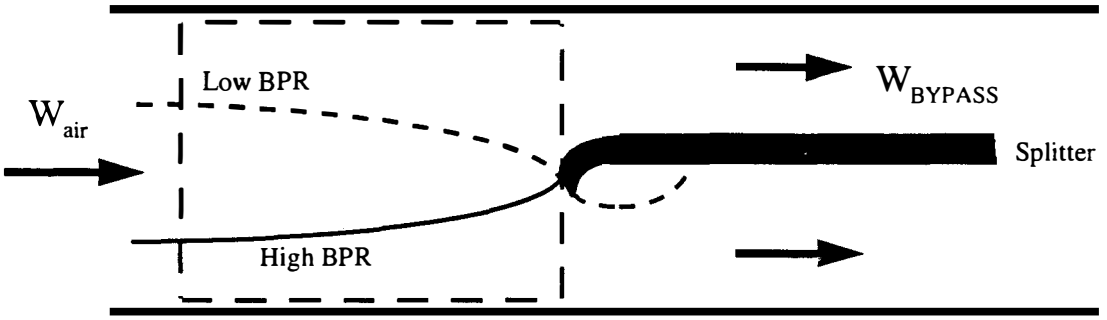

Figure 9. Sketch of Variation in Radial Location of Control Volume Separation Boundary in Gas Turbine Engine Model by Mason, et. al.

Source: Mason, J. R., Park, J. W., and Jaekel, R. F., "Extended frequency Turbofan Model," NASA CR-165261, December, 1980.

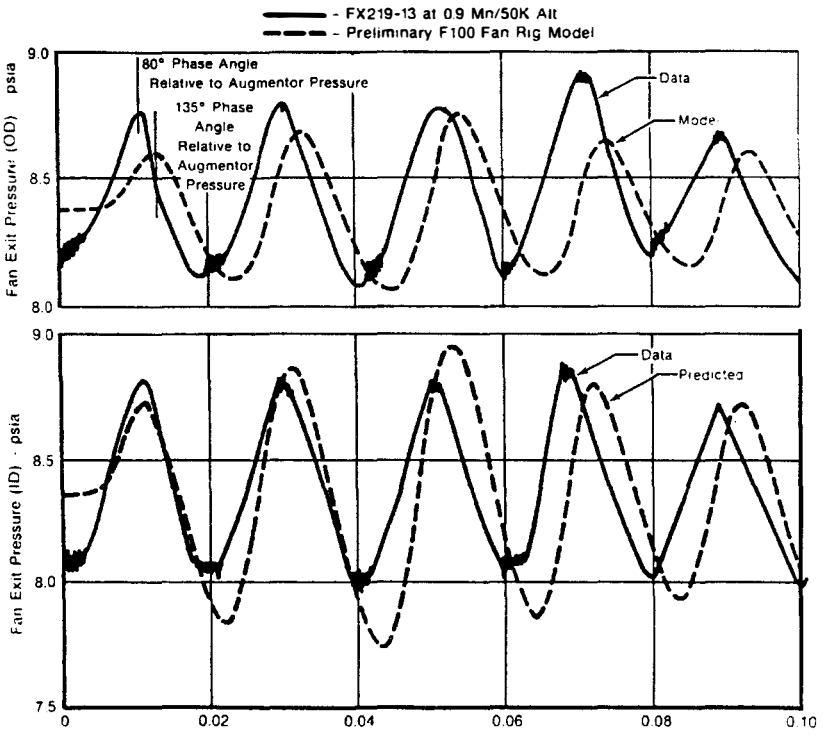

Figure 10. Comparison of Simulation Results to F100 Fan Exit Pressure by Mason, et. al.

Source: Mason, J. R., Park, J. W., and Jaekel, R. F., "Extended frequency Turbofan Model," NASA CR-165261, December, 1980.

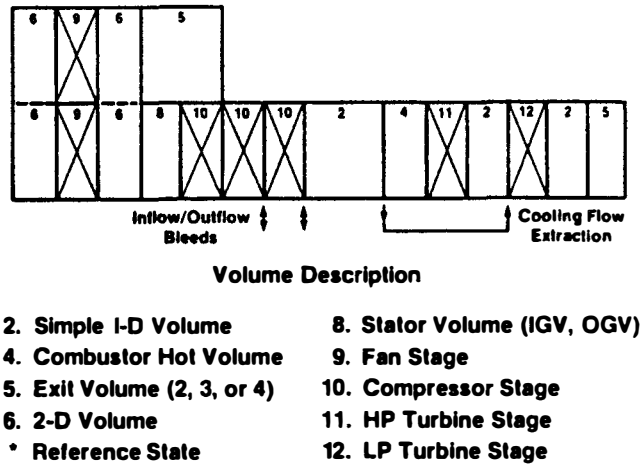

Figure 11. Discretization of the Flow Domain for the Gas Turbine Engine Model by Chung, et. al.

Source: Chung, K., Leamy, K. R., and Collins, T. P.,"A Turbine Engine Aerodynamic Model for In-Stall Transient Simulation," AIAA 85-1429, Presented at the AIAA/SAE/ASME/ASEE 21st Joint Propulsion Conference, Monterey, CA, July 8-10, 1985.

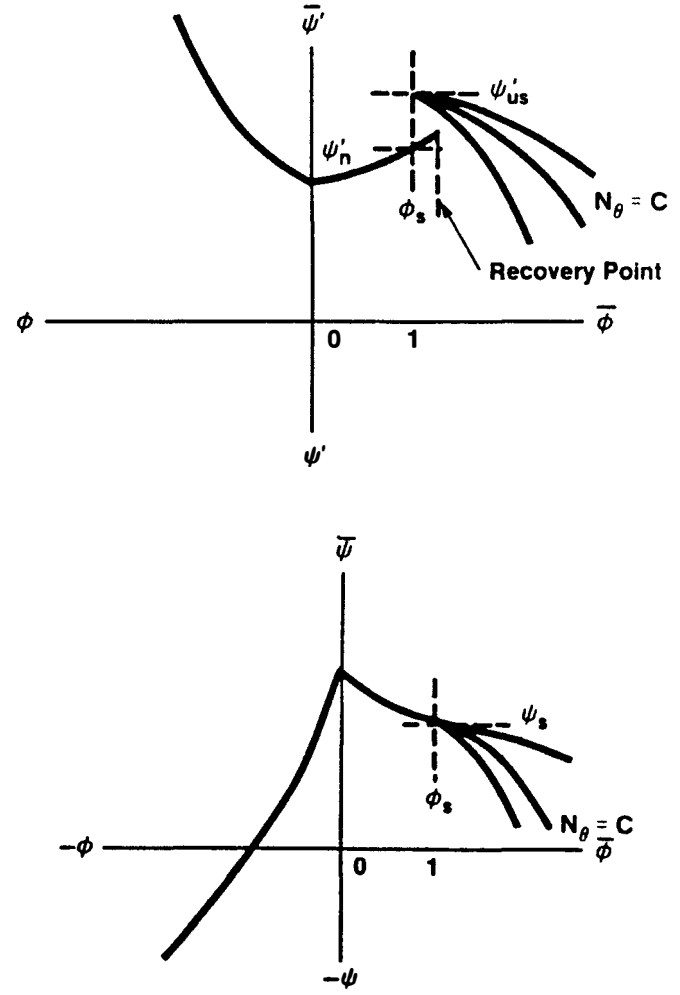

Figure 12. Compressor Characteristics Used by Chung, et. al.

Source: Chung, K., Leamy, K. R., and Collins, T. P.,"A Turbine Engine Aerodynamic Model for In-Stall Transient Simulation," AIAA 85-1429, Presented at the AIAA/SAE/ASME/ASEE 21st Joint Propulsion Conference, Monterey, CA, July 8-10, 1985.

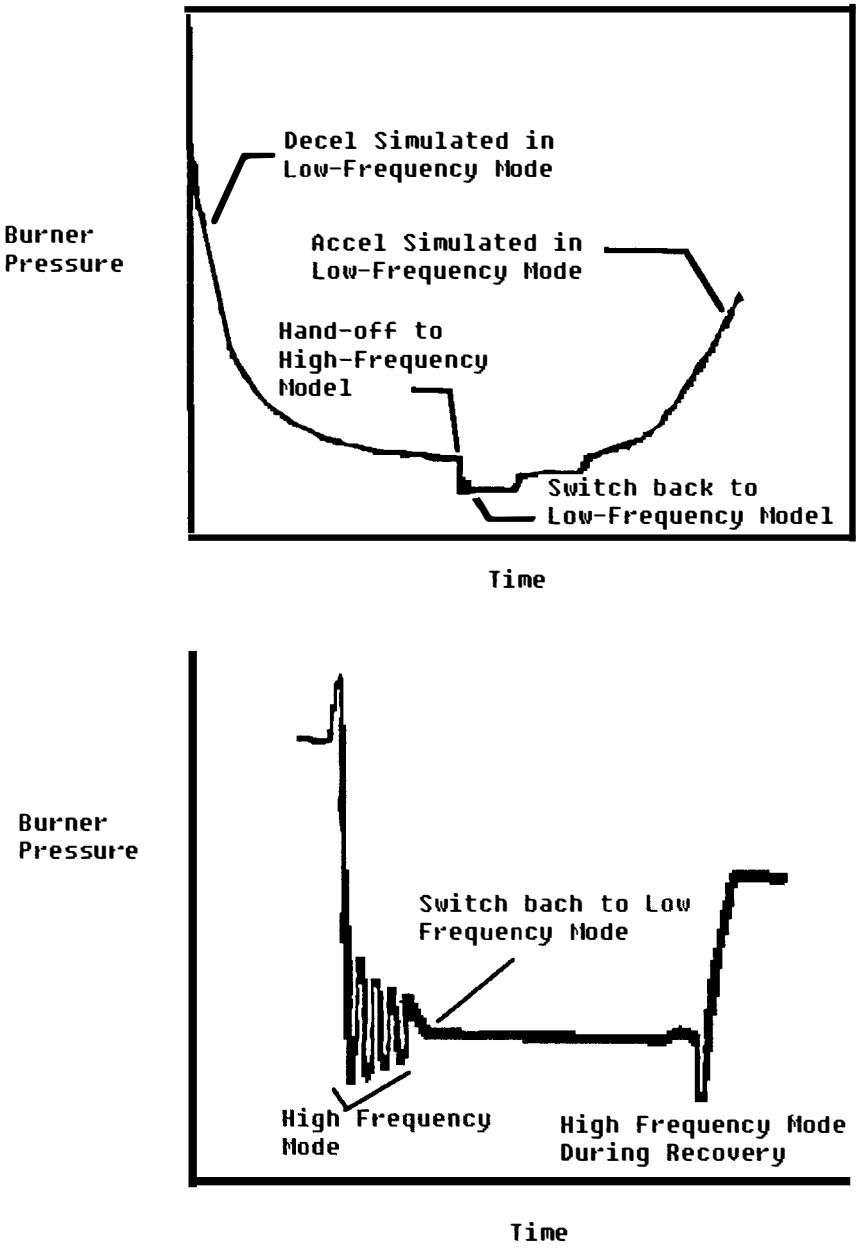

Figure 13. Compressor Inlet Pressure as a Function of Time for Gas Turbine Engine Model by French.

Source: French, J. V., "Modeling Post-Stall Operation of Aircraft Gas Turbine Engines," AIAA 85-1431, Presented at the AIAA/SAE/ASME/ASEE 21st Joint Propulsion Conference, Monterey, CA, July 8-10, 1985.

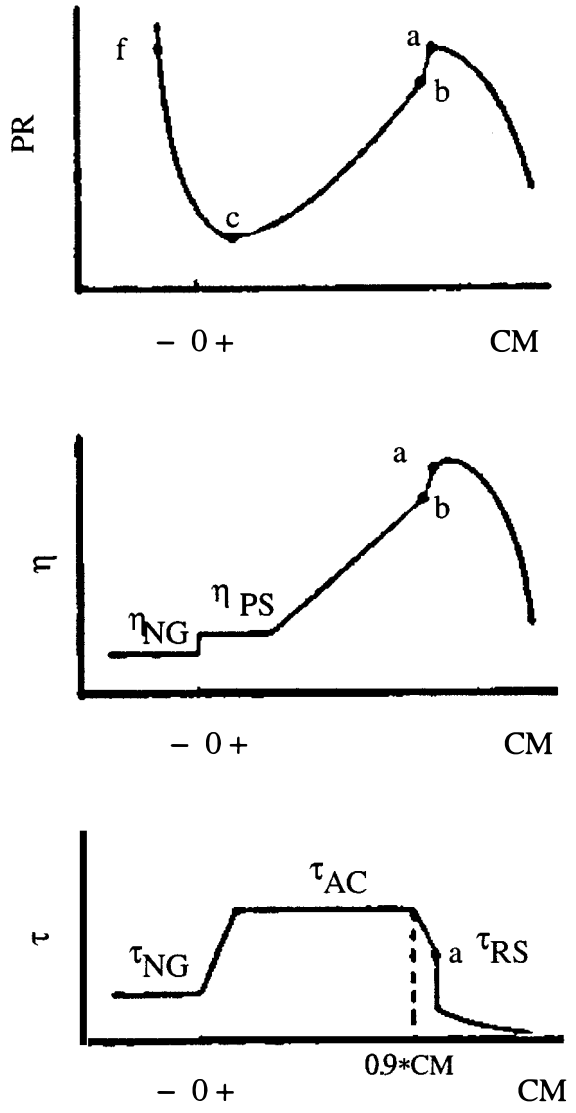

Figure 14. Location of the Operating Points on the Compressor Stage Characteristics for the Gas Turbine Engine Model by Sugiyama, et. al.

Source: Sugiyama, Y., Tabakoff, W., and Hamed, A., "J-85 Surge Transient Simulation," Journal of Propulsion, Vol. 5, No. 3, May-June, 1989, pp. 375-381.

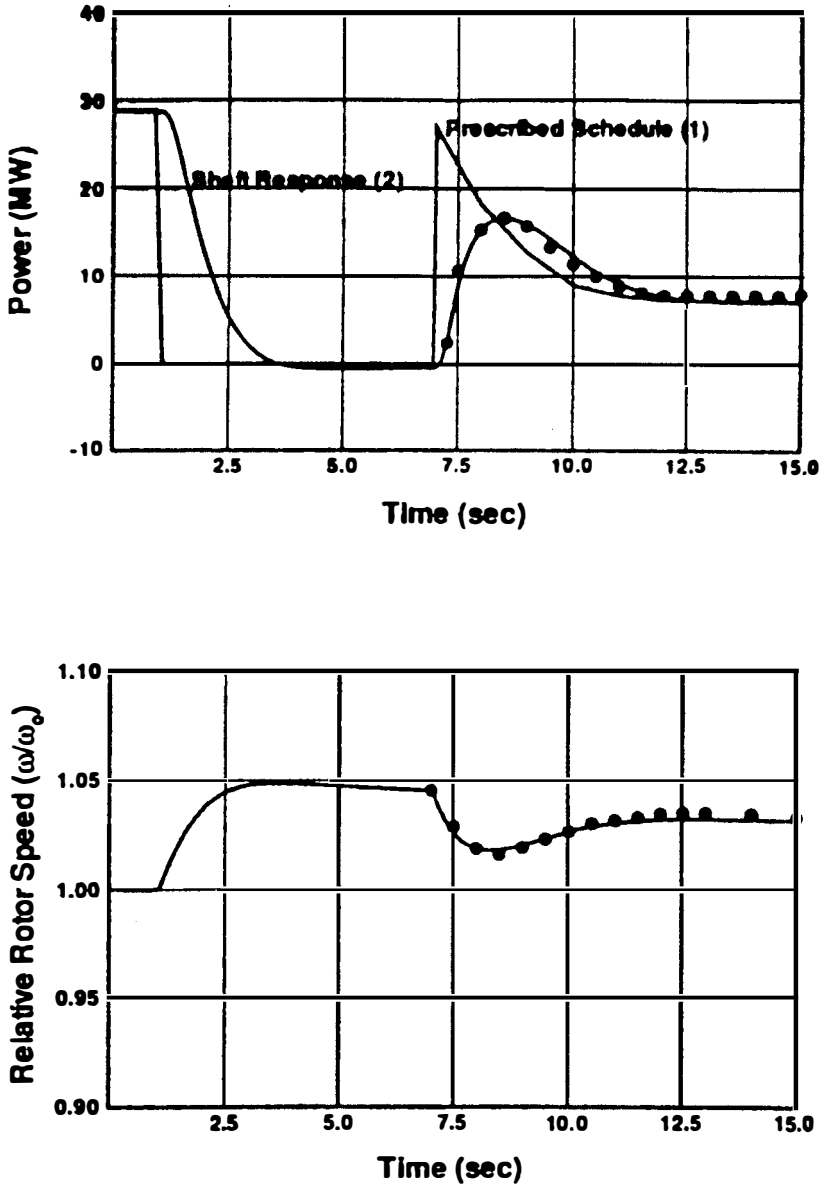

Figure 15. Comparison of Calculated Power Output and Rotor Speed to Test Data for the Gas Turbine Engine Model by Schobeiri, et. al.

Source: Schobeiri, M. T., Attia, M., and Lippke, C., "GETRAN: A Generic, Modularly Structured Computer Code for Simulation of Dynamic Behavior of Aero- and Power Generation Gas Turbine Engines," Journal of Engineering for Gas Turbines and Power, Vol. 116, July, 1994, pp. 483 - 494.

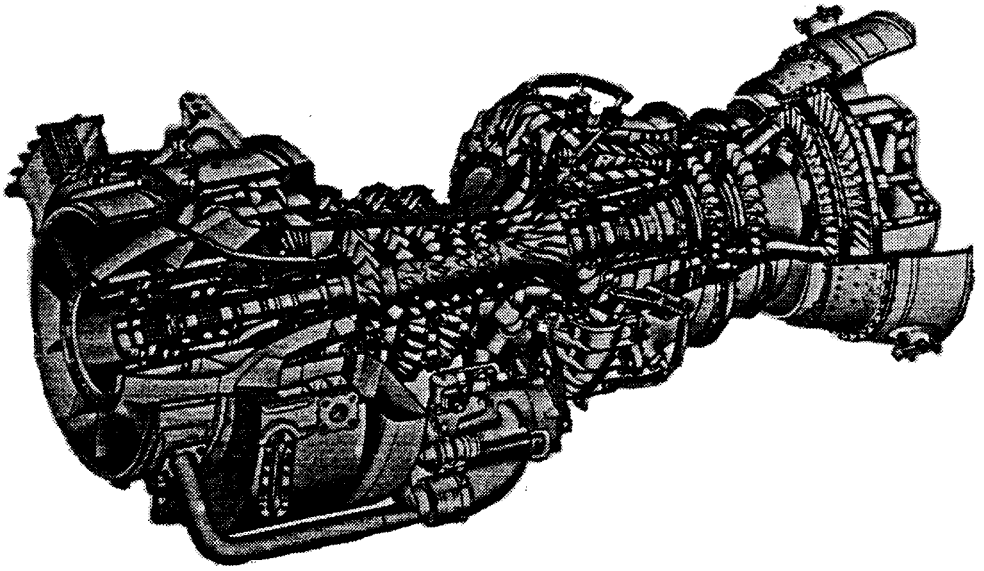

Figure 16. A Single Spool Gas Turbine Engine.

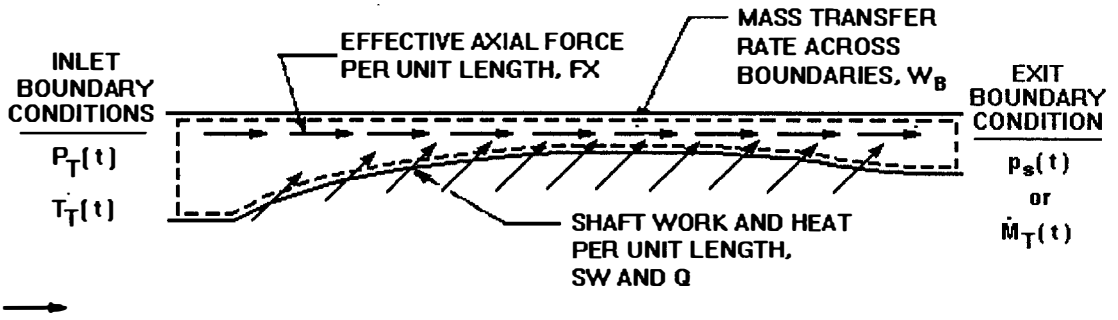

Figure 17. Overall Control Volume Representation of a Gas Turbine Engine.

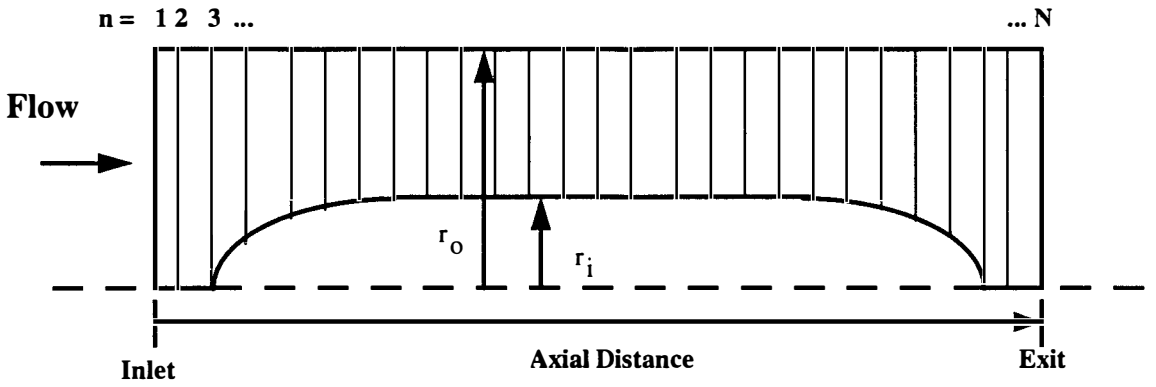

Figure 18. Elemental Control Volume Reprentation of a Gas Turbine Engine.

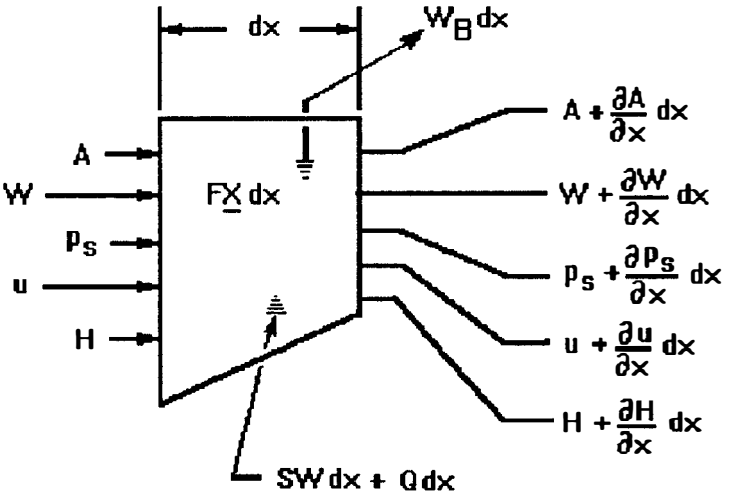

Figure 19. Application of Conservation Equations on Elemental Control Volume.

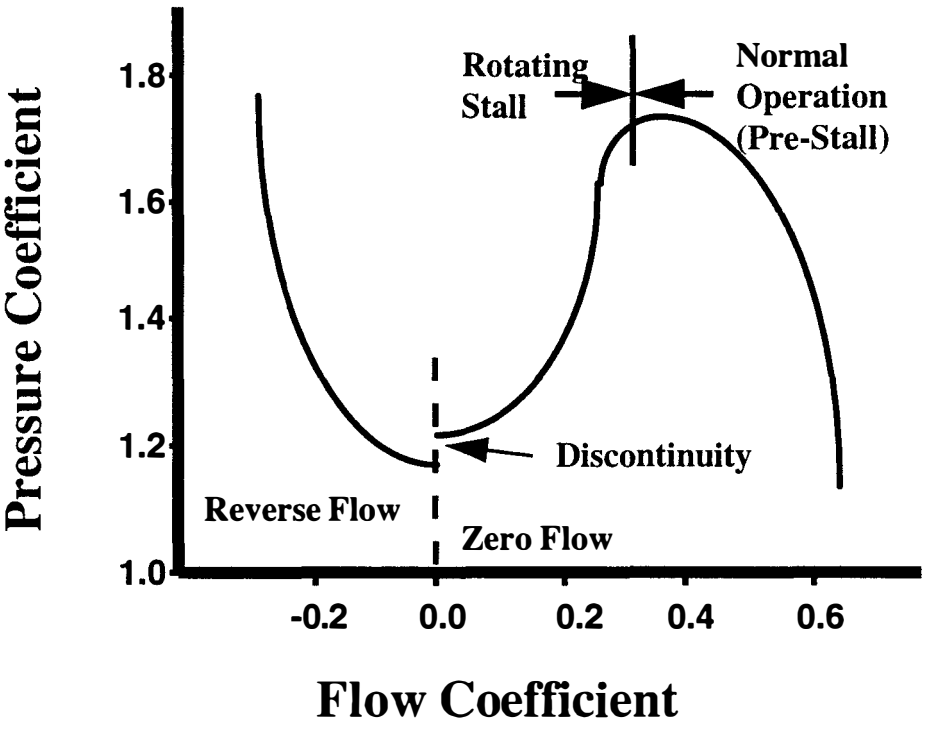

a. Pressure Coefficient as a Function of Flow Coefficient

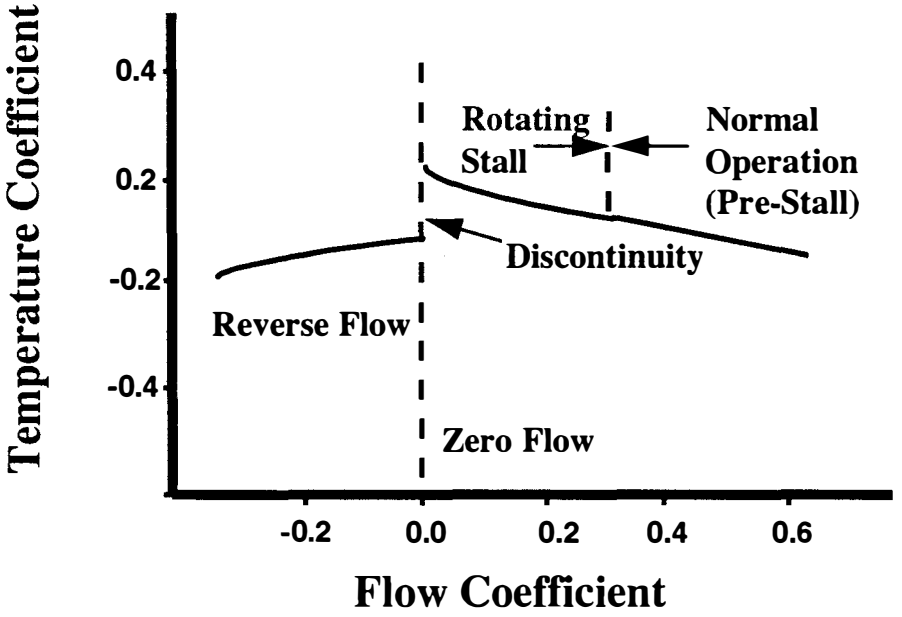

b. Temperature Coefficient as a Function of Flow Coefficient

Figure 20. Typical Compressor Stage Pressure and Temperature Characteristics.

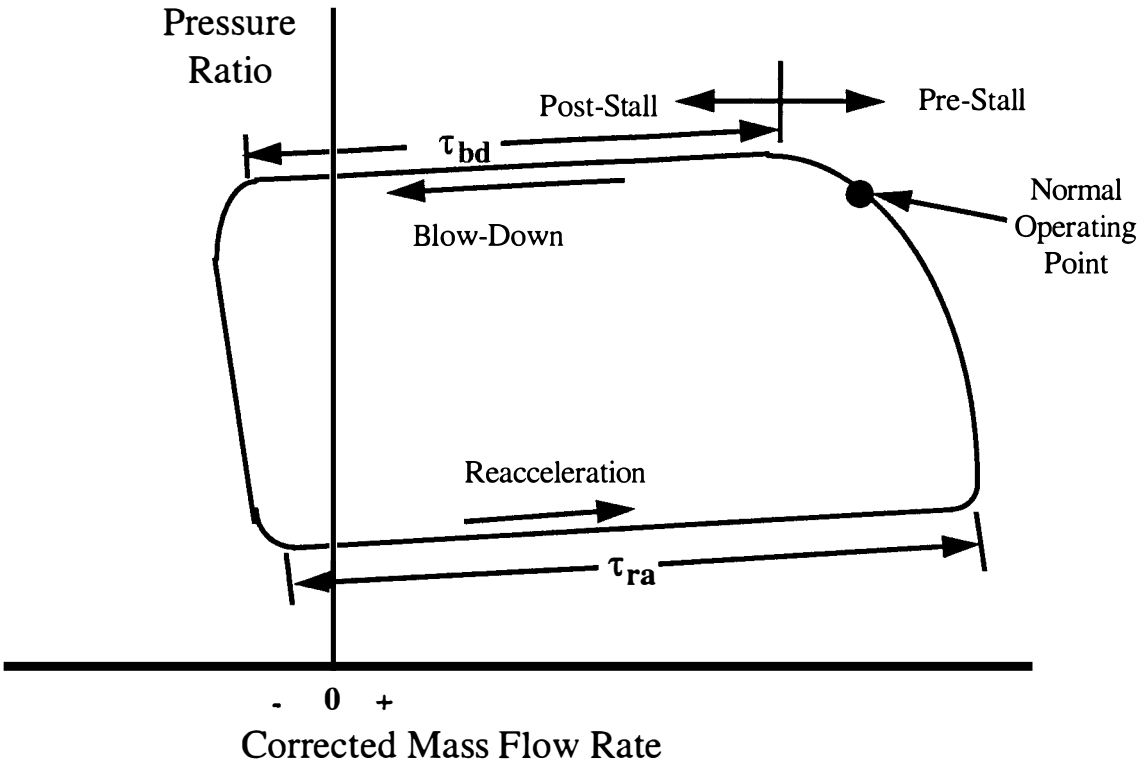

Figure 21. Post-Stall Forcing Function First Order Time Lagging Coefficients.

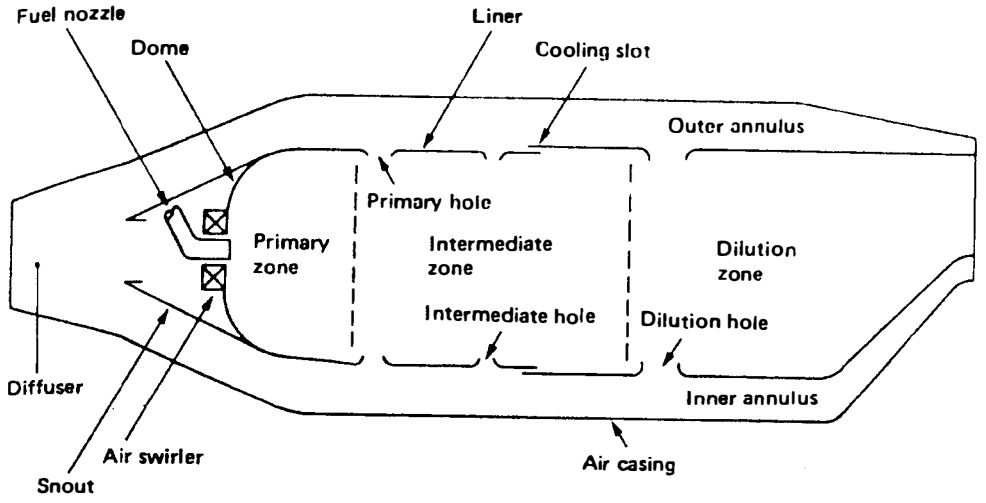

Figure 22. Generic Combustor Components.
Source: Lefebvre, A. H. Gas Turbine Combustion, Hemisphere Publishing Corporation, New York, NY, © 1983, pg. 13.

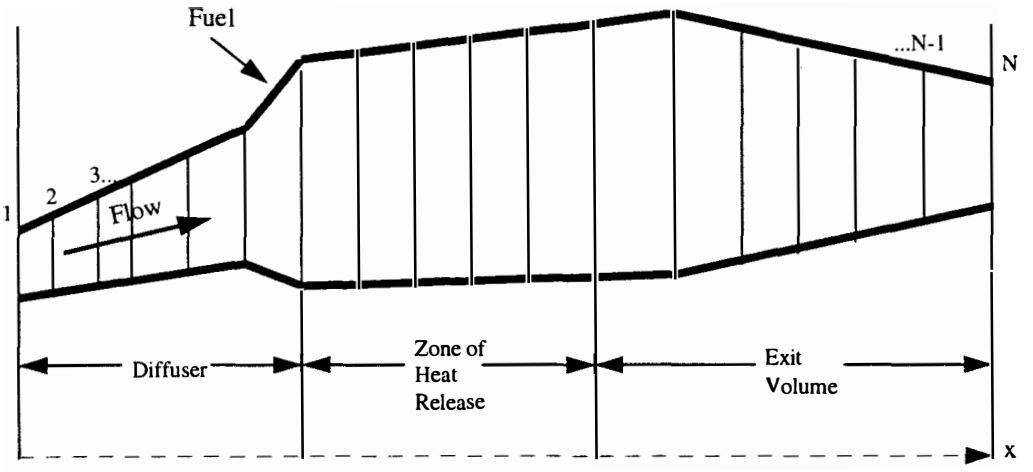

Figure 23. Combustor Discretization.

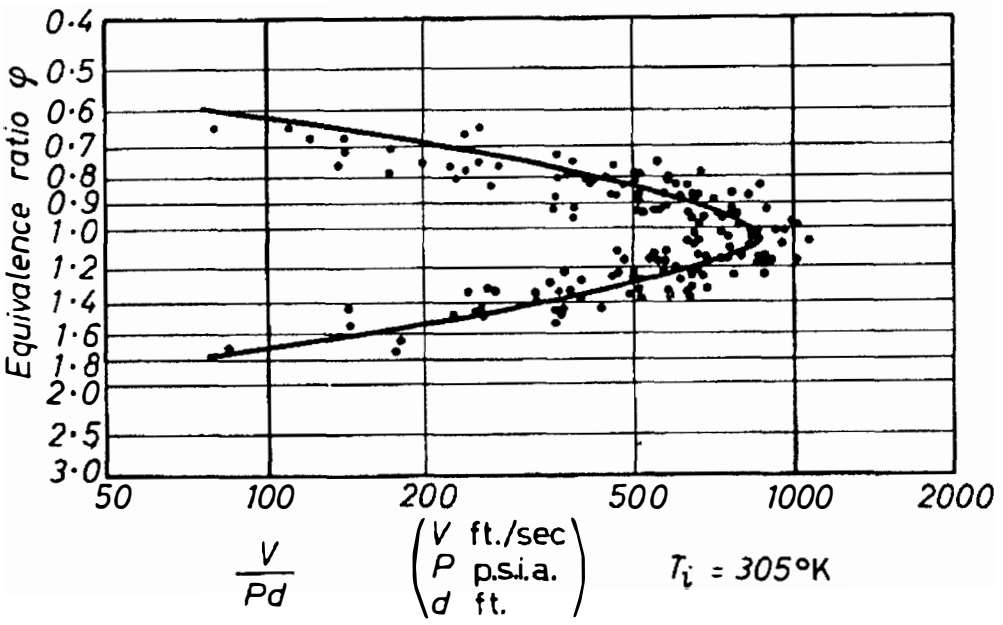

Figure 24. Stability Limits Used in the Combustor Model.

Source: Herbert, M. V., "A Theoretical Analysis of Reaction Rate Controlled Systems - Part 1," Chapter 6 in *Combustion Research and Reviews, 1957*, Agardograph No. 15, Butterworths Scientific Publications, London, England, February, 1957.

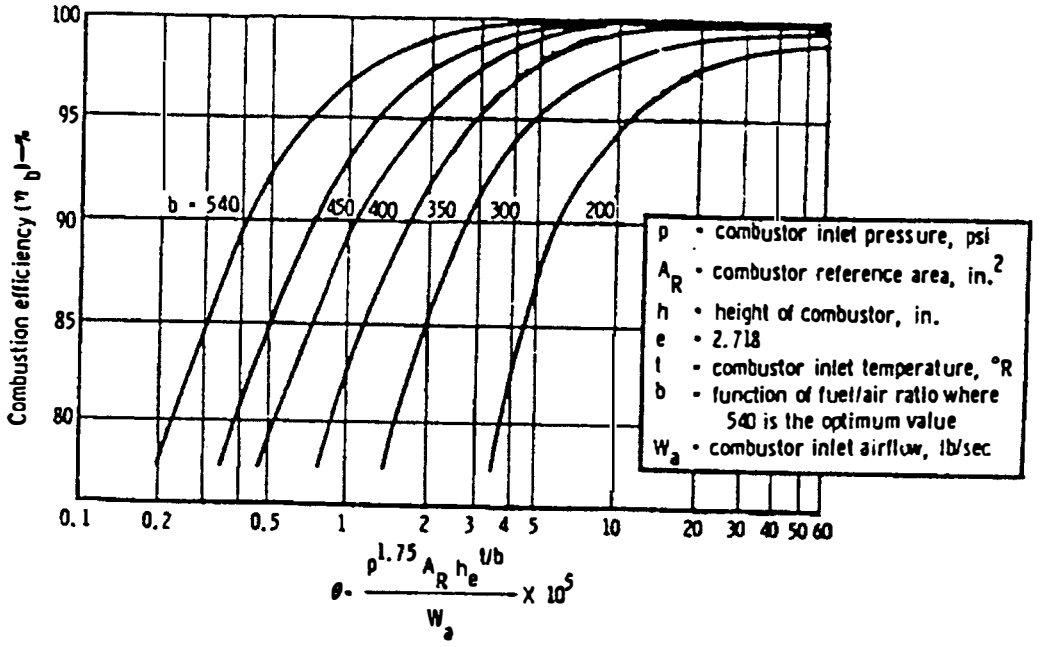

Figure 25. Combustion Efficiency as a Function of Loading Parameter.

Source: Lefebvre, A. H., "Fuel Effects on Gas Turbine Combustion - Ignition, Stability, and Combustion Efficiency," Journal of Engineering for Gas Turbines and Power, Vol. 107, January 1985, pp. 24 - 37.

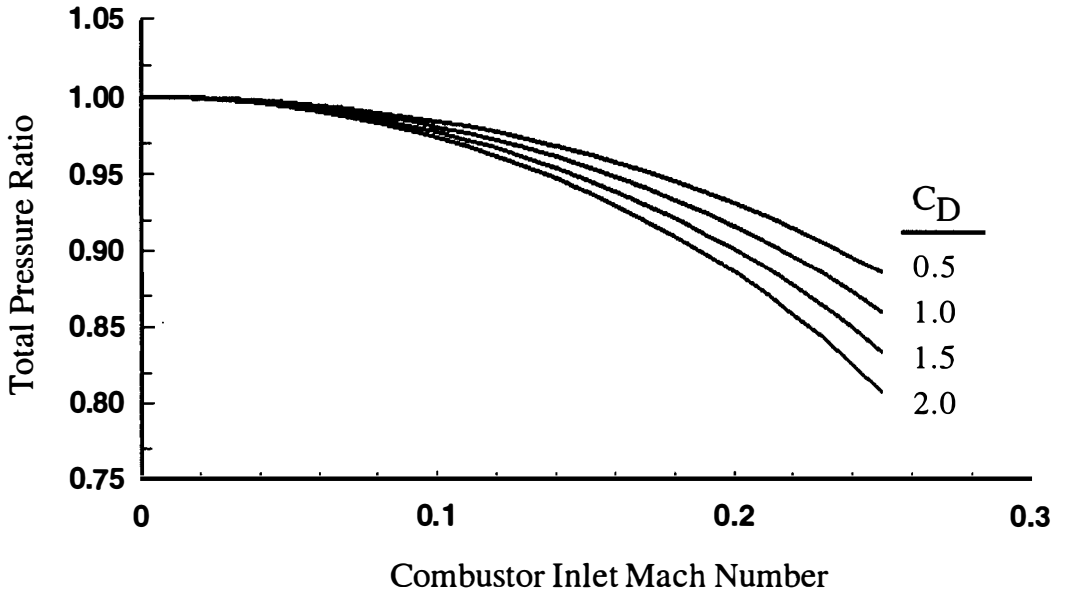

Figure 26. Variation of Combustor Total Pressure Loss as a Function of Inlet Mach Number for Various Loss Coefficients.

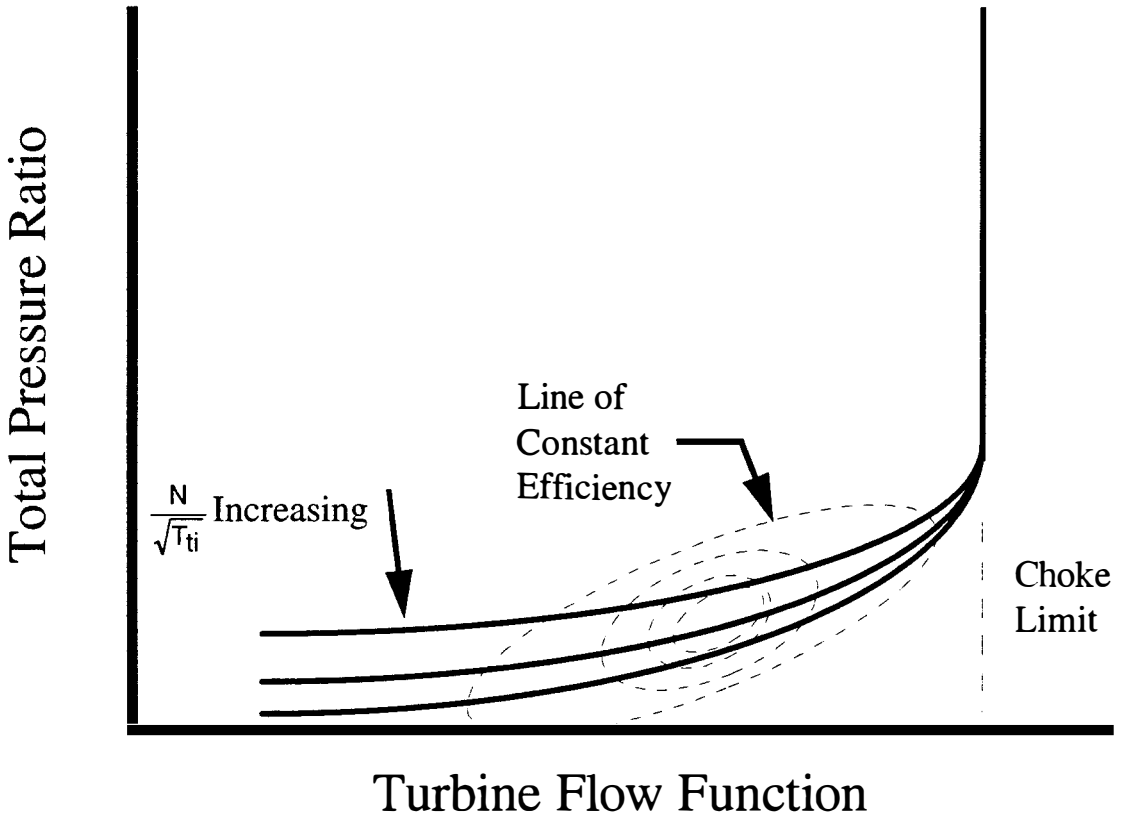

Figure 27. Typical Presentation of Turbine Performance Maps.

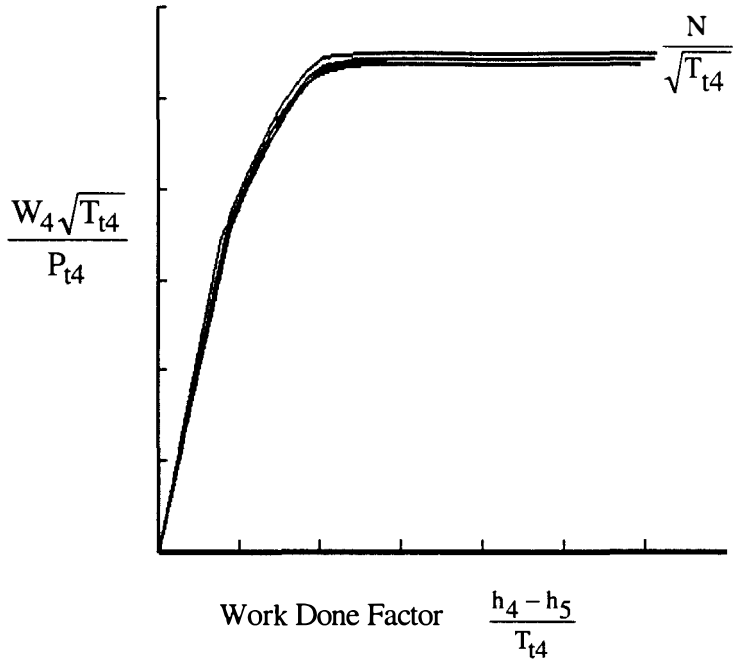

a. Mass Flow Function as a Function of Work Done Factor for Various Corrected Shaft Speeds.

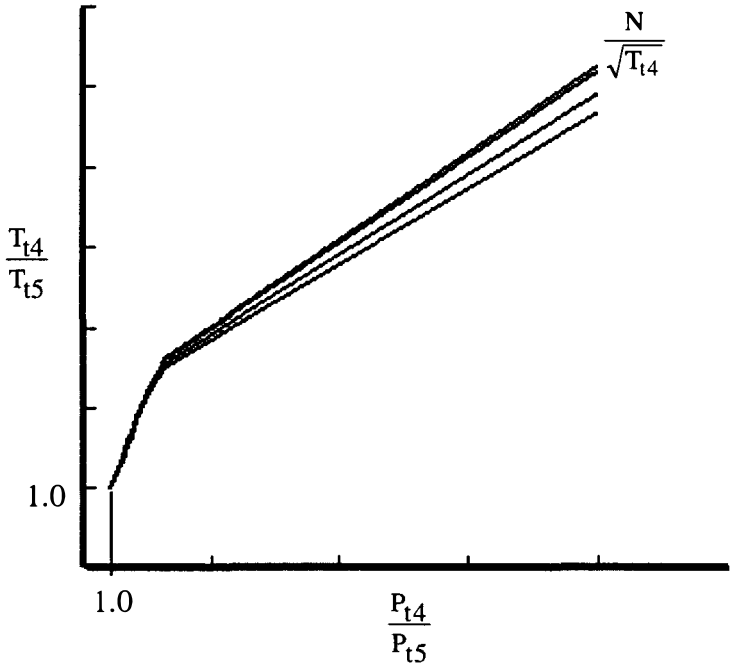

b. Total Temperature Ratio as a Function of Total Pressure Ratio for Various Corrected Shaft Speeds.

Figure 28. Turbine Performance Representation used in ATEC.

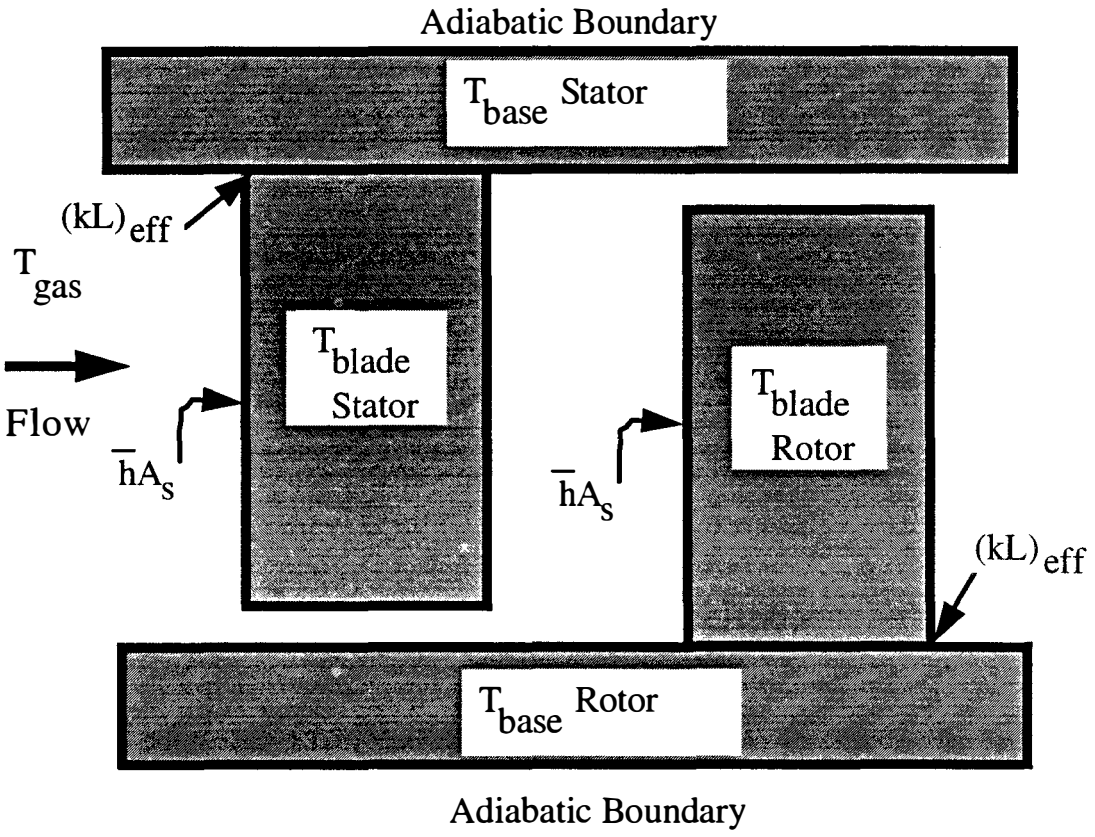

Figure 29. Heat Transfer Model Geometry

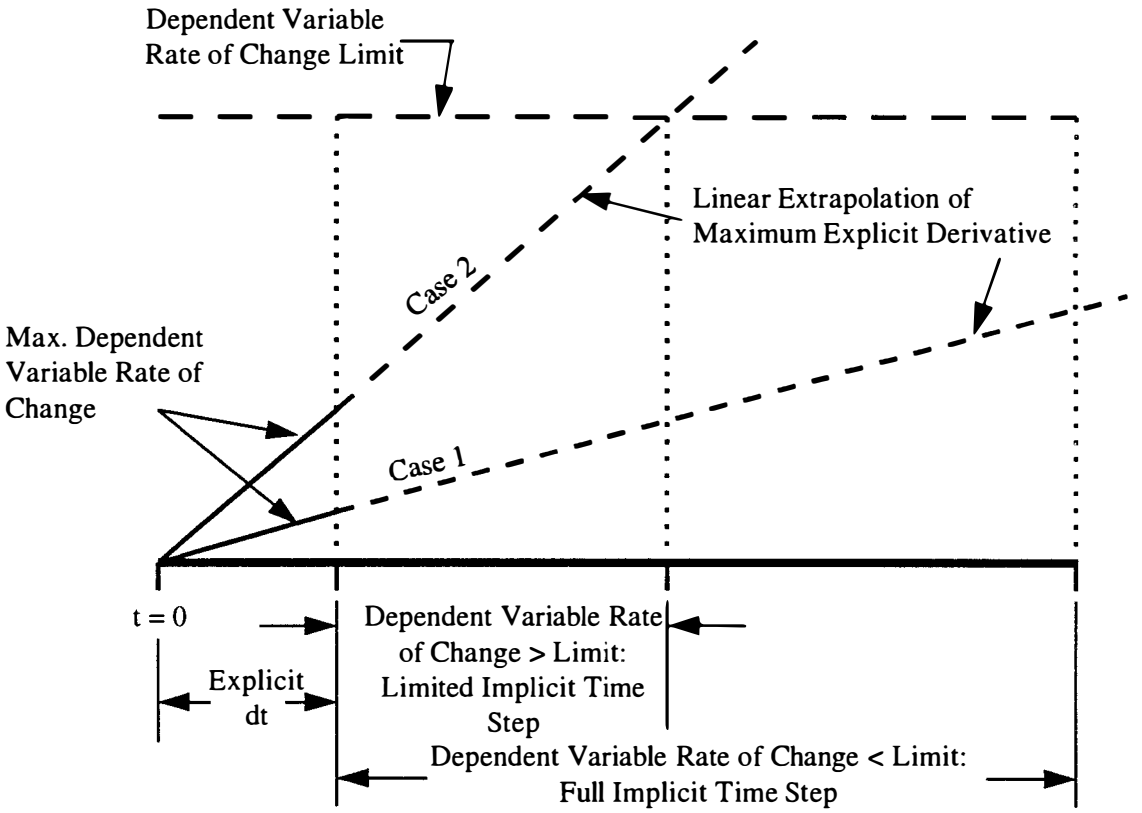

Figure 30. Description of the Variable Time Step Routine Using the Explicit and Implicit Numerical Solvers.

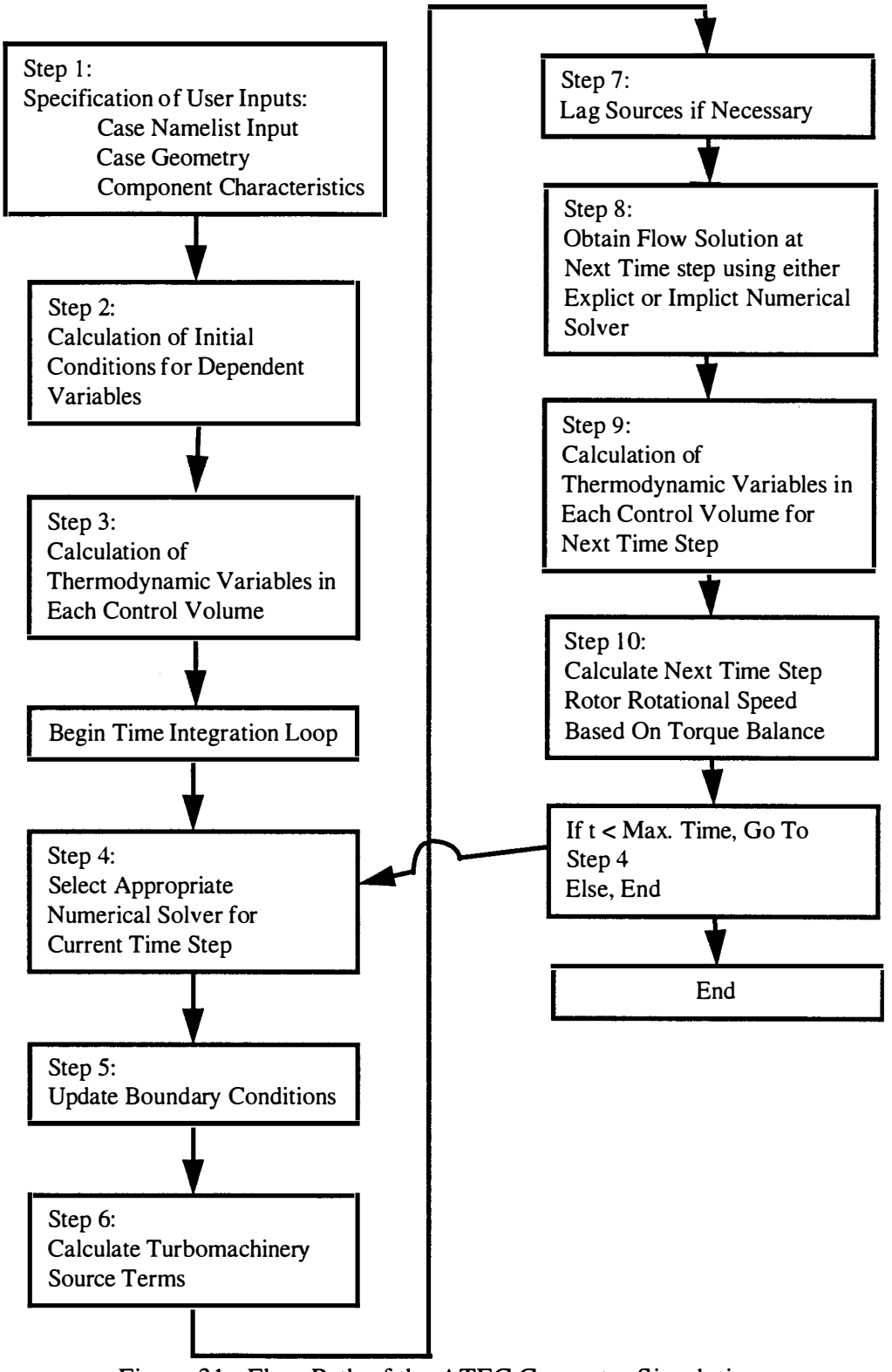

Figure 31. Flow Path of the ATEC Computer Simulation.

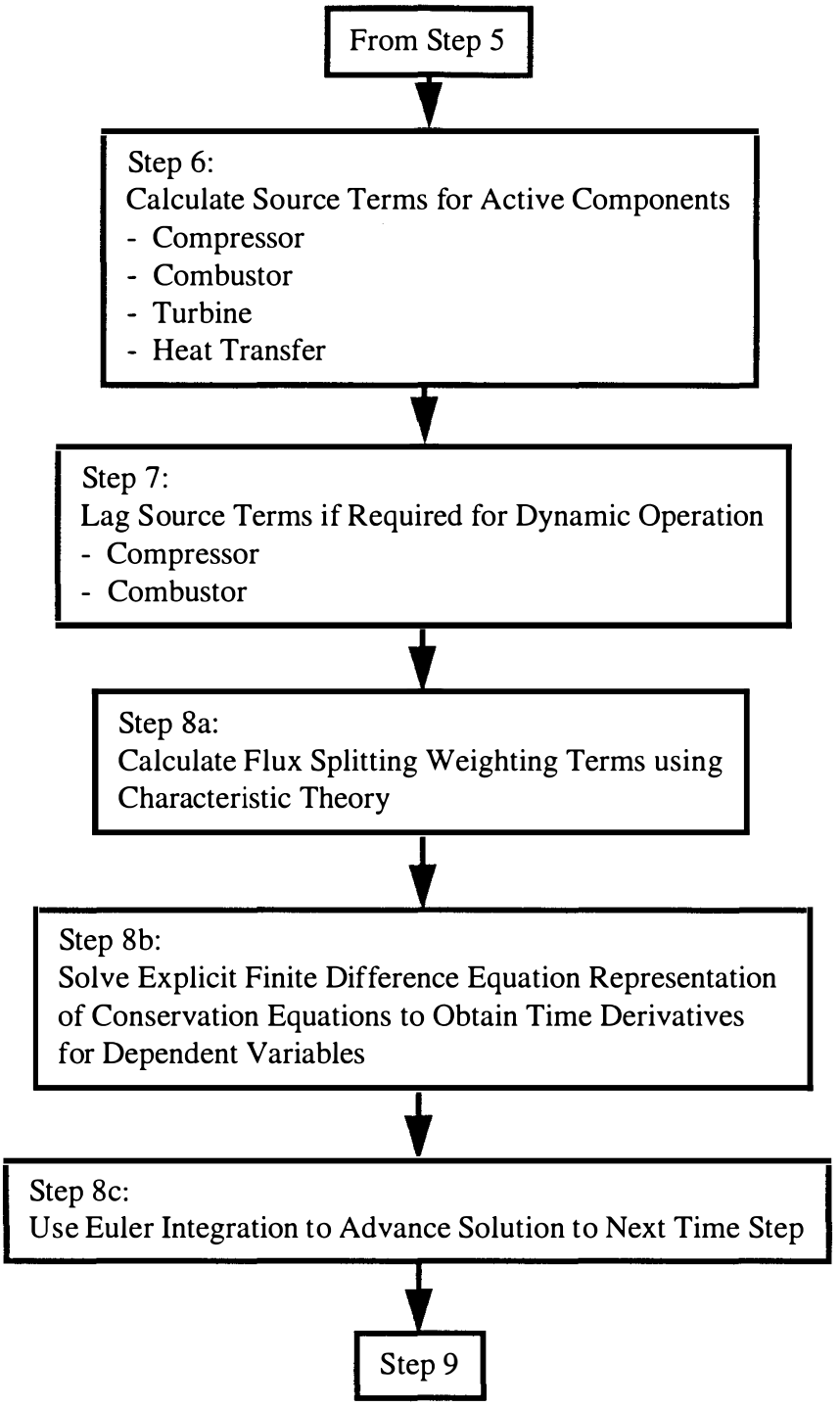

Figure 32. Flow Path of the ATEC Computer Simulation at the Time of Source Term Calculations and Flow Solution: Explict Numerical Solver.

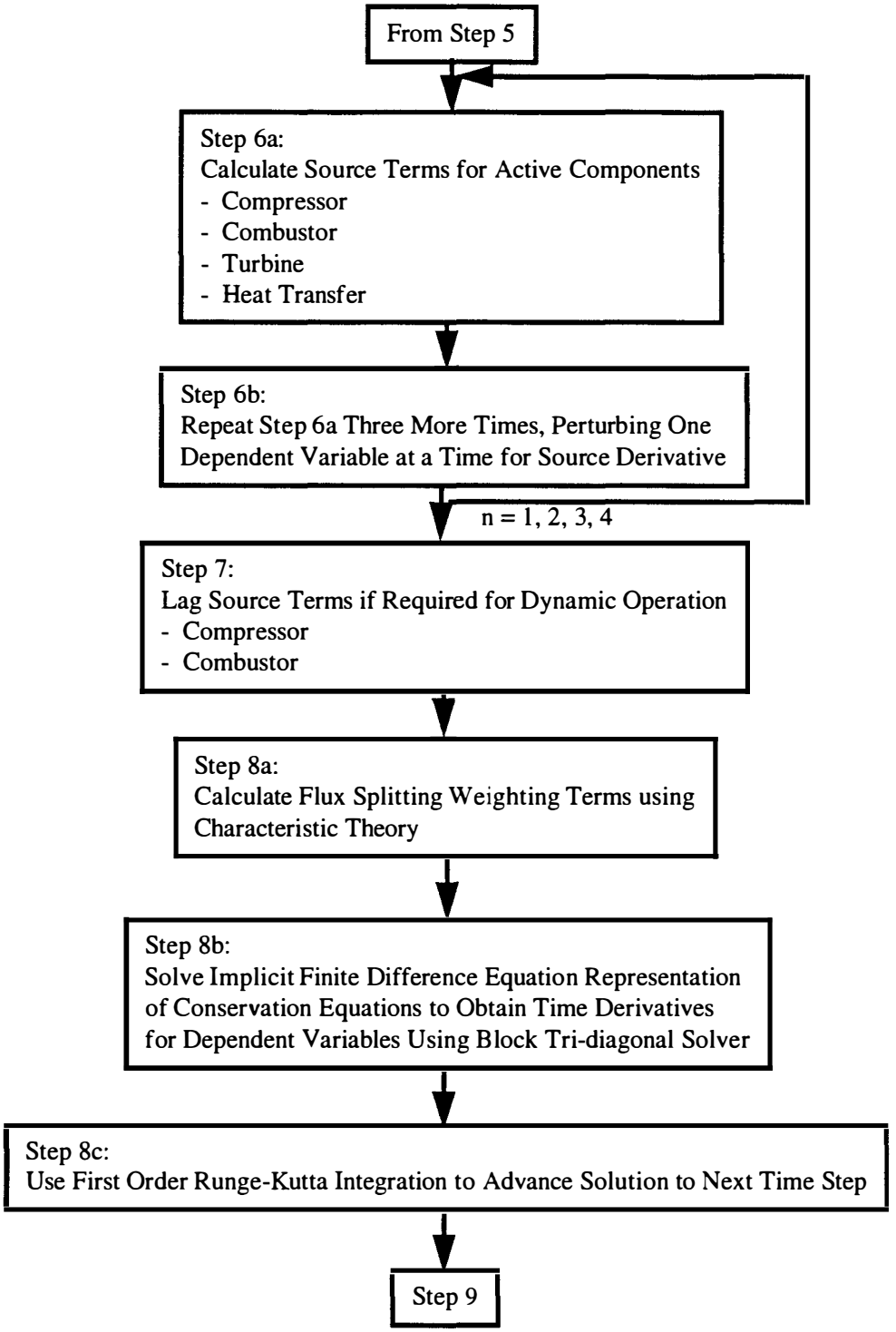

Figure 33. Flow Path of the ATEC Computer Simulation at the Time of Source Term Calculations and Flow Solution: Implicit Numerical Solver.

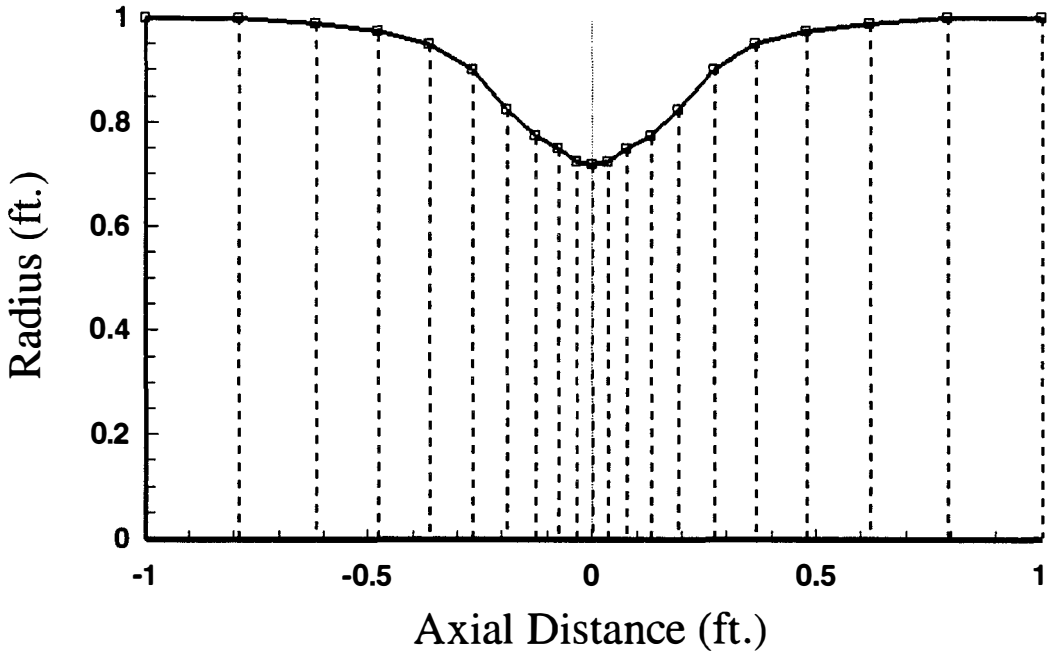

Figure 34. Geometry for the Euler Flow Solver Operational Verification Test Case

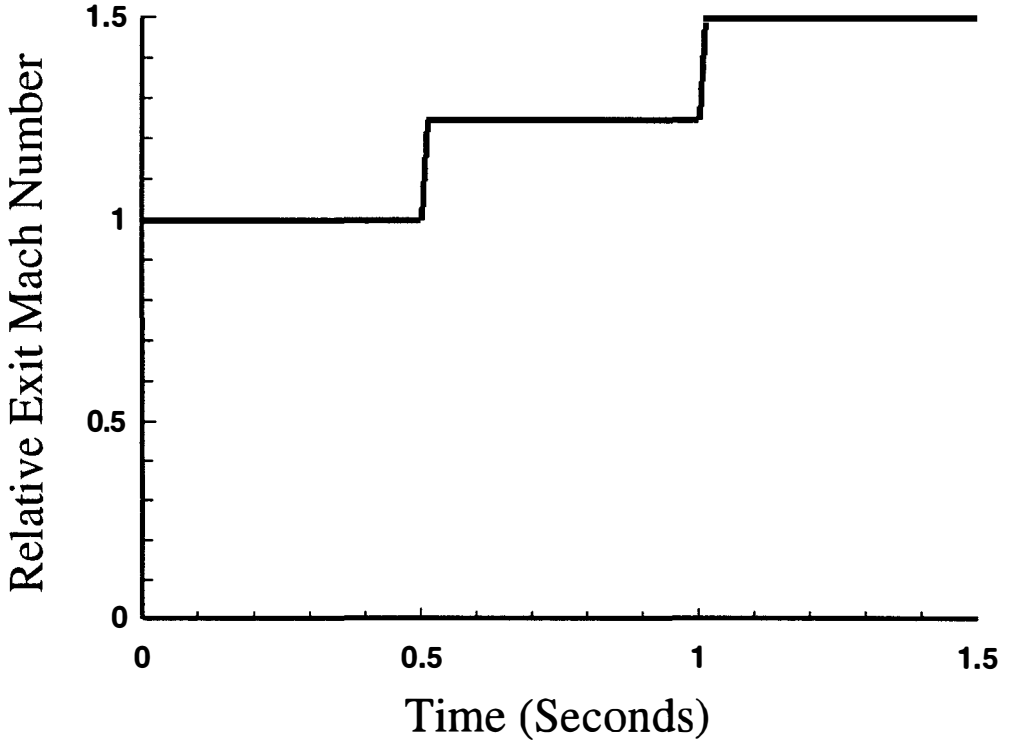

Figure 35. Change in Relative Exit Mach Number for the Euler Flow Solver Operational Verification Test Case

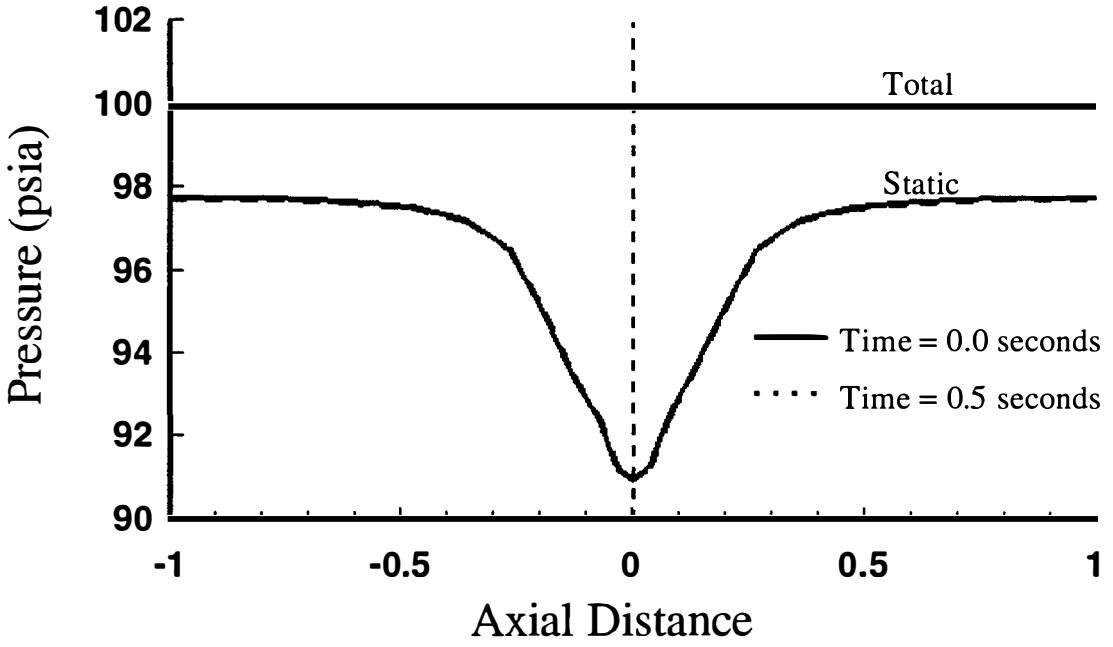

Figure 36. Total and Static Pressure in Converging / Diverging Duct at Start of Simulation and at 0.5 Seconds for the Explicit Euler Flow Solver Operational Verification Test Case

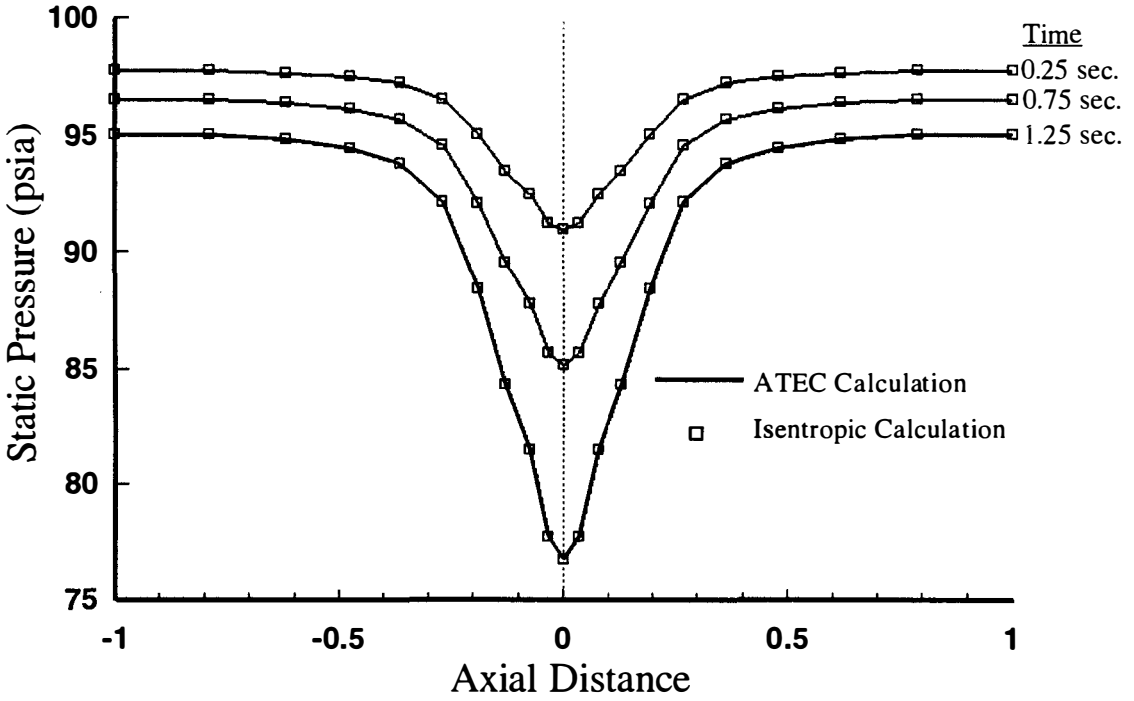

Figure 37. Comparison of Calculated Static Pressure with Isentropic Values for the Explicit Euler Flow Solver Operational Verification Test Case

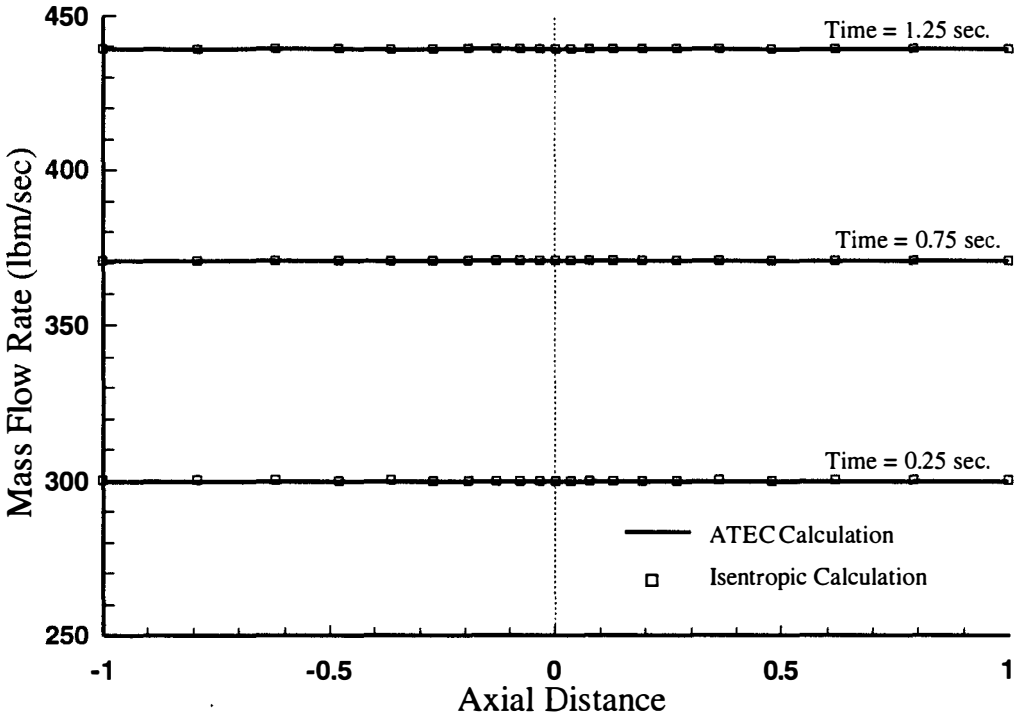

Figure 38. Comparison of ATEC Calculated Mass Flow Rate with Isentropic Values at Selected Times for the Explicit Euler Flow Solver Operational Verification Test Case

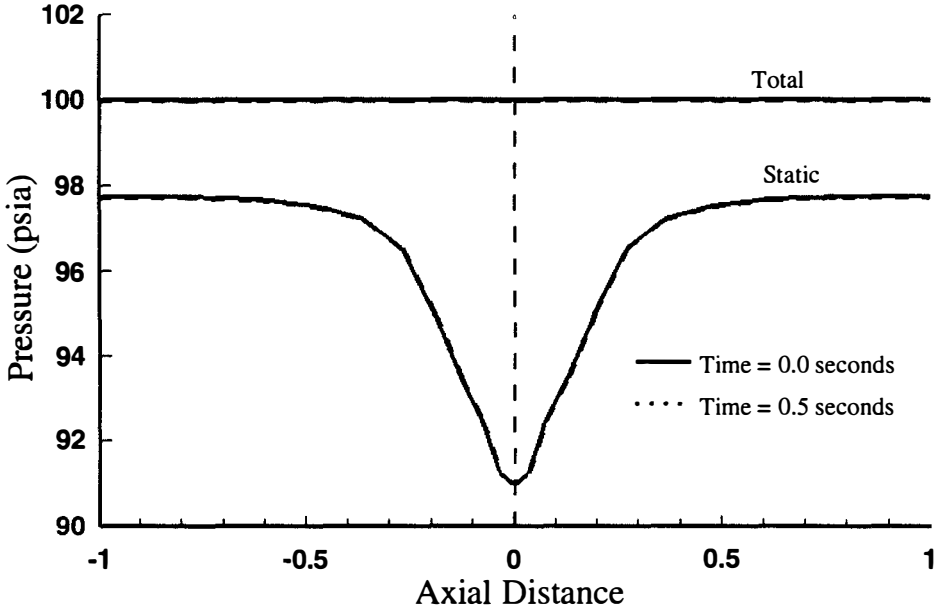

Figure 39. Total and Static Pressure in Converging / Diverging Duct at Start of Simulation and at 0.5 Seconds for the Implicit Euler Flow Solver Operational Verification Test Case

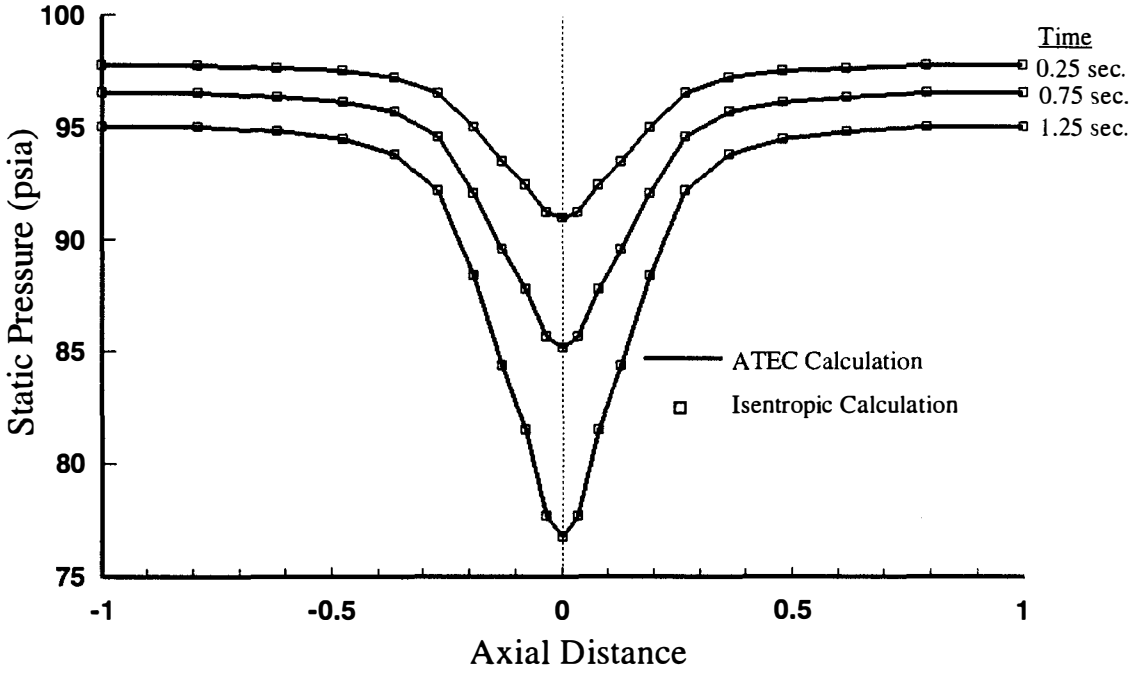

Figure 40. Comparison of Calculated Static Pressure with Isentropic Values for the Implicit Euler Flow Solver Operational Verification Test Case

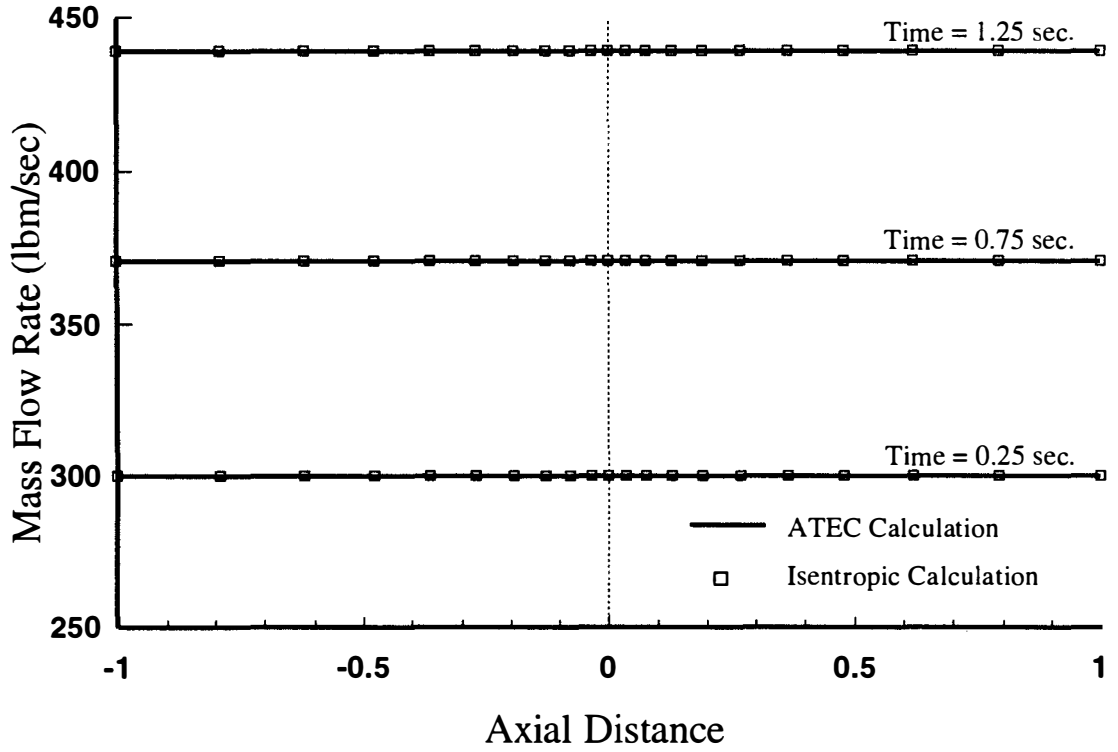

Figure 41. Comparison of ATEC Calculated Mass Flow Rate with Isentropic Values at Selected Times for the Implicit Euler Flow Solver Operational Verification Test Case

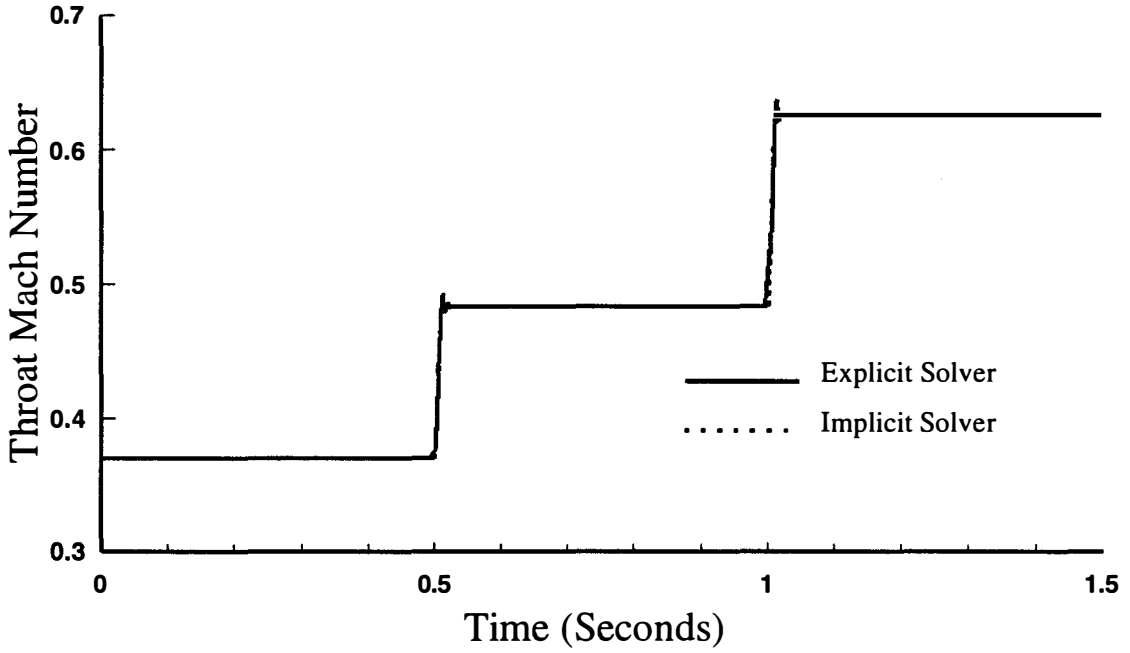

Figure 42. Comparison of Throat Mach Number between the Explicit Euler Flow Solver and the Implicit Euler Flow Solver for the Operational Verification Test Case.

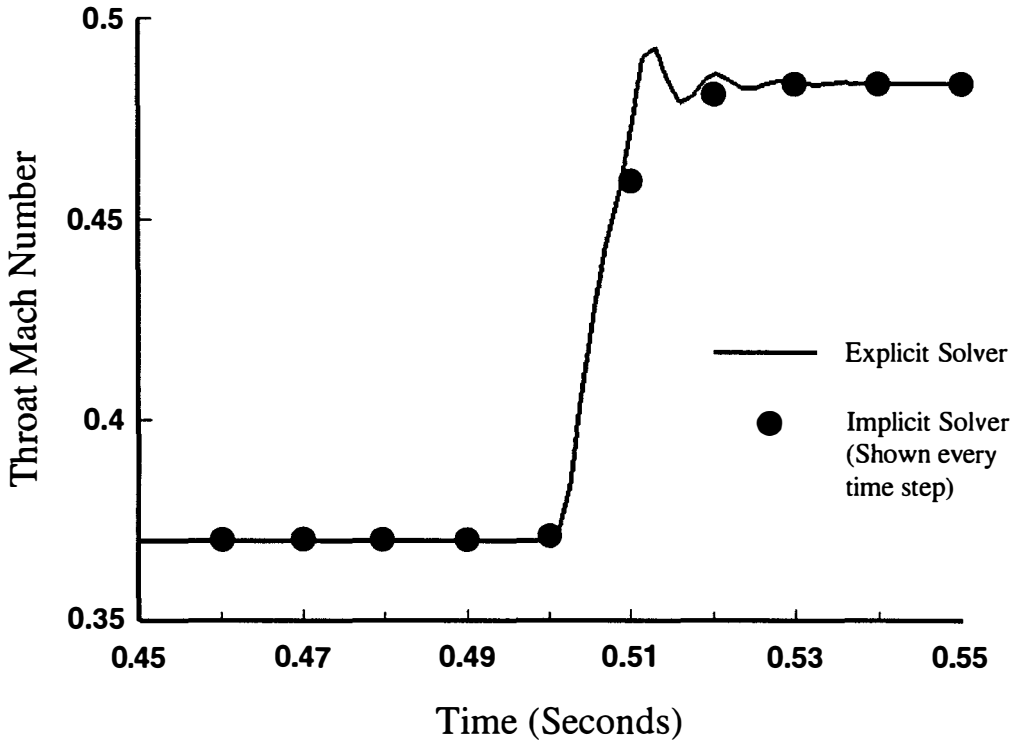

Figure 43. Closer View of the Differences Between the Calculated Throat Mach Number for the Explicit and Implicit Euler Flow Solvers Operational Verification Test Case.

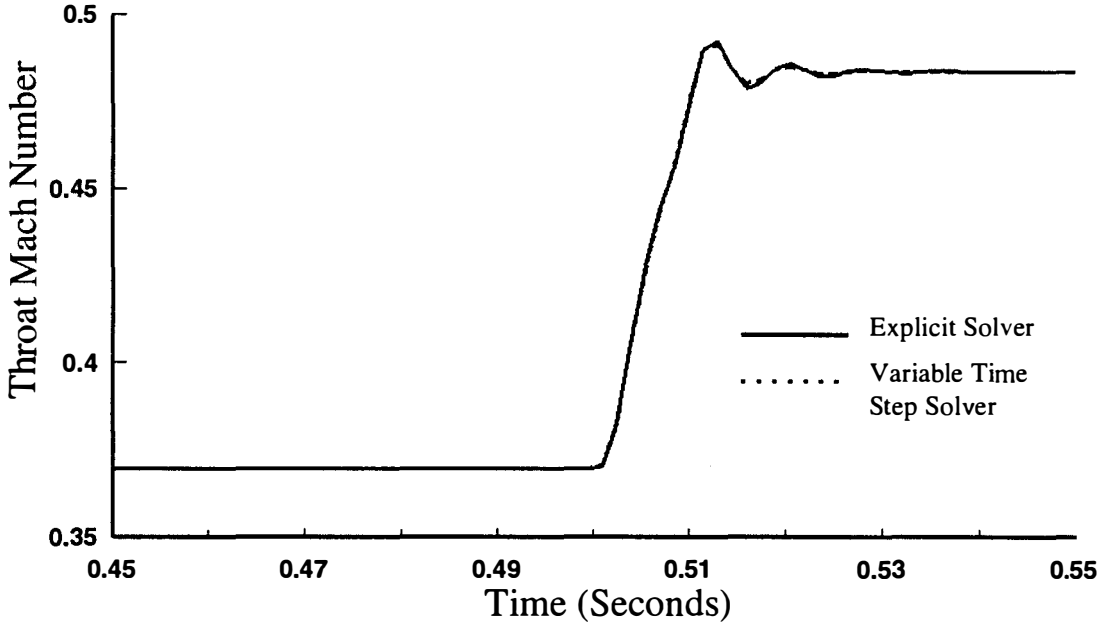

Figure 44. Comparison of Throat Mach Number between the Explicit Euler Flow Solver and the Variable Time Step Size Implicit/Explicit Euler Flow Solver for the Operational Verification Test Case at the Time of the First Exit Mach Number Transient.

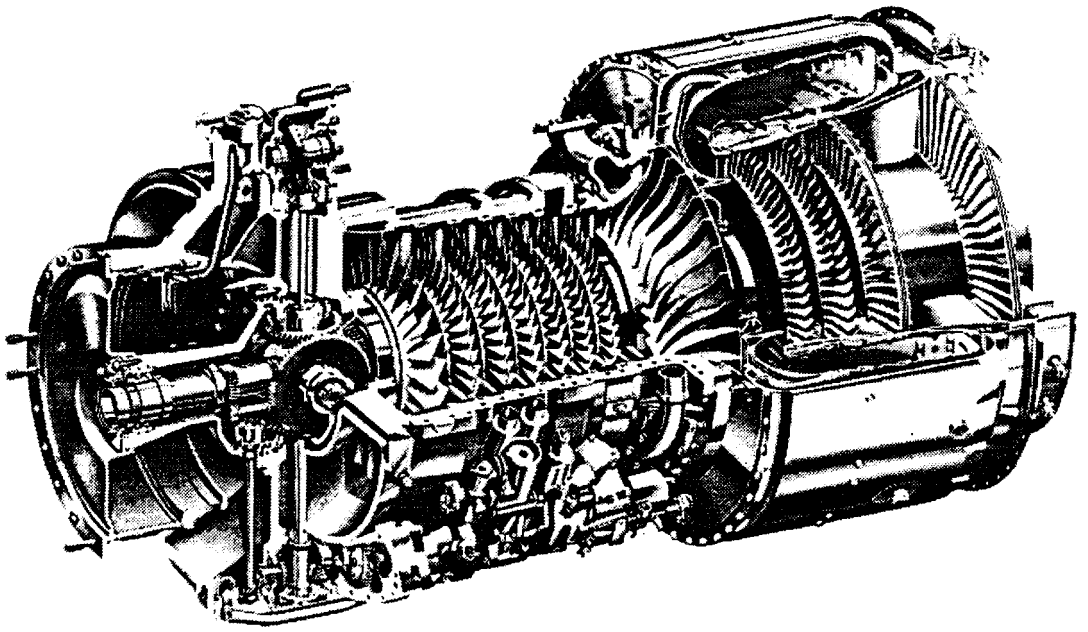

Figure 45. Cutaway Sectional View of the T55-L-712 Turboshaft Engine.

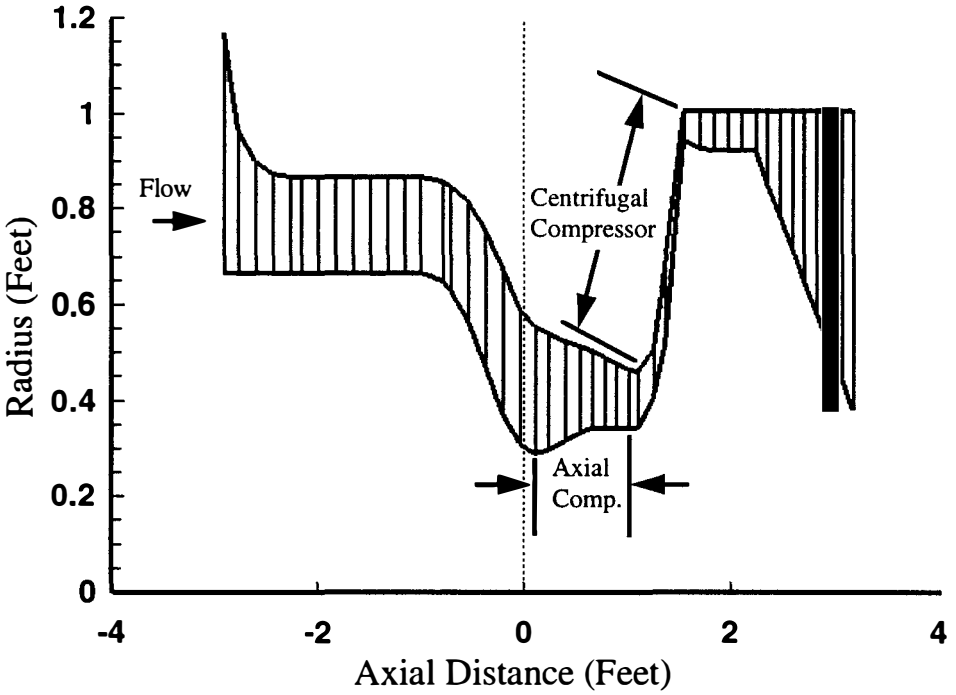

Figure 46. Graphical Representation of T55-L-12 Compressor Rig Test Geometry for the Compressor Model Operational Verification Test Case.

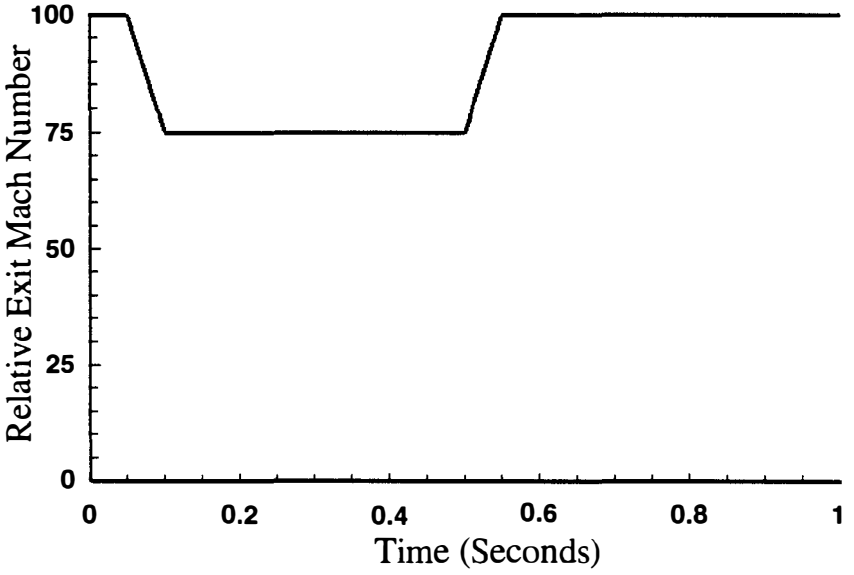

Figure 47. Relative Exit Mach Number Variation with Time for the Compressor Model Operational Verification Test Case.

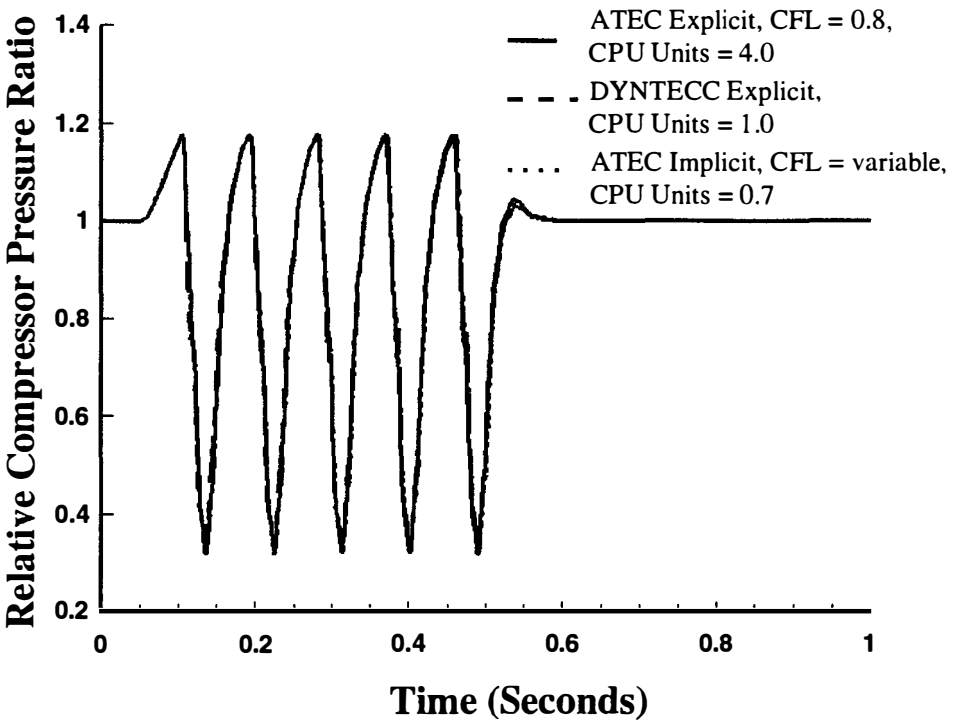

Figure 48. Comparison of ATEC Explicit, DYNTECC Explicit, and ATEC Implicit with Variable Time Step Size Calculated Compressor Ratio During T55-L-712 Compressor System Surge Cycles for the Compressor Model Operational Verification Test Case.

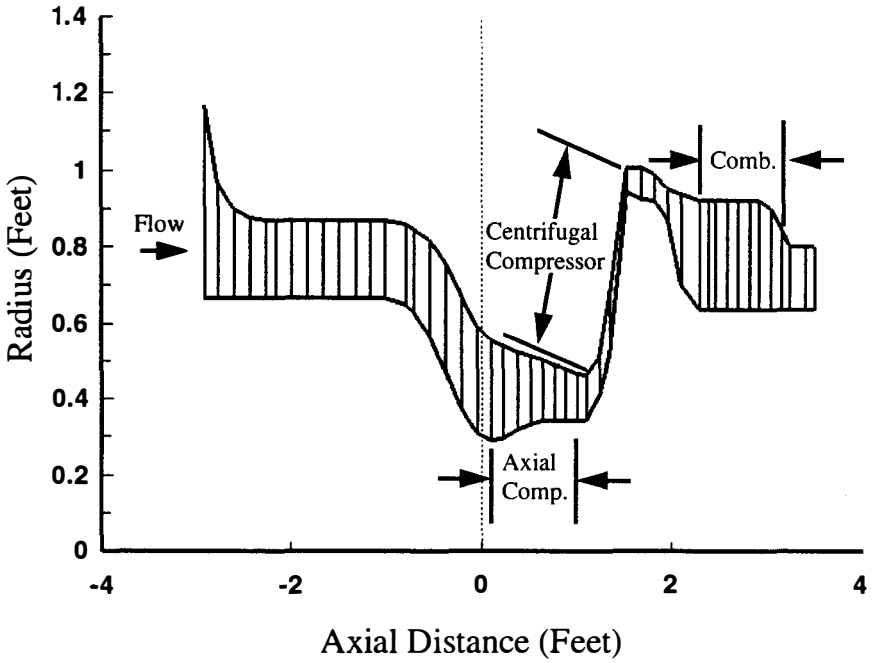

Figure 49. Graphical Representation of T55-L-712 Compressor Rig and Hypothetical Combustor Test Geometry for the Combustor Model Operational Verification Test Case.

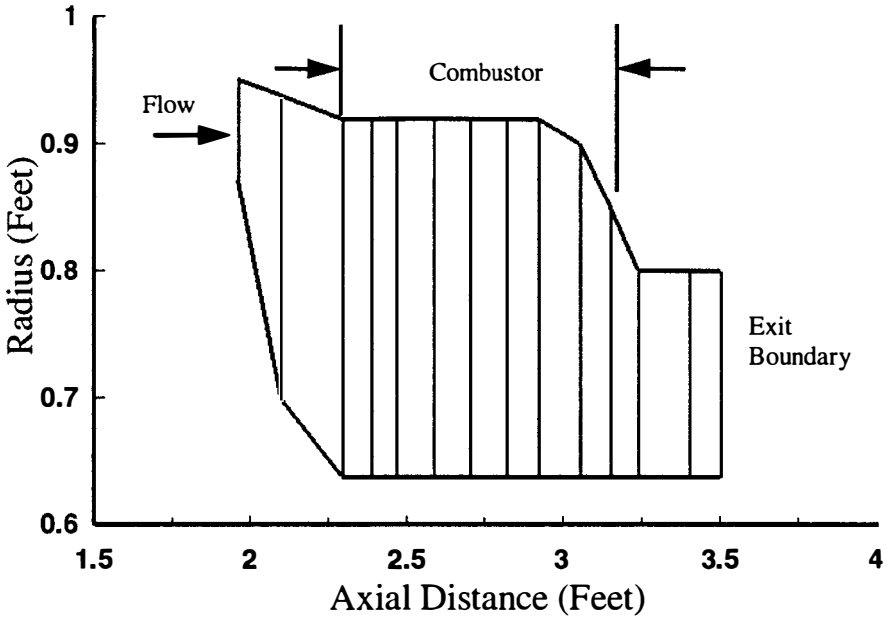

Figure 50. Close-up View of the Combustor Section of the Graphical Representation of T55-L-712 Compressor Rig and Hypothetical Combustor Test Geometry for the Combustor Model Operational Verification Test Case.

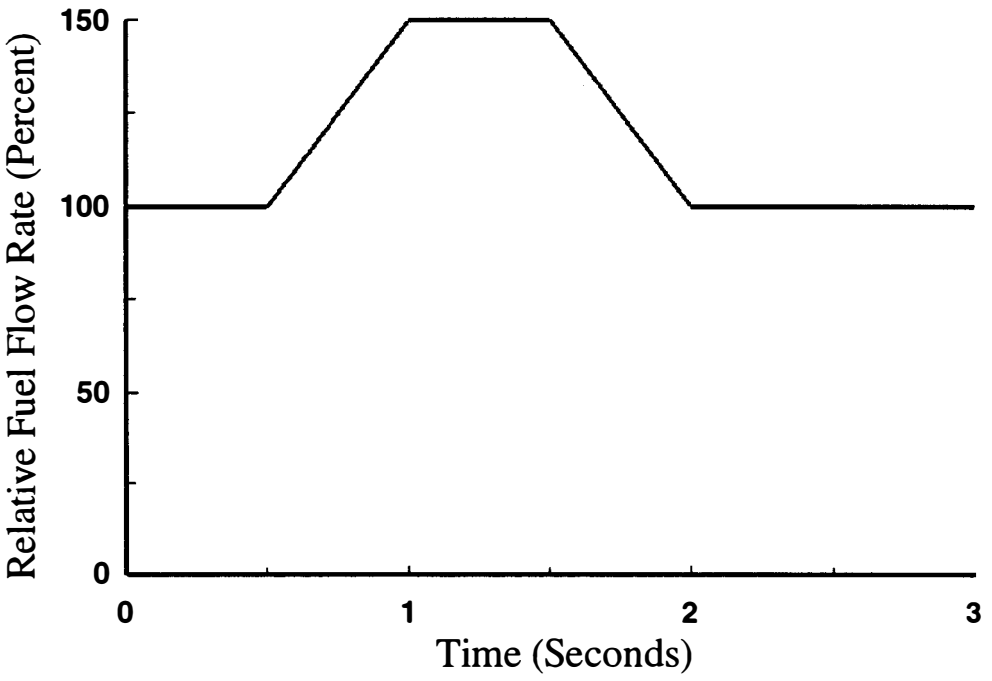

Figure 51. Change in Relative Fuel Flow Rate for the Combustor Model Operational Verification Test Case.

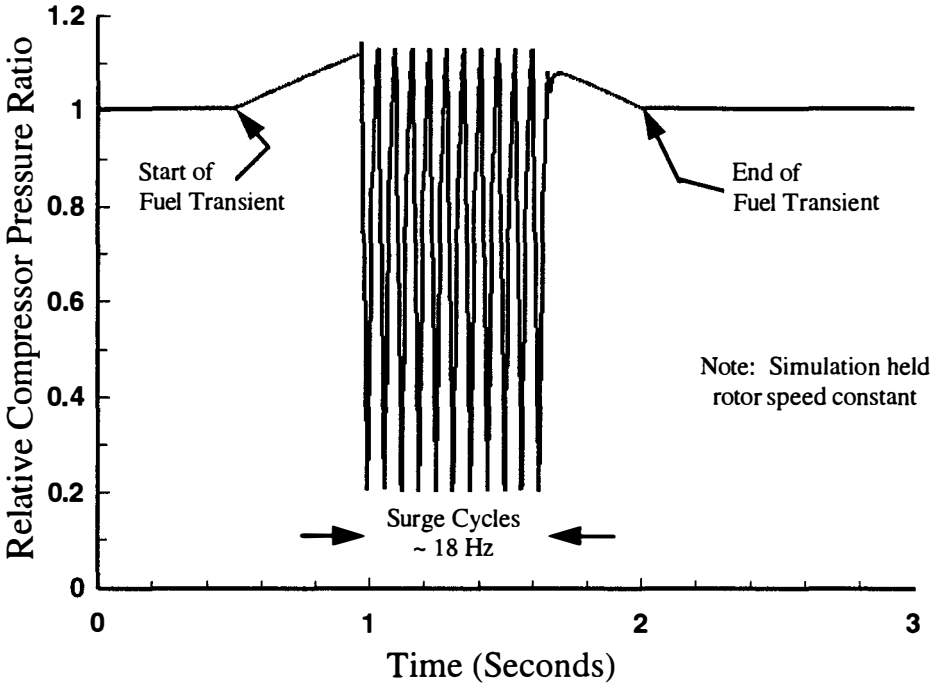

Figure 52. Relative Compressor Pressure Ratio During the Combustor Model Operational Verification Test Case.

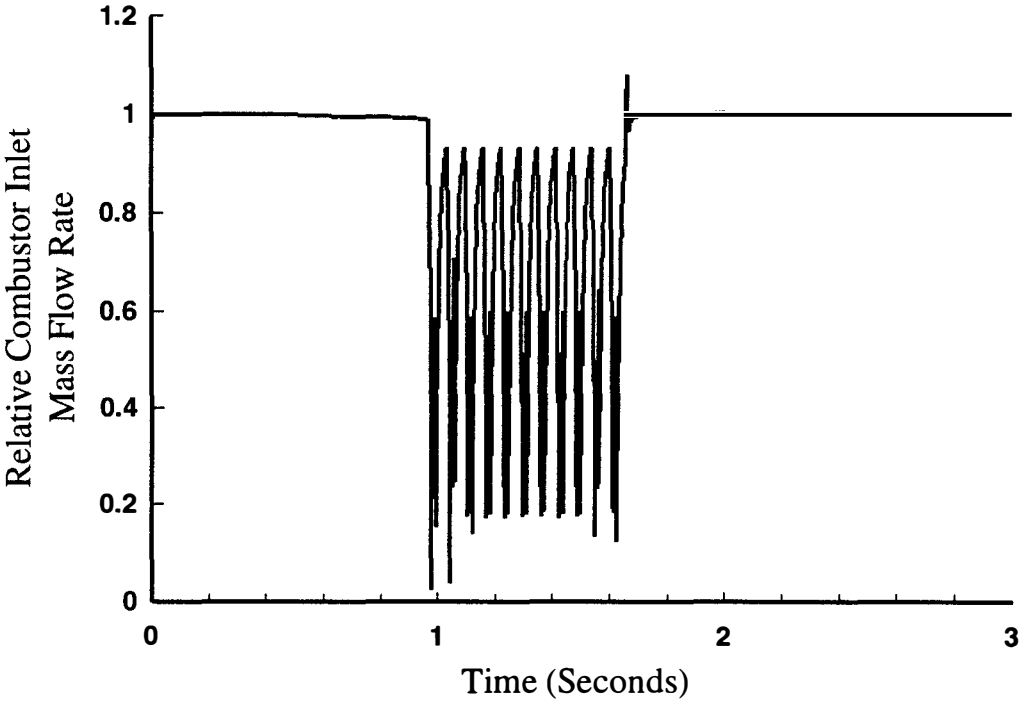

Figure 53. Relative Combustor Inlet Mass Flow Rate During the Combustor Model Operational Verification Test Case.

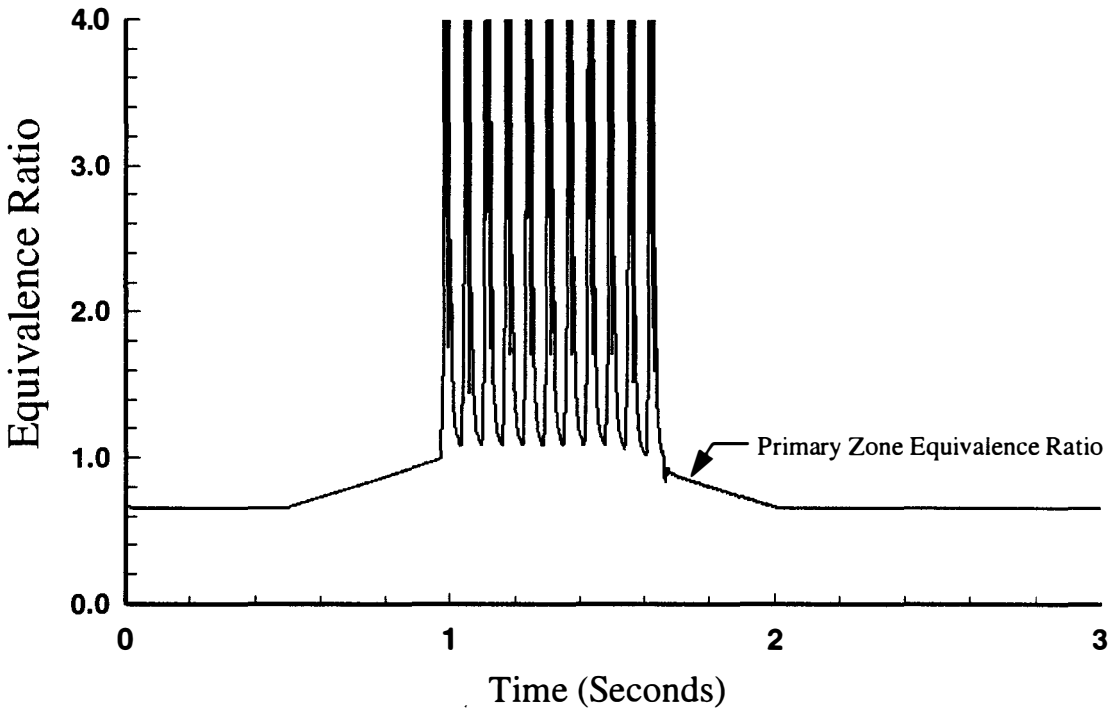

Figure 54. Primary Zone Equivalence Ratio in the Combustor for the Combustor Model Operational Verification Test Case

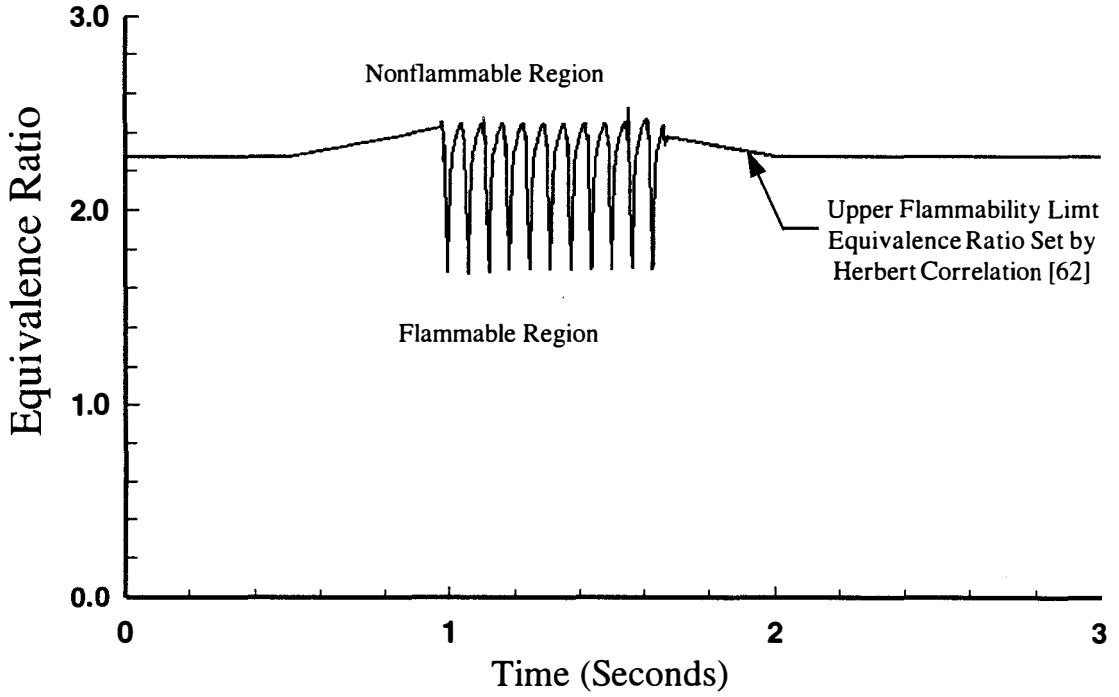

Figure 55. Upper Flammability Limit in the Combustor for the Combustor Model Operational Verification Test Case.

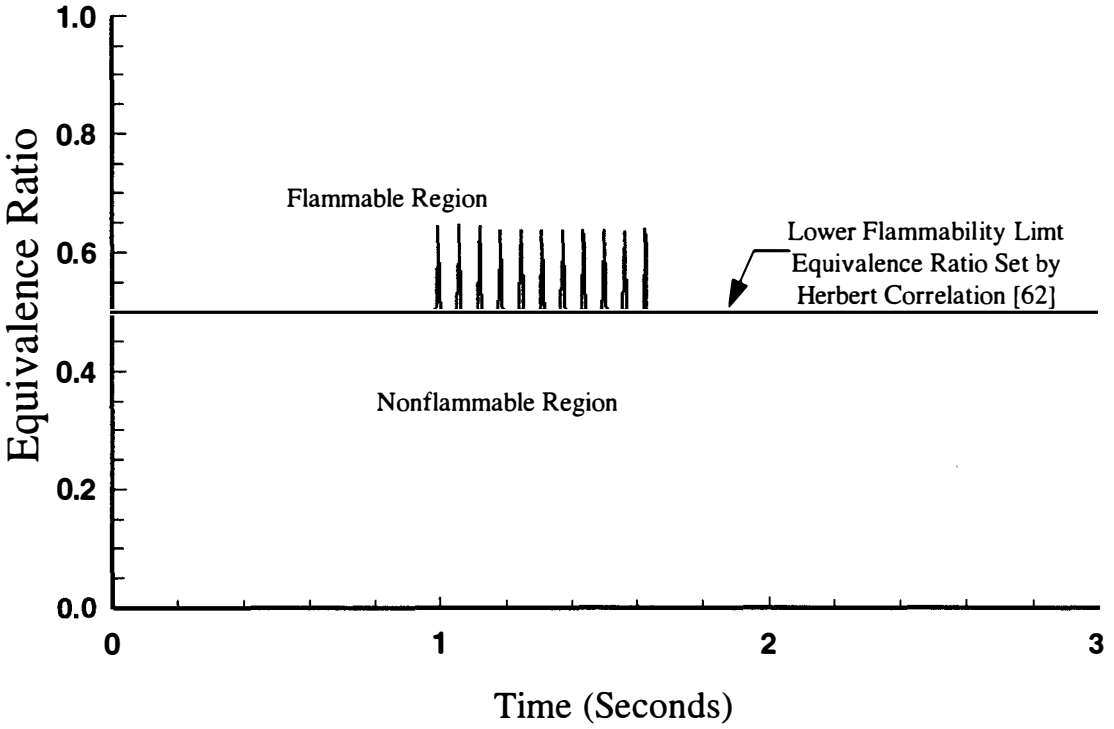

Figure 56. Lower Flammability Limit in the Combustor for the Combustor Model Operational Verification Test Case.

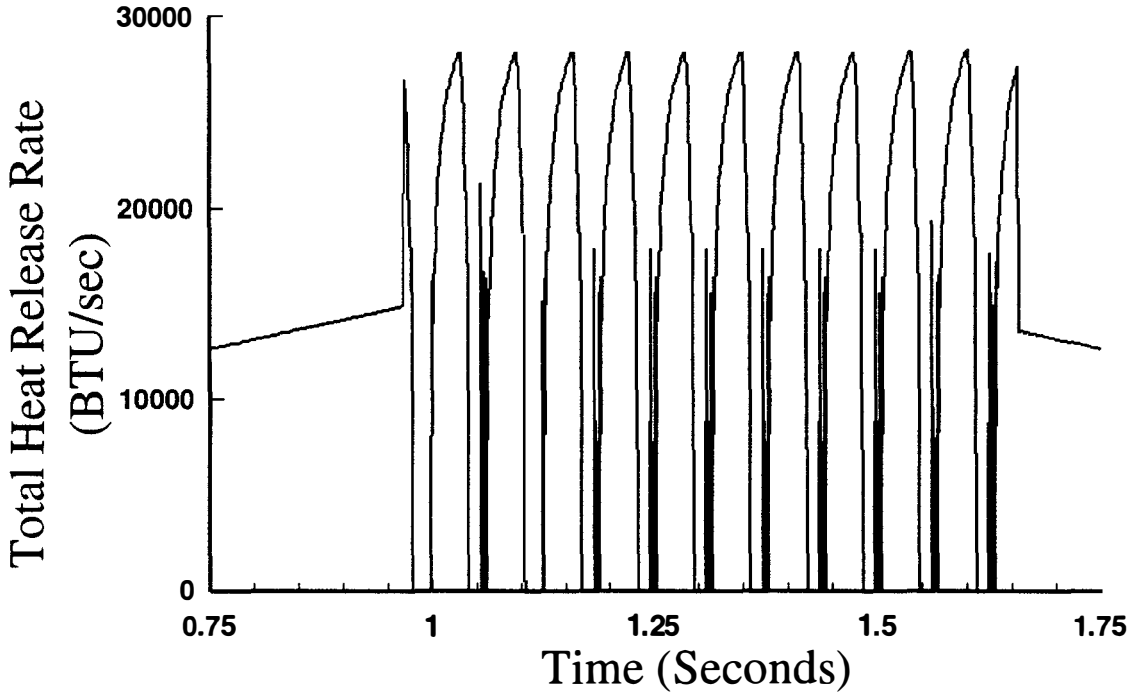

Figure 57. Instantaneous Heat Release Rate in the Combustor Primary Zone for the Combustor Model Operational Verification Test Case.

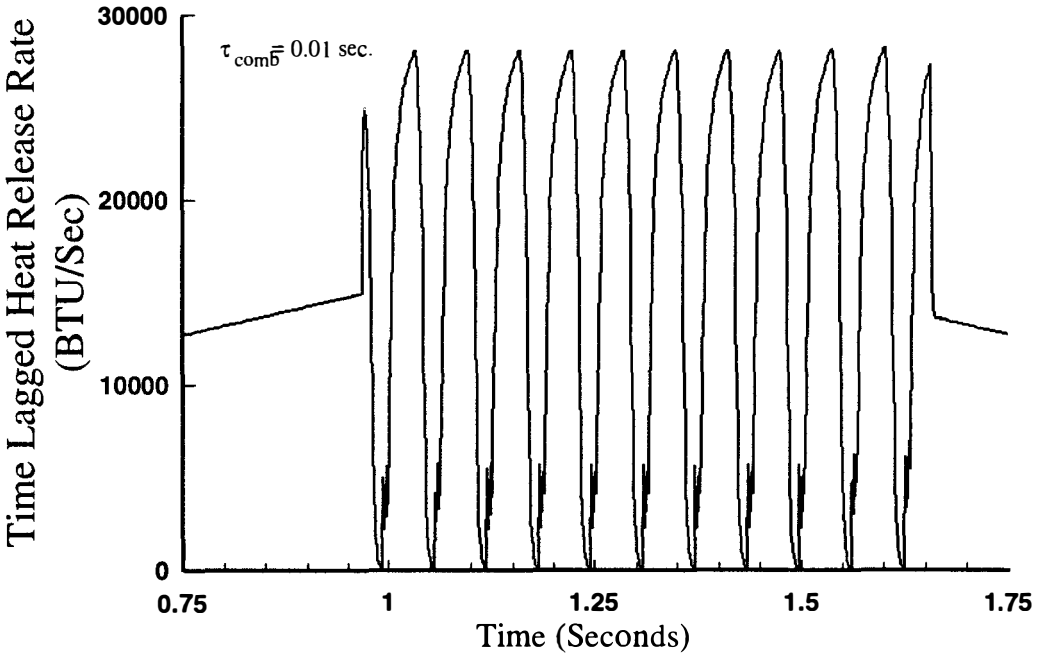

Figure 58. Time Lagged Heat Release Rate in the Combustor Primary Zone for the Combustor Model Operational Verification Test Case.

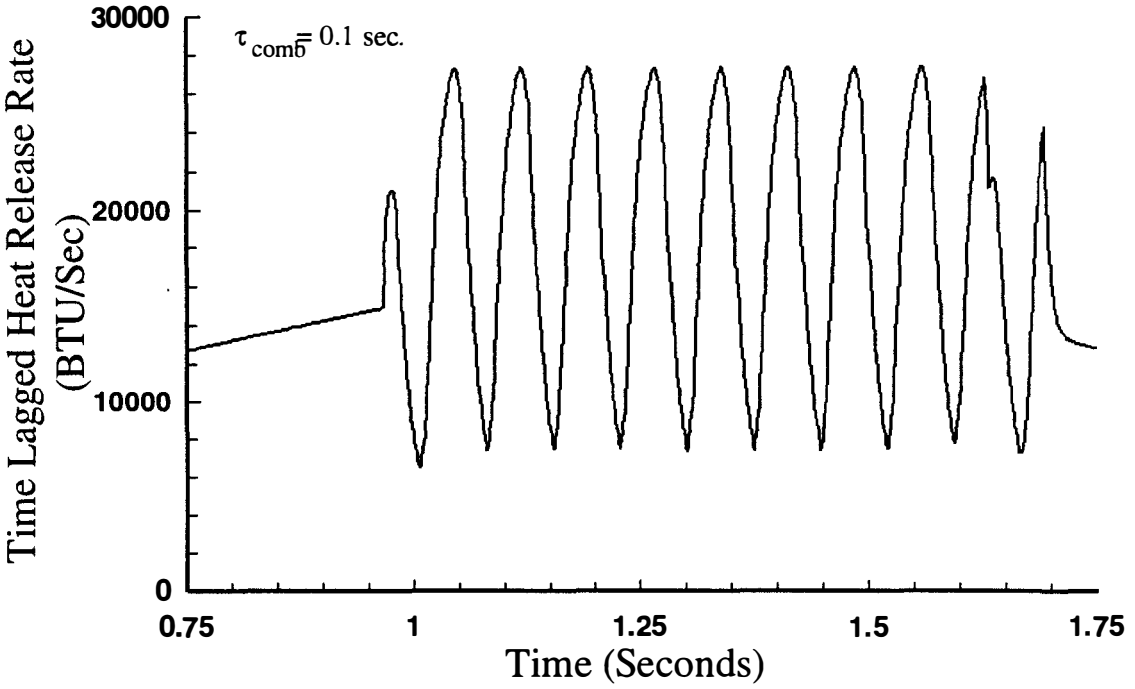

Figure 59. Time Lagged Heat Release Rate in the Combustor Primary Zone with the Light-off and Blow-off Time Constants Increased One Order of Magnitude for the Combustor Model Operational Verification Test Case.

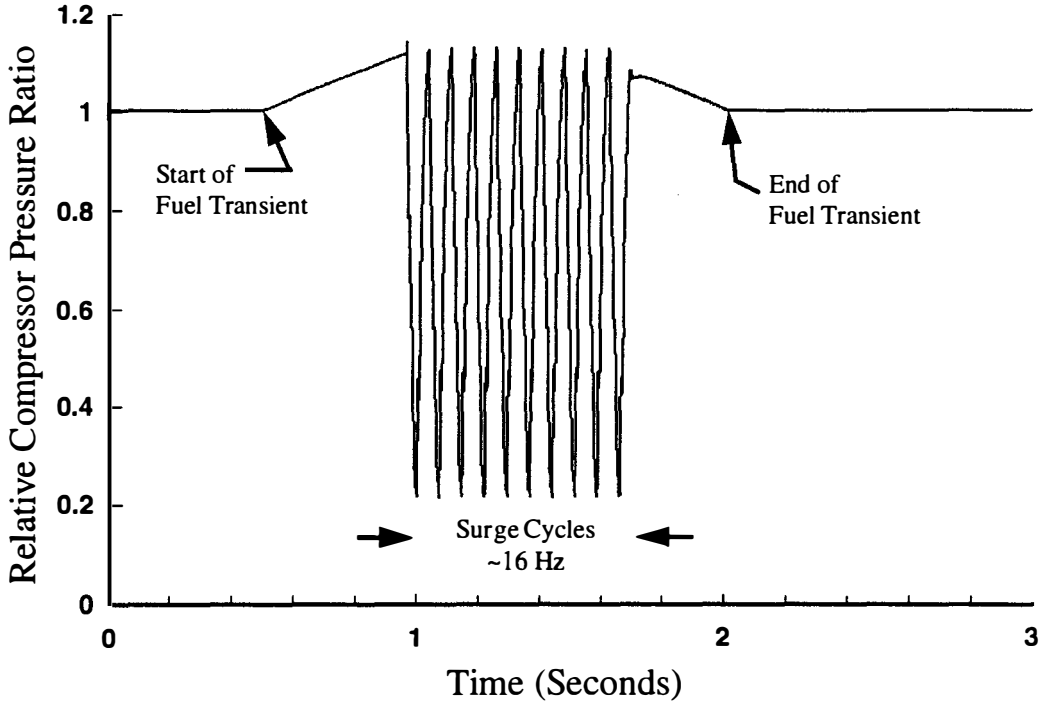

Figure 60. Relative Compressor Pressure Ratio with the Light-off and Blow-off Time Constants Increase One Order of Magnitude for the Combustor Model Operational Verification Test Case.

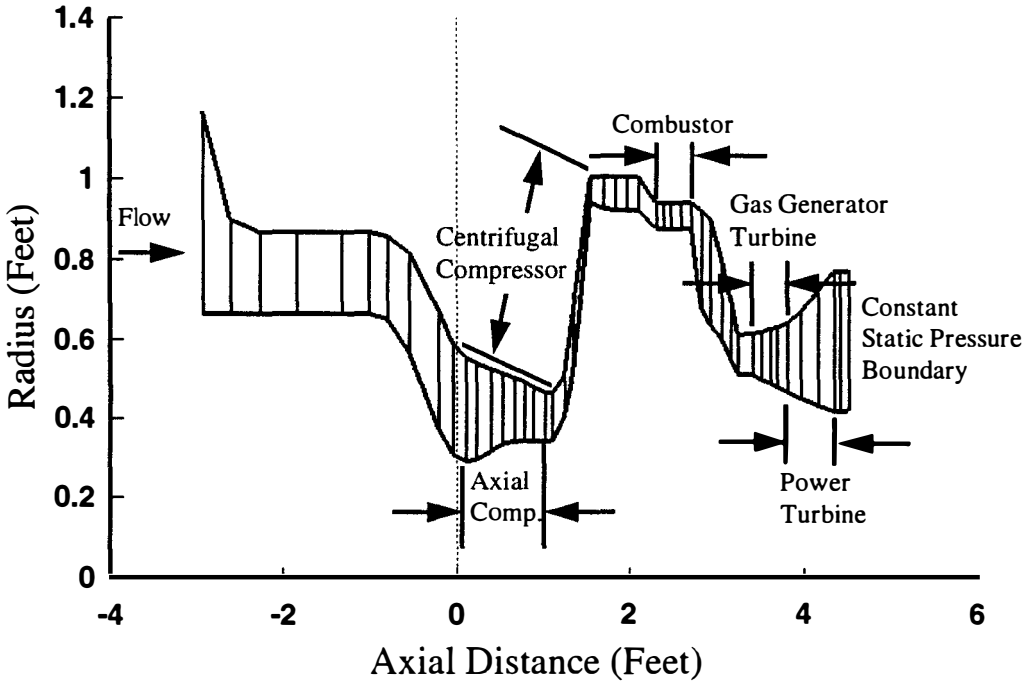

Figure 61. Graphical Representation of T55-L-712 Engine Geometry for the Turbine Model Operational Verification Test Case

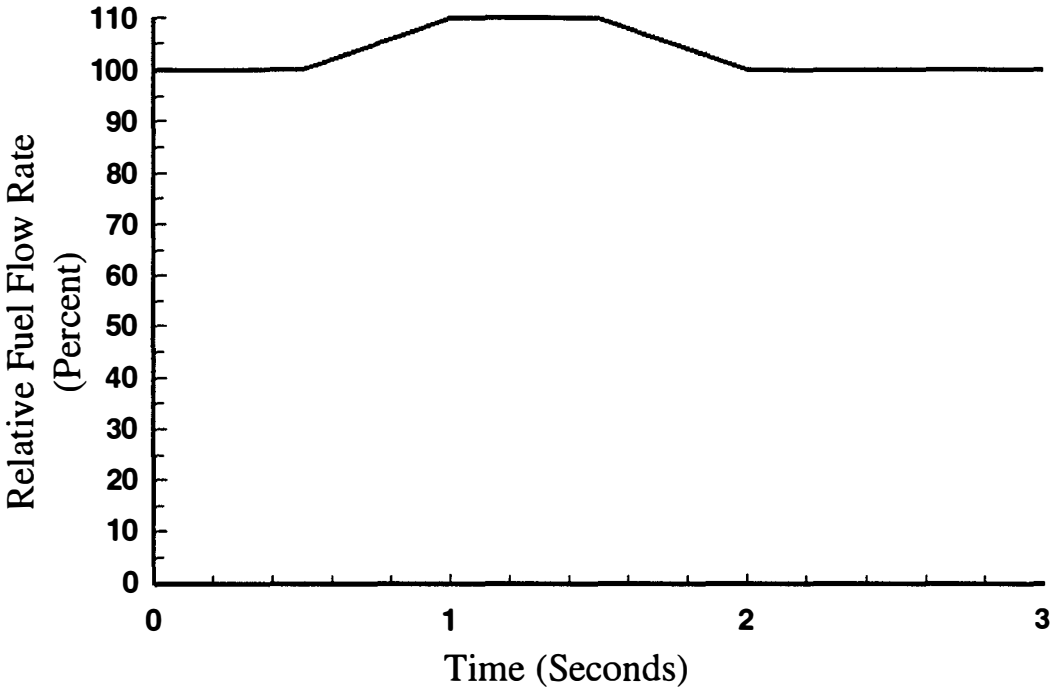

Figure 62. Change in Relative Fuel Flow Rate for the Turbine Model Operational Verification Test Case.

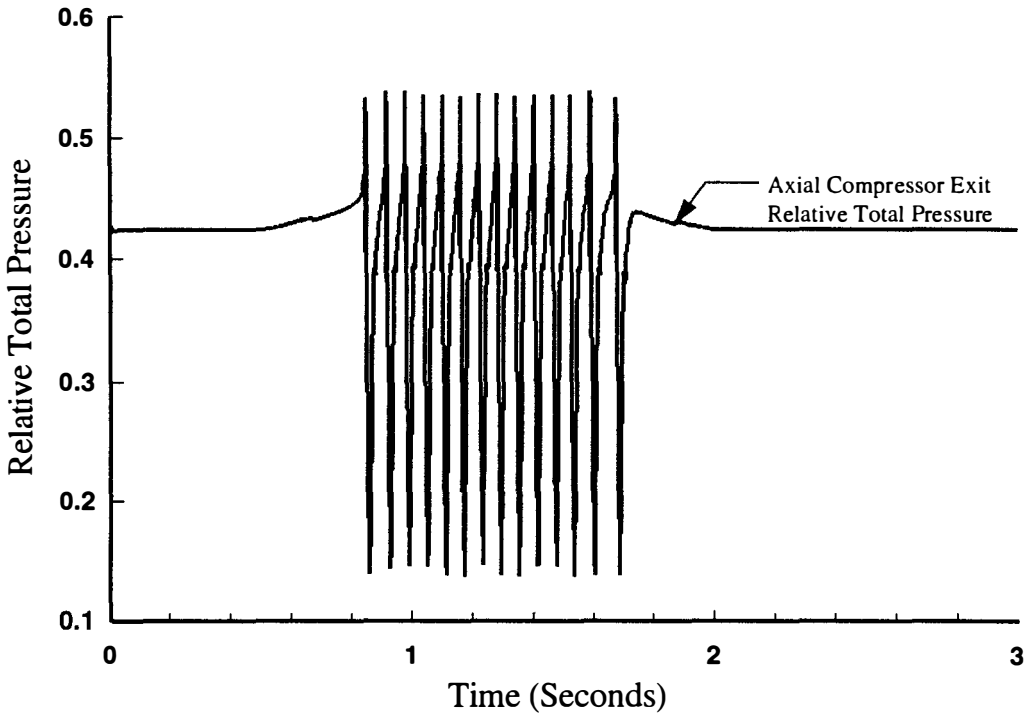

Figure 63. Relative Total Pressure at the Axial Compressor Exit for the T55-L-712 Simulation for the Turbine Model Operational Verification Test Case.

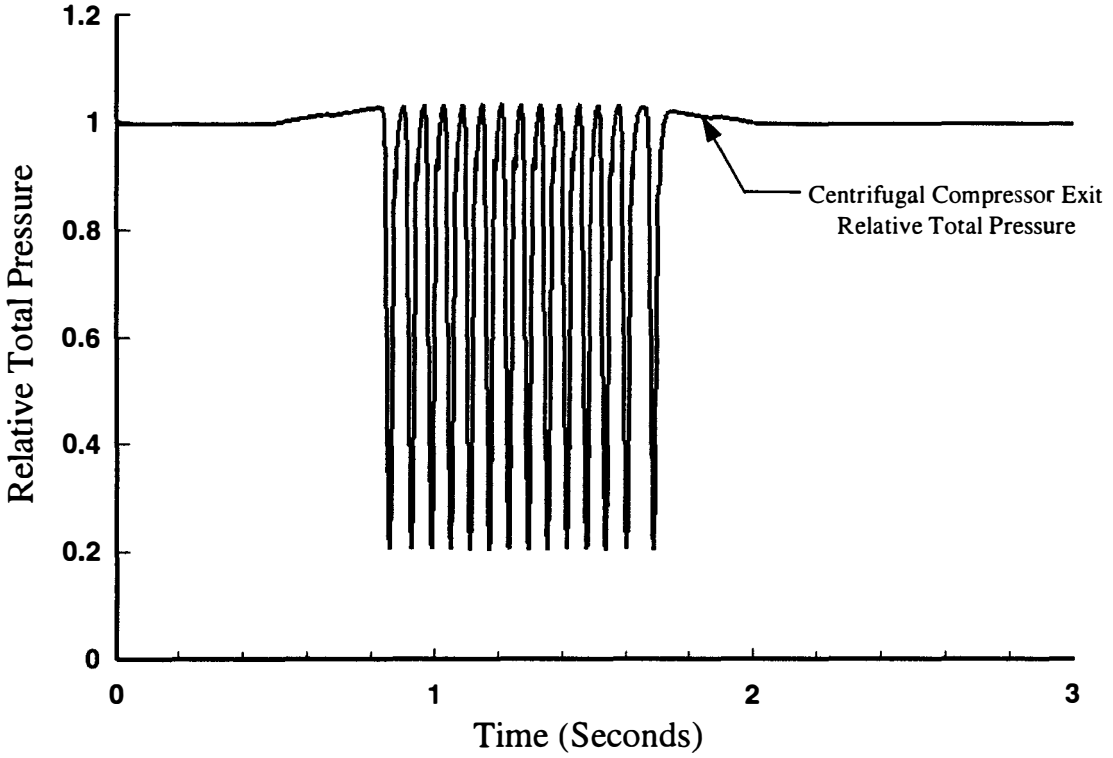

Figure 64. Relative Total Pressure at the Centrifugal Compressor Exit for the T55-L-712 Simulation for the Turbine Model Operational Verification Test Case.

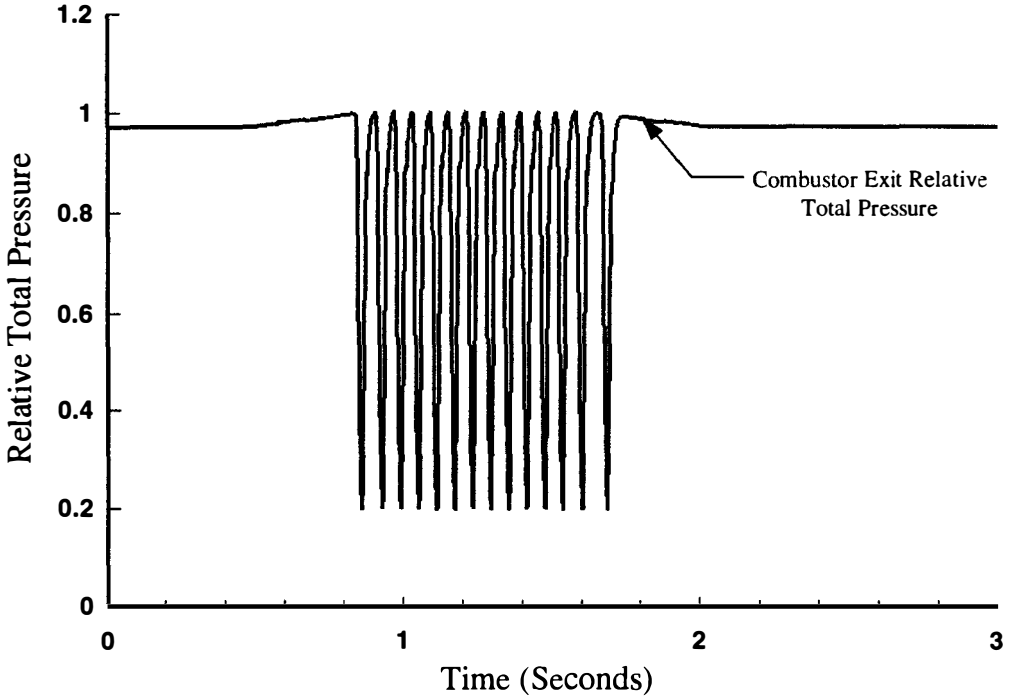

Figure 65. Relative Total Pressure at the Combustor Exit for the T55-L-712 Simulation for the Turbine Model Operational Verification Test Case.

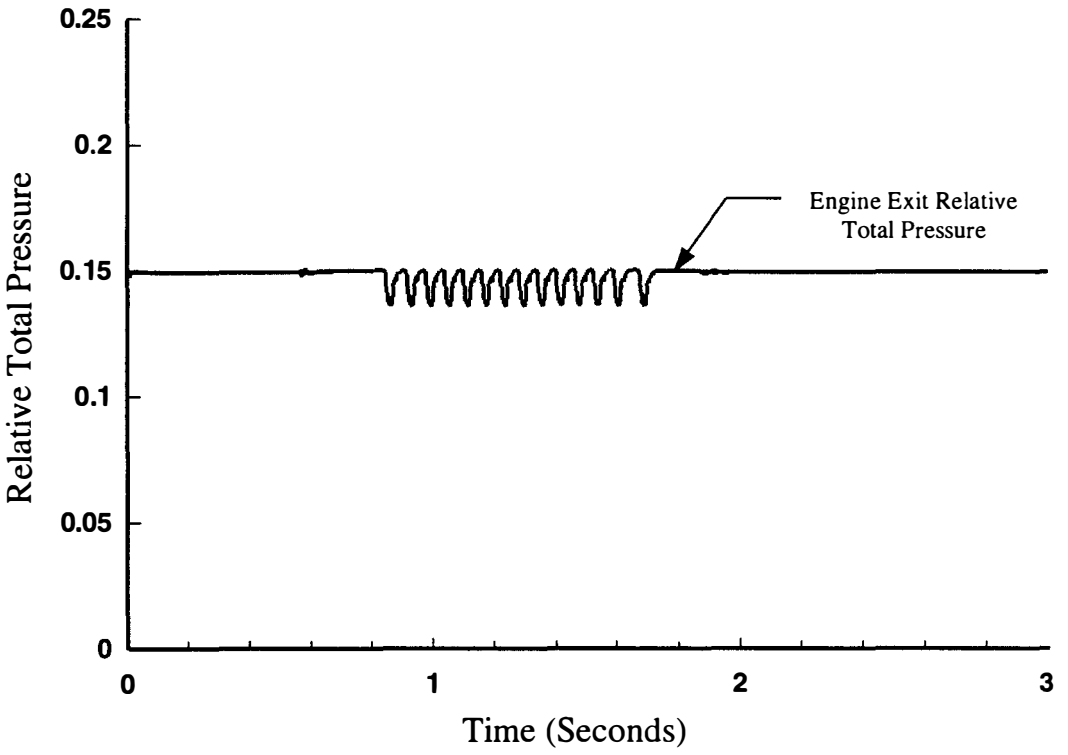

Figure 66. Relative Total Pressure at the Engine Exit for the T55-L-712 Simulation for the Turbine Model Operational Verification Test Case.

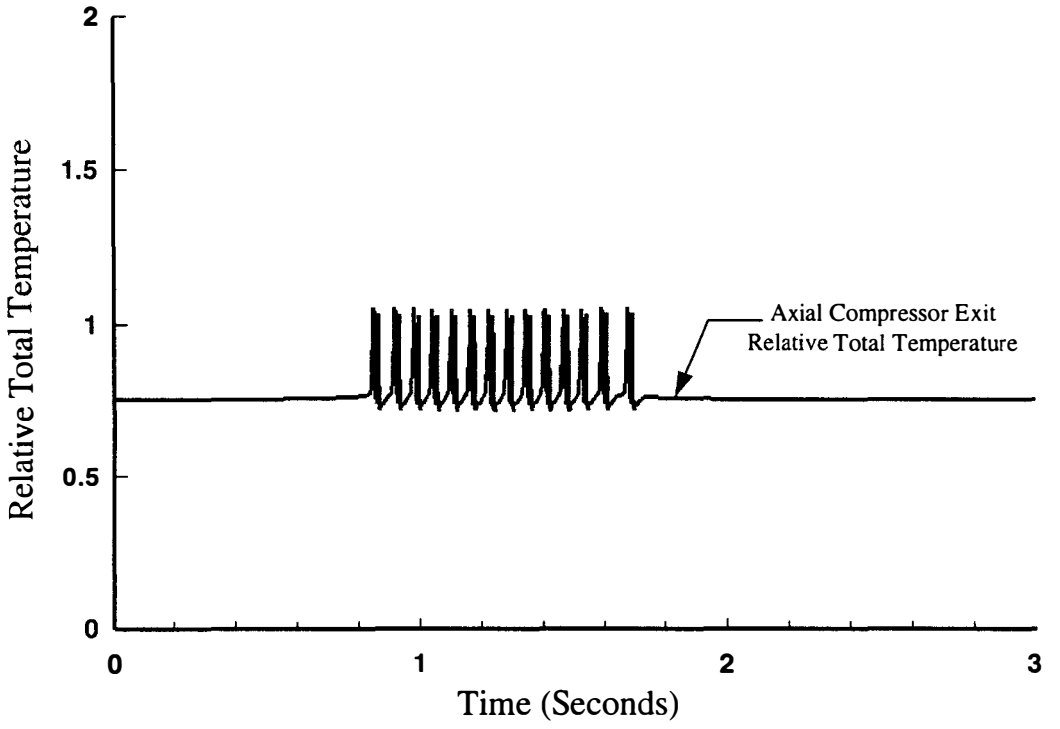

Figure 67. Relative Total Temperature at the Axial Compressor Exit for the T55-L-712 Simulation for the Turbine Model Operational Verification Test Case.

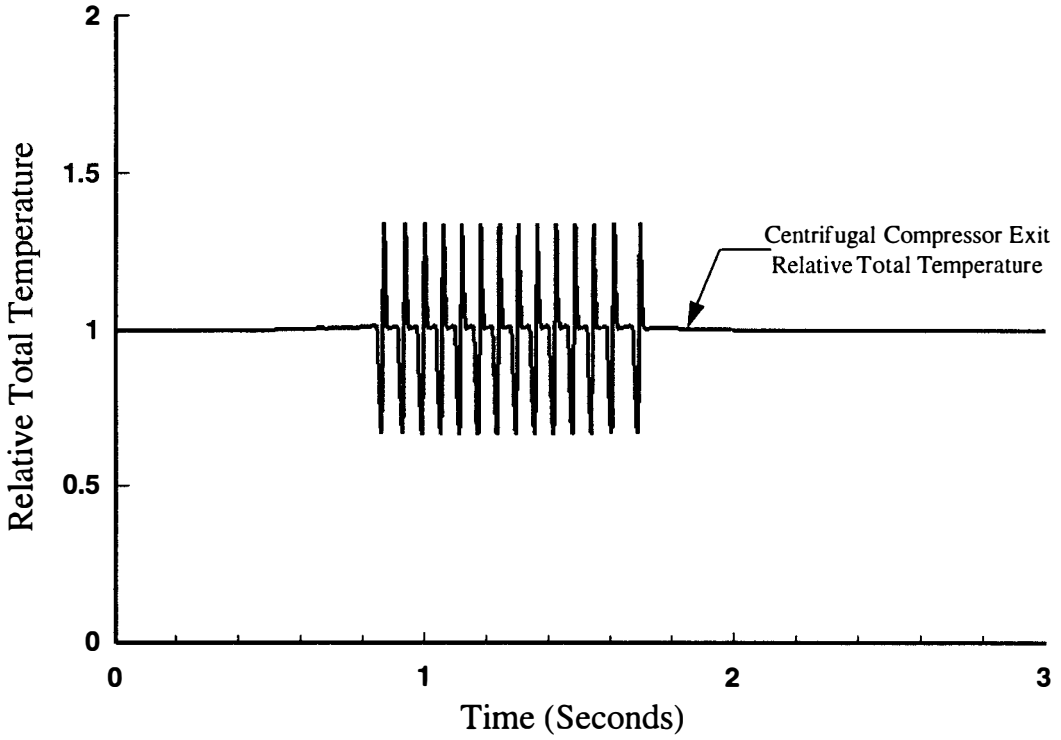

Figure 68. Relative Total Temperature at the Centrifugal Compressor Exit for the T55-L-712 Simulation for the Turbine Model Operational Verification Test Case.

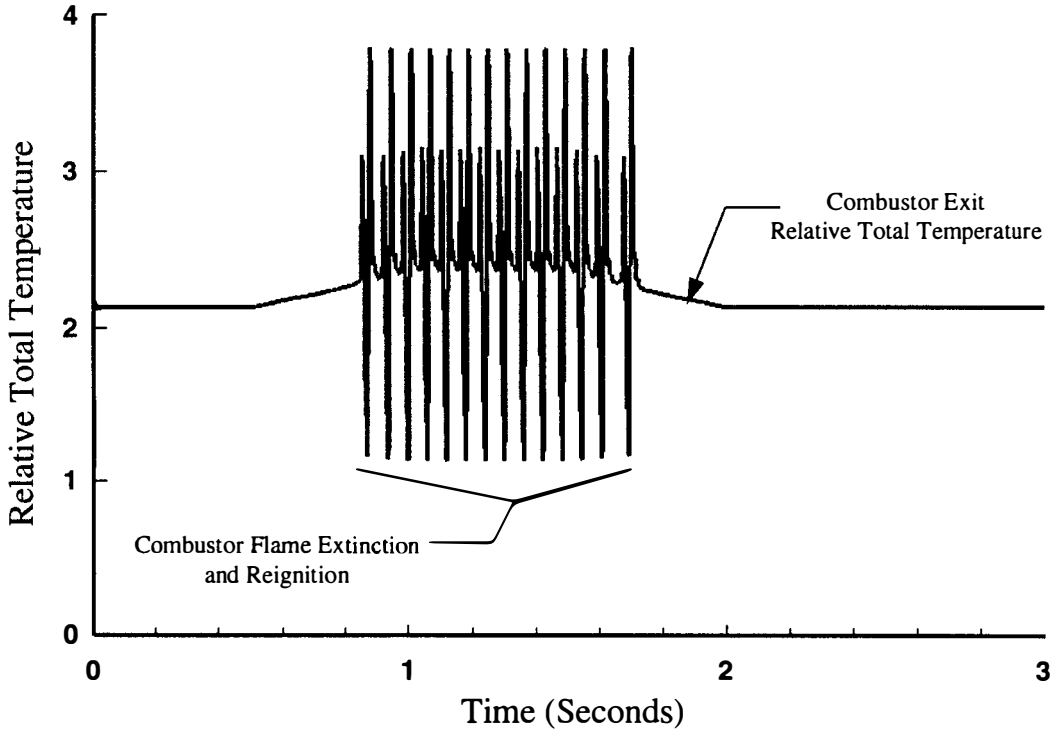

Figure 69. Relative Total Temperature at the Combustor Exit for the T55-L-712 Simulation for the Turbine Model Operational Verification Test Case.

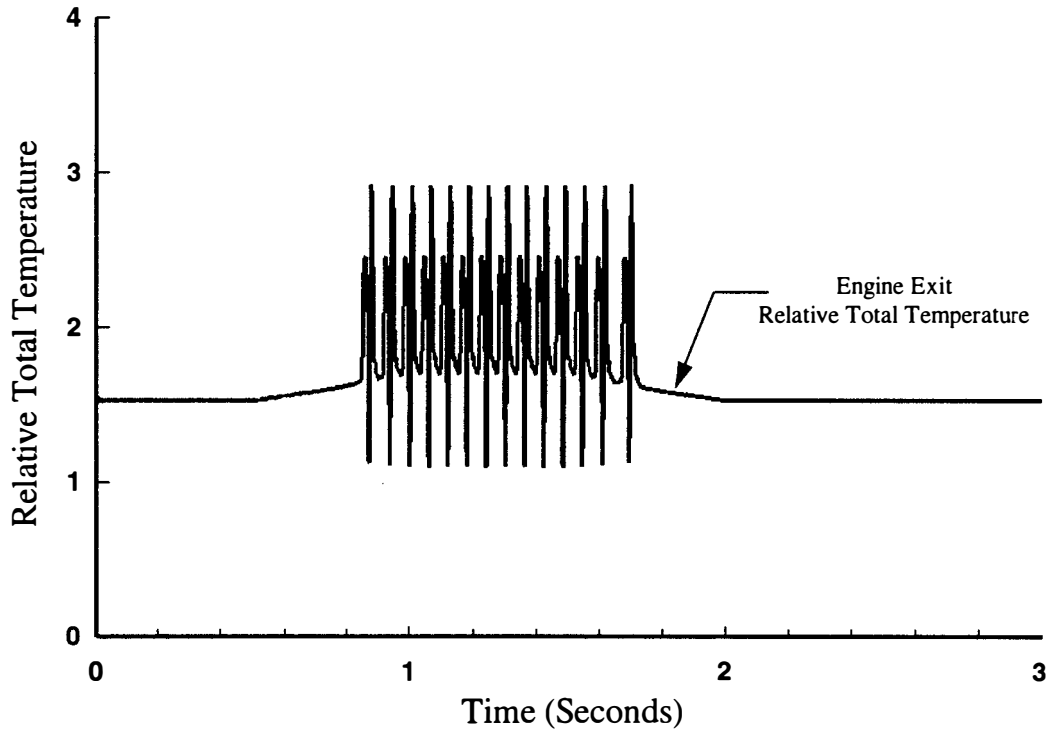

Figure 70. Relative Total Temperature at the Engine Exit for the T55-L-712 Simulation for the Turbine Model Operational Verification Test Case.

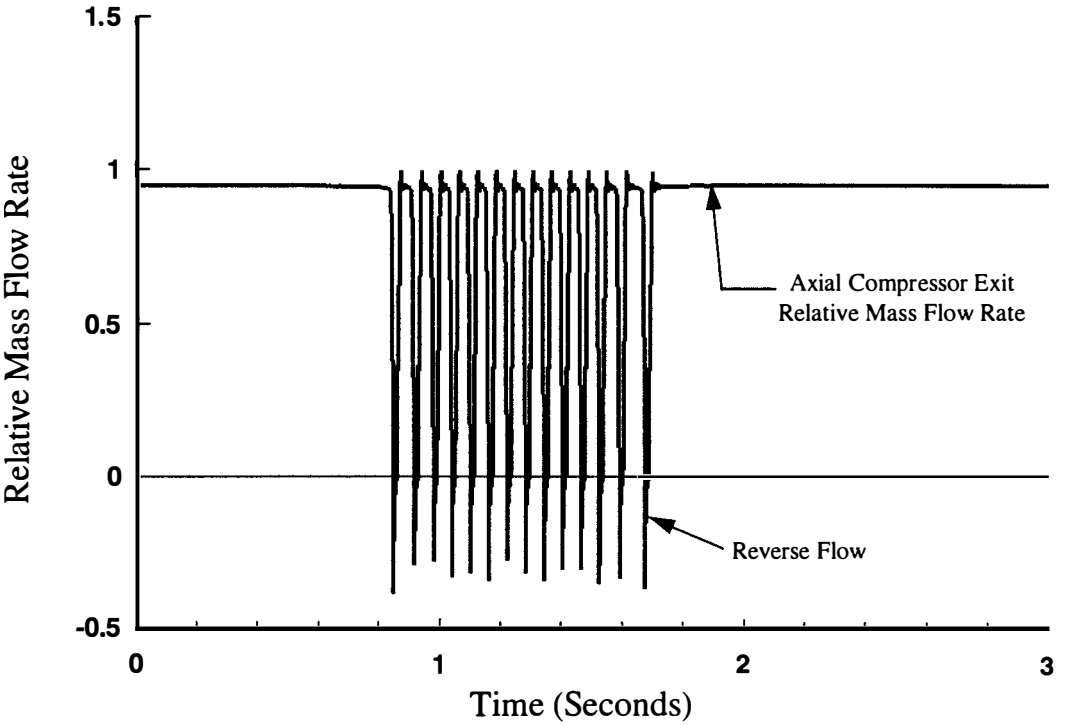

Figure 71. Relative Mass Flow Rate at the Axial Compressor Exit for the T55-L-712 Simulation for the Turbine Model Operational Verification Test Case.

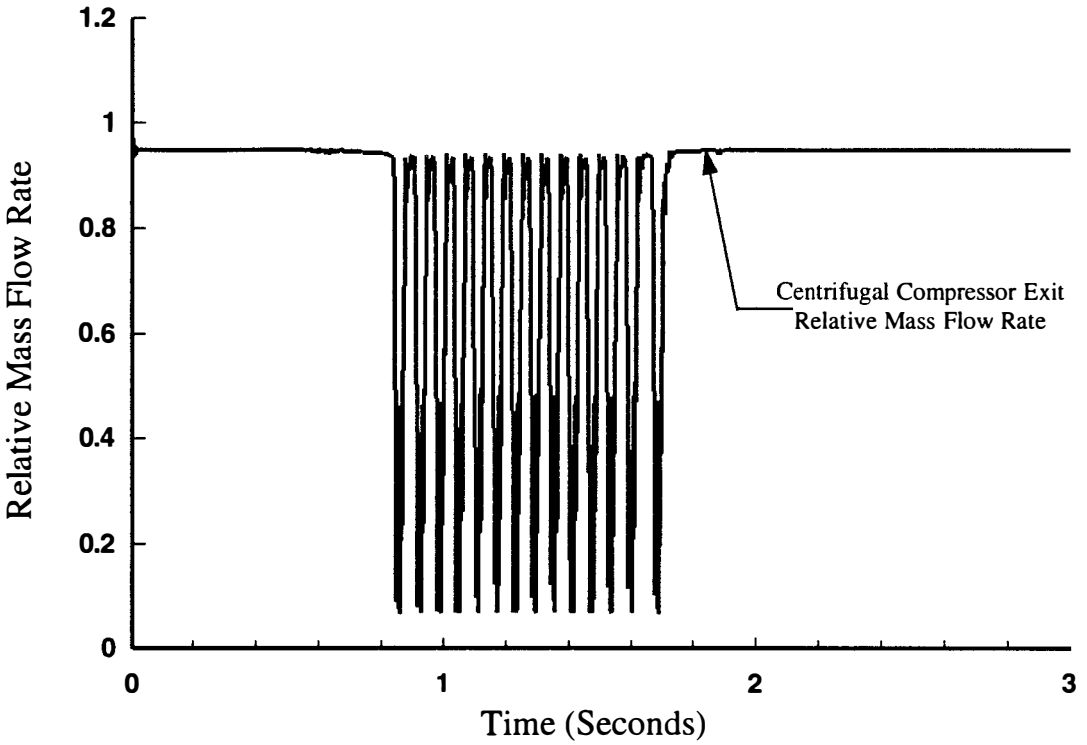

Figure 72. Relative Mass Flow Rate at the Centrifugal Compressor Exit for the T55-L-712 Simulation for the Turbine Model Operational Verification Test Case.

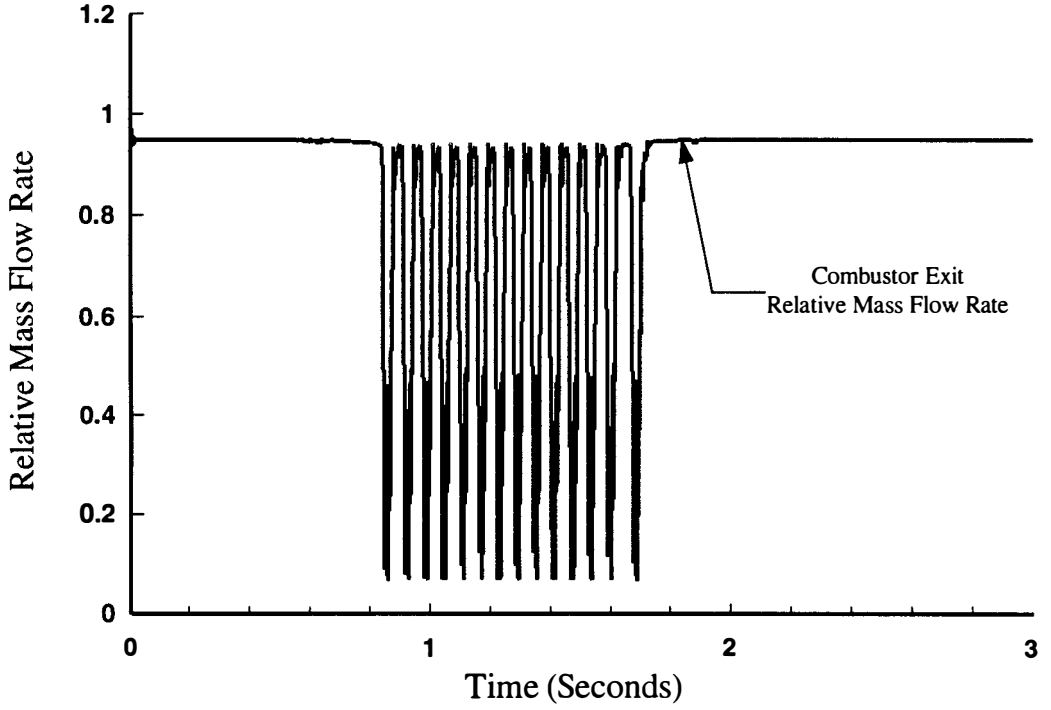

Figure 73. Relative Mass Flow Rate at the Combustor Exit for the T55-L-712 Simulation for the Turbine Model Operational Verification Test Case.

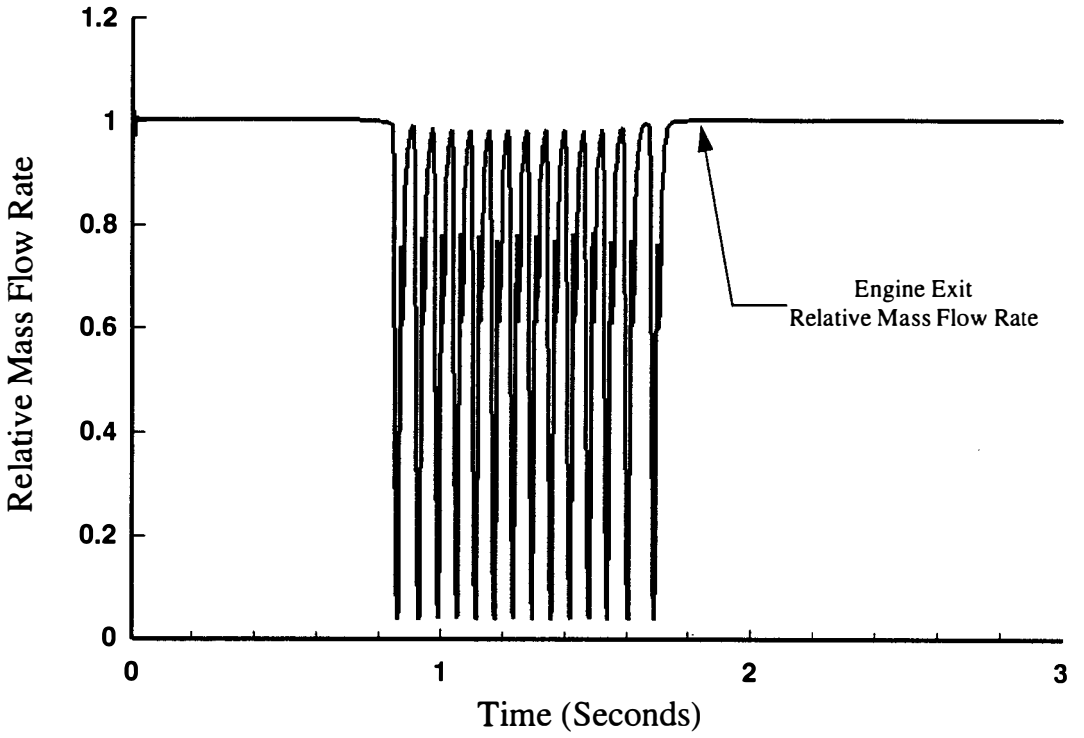

Figure 74. Relative Mass Flow Rate at the Engine Exit for the T55-L-712 Simulation for the Turbine Model Operational Verification Test Case.

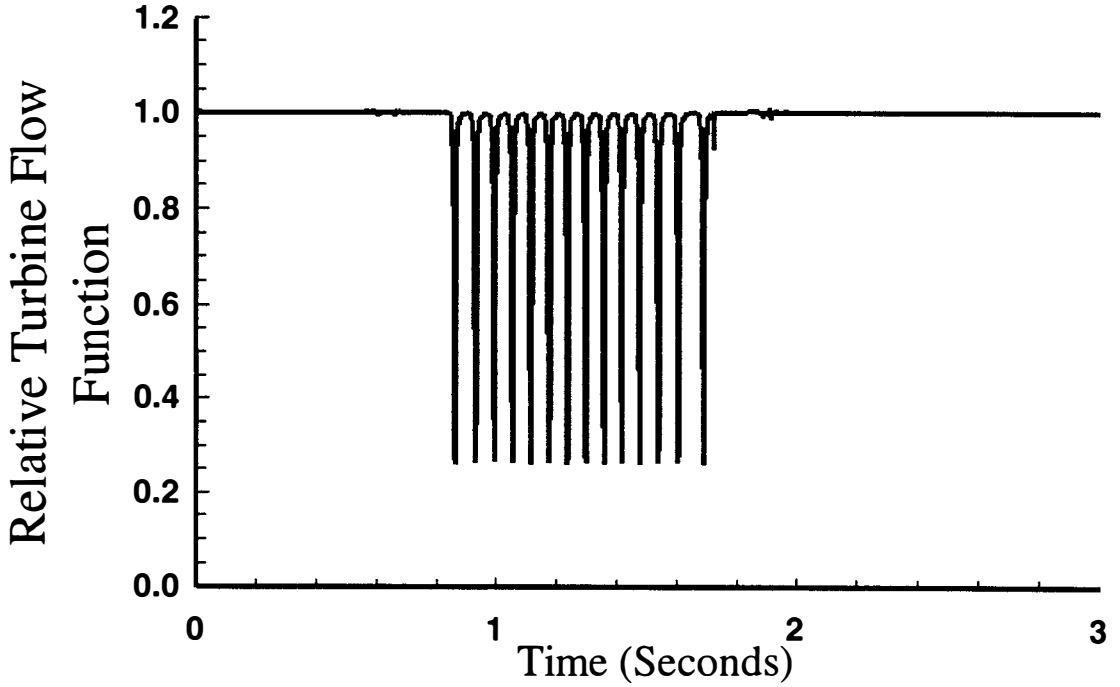

Figure 75. Relative Gas Generator Turbine Mass Flow Function as a Function of Time for the T55-L-712 Simuation for the Turbine Model Operational Verification Test Case.

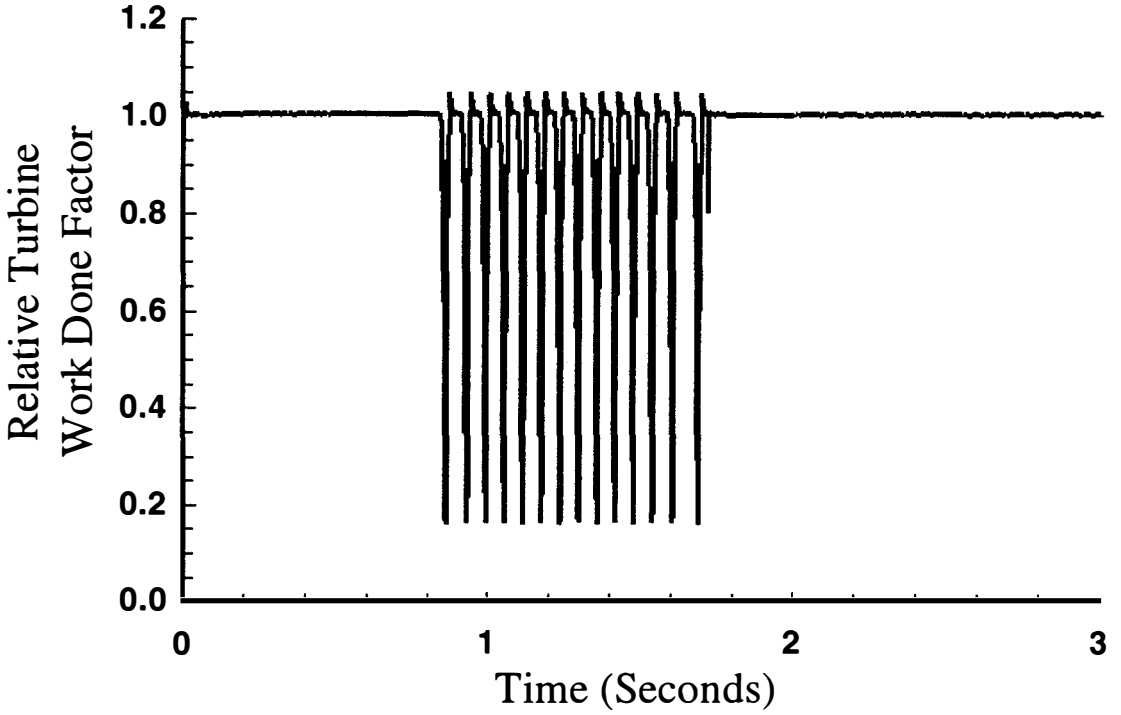

Figure 76. Relative Gas Generator Turbine Work Done Factor as a Function of Time for the T55-L-712 Simulation for the Turbine Model Operational Verification Test Case.

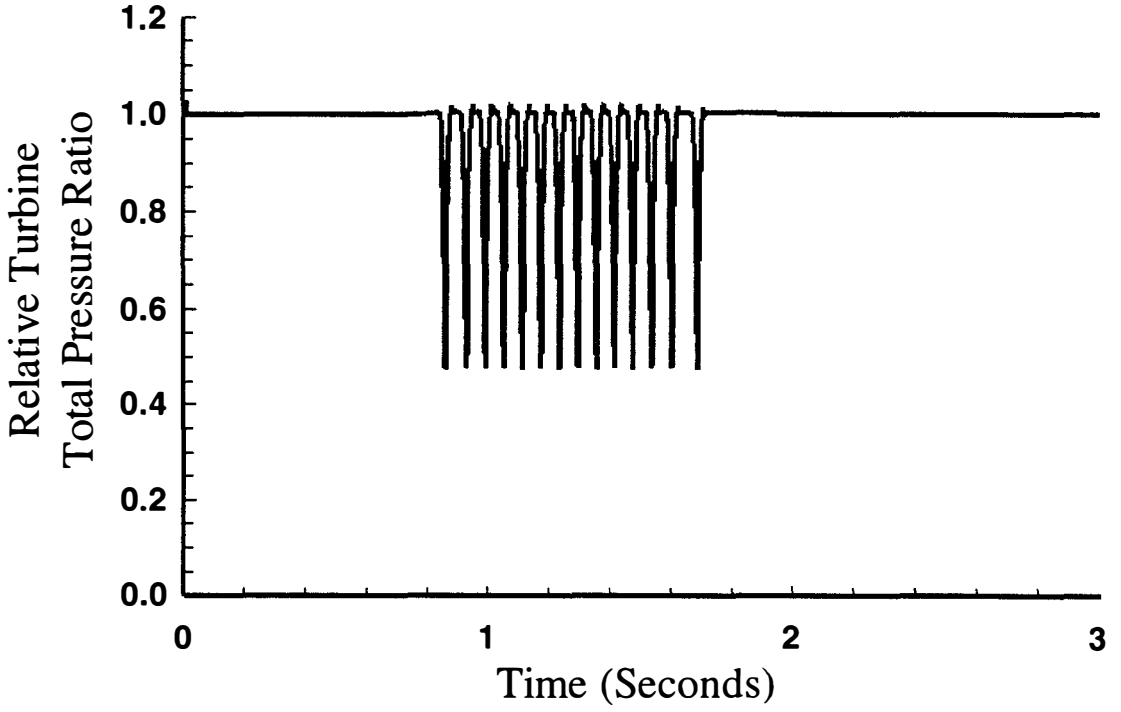

Figure 77. Relative Gas Generator Turbine Total Pressure Ratio as a Function of Time for the T55-L-712 Simulation for the Turbine Model Operational Verification Test Case.

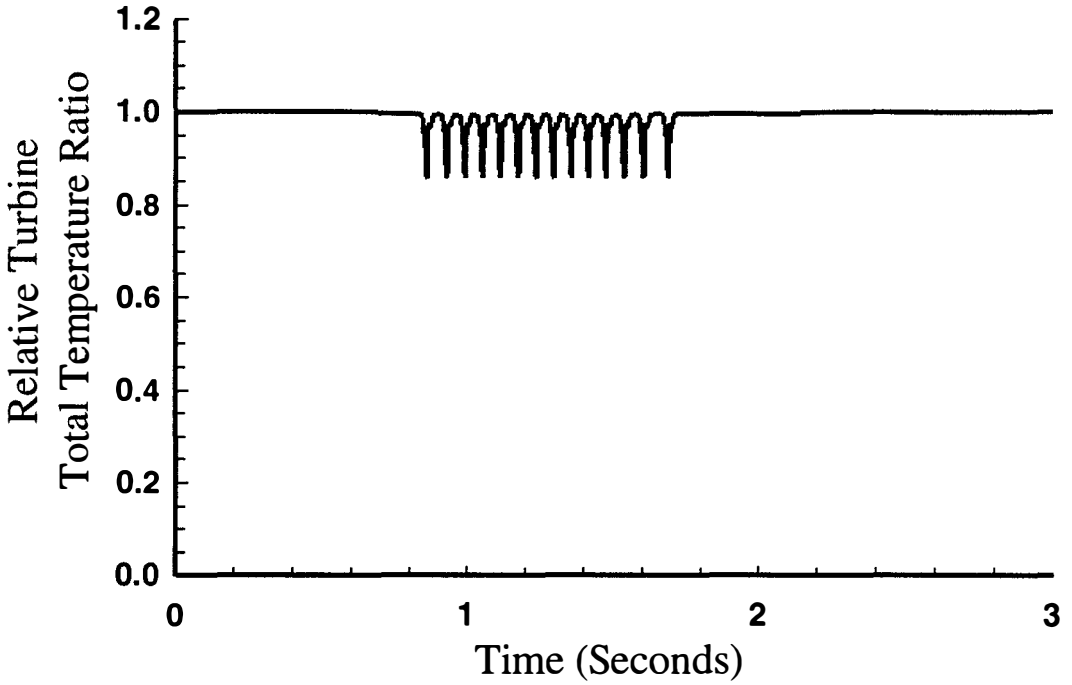

Figure 78. Relative Gas Generator Turbine Total Temperature Ratio as a Function of Time for the T55-L-712 Simulation for the Turbine Model Operational Verification Test Case.

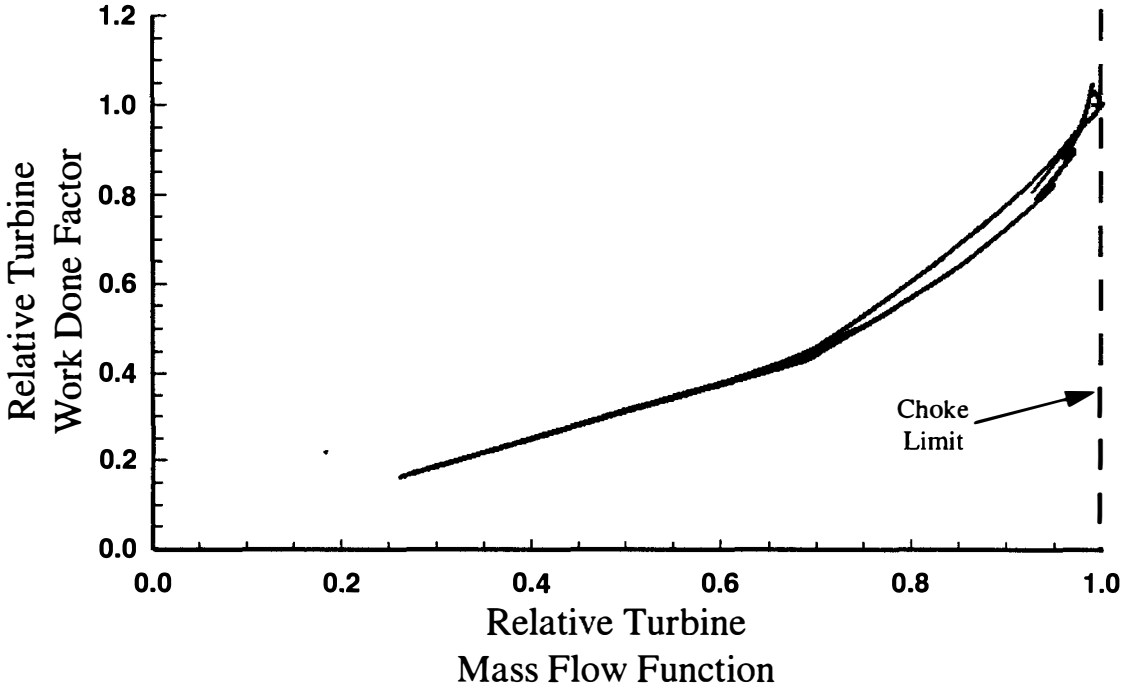

Figure 79. Relative Gas Generator Turbine Work Done Factor as a Function of Relative Gas Generator Turbine Mass Flow Function for the T55-L-712 Simulation for the Turbine Model Operational Verification Test Case.

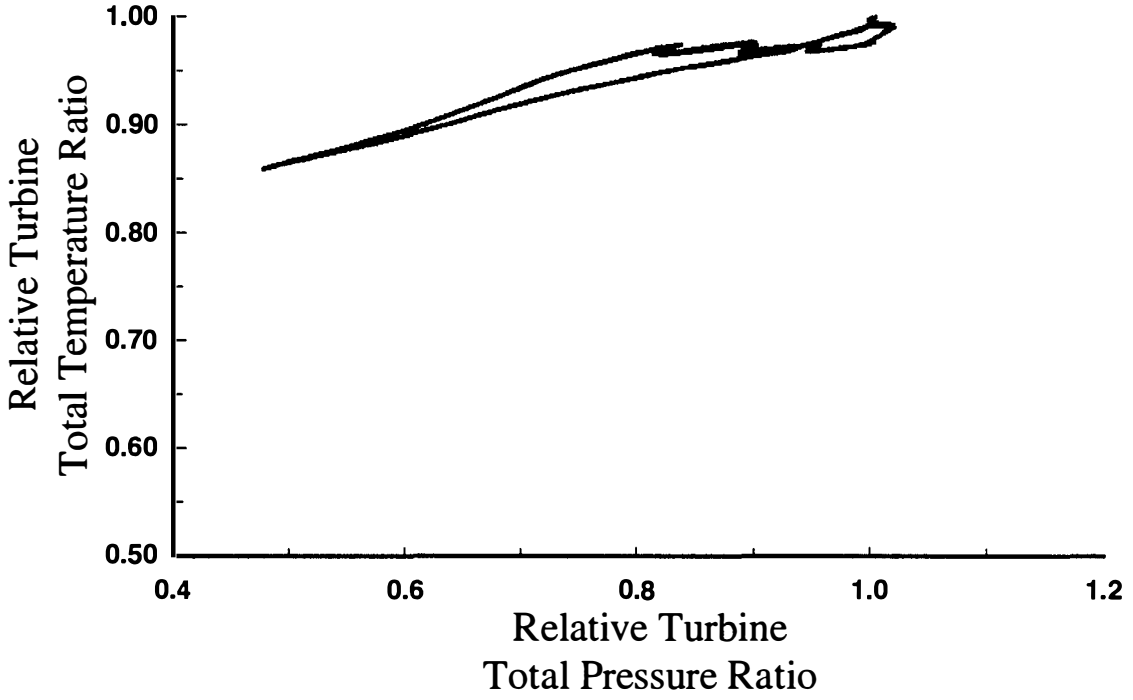

Figure 80. Relative Gas Generator Turbine Total Temperature Ratio as a Function of Relative Gas Generator Turbine Total Pressure Ratio for the T55-L-712 Simulation for the Turbine Model Operational Verification Test Case.

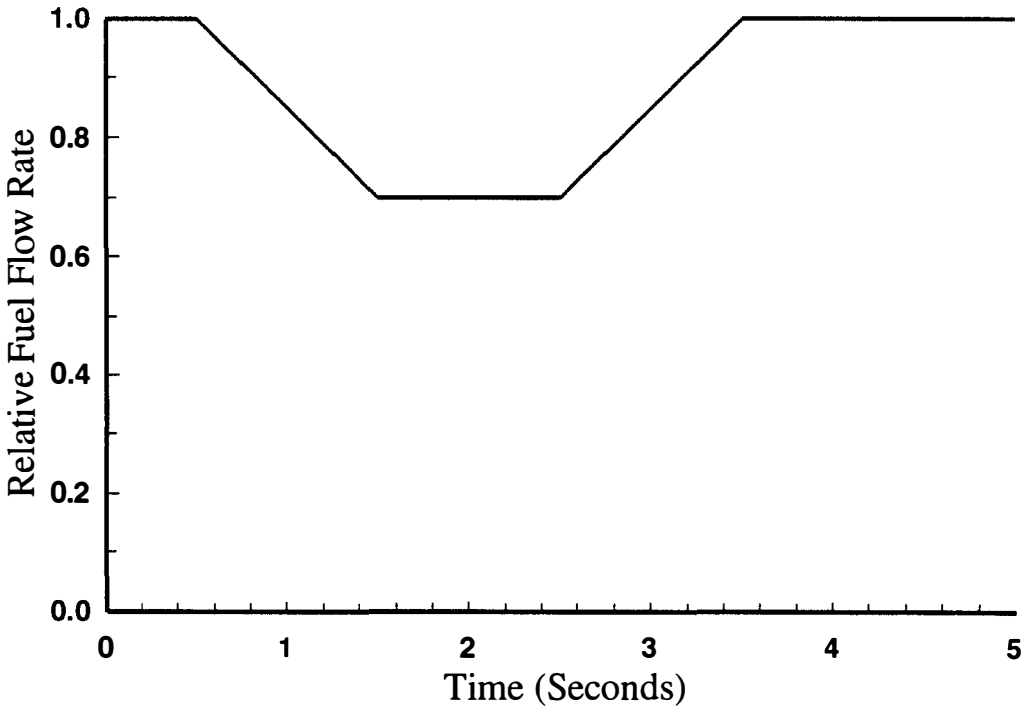

Figure 81. Relative Fuel Flow Rate as a Function of Time for the Rotor Dynamics Model Operational Verification Test Case.

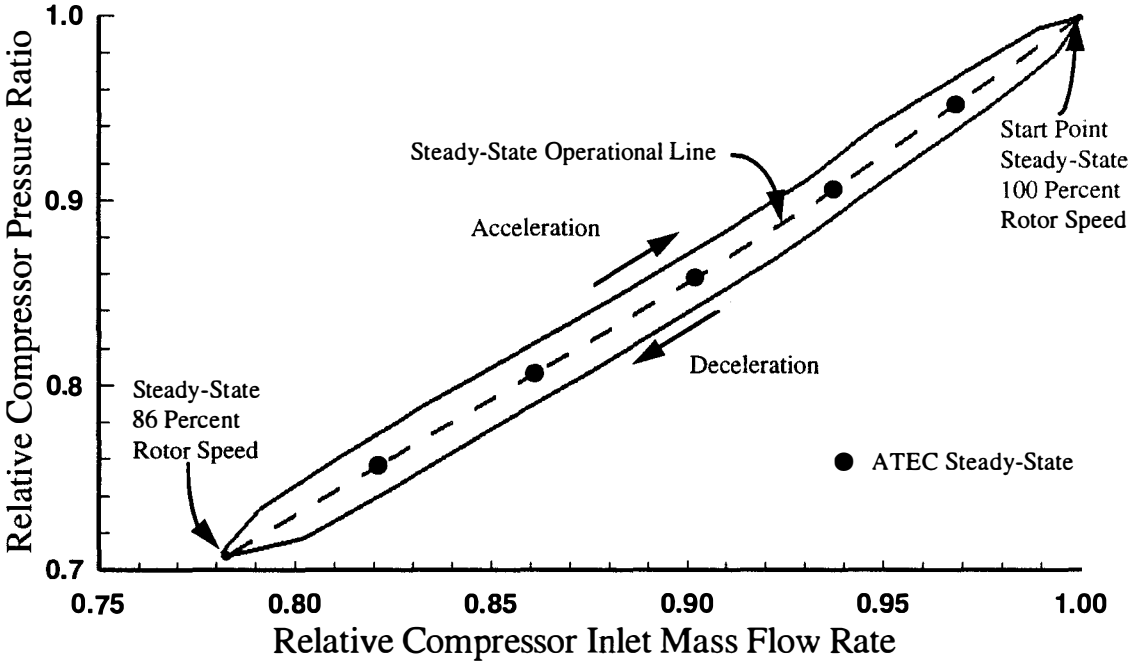

Figure 82. Relative Compressor Pressure Ratio as a Function of Relative Compressor Inlet Mass Flow Rate for the Rotor Dynamics Model Operational Verification Test Case.

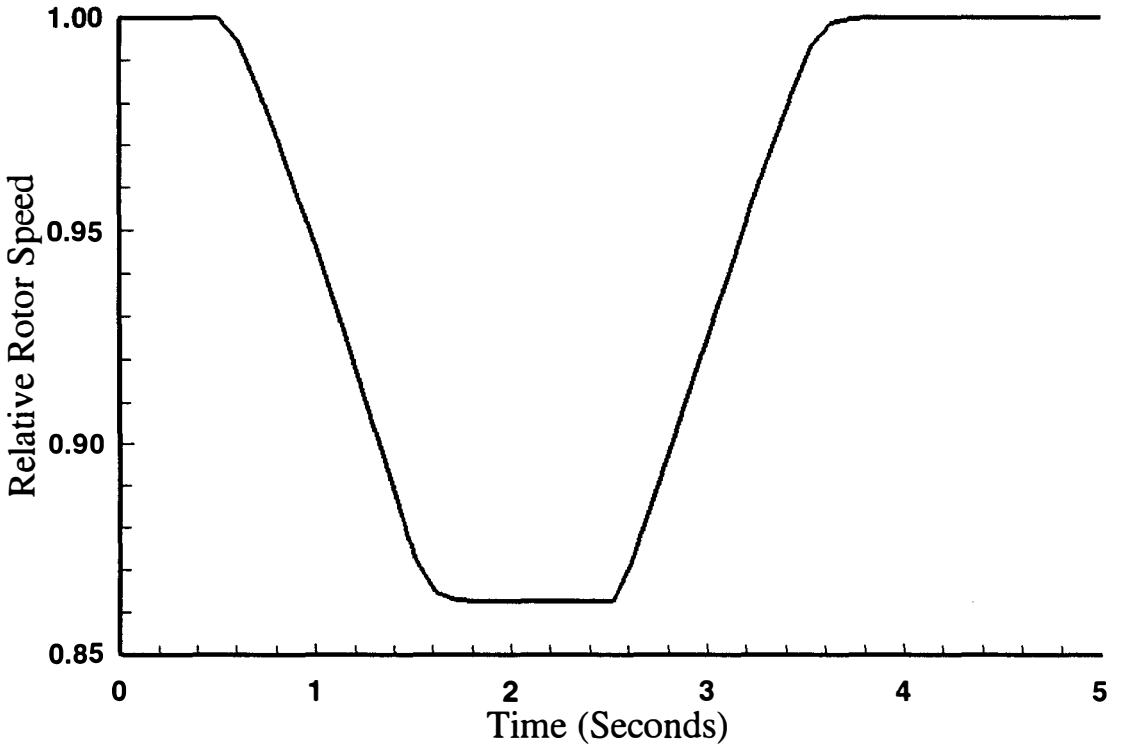

Figure 83. Relative Rotor Speed as a Function of Time for the Rotor Dynamics Model Operational Verification Test Case.

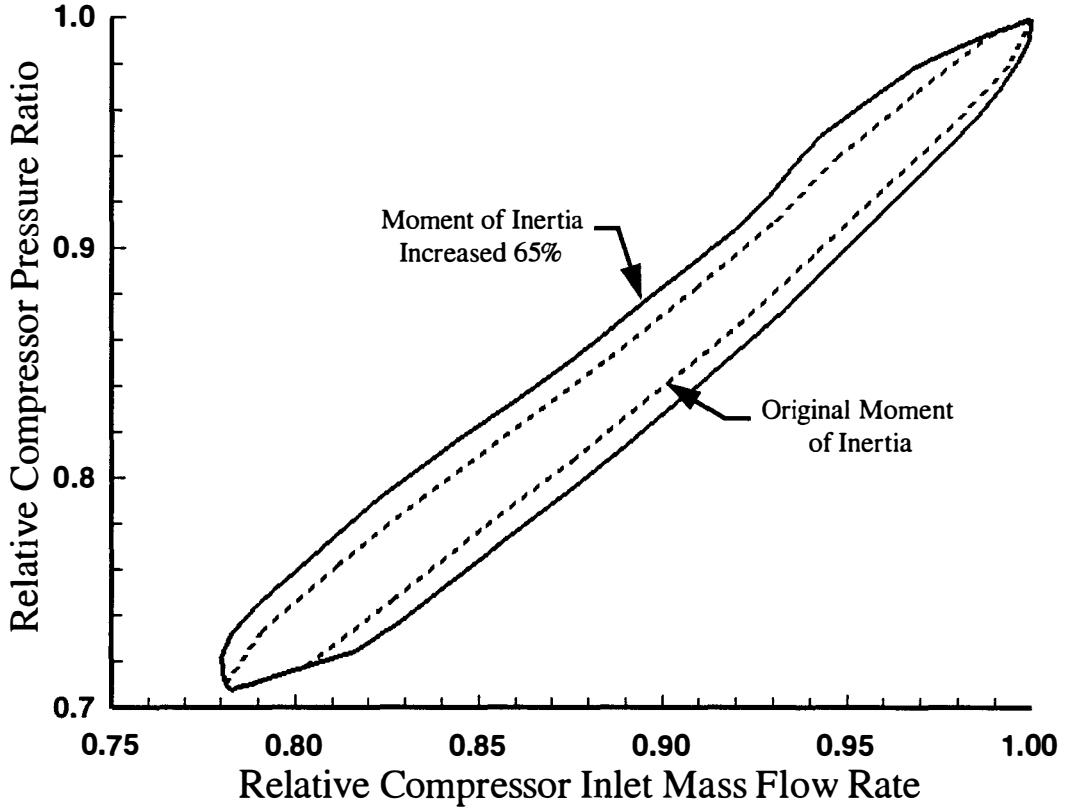

Figure 84. Relative Rotor Speed as a Function of Relative Compressor Inlet Mass Flow Rate to Show the Influence of Rotor Moment of Inertia for the Rotor Dynamics Model Operational Verification Test Case.

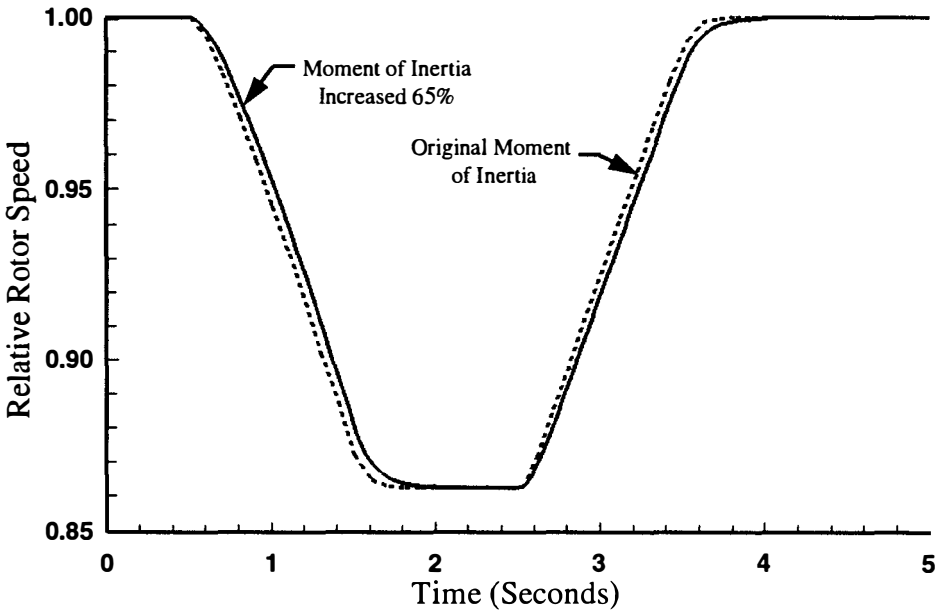

Figure 85. Relative Rotor Speed as a Function of Time to Show the Influence of Rotor Moment of Inertia for the Rotor Dynamics Model Operational Verification Test Case.

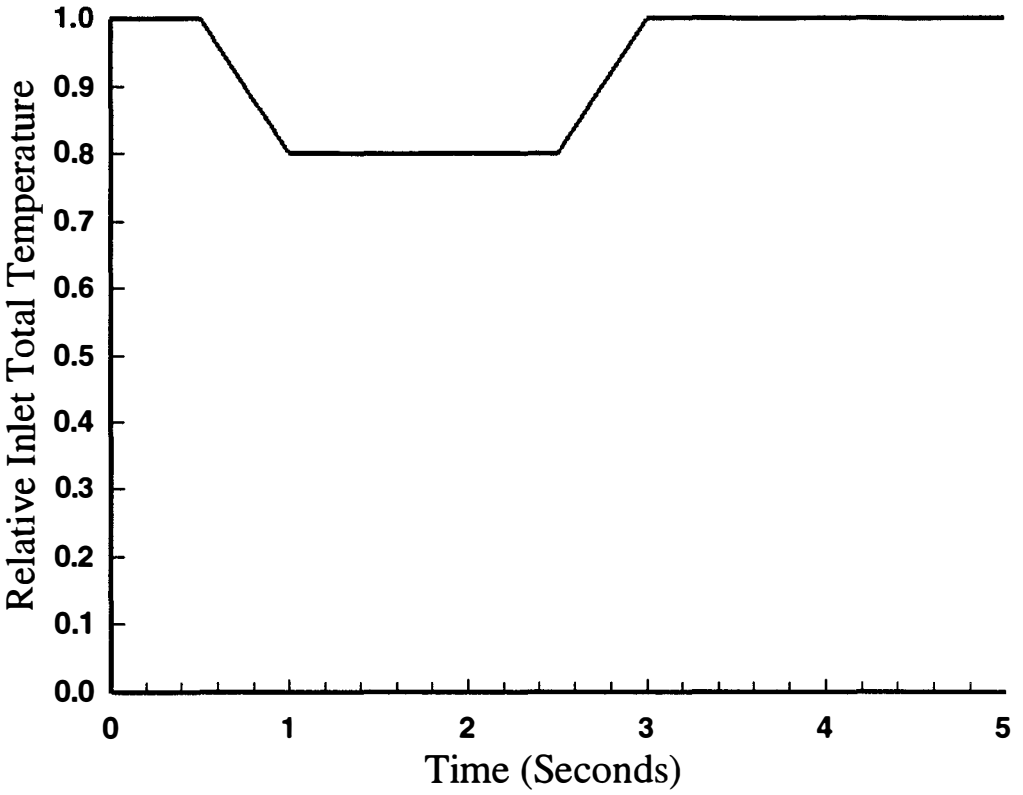

Figure 86. Relative Inlet Air Total Temperature as a Function of Time for the Heat Transfer Model Operational Verification Test Case.

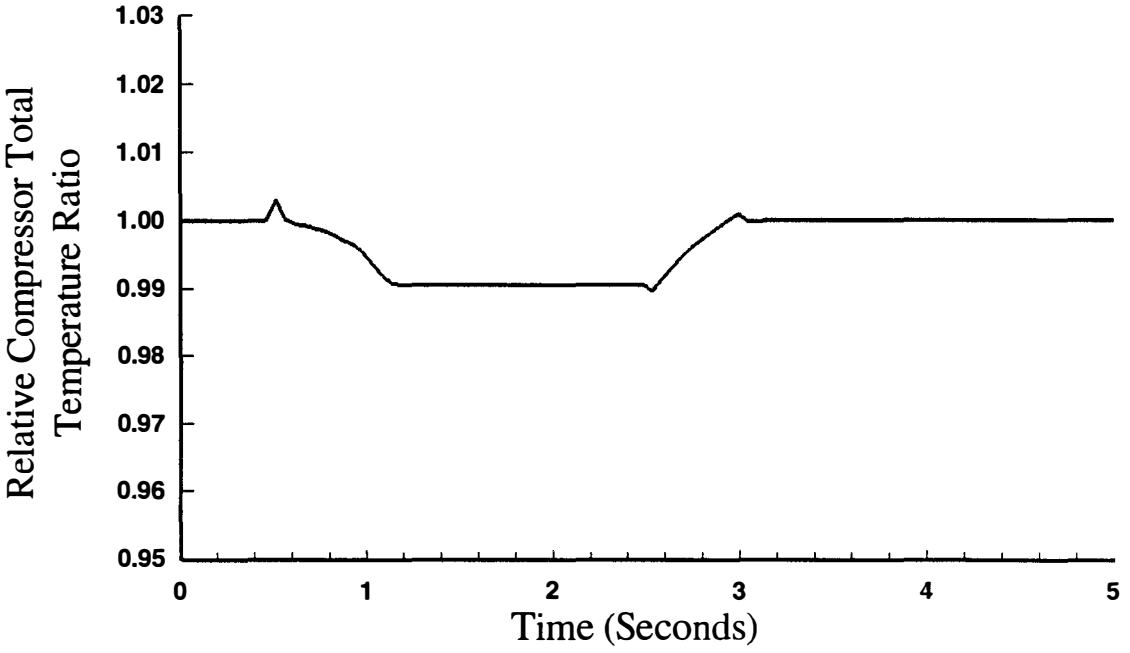

Figure 87. Relative Compressor Total Temperature Ratio as a Function of Time with No Heat Transfer for the Heat Transfer Model Operational Verification Test Case.

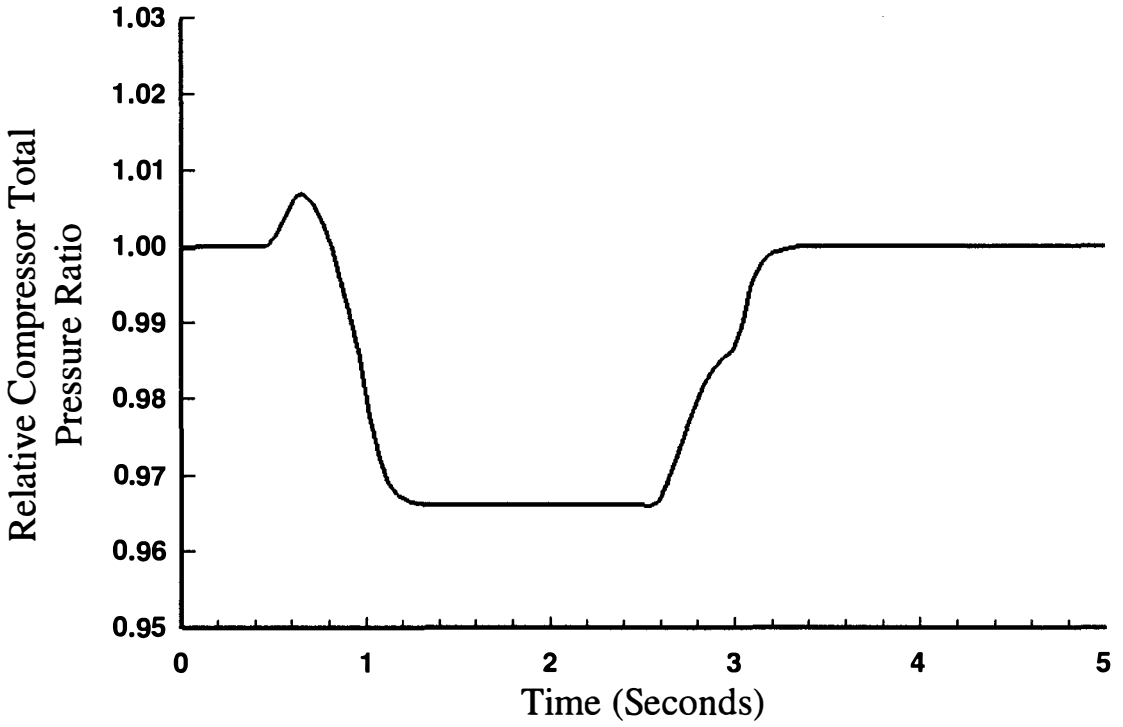

Figure 88. Relative Compressor Total Pressure Ratio as a Function of Time with No Heat Transfer for the Heat Transfer Model Operational Verification Test Case.

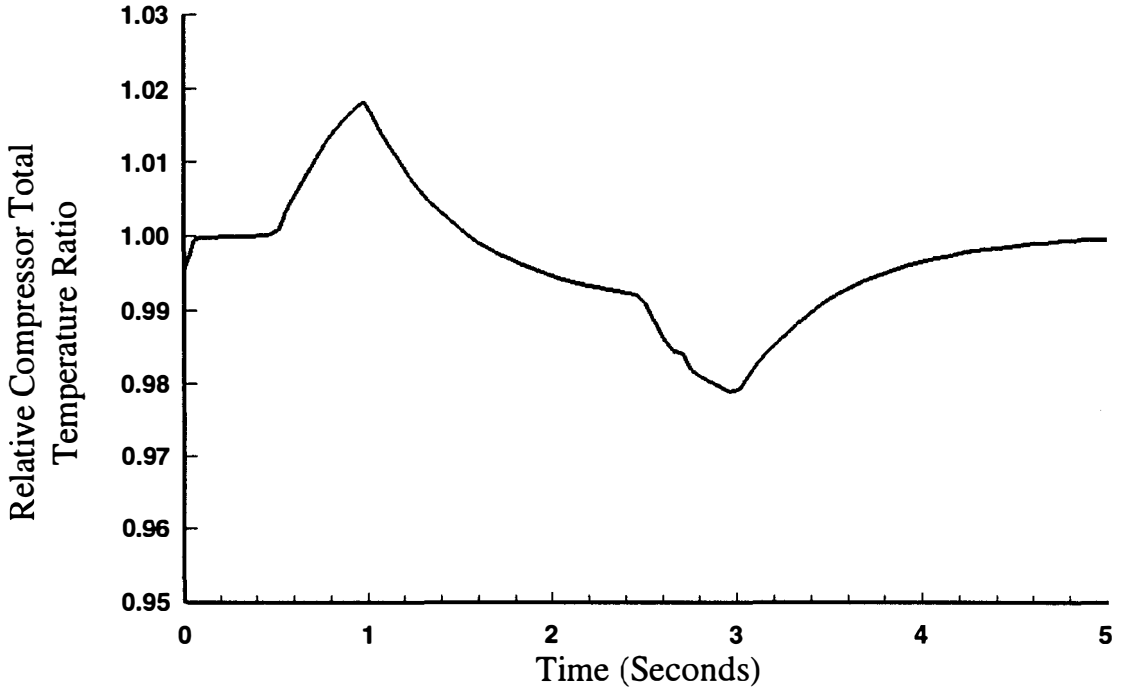

Figure 89. Relative Compressor Total Temperature Ratio as a Function of Time with the Heat Transfer Model Activated for the Heat Transfer Model Operational Verification Test Case.

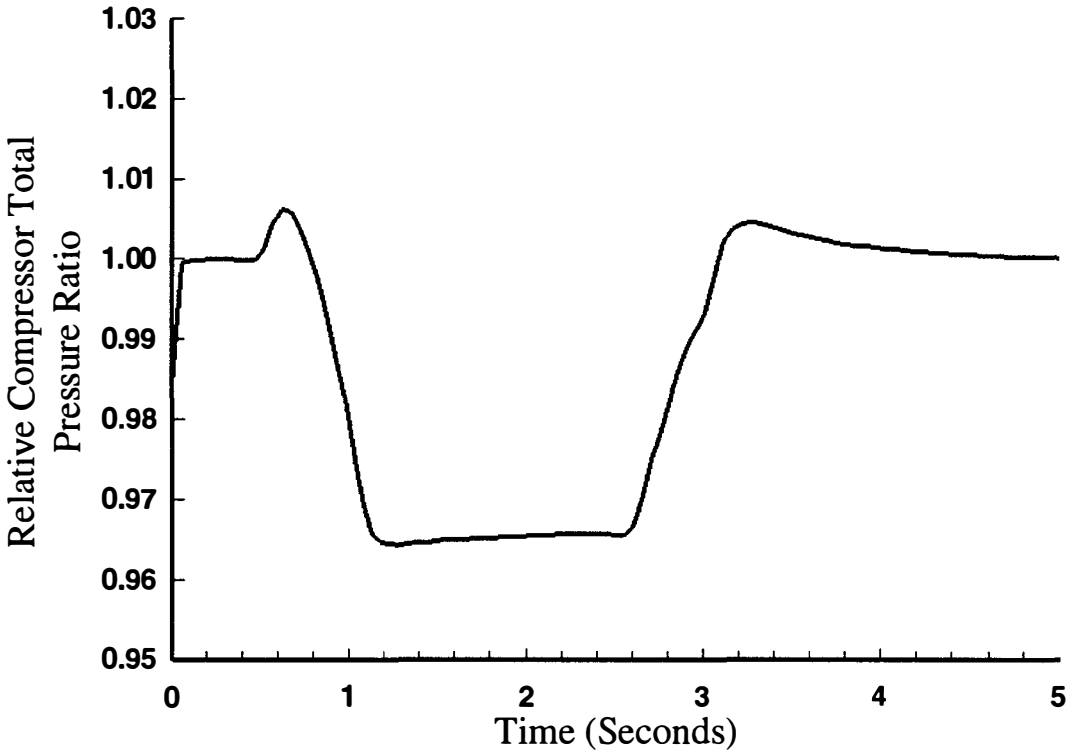

Figure 90. Relative Compressor Total Pressure Ratio as a Function of Time with the Heat Transfer Model Activated for the Heat Transfer Model Operational Verification Test Case.

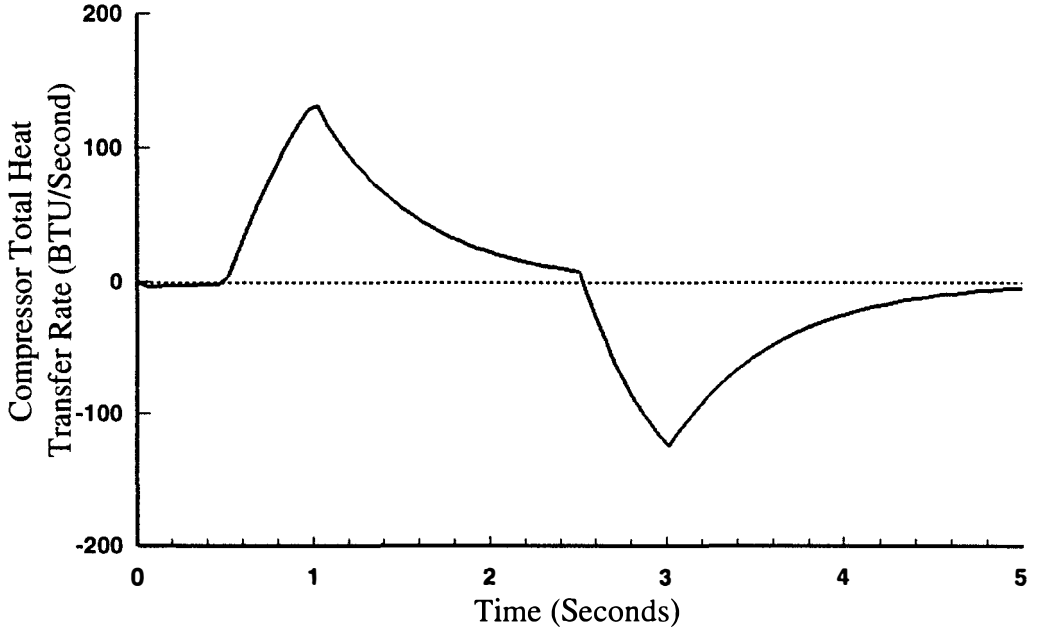

Figure 91. Compressor Total Heat Transfer Rate as a Function of Time for the Heat Transfer Model Operational Verification Test Case.

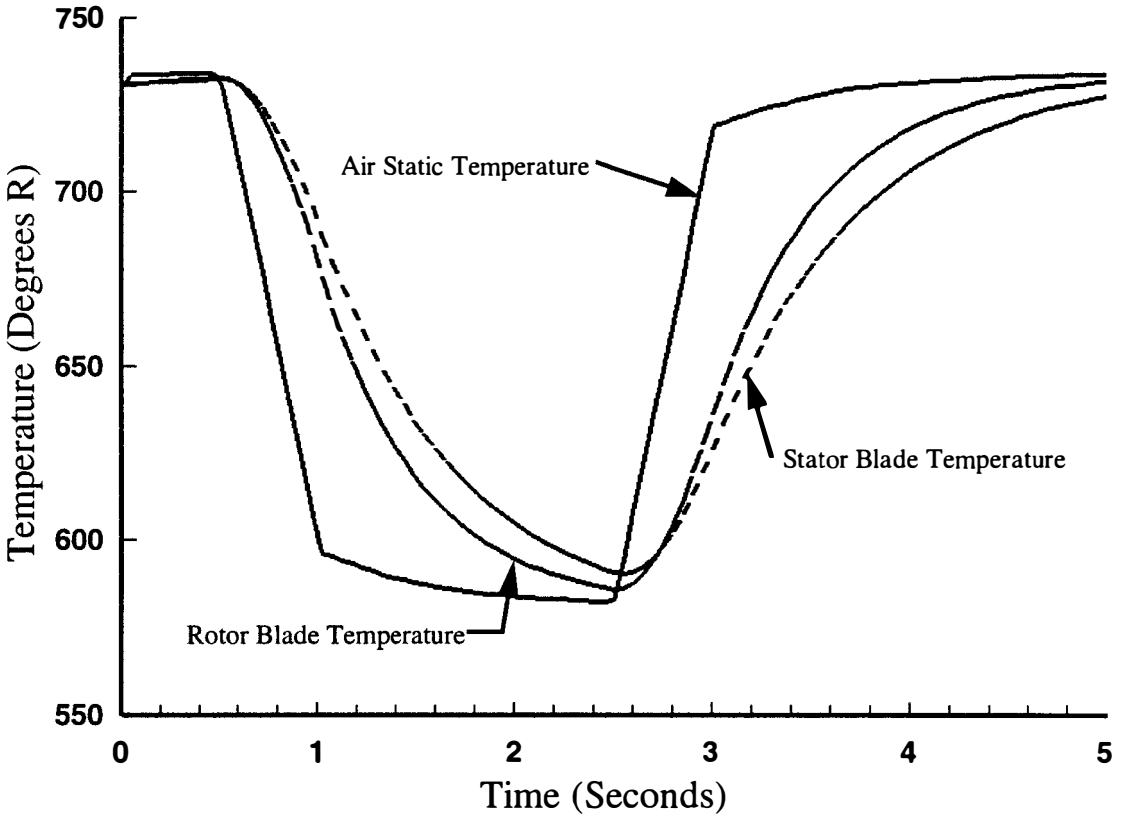

Figure 92. Air and Metal Temperatures in the Seventh Stage of the T55-L-712 Engine as a Function of Time for the Heat Transfer Model Operational Verification Test Case.

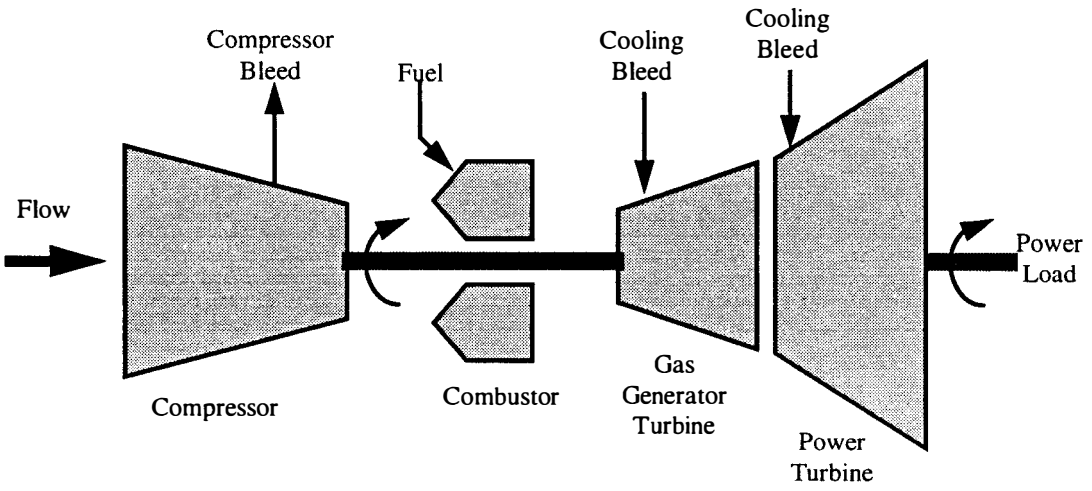

Figure 93. Component Representation of T55-L-712 Engine as used by the Advanced Turbine Engine Simulation Technique (ATEST) Model and Simulation.

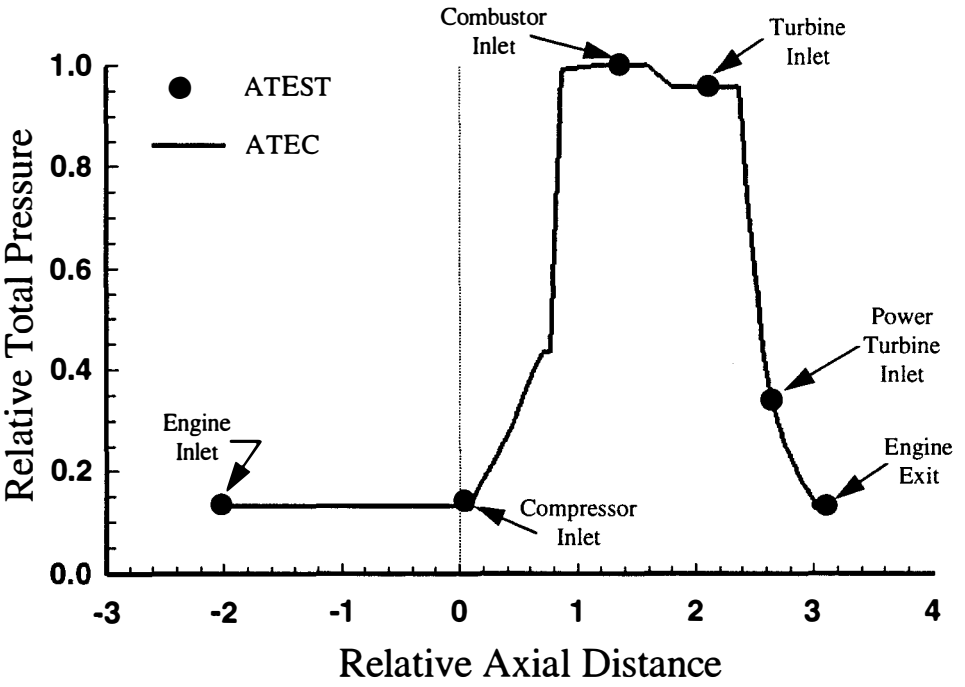

Figure 94. Steady-State Calibration of ATEC to ATEST Results Showing Relative Total Pressure as a Function of Relative Axial Distance inside the T55-L-712 Engine for the Sixty Five Degree Power Request Throttle Angle Test Case.

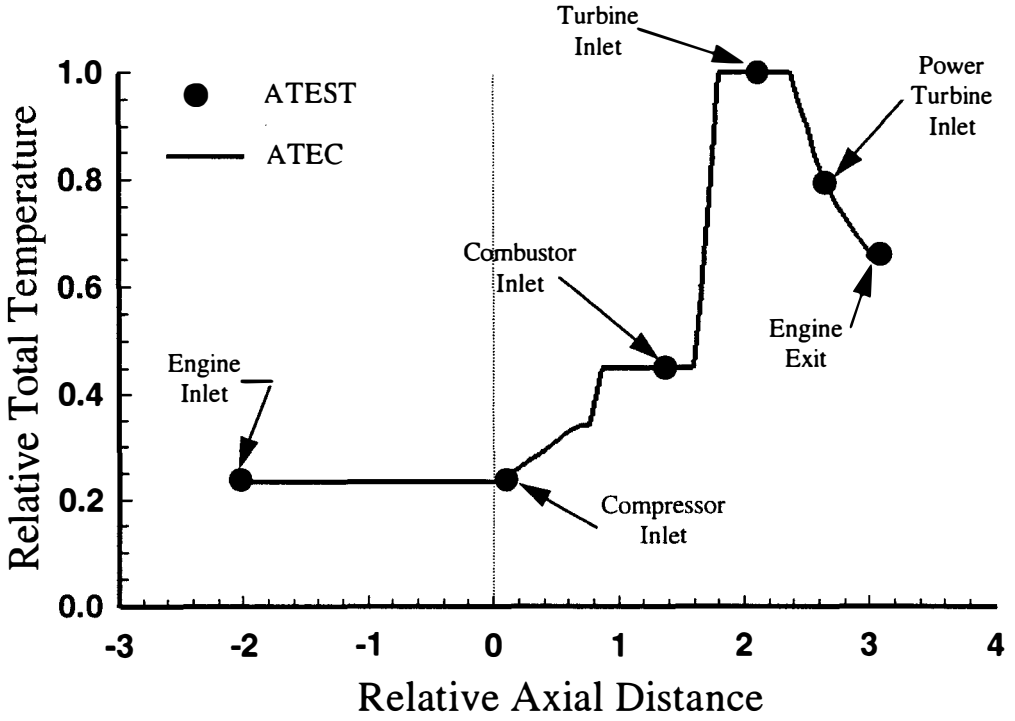

Figure 95. Steady-State Calibration of ATEC to ATEST Results Showing Relative Total Temperature as a Function of Relative Axial Distance inside the T55-L-712 Engine for the Sixty Five Degree Power Request Throttle Angle Test Case.

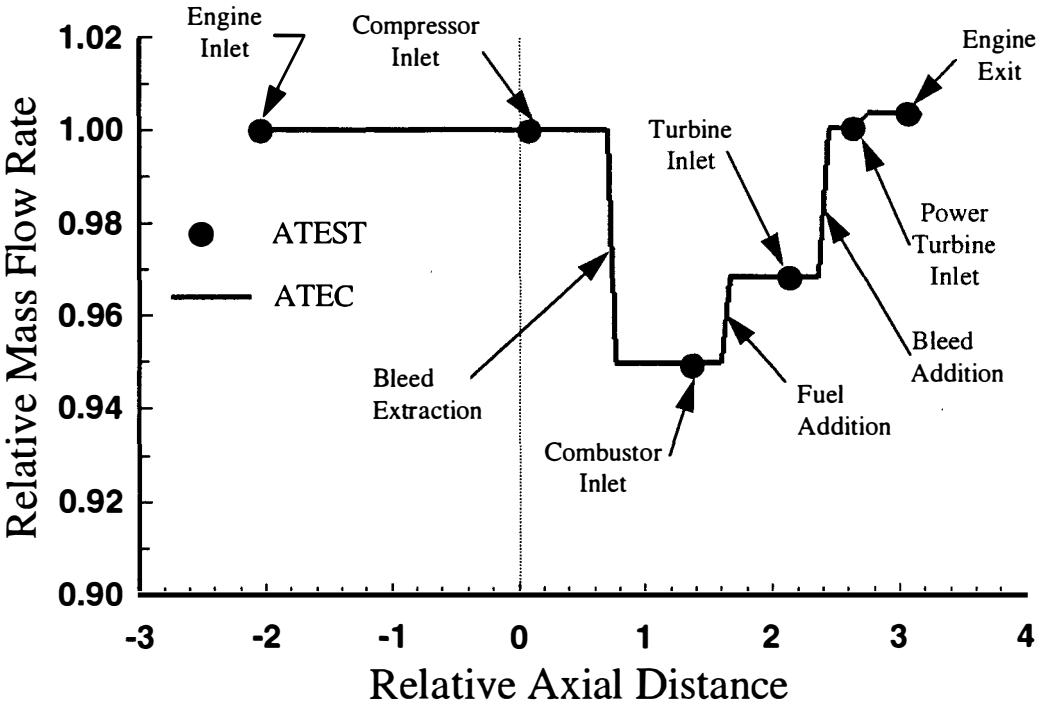

Figure 96. Steady-State Calibration of ATEC to ATEST Results Showing Relative Mass Flow Rate as a Function of Relative Axial Distance inside the T55-L-712 Engine for the Sixty Five Degree Power Request Throttle Angle Test Case.

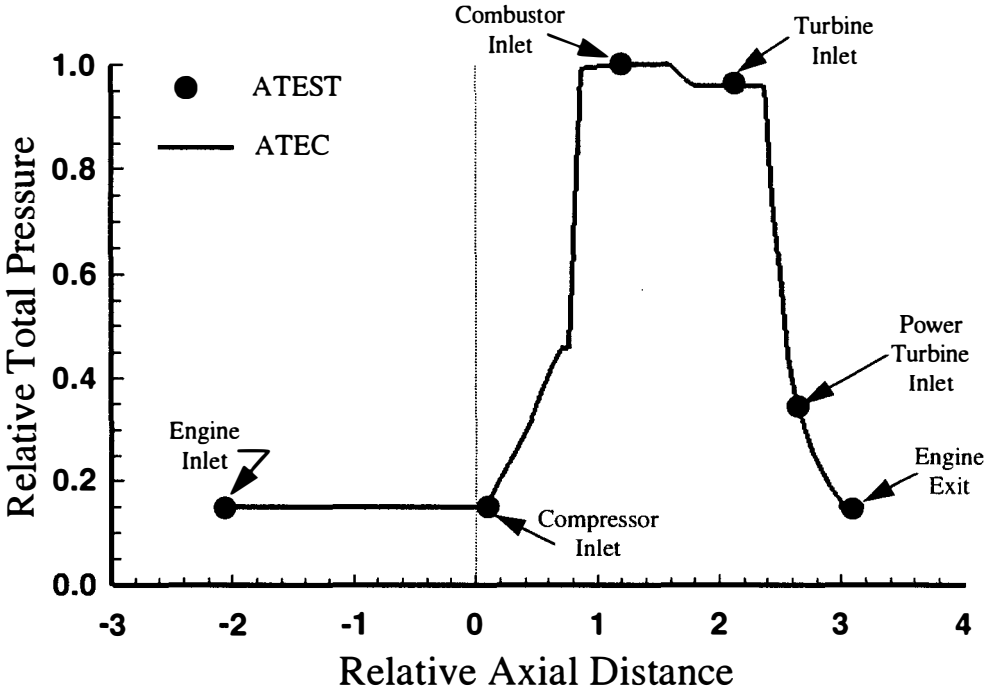

Figure 97. Steady-State Calibration of ATEC to ATEST Results Showing Relative Total Pressure as a Function of Relative Axial Distance inside the T55-L-712 Engine for the Sixty Degree Power Request Throttle Angle Test Case.

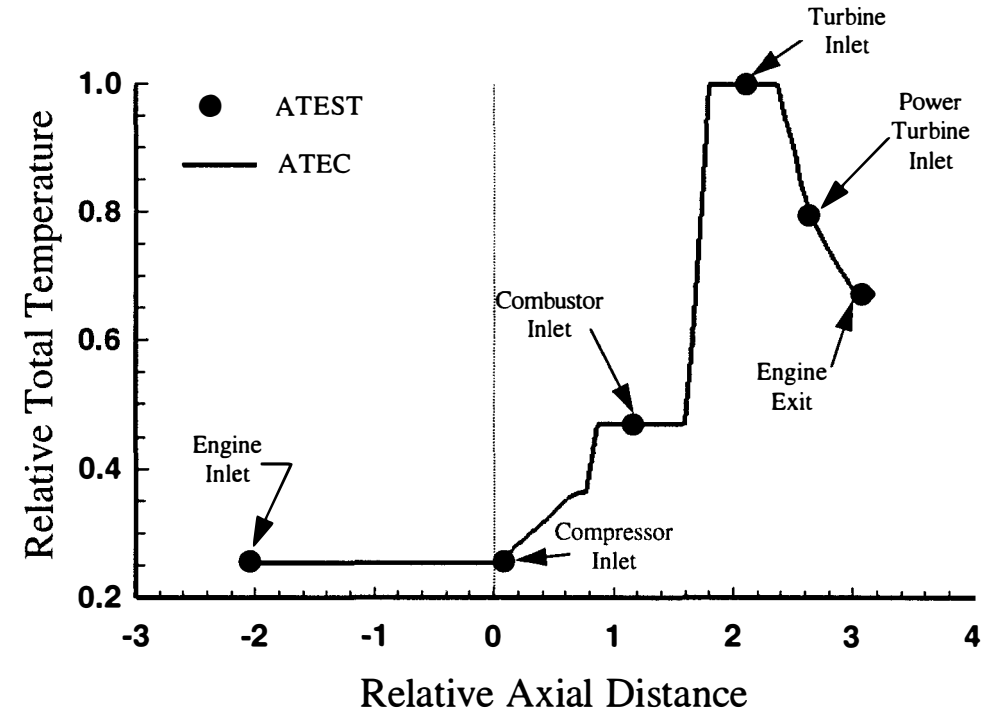

Figure 98. Steady-State Calibration of ATEC to ATEST Results Showing Relative Total Temperature as a Function of Relative Axial Distance inside the T55-L-712 Engine for the Sixty Degree Power Request Throttle Angle Test Case.

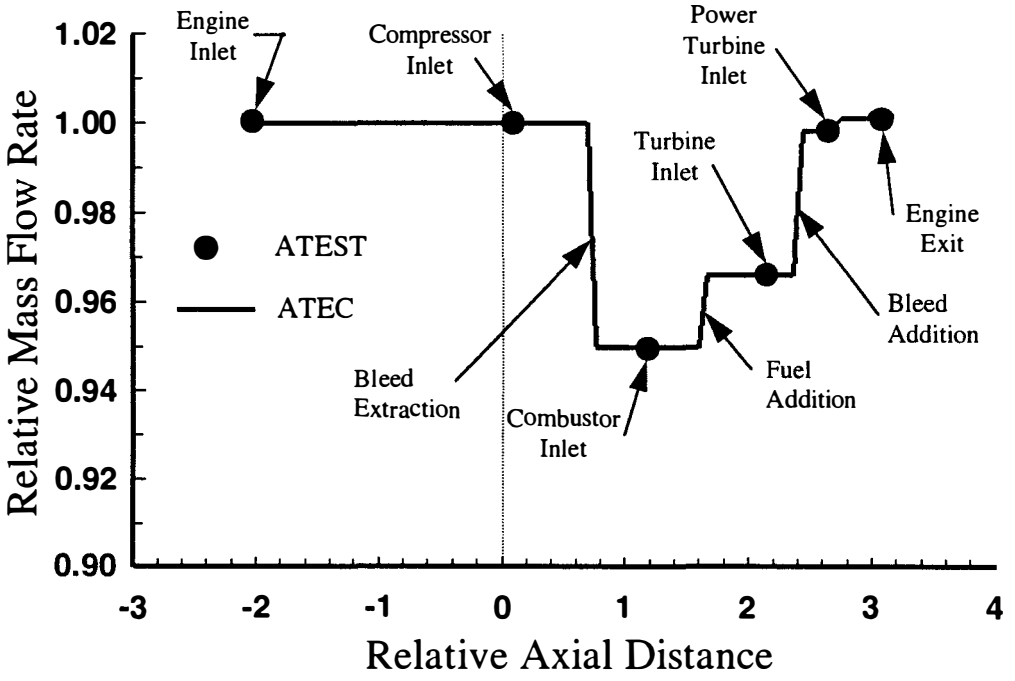

Figure 99. Steady-State Calibration of ATEC to ATEST Results Showing Relative Mass Flow Rate as a Function of Relative Axial Distance inside the T55-L-712 Engine for the Sixty Five Degree Power Request Throttle Angle Test Case.

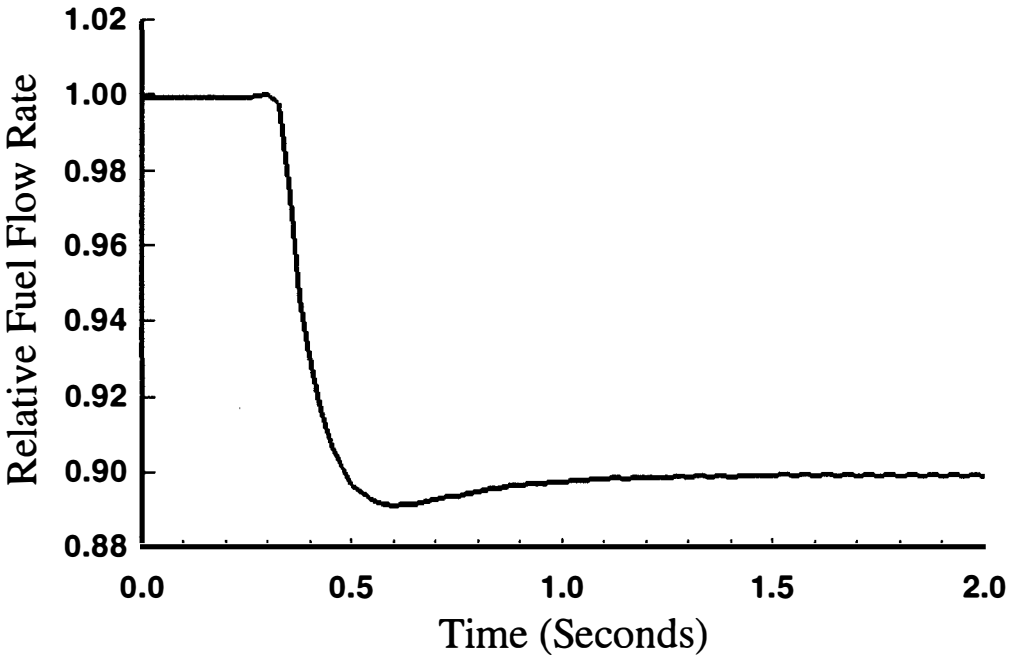

Figure 100. Relative Fuel Flow Rate as a Function of Time Provided to the T55-L-712 Combustor in the ATEST Model and Simulation for the Sixty Five Degree Power Request Throttle Angle Transient Deceleration Test Case.

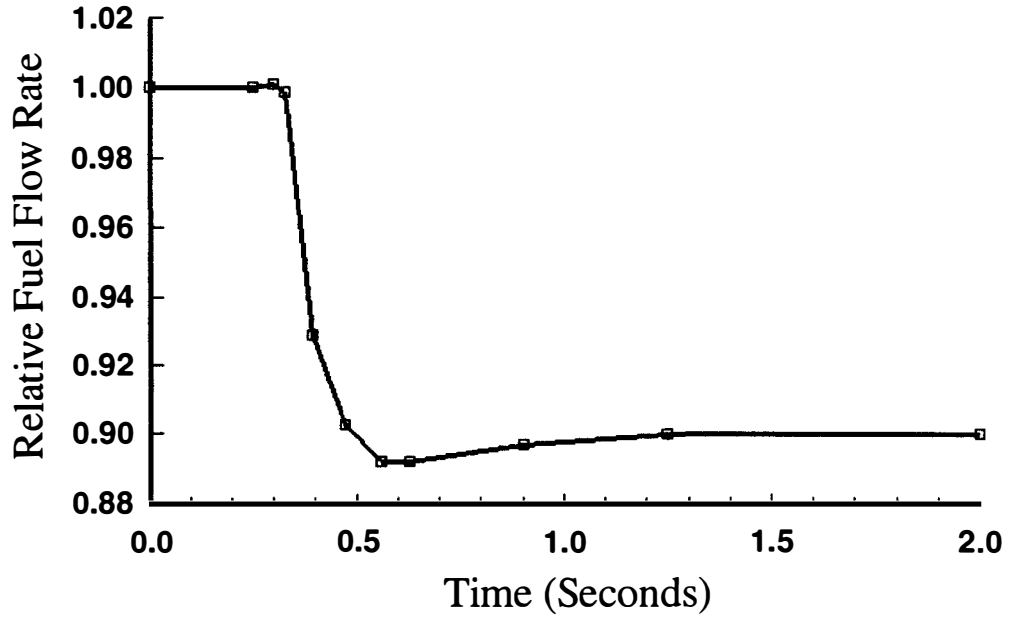

Figure 101. Straight Line Segment Representation of the Relative Fuel Flow Rate as a Function of Time Provided to the T55-L-712 Combustor in the ATEC Model and Simulation for the Sixty Five Degree Power Request Throttle Angle Transient Deceleration Test Case.

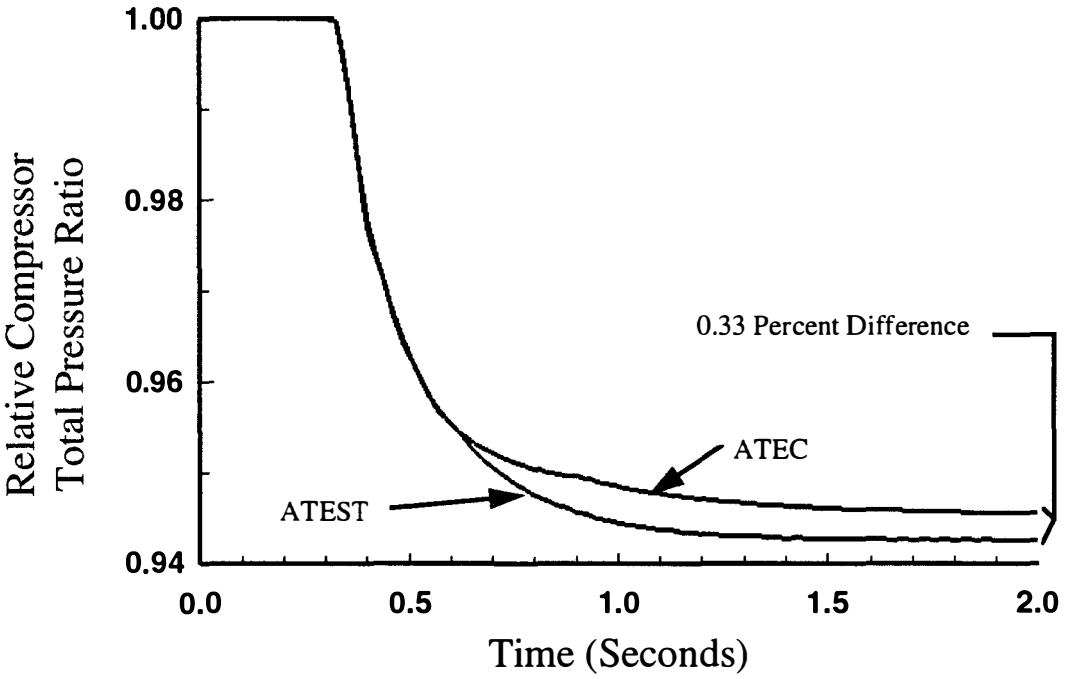

Figure 102. Comparison of ATEST and ATEC Relative Compressor Total Pressure Ratios as a Function of Time for the Sixty Five Degree Power Request Throttle Angle Transient Deceleration Test Case.

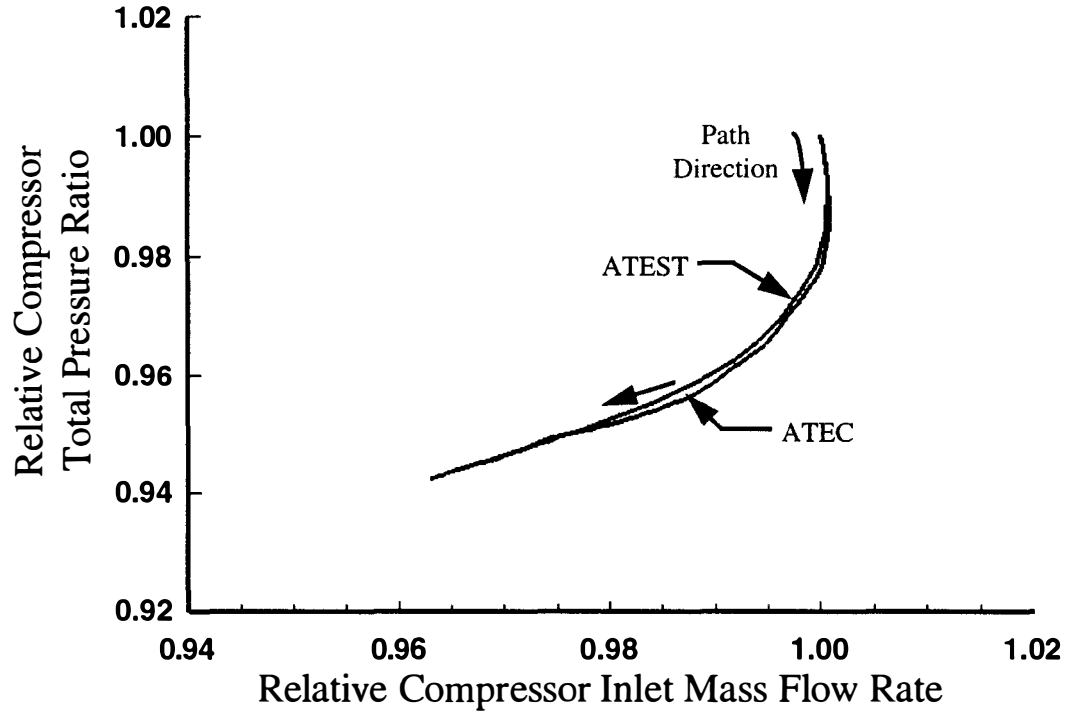

Figure 103. Comparison of ATEST and ATEC Relative Compressor Total Pressure Ratios as a Function of Relative Compressor Inlet Mass Flow Rate for the Sixty Five Degree Power Request Throttle Angle Transient Deceleration Test Case.

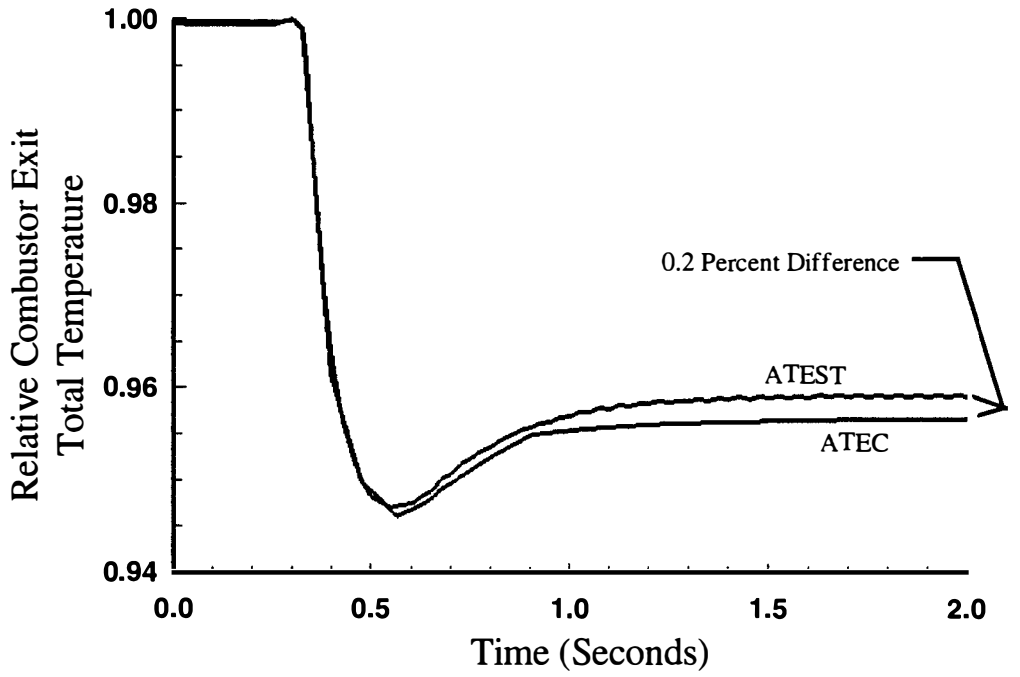

Figure 104. Comparison of ATEST and ATEC Relative Combustor Exit Total Temperature as a Function of Time for the Sixty Five Degree Power Request Throttle Angle Transient Deceleration Test Case.

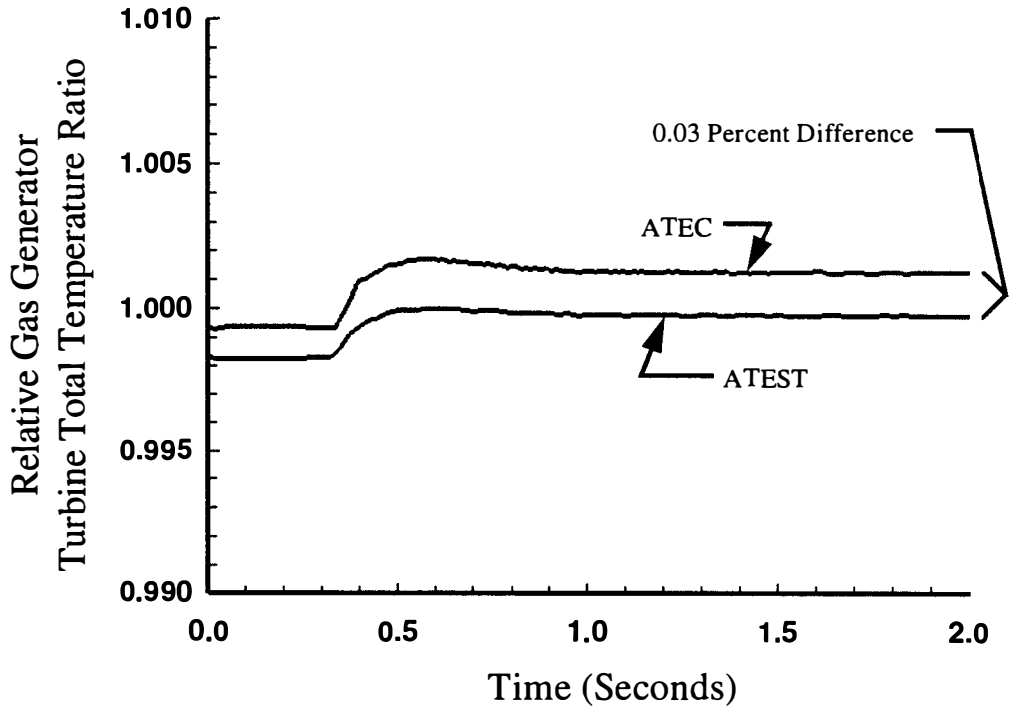

Figure 105. Comparison of ATEST and ATEC Relative Gas Generator Turbine Total Temperature Ratio as a Function of Time for the Sixty Five Degree Power Request Throttle Angle Transient Deceleration Test Case.

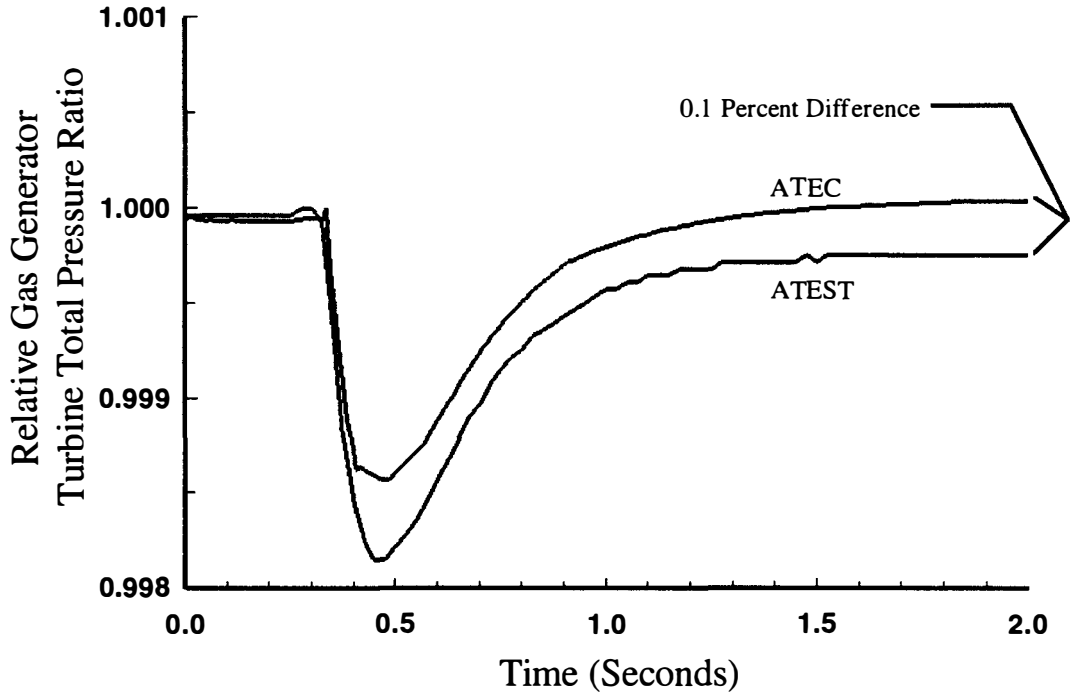

Figure 106. Comparison of ATEST and ATEC Relative Gas Generator Turbine Total Pressure Ratio as a Function of Time for the Sixty Five Degree Power Request Throttle Angle Transient Deceleration Test Case.

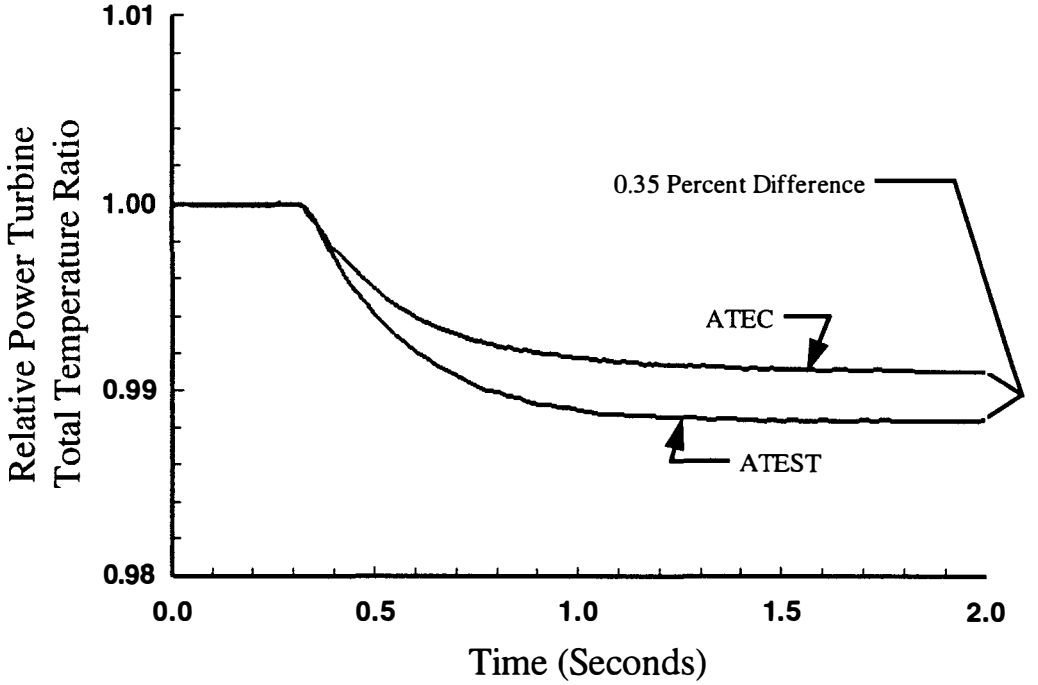

Figure 107. Comparison of ATEST and ATEC Relative Power TurbineTotal Temperature Ratio as a Function of Time for the Sixty Five Degree Power Request Throttle Angle Transient Deceleration Test Case.

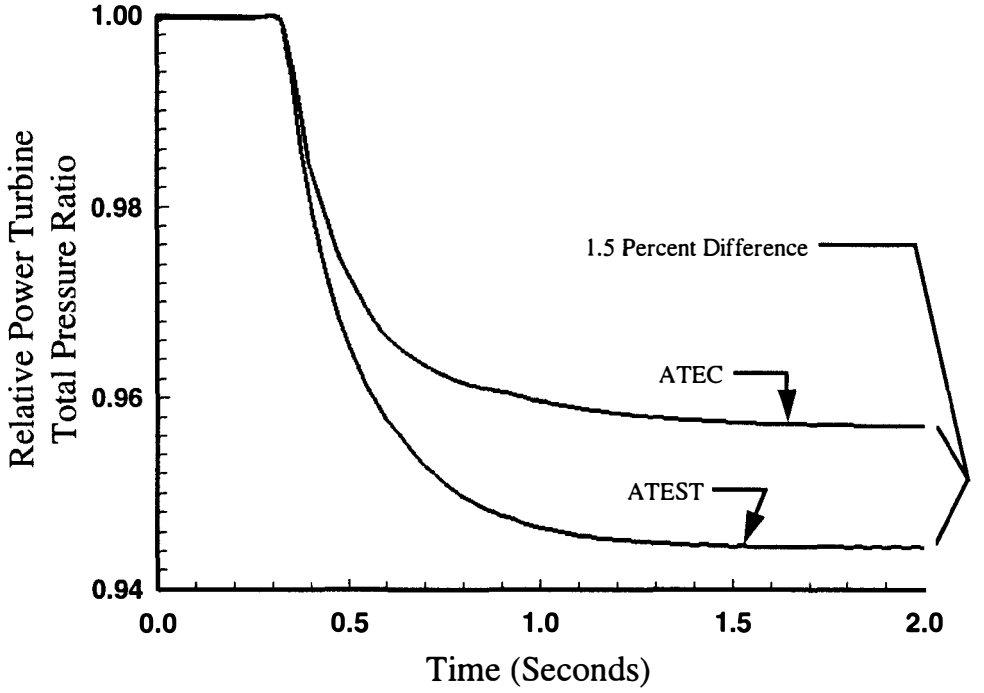

Figure 108. Comparison of ATEST and ATEC Relative Power TurbineTotal Pressure Ratio as a Function of Time for the Sixty Five Degree Power Request Throttle Angle Transient Deceleration Test Case.

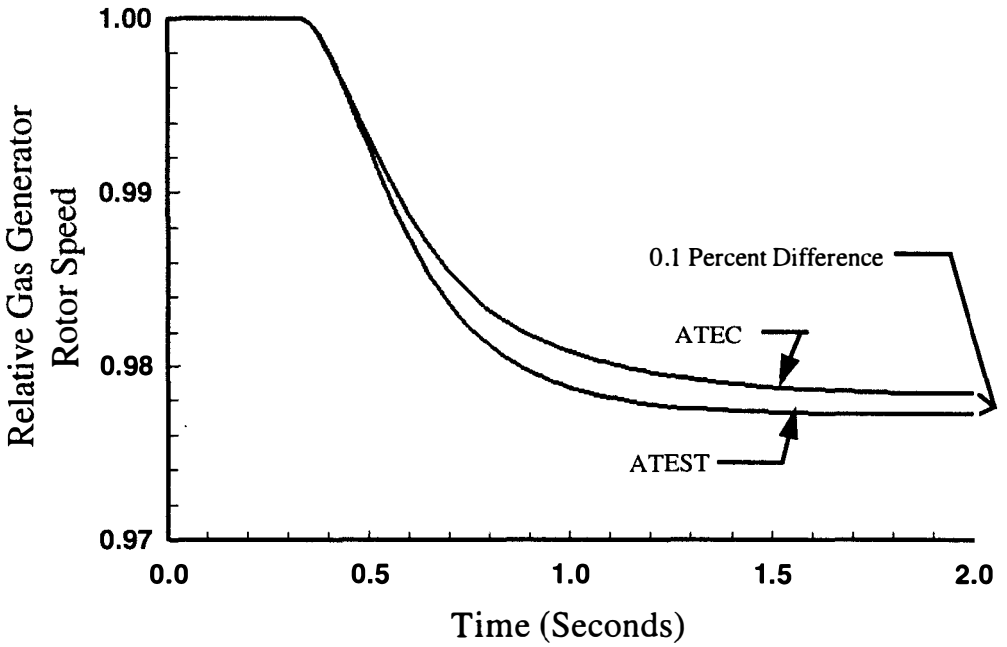

Figure 109. Comparison of ATEST and ATEC Relative Gas Generator Rotor Speed as a Function of Time for the Sixty Five Degree Power Request Throttle Angle Transient Deceleration Test Case.

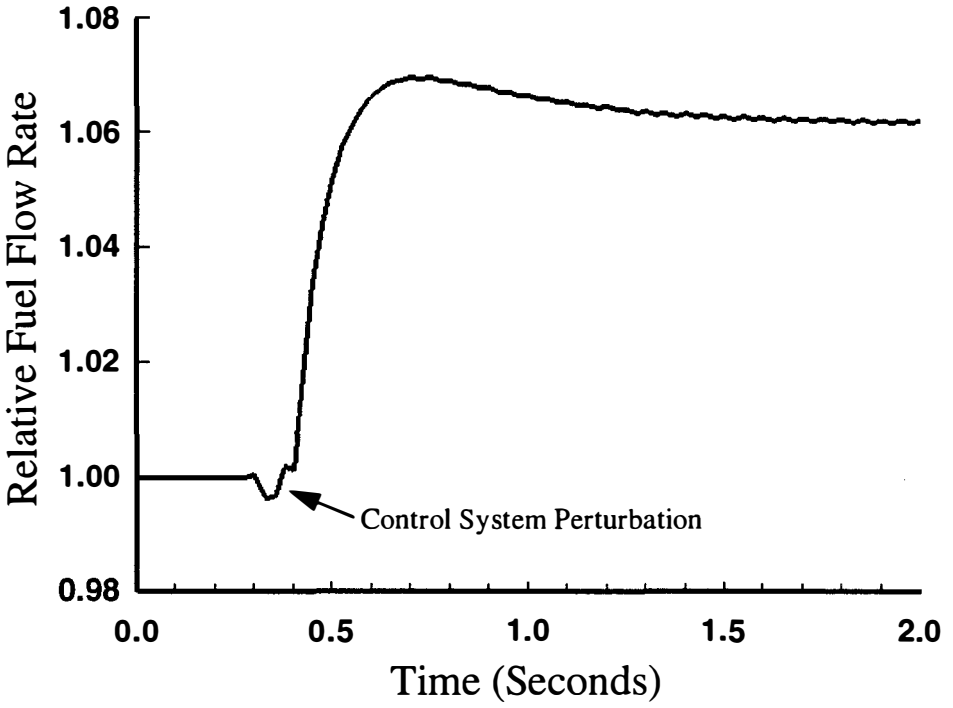

Figure 110. Relative Fuel Flow Rate as a Function of Time Provided to the T55-L-712 Combustor in the ATEST Model and Simulation for the Sixty Five Degree Power Request Throttle Angle Transient Acceleration Test Case.

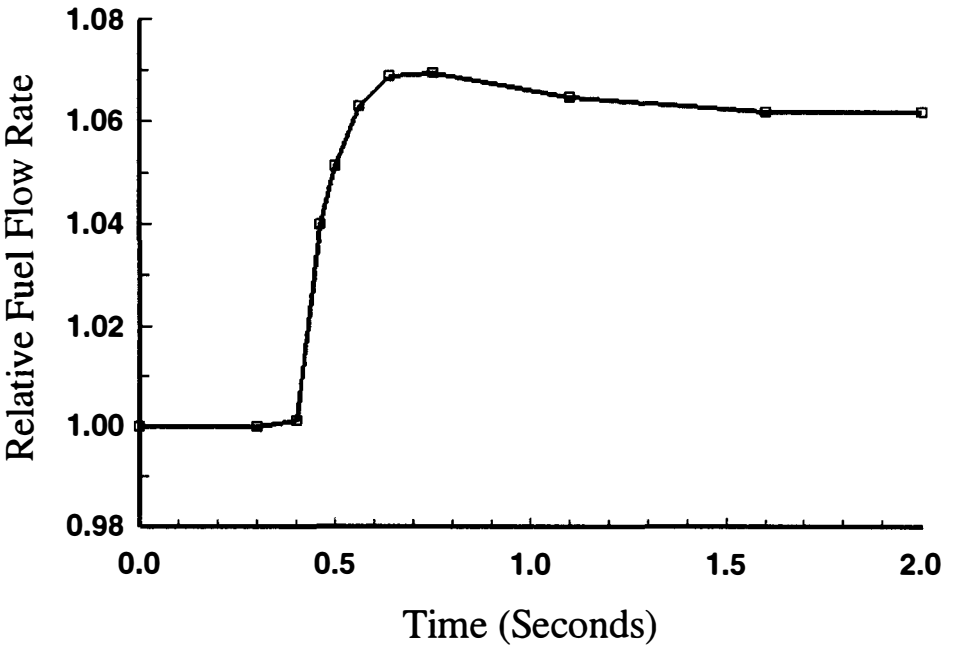

Figure 111. Straight Line Segment Representation of the Relative Fuel Flow Rate as a Function of Time Provided to the T55-L-712 Combustor in the ATEC Model and Simulation for the Sixty Five Degree Power Request Throttle Angle Transient Acceleration Test Case.

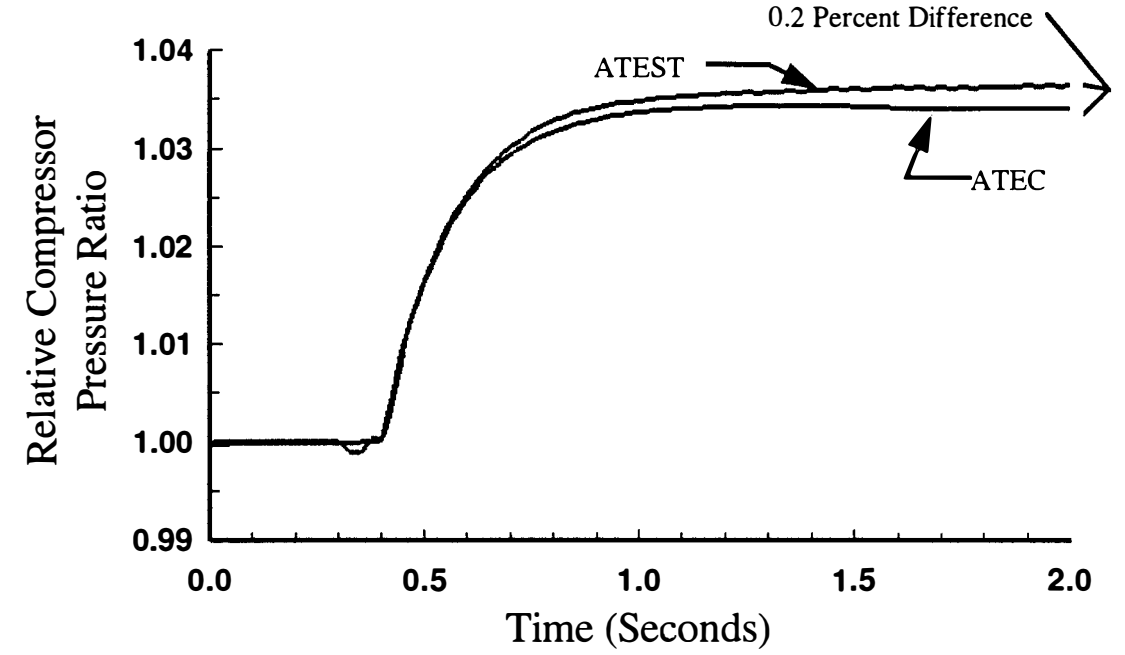

Figure 112. Comparison of ATEST and ATEC Relative Compressor Total Pressure Ratios as a Function of Time for the Sixty Five Degree Power Request Throttle Angle Transient Acceleration Test Case.

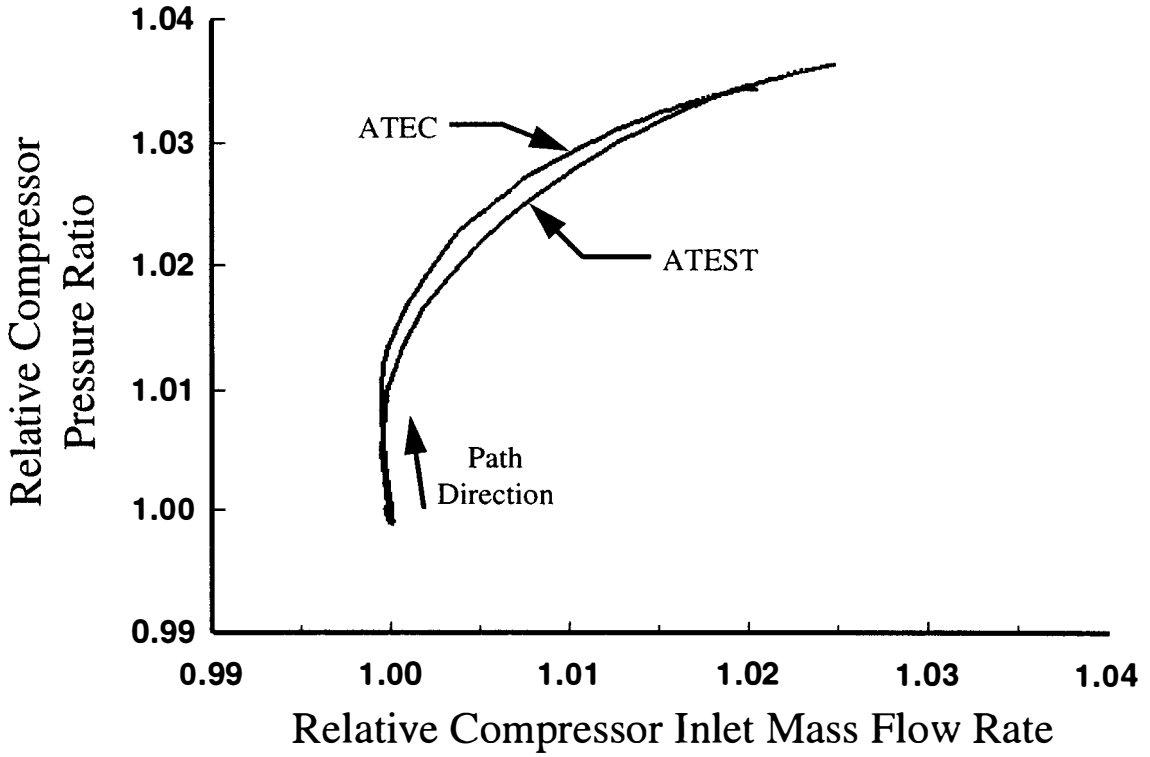

Figure 113. Comparison of ATEST and ATEC Relative Compressor Total Pressure Ratios as a Function of Relative Compressor Inlet Mass Flow Rate for the Sixty Five Degree Power Request Throttle Angle Transient Acceleration Test Case.

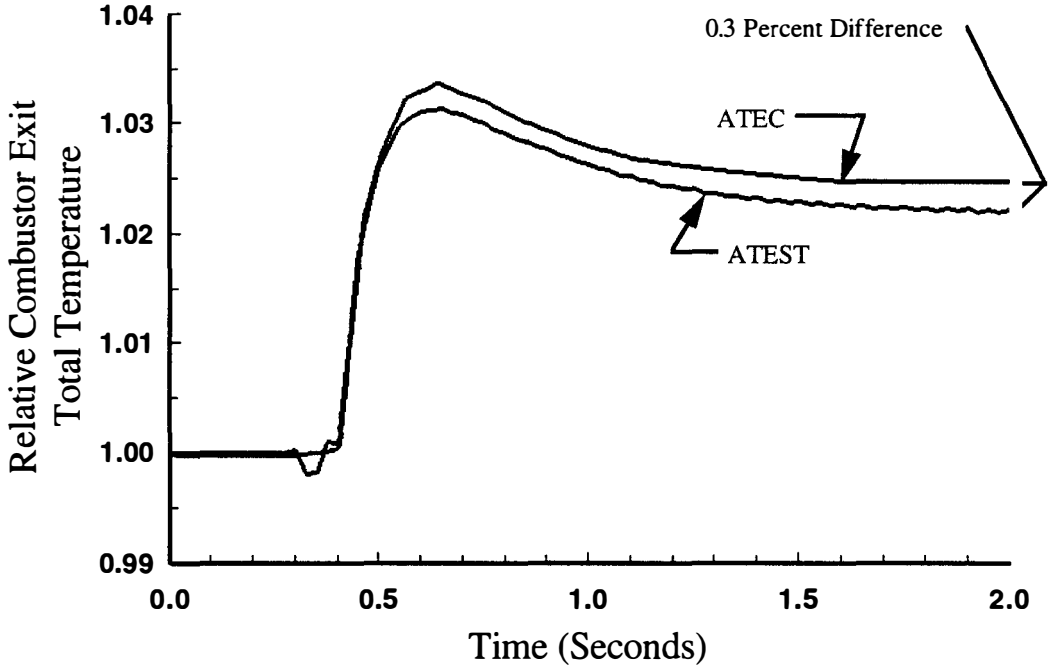

Figure 114. Comparison of ATEST and ATEC Relative Combustor Exit Total Temperature as a Function of Time for the Sixty Five Degree Power Request Throttle Angle Transient Acceleration Test Case.

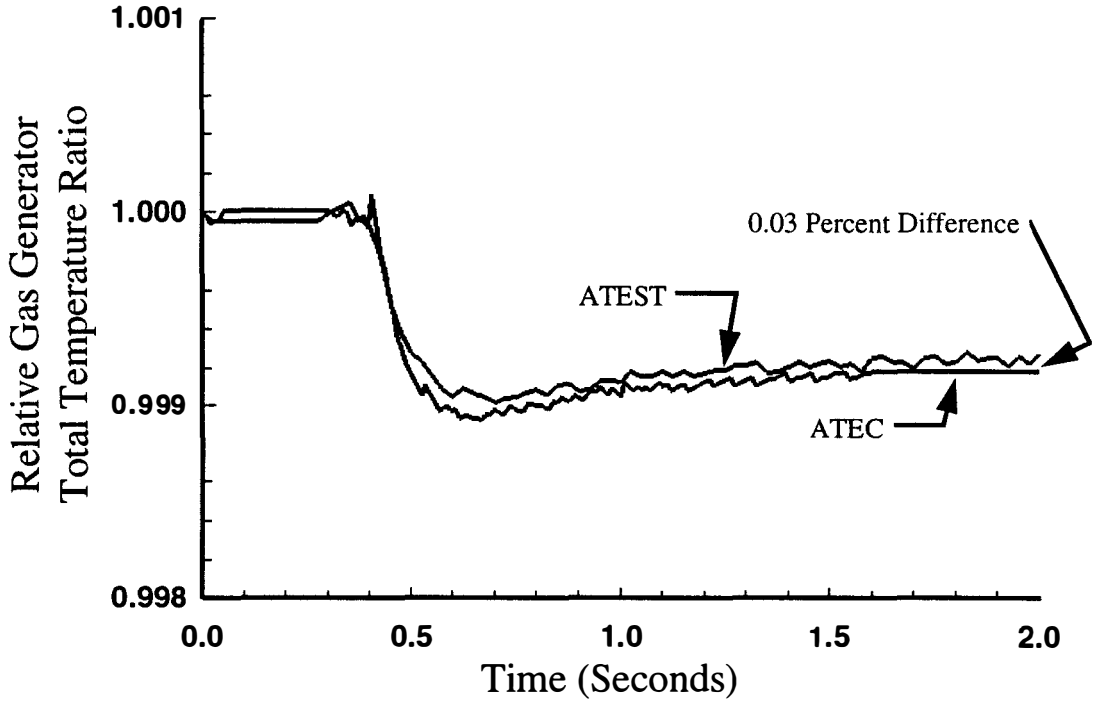

Figure 115. Comparison of ATEST and ATEC Relative Gas Generator Turbine Total Temperature Ratio as a Function of Time for the Sixty Five Degree Power Request Throttle Angle Transient Acceleration Test Case.

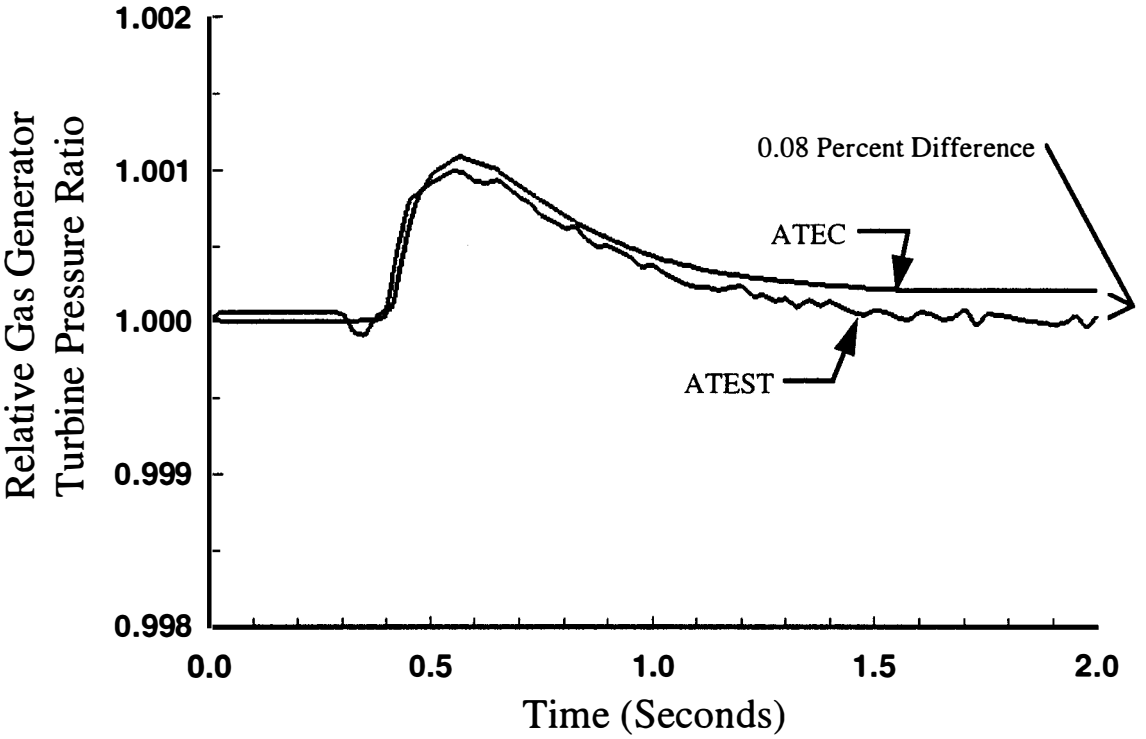

Figure 116. Comparison of ATEST and ATEC Relative Gas Generator Turbine Total Pressure Ratio as a Function of Time for the Sixty Five Degree Power Request Throttle Angle Transient Acceleration Test Case.

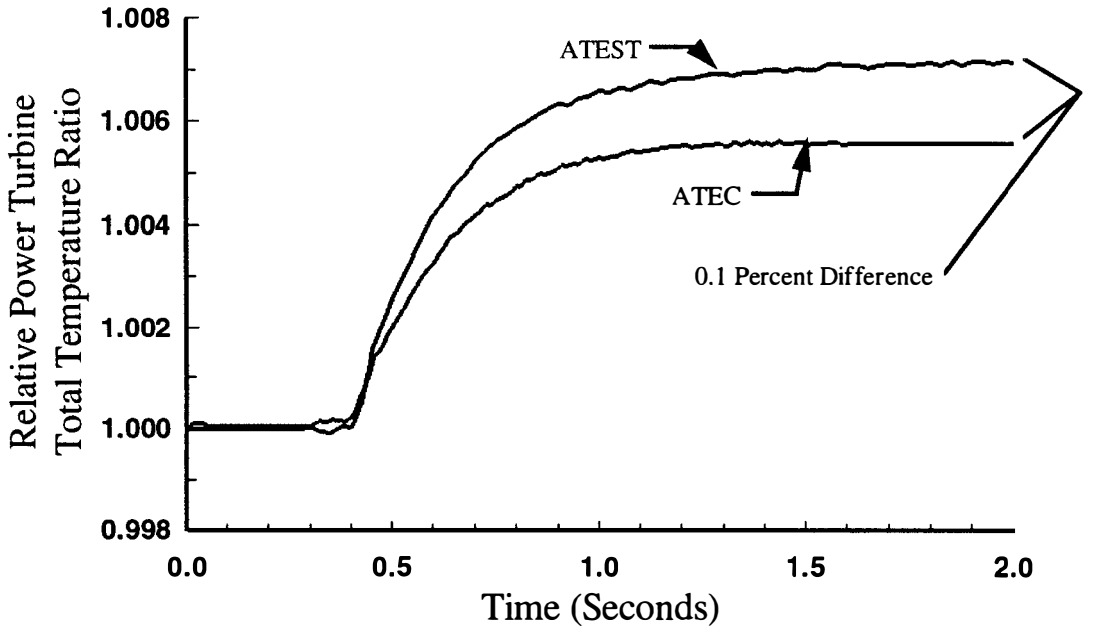

Figure 117. Comparison of ATEST and ATEC Relative Power TurbineTotal Temperature Ratio as a Function of Time for the Sixty Five Degree Power Request Throttle Angle Transient Acceleration Test Case.

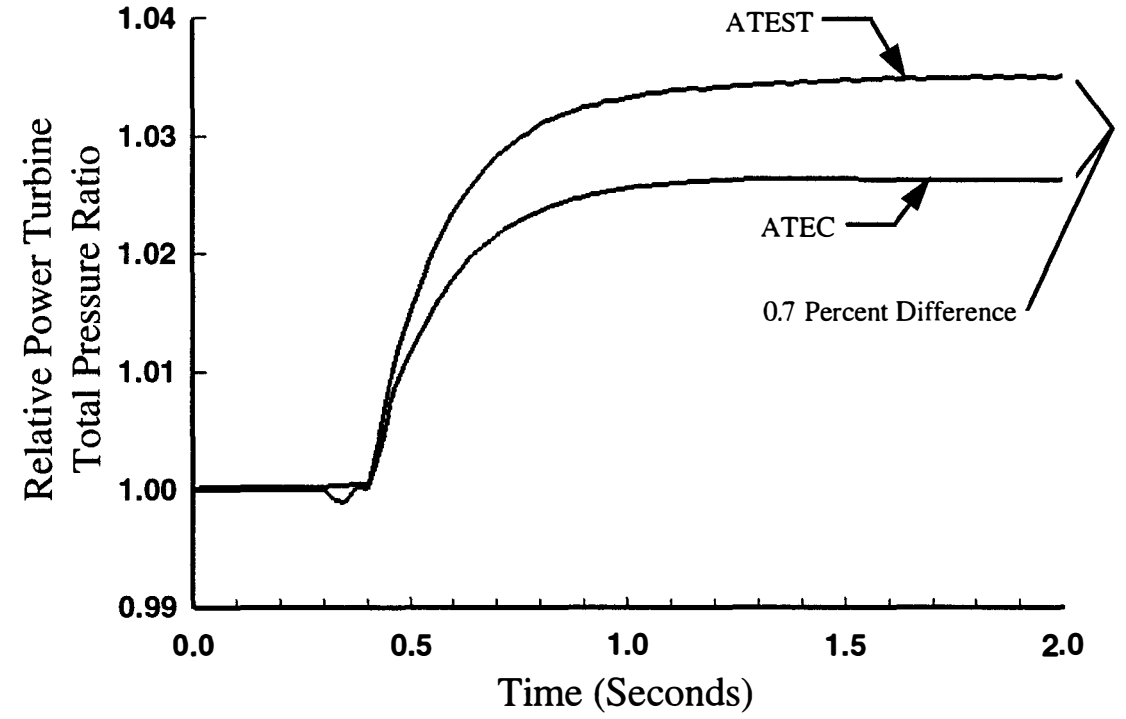

Figure 118. Comparison of ATEST and ATEC Relative Power TurbineTotal Pressure Ratio as a Function of Time for the Sixty Five Degree Power Request Throttle Angle Transient Acceleration Test Case.

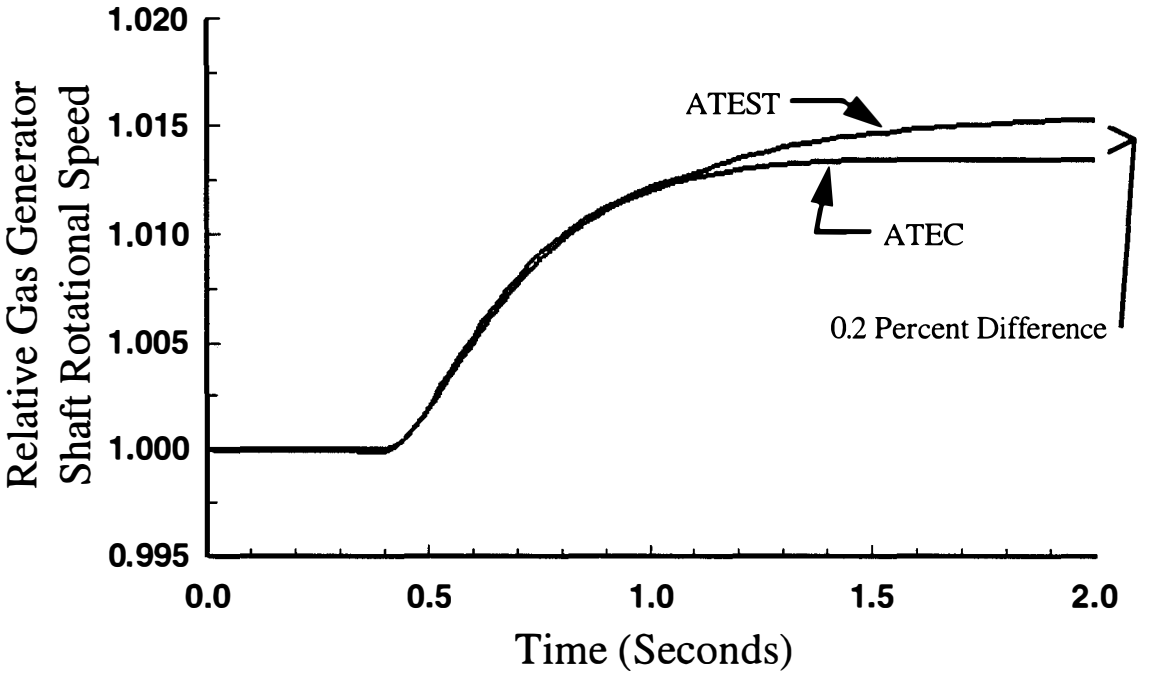

Figure 119. Comparison of ATEST and ATEC Relative Gas Generator Rotor Speed as a Function of Time for the Sixty Five Degree Power Request Throttle Angle Transient Acceleration Test Case.

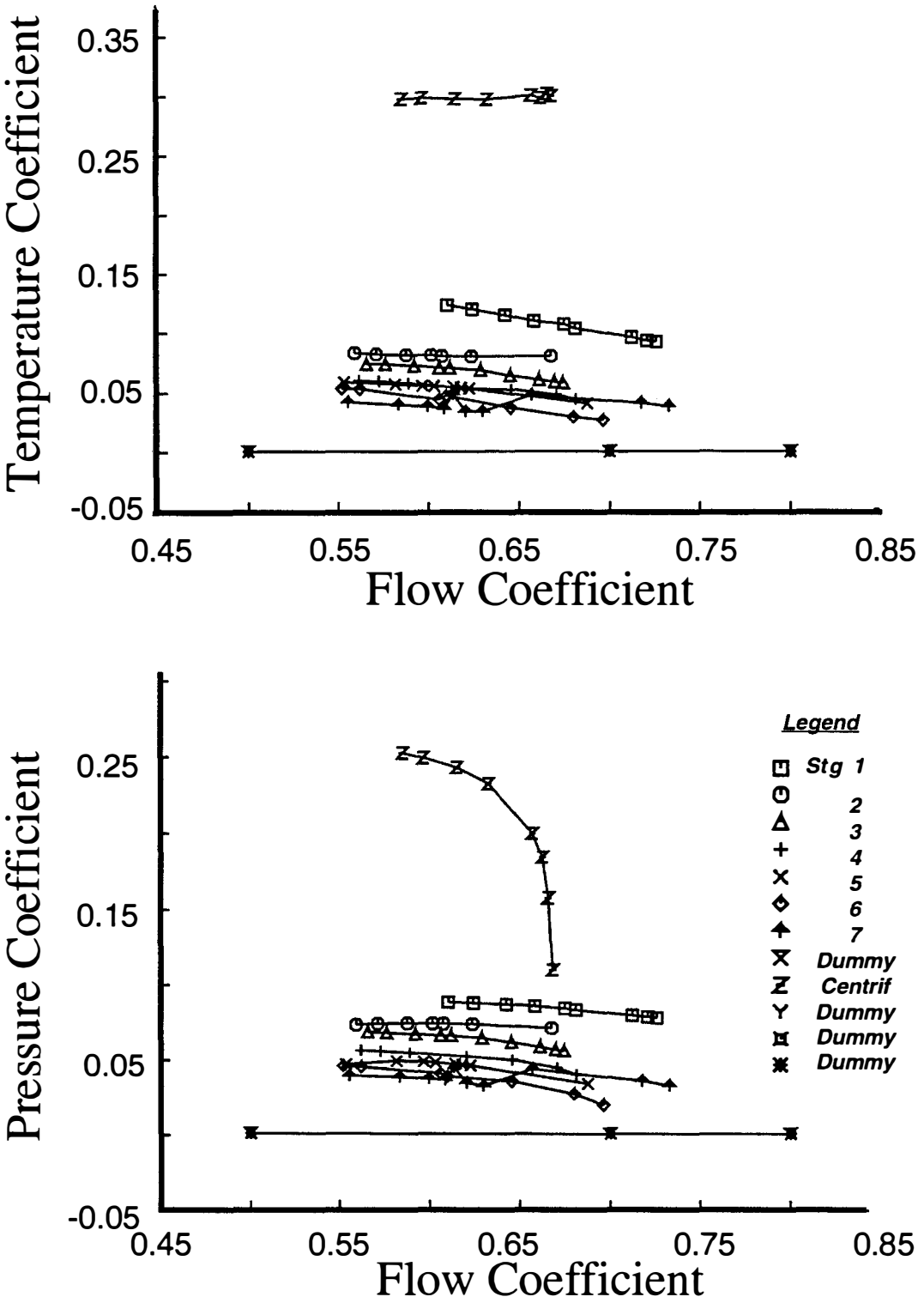

Figure 120. Steady-State, Pre-Stall Temperature and Pressure Stage Characteristics for the T55-L-712 Turobshaft Engine Compressor System Operating at 80 Percent Speed.

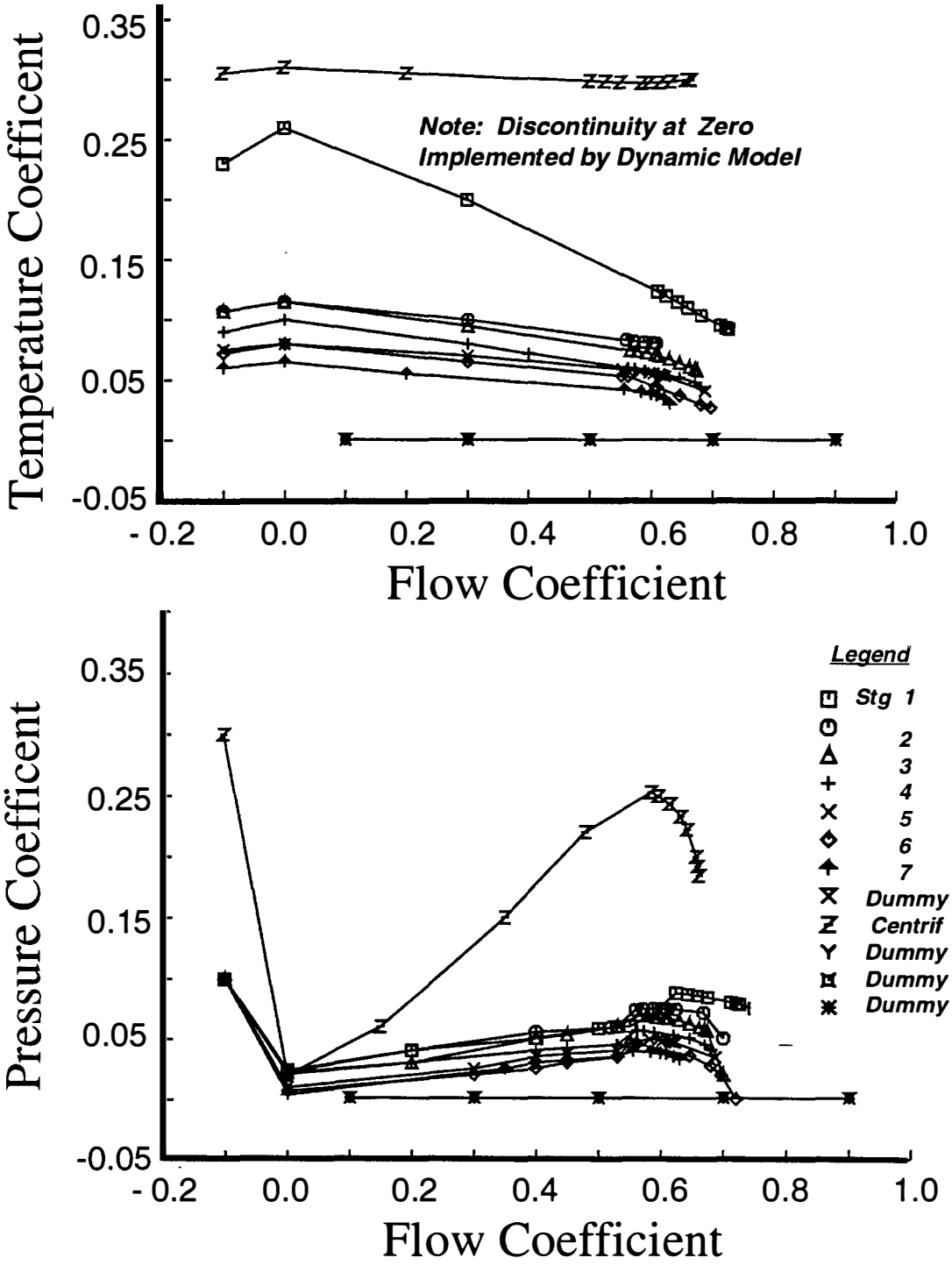

Figure 121. Post-Stall Temperature and Pressure Stage Characteristics for the T55-L-712 Turobshaft Engine Compressor System Operating at 80 Percent Speed.

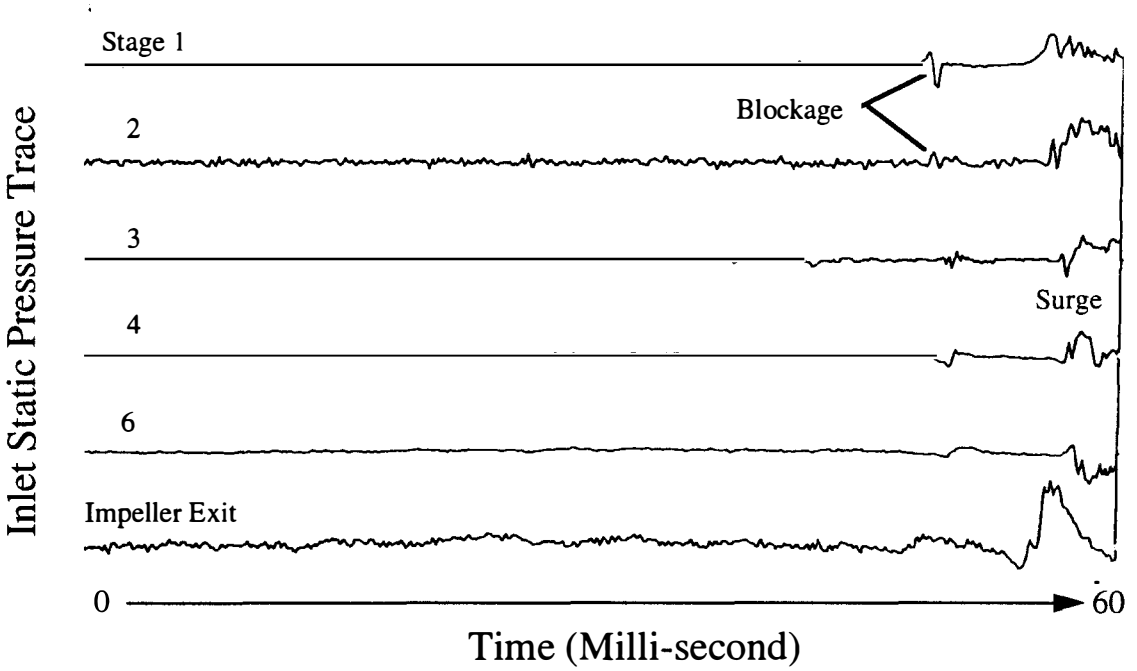

Figure 122. Inlet Static Pressure Traces for Various Stages of the T55-L-712 Turboshaft Engine Compression System Operating at 70 Percent Speed.

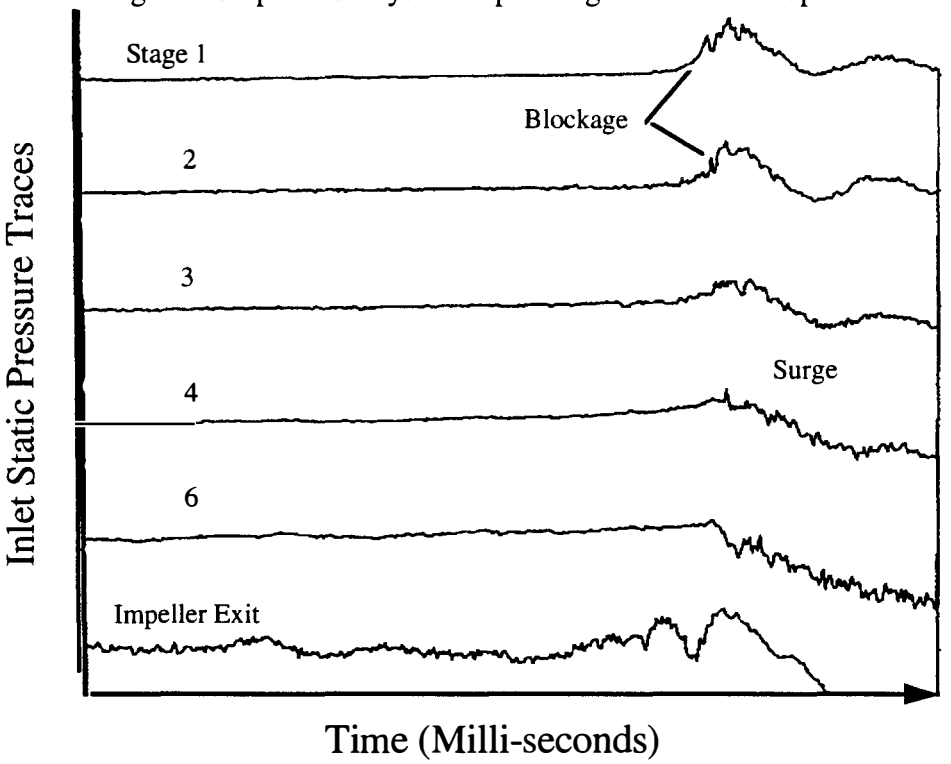

Figure 123. Inlet Static Pressure Traces for Various Stages of the T55-L-712 Turboshaft Engine Compression System Operating at 80 Percent Speed.

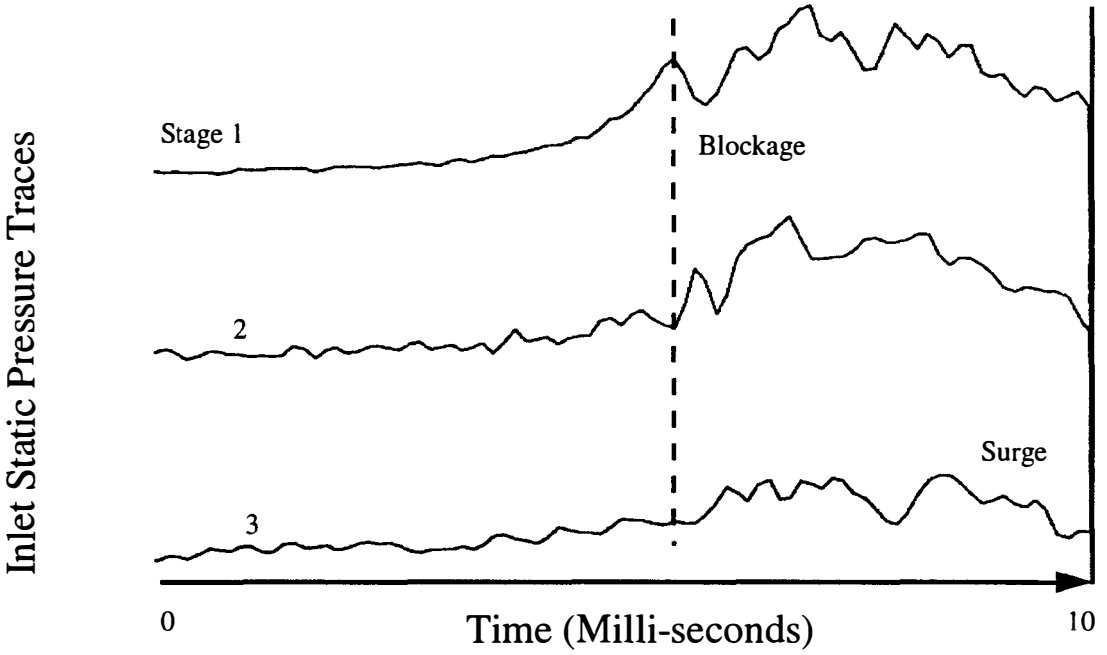

Figure 124. Inlet Static Pressure Traces for the First Three Stages of the T55-L-712 Turboshaft Engine Compression System Operating at 80 Percent Speed Near the Time of System Post-Stall Operation.

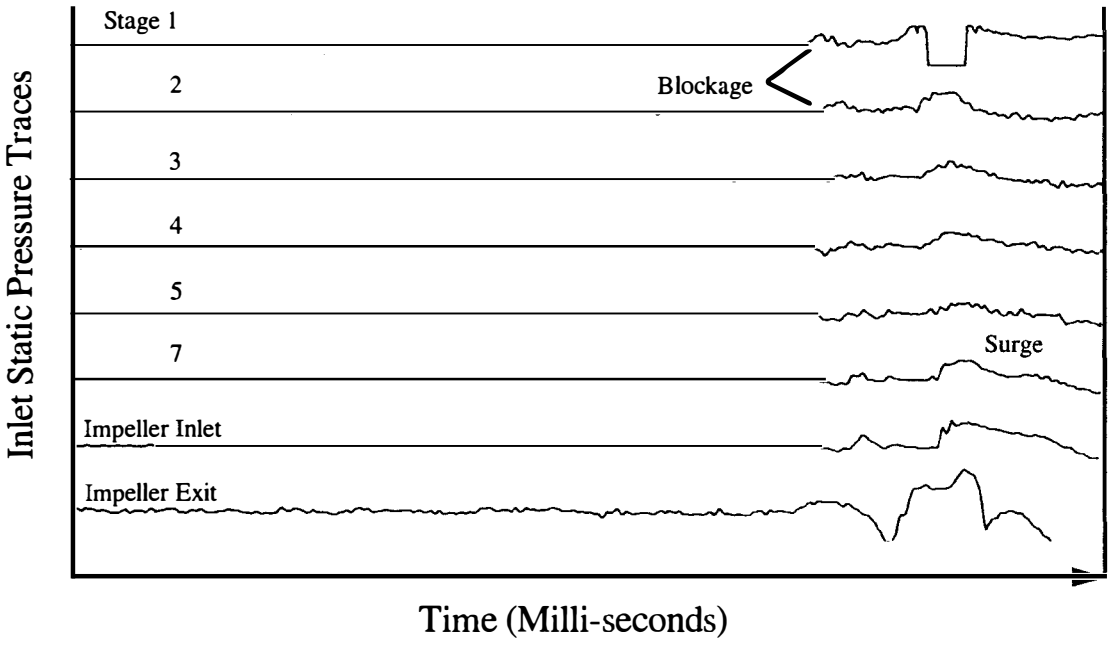

Figure 125. Inlet Static Pressure Traces for Various Stages of the T55-L-712 Turboshaft Engine Compression System Operating at 85 Percent Speed.

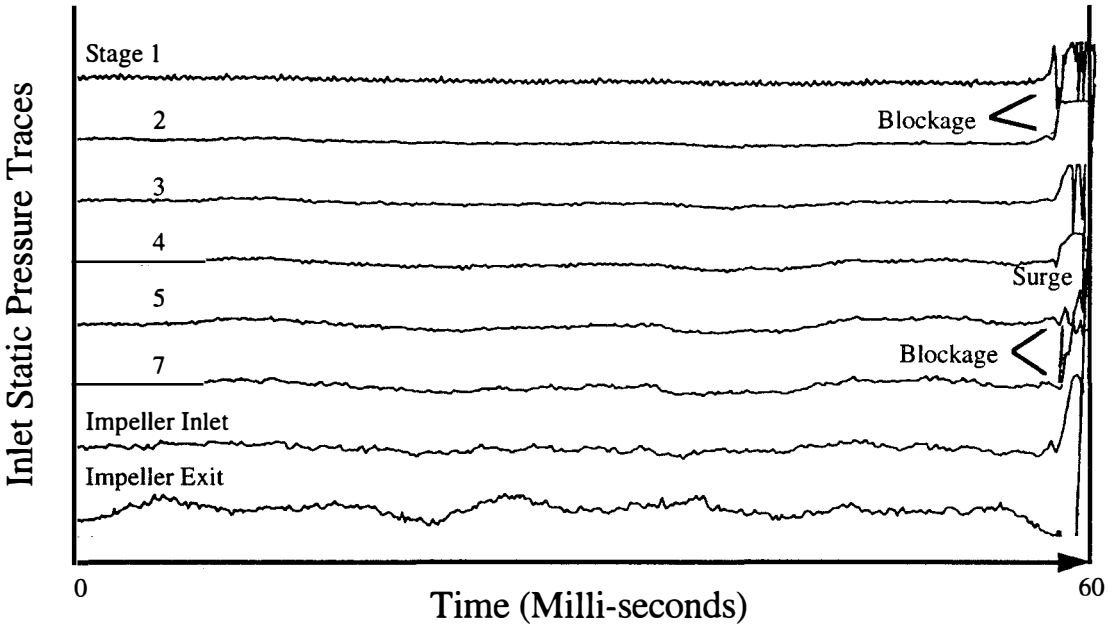

Figure 126. Inlet Static Pressure Traces for Various Stages of the T55-L-712 Turboshaft Engine Compression System Operating at 100 Percent Speed.

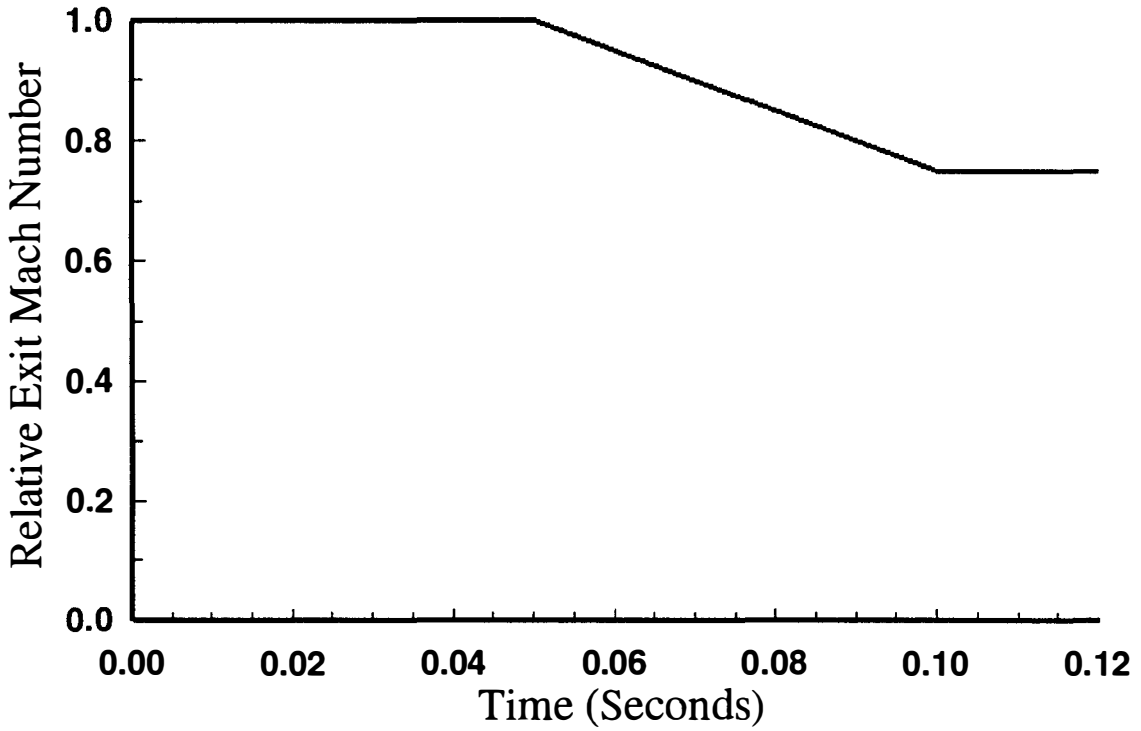

Figure 127. ATEC Relative Exit Mach Number Boundary Condition as a Function of Time for the Dynamic Calibration Critical Stage Analysis

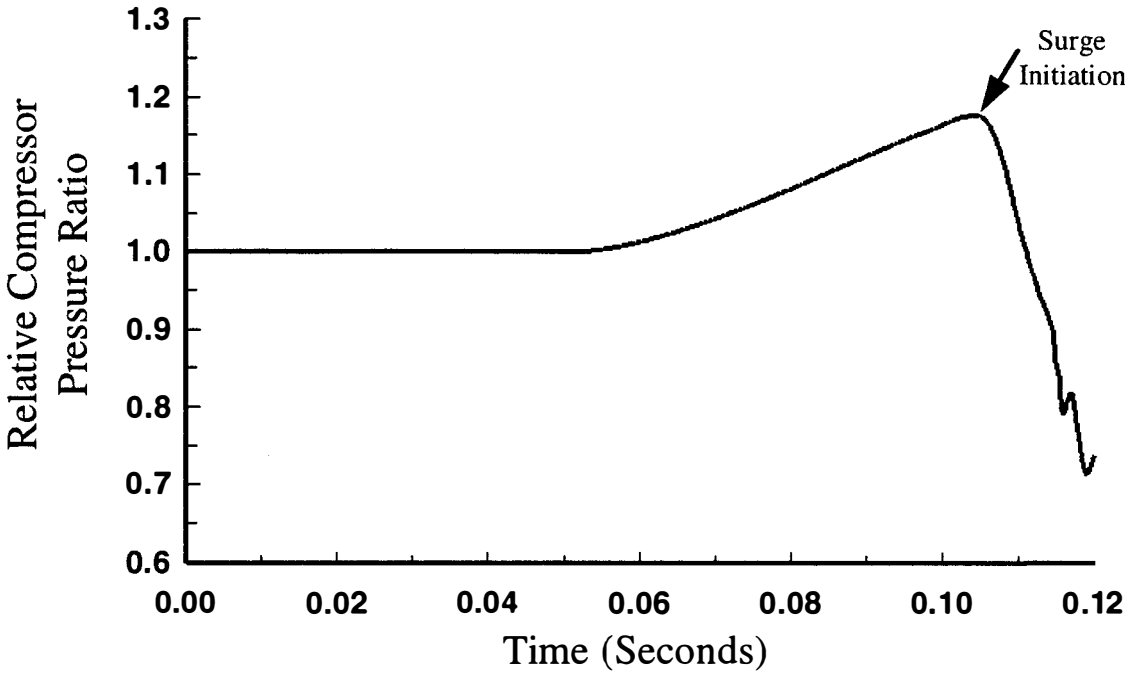

Figure 128. Relative Compressor Ratio as a Function of Time During the 80 Percent Speed Operation for the ATEC Dynamic Calibration.

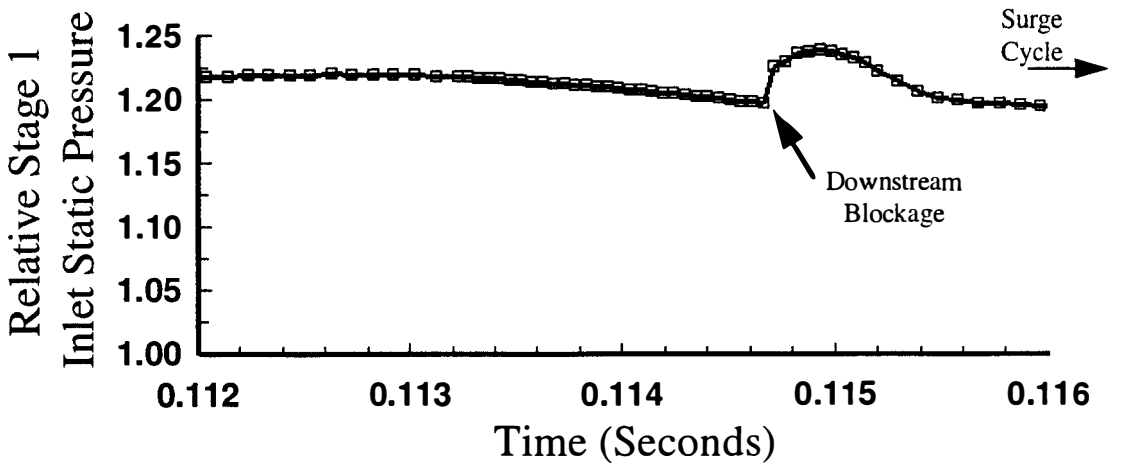

a. Relative Inlet Static Pressure for Stage 1

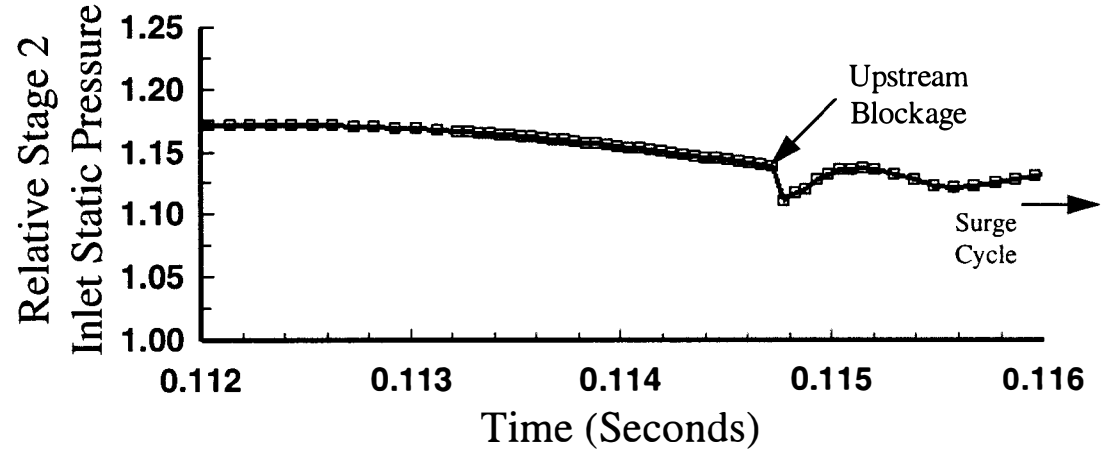

b. Relative Inlet Static Pressure for Stage 2

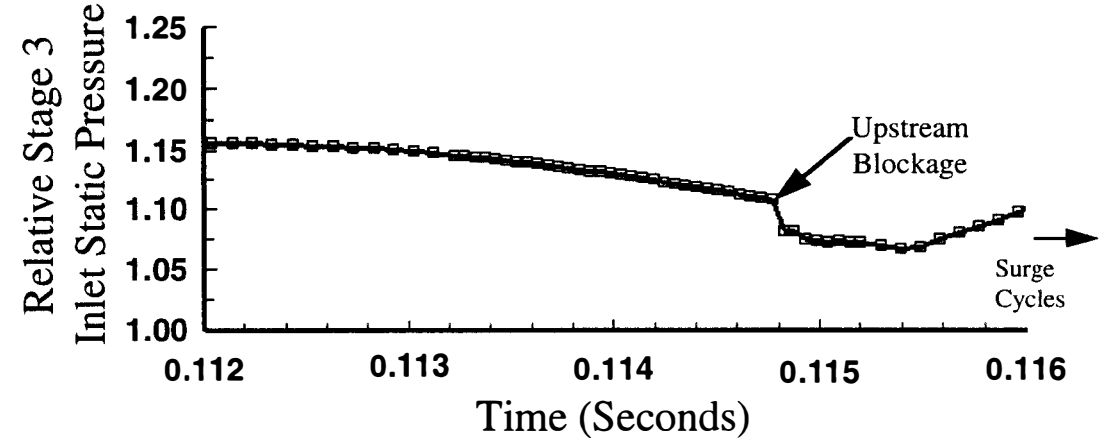

c. Relative Inlet Static Pressure for Stage 3

Figure 129. Relative Inlet Static Pressure for the First Three Stages of the T55-L-712 Compressor System Showing the Critical Stage Initiating the Surge Event During the ATEC Dynamic Calibration Test Case.

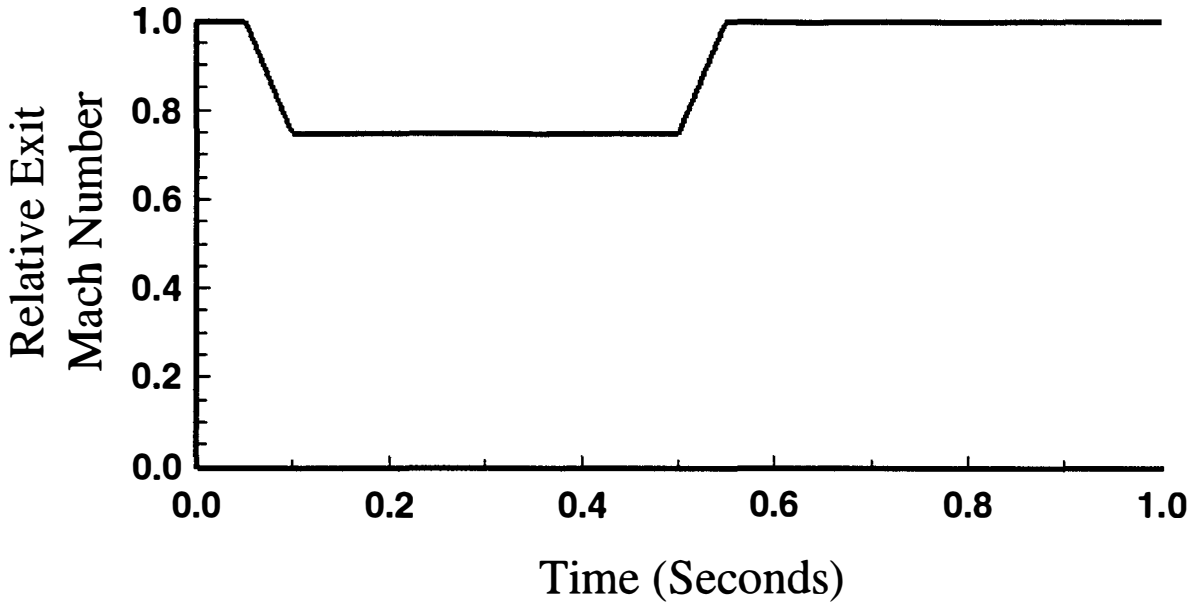

Figure 130. Relative Exit Mach Number Transient Used to Force the T55-L-712 Compression System into Post-Stall Operation During the ATEC Dynamic Calibration Test Case

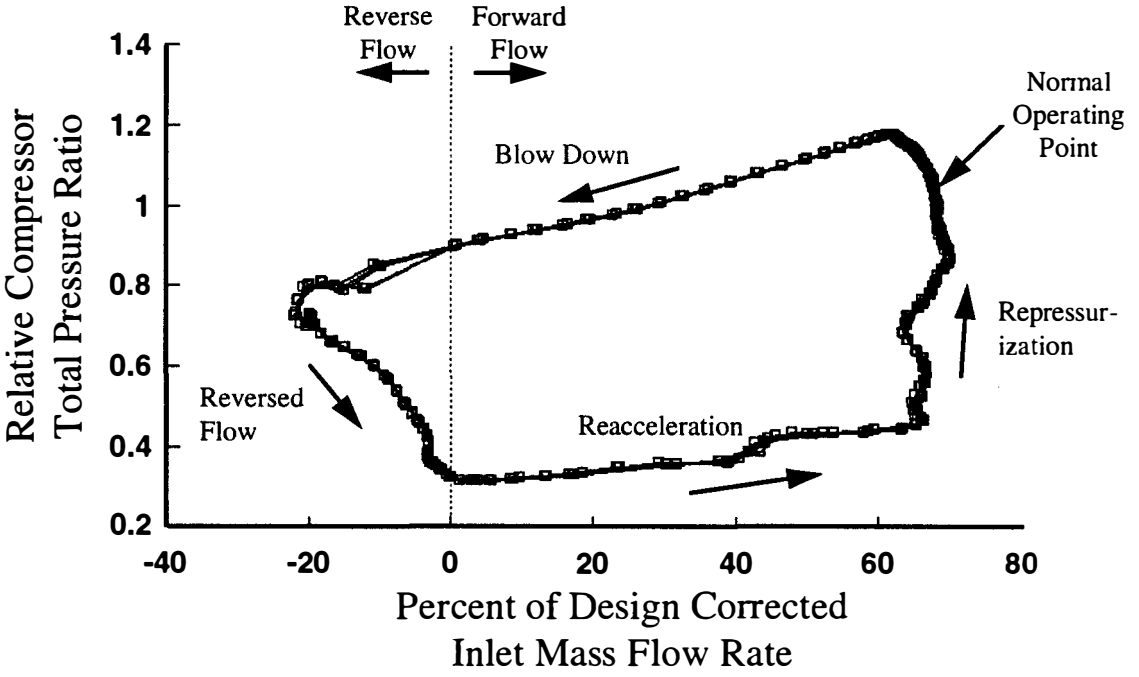

Figure 131. Relative Compressor Pressure Ratio as a Function of Percent of Design Corrected Inlet Mass Flow Rate for the T55-L-712 Compression System During Post-Stall Operation for the ATEC Dynamic Calibration Test Case.

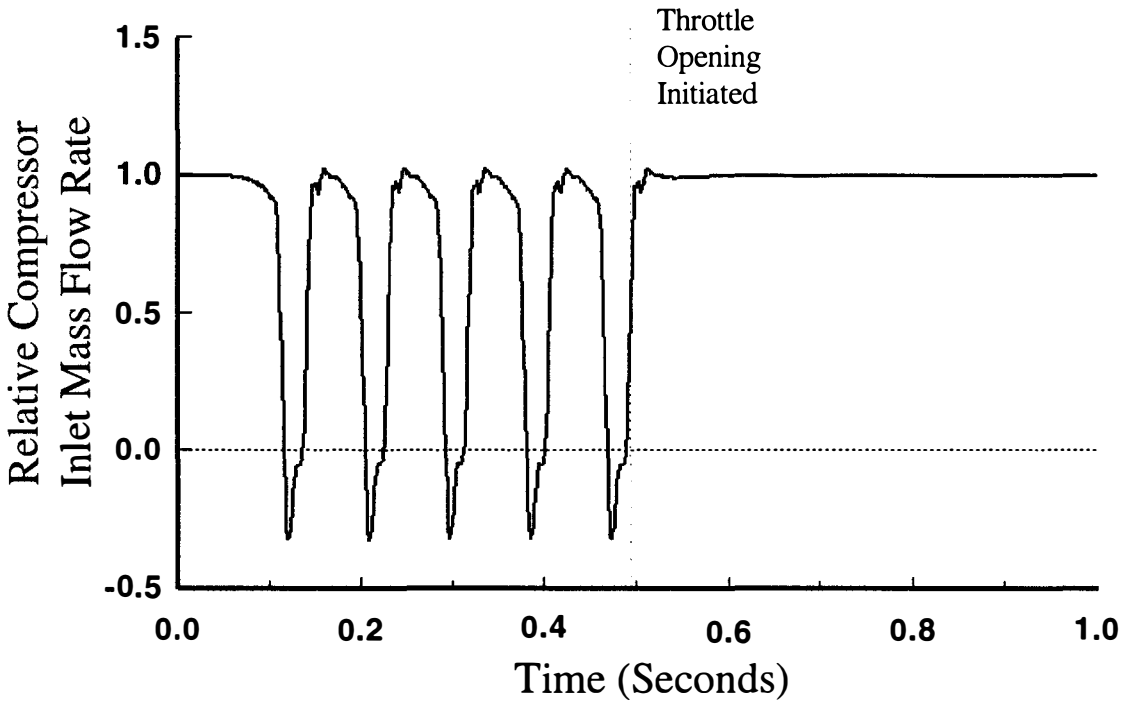

Figure 132. Relative Compressor Inlet Mass Flow Rate as a Function of Time for the T55-L-712 Compression System During Post-Stall Operation for the ATEC Dynamic Calibration Test Case.

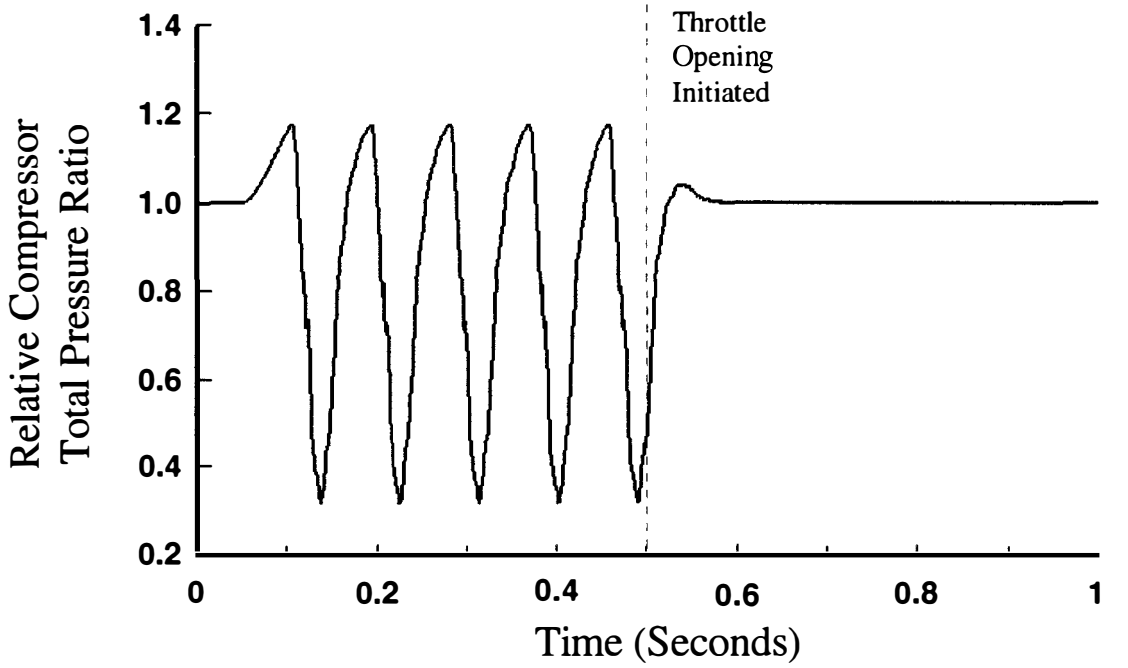

Figure 133. Relative Compressor Total Pressure Ratio as a Function of Time for the T55-L-712 Compression System During Post-Stall Operation for the ATEC Dynamic Calibration Test Case.

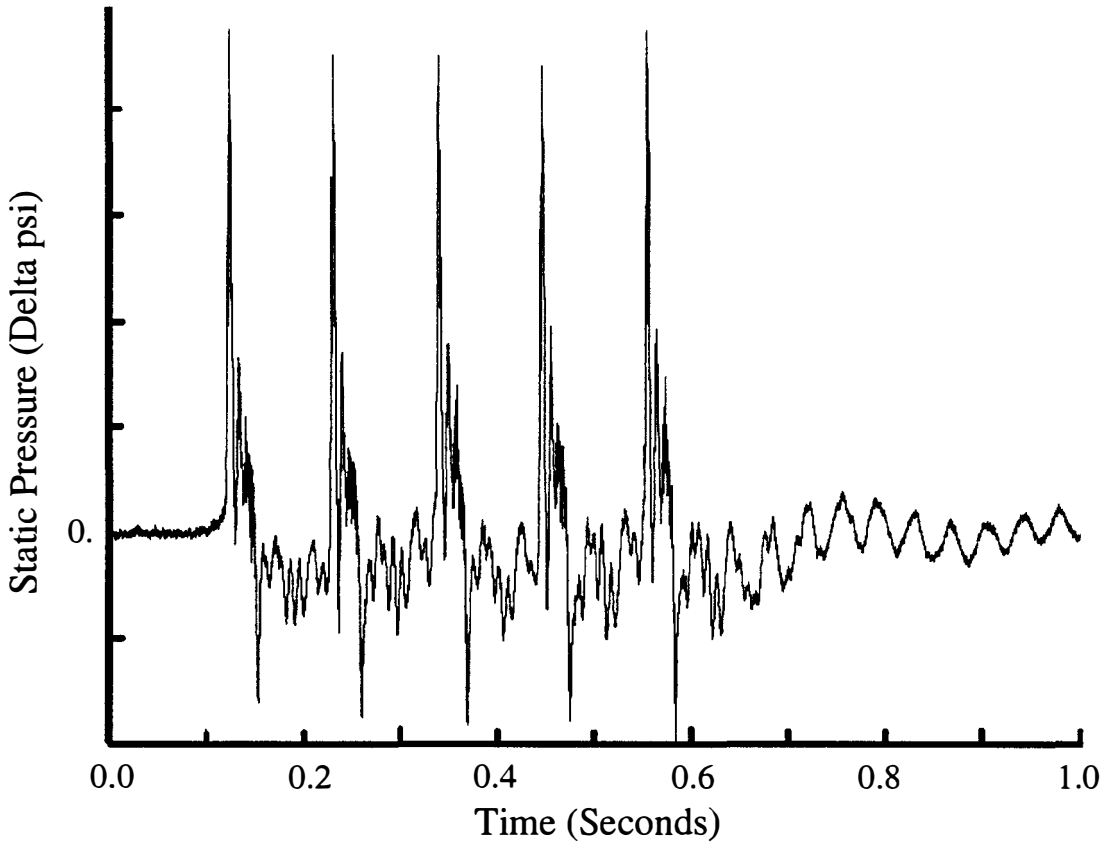

a. Experimental Data

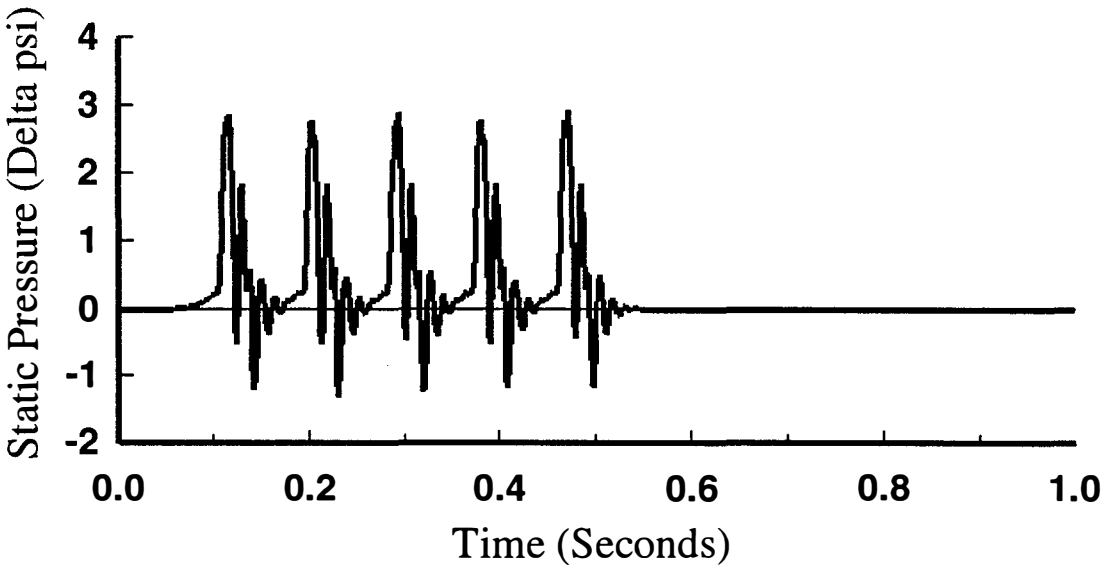

b. Simulation Results

Figure 134. Comparison of Static Pressure Difference in Front of the First Stage During Post Stall Operation for the T55-L-712 Compressor System for the ATEC Dynamic Calibration Test Case.

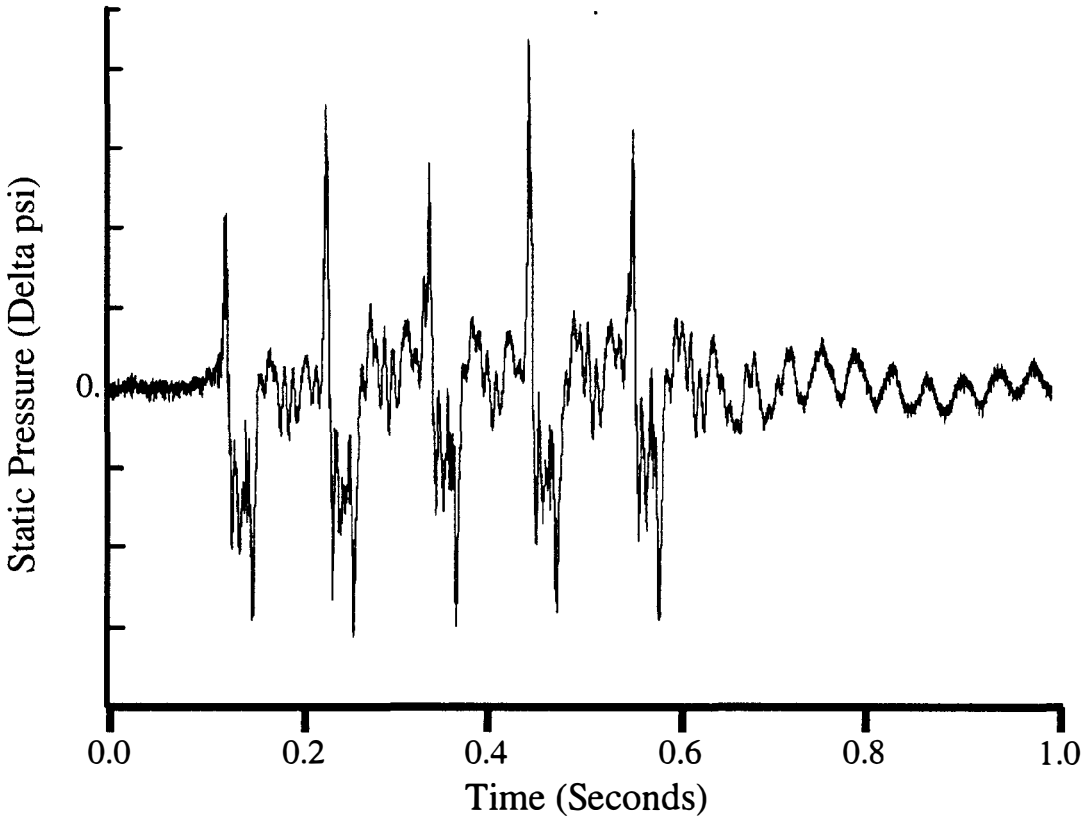

a. Experimental Data

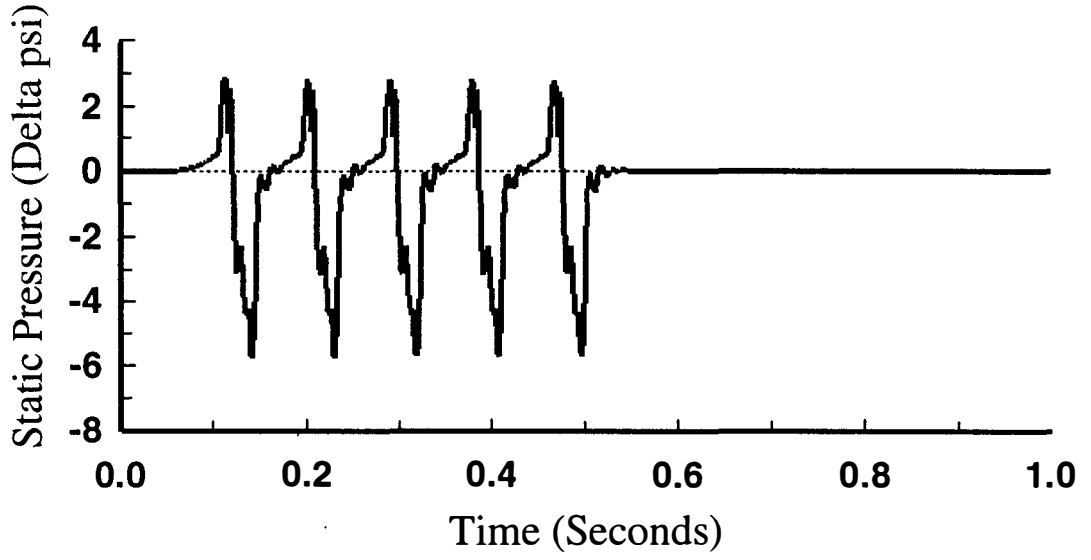

b. Simulation Results

Figure 135. Comparison of Static Pressure Difference in Front of the Third Stage During Post Stall Operation for the T55-L-712 Compressor System for the ATEC Dynamic Calibration Test Case.

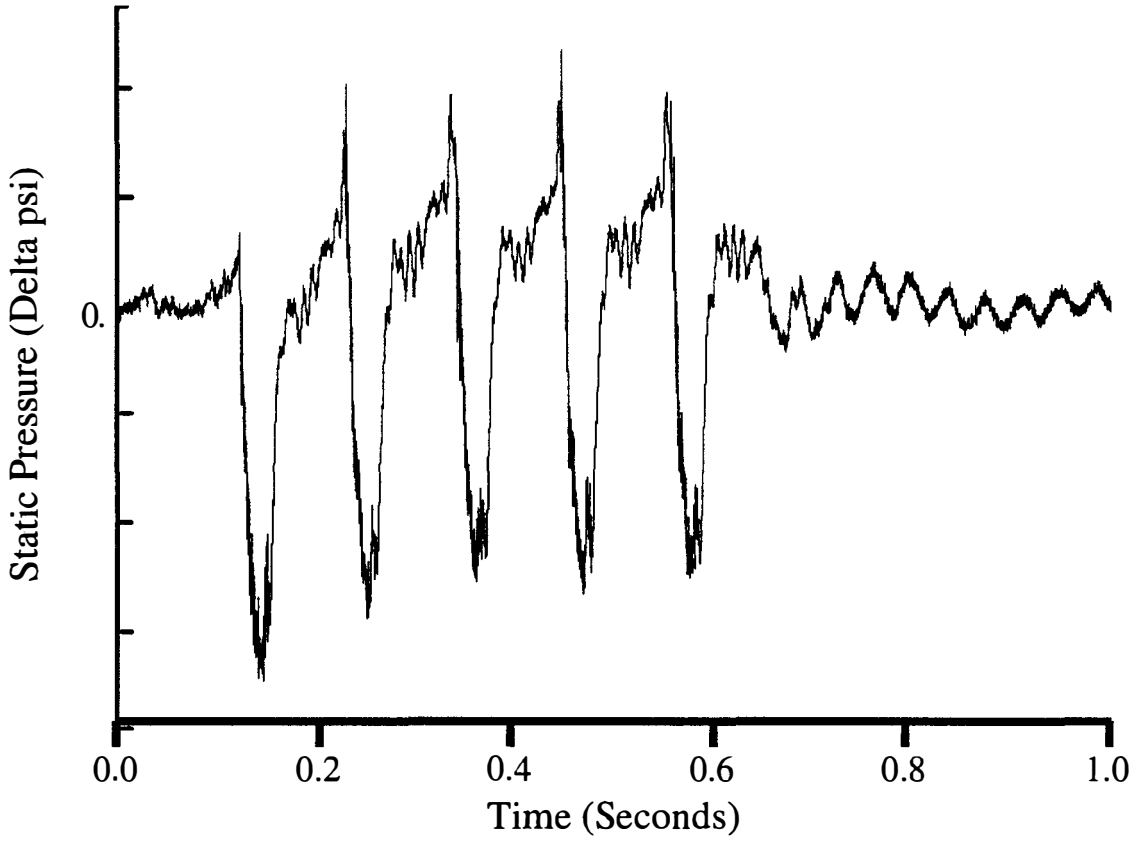

a. Experimental Data

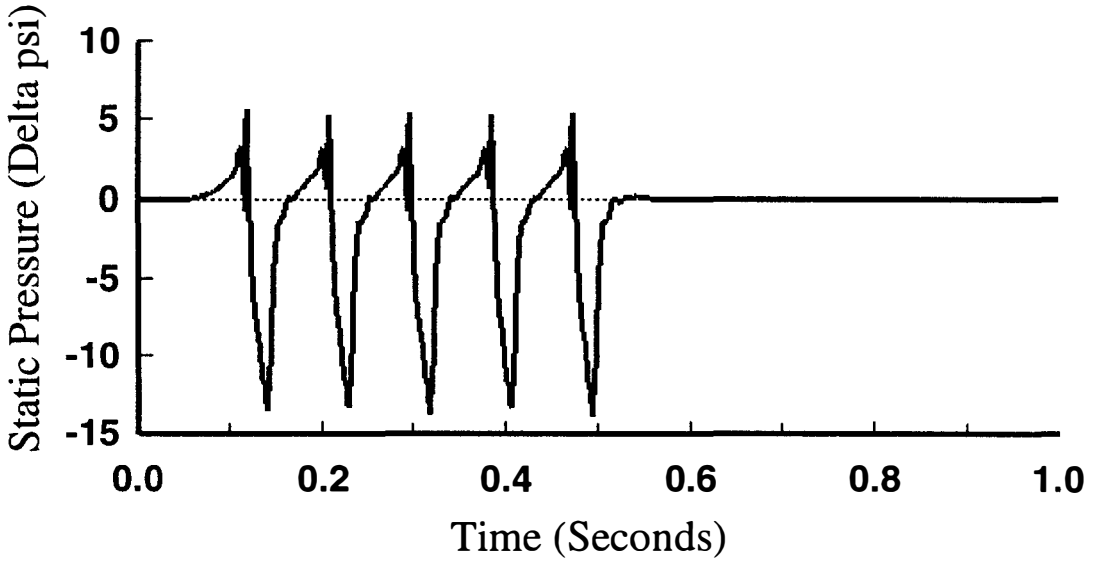

b. Simulation Results

Figure 136. Comparison of Static Pressure Difference in Front of the Sixth Stage During Post Stall Operation for the T55-L-712 Compressor System for the ATEC Dynamic Calibration Test Case.

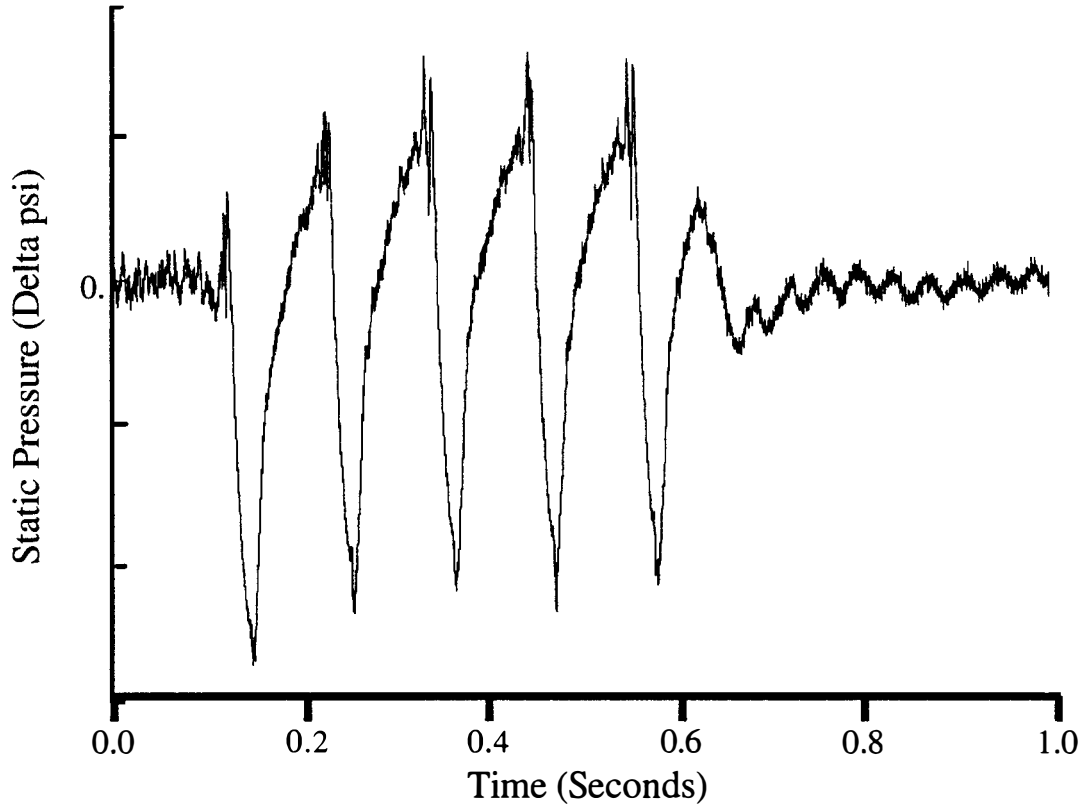

a. Experimental Data

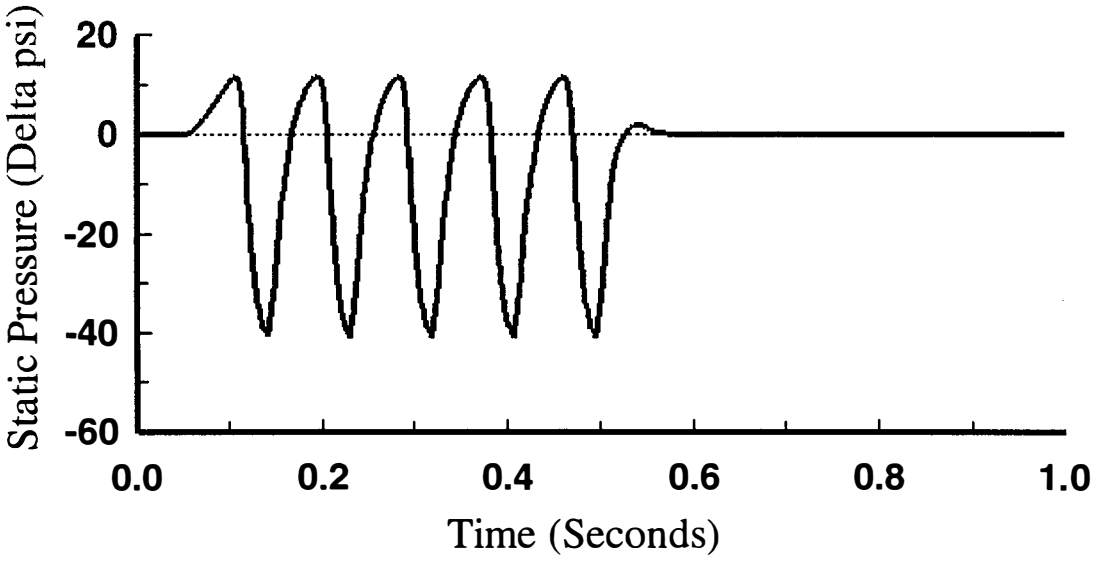

b. Simulation Results

Figure 137. Comparison of Static Pressure Difference in Rear of the Centrifugal Compressor Impeller During Post Stall Operation for the T55-L-712 Compressor System for the ATEC Dynamic Calibration Test Case.

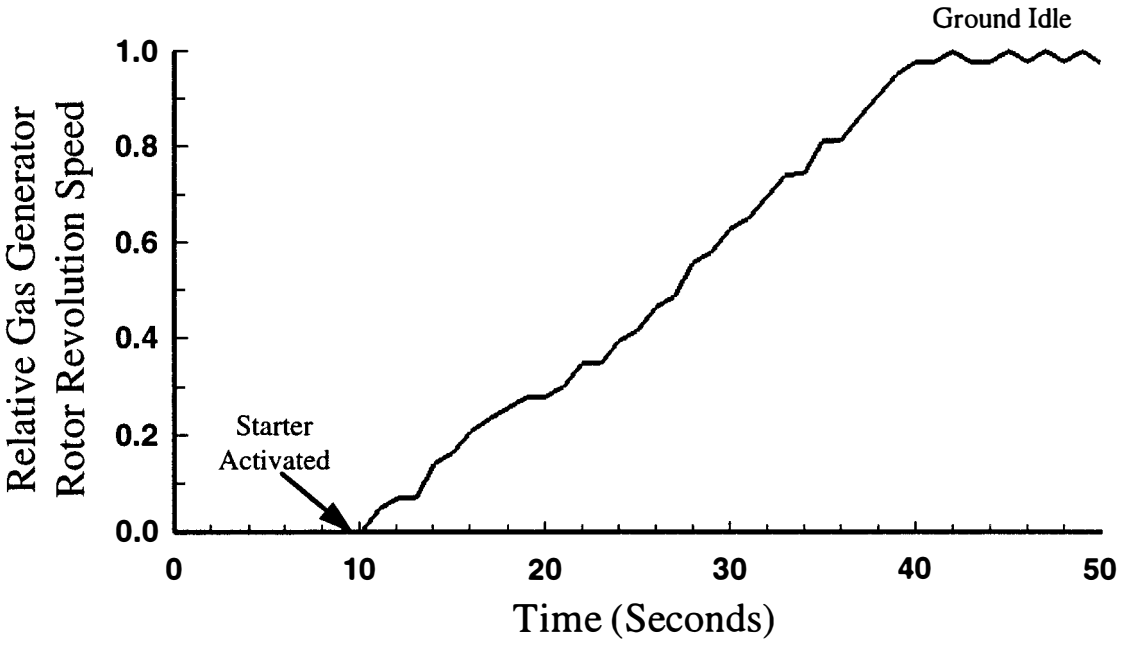

Figure 138. Experimental Data Relative Gas Generator Rotor Revolution Speed as a Function of Time for the T55-L-712 Engine for the ATEC Engine Starting Calibration Test Case.

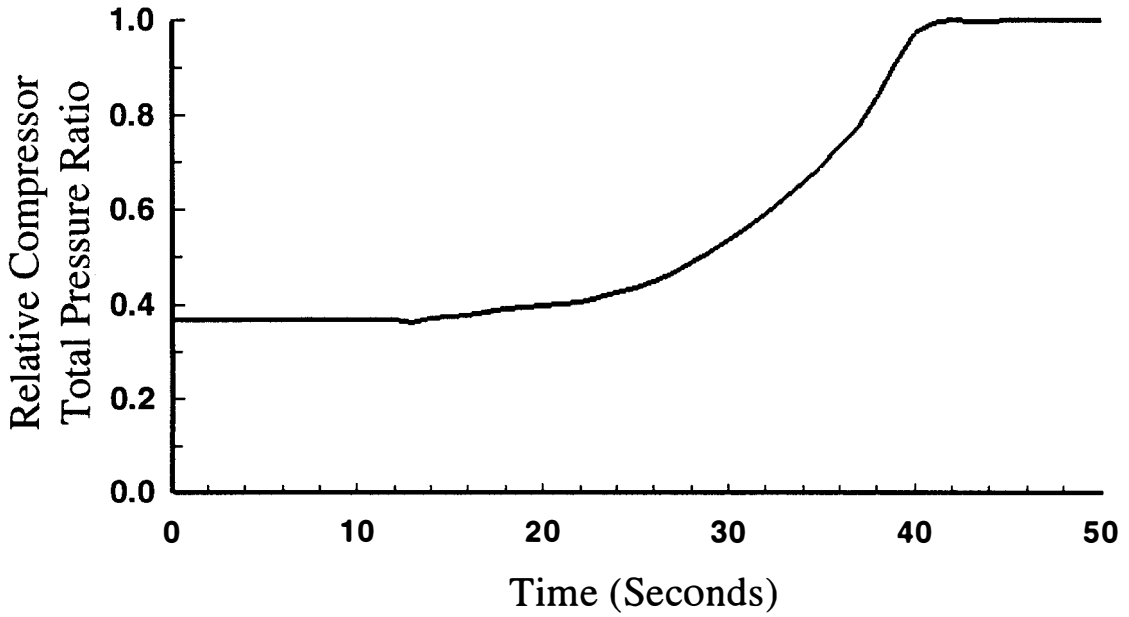

Figure 139. Experimental Data Relative Compressor Total Pressure Ratio as a Function of Time for the T55-L-712 Engine for the ATEC Engine Starting Calibration Test Case.

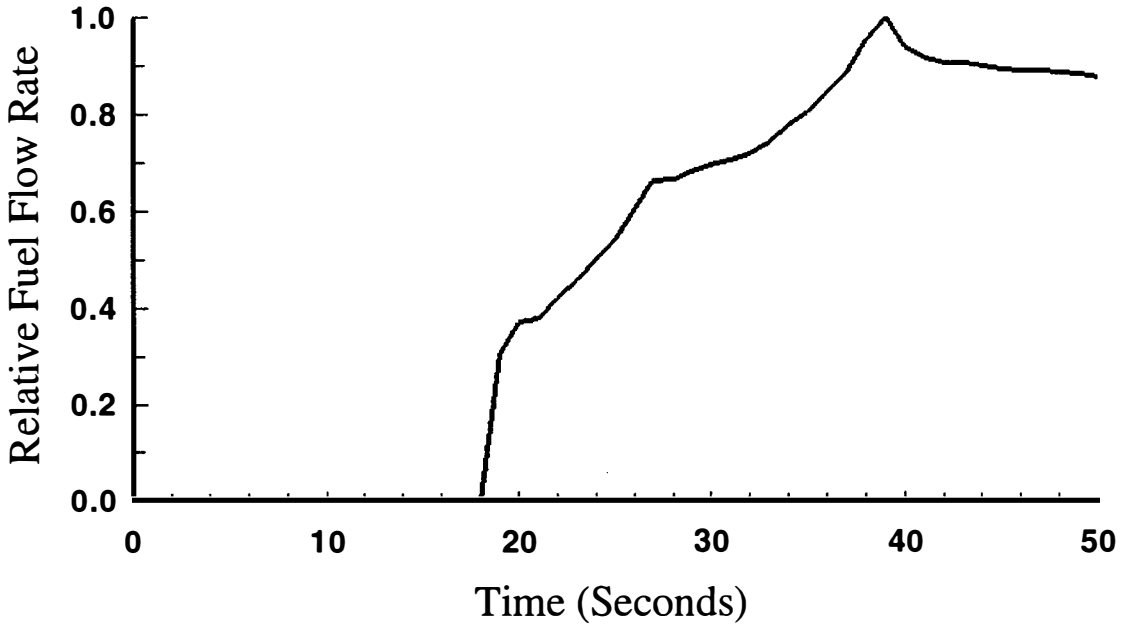

Figure 140. Experimental Data Relative Fuel Flow Rate as a Function of Time for the T55-L-712 Engine for the ATEC Engine Starting Calibration Test Case.

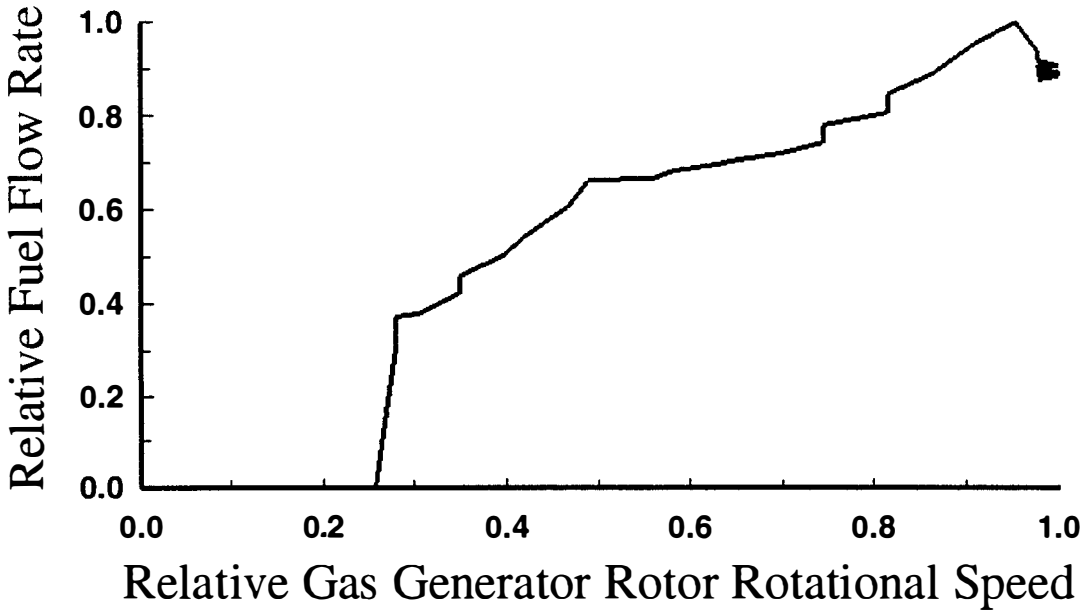

Figure 141. Experimental Data Relative Fuel Flow Rate as a Function of Relative Gas Generator Rotor Rotational Speed for the T55-L-712 Engine for the ATEC Engine Starting Calibration Test Case.

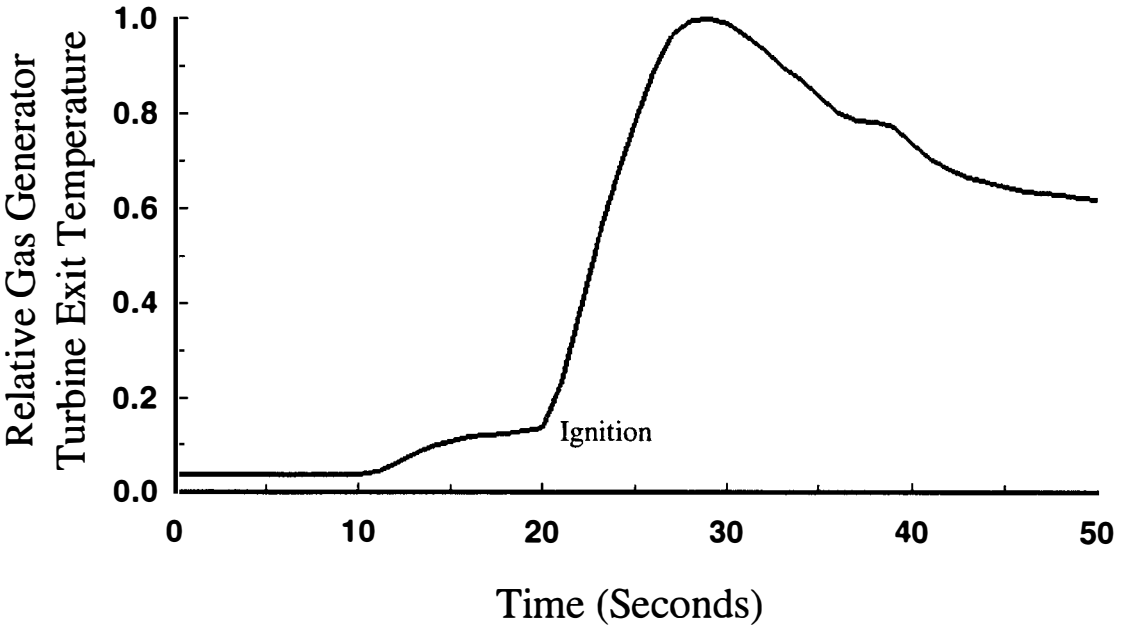

Figure 142. Experimental Data Relative Gas Generator Turbine Exit Temperature as a Function of Time for the T55-L-712 Engine for the ATEC Engine Starting Calibration Test Case.

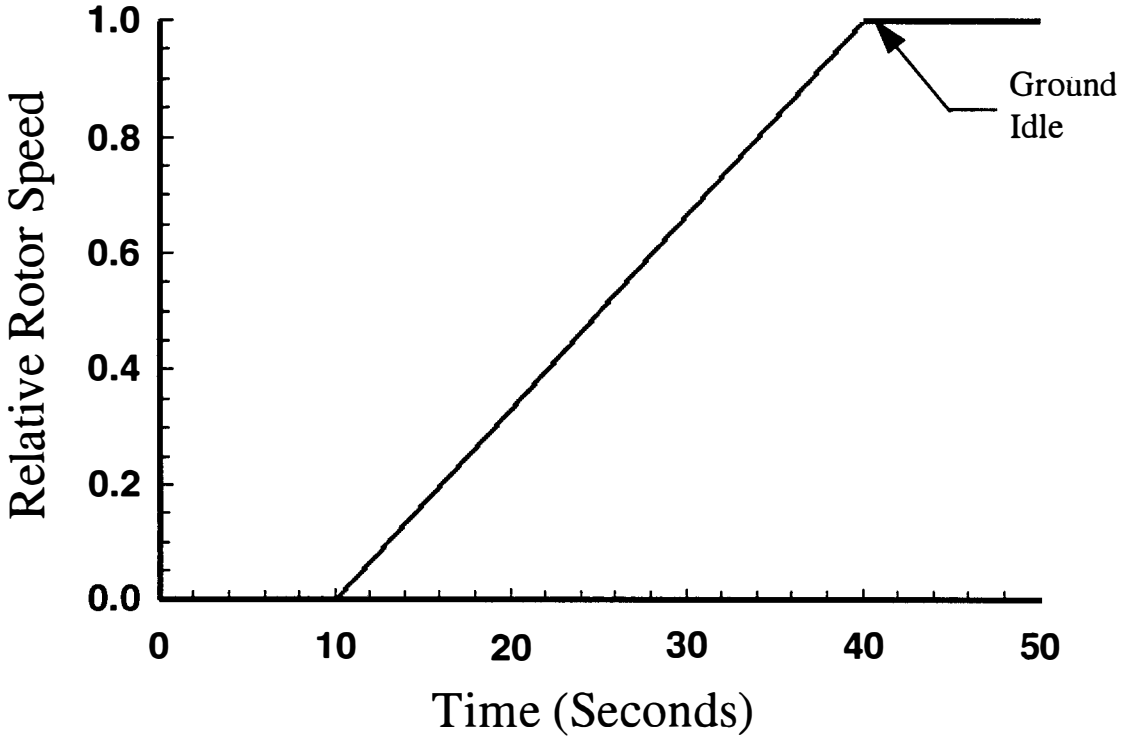

Figure 143. Relative Rotor Speed as a Function of Time Input into the ATEC Simulation for the T55-L-712 Engine for the ATEC Engine Starting Calibration Test Case.

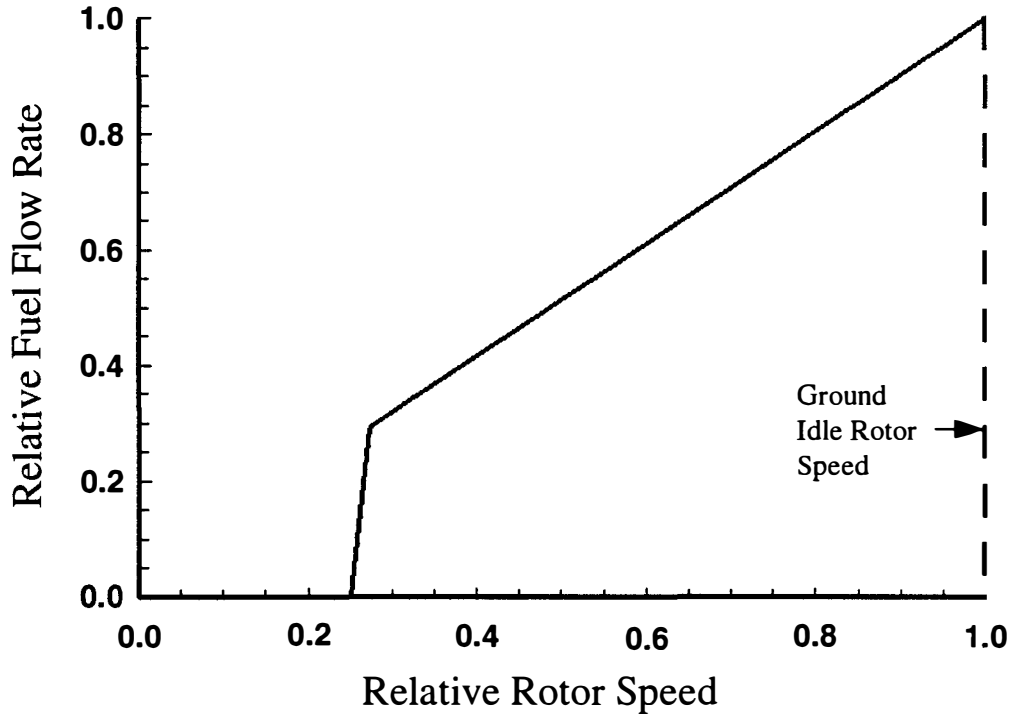

Figure 144. Relative Fuel Flow Rate as a Function of Relative Rotor Speed Input into ATEC Simulation for the T55-L-712 Engine for the ATEC Engine Starting Calibration Test Case.

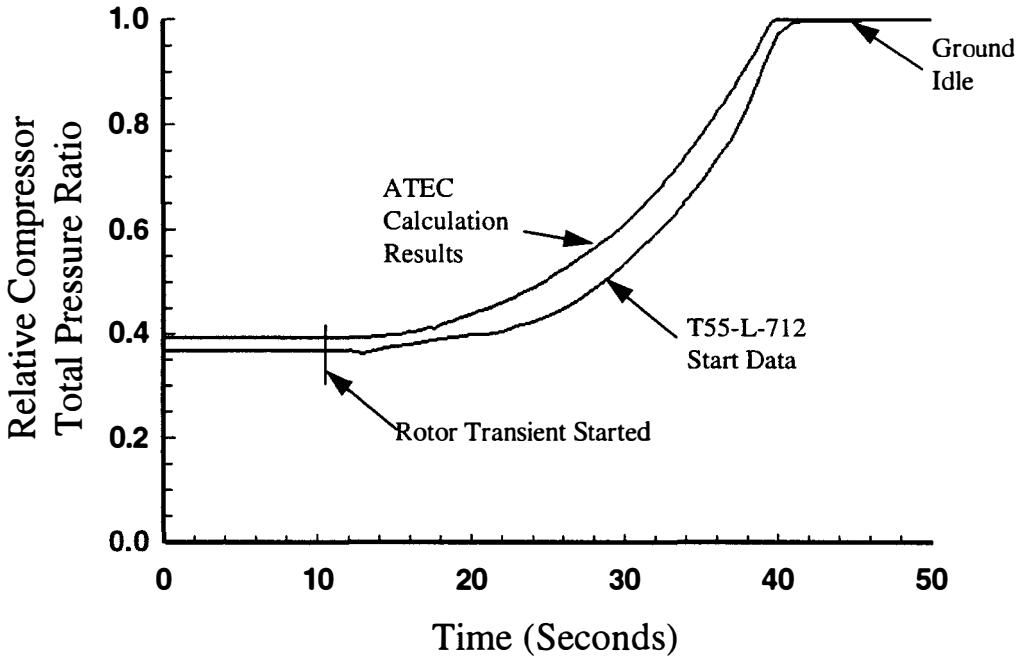

Figure 145. Relative Compressor Total Pressure Ratio as a Function of Time for the T55-L-712 Engine for the ATEC Engine Starting Calibration Test Case.

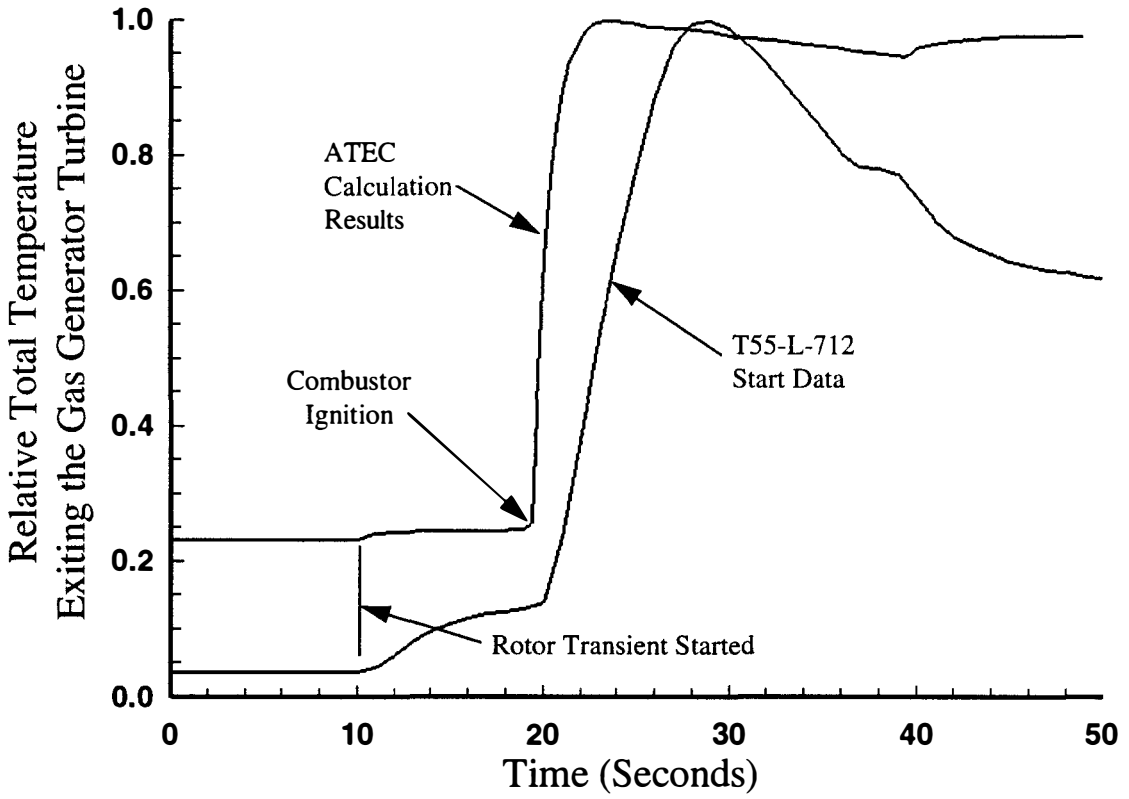

Figure 146. Relative Total Temperature Exiting the Gas Generator Turbine as a Function of Time for the T55-L-712 Engine for the ATEC Starting Calibration Test Case.

APPENDIX C: NUMERICAL SOLUTION TO THE GOVERNING EQUATIONS

K. R. Kneile and A. A. Hale
Sverdrup Technology, Inc.
AEDC Group
Arnold AS, TN 37389-9013

Explicit 1-D Algorithm

A finite difference algorithm to numerically solve the area weighted quasi-one-dimensional Euler equations has been developed. The algorithm is based upon the method of characteristics with modifications to maintain strong conservation properties. This section gives a description of the characteristic principles used in its development. The one-dimensional Euler equations with source terms in conservation form applied to a fixed grid are:

$$\frac{\partial \mathbf{U}}{\partial t} + \frac{\partial \mathbf{F}}{\partial x} = \mathbf{G} \qquad [1]$$

where

$$\mathbf{U} = \begin{Bmatrix} S\rho \\ S\rho u \\ SE \end{Bmatrix} \qquad [2]$$

$$\mathbf{F} = \begin{Bmatrix} S\rho u \\ S\rho u^2 + SP \\ u(SE + SP) \end{Bmatrix} \qquad [3]$$

$$\mathbf{G} = \begin{Bmatrix} -W_{Bx} \\ F_x \\ Q_x + SW_x - H_{Bx} \end{Bmatrix} \qquad [4]$$

Closure to the equation set is provided by the ideal gas law:

$$P = \rho RT \qquad [5]$$

The source term matrix $\mathbf{G}$ contains the turbomachinery source terms for bleed mass flow W_{Bx}, blade and case forces F_x, heat transfer Q_x, shaft work SW_x, and bleed enthalpy H_{Bx}. The flow variables in the flux arrays $\mathbf{F}$ are density ρ, static pressure P, total energy per unit volume E, and the axial velocity u with S defined as cross-sectional area.

Equation 1 can be written as

$$\mathbf{U}_t + \mathbf{A}\mathbf{U}_x = \mathbf{G} \qquad [6]$$

where the flux Jacobean matrix is given by:

$$\mathbf{A} = \frac{\partial \mathbf{F}}{\partial \mathbf{U}} \qquad [7]$$

Defining Λ to be a diagonal matrix containing the three eigenvalues of $\mathbf{A}$ ($\lambda_1 = u - a, \lambda_2 = u, \lambda_3 = u + a$) and $\mathbf{Q}$ as a matrix containing the three eigenrows $\mathbf{Q}_i$ of $\mathbf{A}$, then:

$$\mathbf{Q}_i\mathbf{A} = \lambda_i\mathbf{Q}_i \; ; i=1,2,3 \qquad [8]$$

The individual relations in Equation 8 may be written in the form:

$$\mathbf{QA} = \Lambda\mathbf{Q} \qquad [9]$$

or:

$$\mathbf{A} = \mathbf{Q}^{-1}\Lambda\mathbf{Q} \qquad [10]$$

By multiplying Equation 6 by $\mathbf{Q_i}$ and substituting the result into Equation 9, the following equation is obtained:

$$\mathbf{Q}_i \mathbf{U}_t + \lambda_i \mathbf{Q}_i \mathbf{U}_x = \mathbf{Q}_i \mathbf{G} \qquad [11]$$

From Equation 11, it is observed that along the path given by:

$$\frac{dx}{dt} = \lambda_i \qquad [12]$$

Equation 11 becomes:

$$\mathbf{Q}_i \frac{d\mathbf{U}}{dt} = \mathbf{Q}_i \mathbf{G} \qquad [13]$$

since:

$$\frac{d\mathbf{U}}{dt} = \frac{\partial \mathbf{U}}{\partial t} + \frac{dx}{dt}\frac{\partial \mathbf{U}}{\partial x} \qquad [14]$$

Equation 13 represents the compatibility equations along the chosen direction defined by Equation 12. The sign of λ_i determines which direction the information in Equation 13 travels. Equation 13 is obtained by premultiplying Equation 6 by $\mathbf{Q}_i$. Likewise, the i^{th} compatibility equation can be obtained from Equation 1 by pre-multiplying by $\mathbf{Q}_i$. The new explicit algorithm uses a finite difference representation of Equation 1 to obtain a finite difference representation of Equation 13.

Pre-multiplying Equation 1 by $\mathbf{Q}_i$ and rewriting gives:

$$\mathbf{Q}_i\left(\frac{\partial \mathbf{U}}{\partial t}\right) = \mathbf{Q}_i\left(\mathbf{G} - \frac{\partial \mathbf{F}}{\partial x}\right) \qquad [15]$$

A finite difference representation of Equation 15 can be applied between grid points j and j+1 with the fluxes evaluated at the nodes and the sources evaluated at the center of the volume as given by:

$$\mathbf{Q}_i\left(\frac{\Delta \mathbf{U}}{\Delta t}\right)_{j+\frac{1}{2}} = \mathbf{Q}_i\left[\mathbf{G}_{j+\frac{1}{2}} - \frac{(\mathbf{F}_{j+1} - \mathbf{F}_j)}{(x_{j+1} - x_j)}\right] \qquad [16]$$

This is shown graphically by:

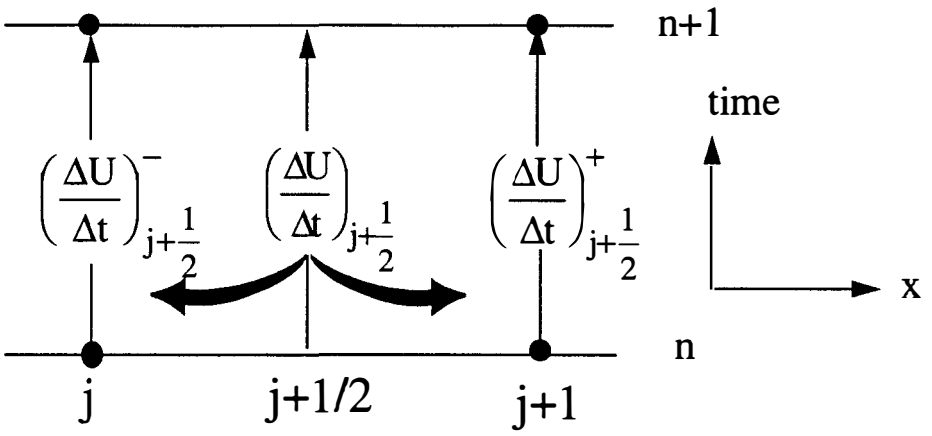

Time Derivative Split to Adjacent nodes by Explicit Characteristic Based Split Flux Difference Scheme

The eigenrows are defined over the interval by applying Roe averaging[1] over adjacent node-defined flow variables. The relations presented in Equation 16 are conservative forms of the compatibility relations represented by Equation 13. These three equations can be combined into the form:

$$\mathbf{Q}\left(\frac{\Delta \mathbf{U}}{\Delta t}\right)_{j+\frac{1}{2}} = \mathbf{Q}\left[\mathbf{G}_{j+\frac{1}{2}} - \frac{(\mathbf{F}_{j+1} - \mathbf{F}_j)}{(x_{j+1} - x_j)}\right] \qquad [17]$$

---

[1] Roe, P. L., "Approximate Riemann Solvers, Parameter Vectors and Difference Schemes, Journal of Computational Physics, Vol. 43, 1981, pp. 357-372.

Define $\mathbf{I}_D^+$ as a square matrix with a value of one on the diagonal for positive characteristics and a value of zero elsewhere and $\mathbf{I}_D^-$ similarly with a value of one on the diagonal for negative eigenvalues and a value of zero elsewhere. Then, pre-multiplying Equation 17 by $\mathbf{I}_D^+$ and $\mathbf{I}_D^-$ separates Equation 17 into positively and negatively moving characteristic relations. Pre-multiplying Equation 17 by $\mathbf{Q}^{-1}\mathbf{I}_D^+$ and $\mathbf{Q}^{-1}\mathbf{I}_D^-$ gives:

$$\left(\frac{\Delta \mathbf{U}}{\Delta t}\right)^+_{j+1} = \mathbf{I}^+_{j+\frac{1}{2}}\left(\frac{\Delta \mathbf{U}}{\Delta t}\right)_{j+\frac{1}{2}} = \mathbf{I}^+_{j+\frac{1}{2}}\left[\mathbf{G}_{j+\frac{1}{2}} - \frac{(\mathbf{F}_{j+1} - \mathbf{F}_j)}{(x_{j+1} - x_j)}\right] \qquad [18]$$

and

$$\left(\frac{\Delta \mathbf{U}}{\Delta t}\right)^-_{j} = \mathbf{I}^-_{j+\frac{1}{2}}\left(\frac{\Delta \mathbf{U}}{\Delta t}\right)_{j+\frac{1}{2}} = \mathbf{I}^-_{j+\frac{1}{2}}\left[\mathbf{G}_{j+\frac{1}{2}} - \frac{(\mathbf{F}_{j+1} - \mathbf{F}_j)}{(x_{j+1} - x_j)}\right] \qquad [19]$$

where

$$\mathbf{I}^+_{j+\frac{1}{2}} = \mathbf{Q}^{-1}\mathbf{I}_D^+\mathbf{Q} \qquad [20]$$

and

$$\mathbf{I}^-_{j+\frac{1}{2}} = \mathbf{Q}^{-1}\mathbf{I}_D^-\mathbf{Q} \qquad [21]$$

Notice that since $\mathbf{I}^+_{J+\frac{1}{2}} + \mathbf{I}^-_{j+\frac{1}{2}} = \mathbf{I}$, where $\mathbf{I}$ is the identity matrix, summing Equations 18 and 19 gives:

$$\left(\frac{\Delta \mathbf{U}}{\Delta t}\right)^+_{j+1} + \left(\frac{\Delta \mathbf{U}}{\Delta t}\right)^-_{j} = \left(\frac{\Delta \mathbf{U}}{\Delta t}\right)_{j+\frac{1}{2}} = \left[\mathbf{G}_{j+\frac{1}{2}} - \frac{(\mathbf{F}_{j+1} - \mathbf{F}_j)}{(x_{j+1} - x_j)}\right] \qquad [22]$$

Therefore, Equations 18 and 19 define a characteristic splitting of the conservative interval time derivatives. The time derivatives at the nodes can be obtained by summing the right characteristic weighted time derivative from an upstream interval and the left characteristic weighted time derivative from the downstream interval as:

$$\left(\frac{\Delta \mathbf{U}}{\Delta t}\right)_j = \left(\frac{\Delta \mathbf{U}}{\Delta t}\right)_j^+ + \left(\frac{\Delta \mathbf{U}}{\Delta t}\right)_j^- \qquad [23]$$

or

$$\left(\frac{\Delta \mathbf{U}}{\Delta t}\right)_j = \mathbf{I}^+_{j-\frac{1}{2}}\left[\mathbf{G}_{j-\frac{1}{2}} - \frac{(\mathbf{F}_j - \mathbf{F}_{j-1})}{(x_j - x_{j-1})}\right] + \mathbf{I}^-_{j+\frac{1}{2}}\left[\mathbf{G}_{j+\frac{1}{2}} - \frac{(\mathbf{F}_{j+1} - \mathbf{F}_j)}{(x_{j+1} - x_j)}\right] \qquad [24]$$

A solution is now obtainable at the n+1 time step by a forward Euler time integration procedure [72].

Boundary Conditions: Inlet: The inlet boundary is applied at the physical inlet of the grid and is assumed to be subsonic. Boundary conditions are developed using characteristics as developed above but with modifications to account for the fact that the algorithm is applied to the first node point. Characteristic compatibility equations are obtained from the interior algorithm by pre-multiplying the explicit equations of the first interval by the eigenrows giving:

$$\mathbf{Q}_1\ \Delta \mathbf{U} = \mathbf{Q}_1 \begin{Bmatrix} \Delta\rho \\ \Delta\rho u \\ \Delta E \end{Bmatrix} = \mathbf{Q}_1 \left[\mathbf{G}_{1+\frac{1}{2}} - \frac{(\mathbf{F}_2 - \mathbf{F}_1)}{(x_2 - x_1)}\right] \qquad [25]$$

The only applicable compatibility equation (Equation 13) at the inlet is along the $\lambda = u - a$ characteristic. This characteristic transfers information from the interior to the

inlet boundary. Therefore, only one row of the above system is calculated. A linear combination of conservative variables at the inlet node is set equal to the same linear combination of the interval conservative variables giving:

$$\mathbf{Q}_1\,\delta\mathbf{U} = \mathbf{Q}_1\left[\mathbf{G}_{1+\frac{1}{2}} - \frac{(\mathbf{F}_2 - \mathbf{F}_1)}{(x_2 - x_1)}\right] \qquad [26]$$

The other two compatibility equations are inappropriate at the inlet boundary and are replaced by linearizing the following two gas dynamic relationships and specifying the change in inlet total temperature and inlet total pressure, respectively:

$$\frac{a}{a_t} = \left[1 - \frac{(\gamma-1)}{2}\left(\frac{u}{a_t}\right)^2\right]^{\frac{1}{2}} \qquad [27]$$

$$\frac{P}{P_t} = \left[1 - \frac{(\gamma-1)}{2}\left(\frac{u}{a_t}\right)^2\right]^{\frac{\gamma}{\gamma-1}} \qquad [28]$$

using $a^2 = \frac{\gamma p}{\rho}$ and $p = (\gamma-1)\left[E - \frac{(\rho u)^2}{2\rho}\right]$.

Equation 26 and the linearized form of Equations 27 and 28 can be manipulated into the following form to calculate the change in axial velocity (δu) at the inlet:

$$\delta u = \frac{\frac{p\,\delta P_t}{P_t} + \frac{\rho u^2\,\delta a_t^2}{2a_t^2} - \left[au + \frac{u^2(\gamma-1)}{2}\right]\Delta\rho + \left[a + u(\gamma-1)\right]\Delta\rho u - (\gamma-1)\Delta E}{\rho(a+u)} \qquad [29]$$

The above expression is used with a forward Euler time integration method to solve for u and combined with Equations 27 and 28 to calculate all other thermodynamic properties at the new time interval.

Exit: The exit boundary condition is applied at the physical exit of the grid and is assumed to be subsonic. Characteristic compatibility equations are used to pass information from the interior algorithm developed above to the exit boundary by pre-multiplying the explicit equations of the last interval by the eigenrows giving:

$$\mathbf{Q}\,\Delta\mathbf{U} = \mathbf{Q}\begin{Bmatrix}\Delta\rho\\ \Delta\rho u\\ \Delta E\end{Bmatrix} = \mathbf{Q}\left[\mathbf{G}_{j\max-\frac{1}{2}} - \frac{(\mathbf{F}_{j\max} - \mathbf{F}_{j\max-1})}{(x_{j\max} - x_{j\max-1})}\right] \qquad [30]$$

Only the compatibility relations along the $\lambda = u$ and $\lambda = u + a$ characteristics are appropriate so only these two equations are calculated. A linear combination of conservative variables at the exit node is set equal to the same linear combination of the interval conservative variables giving:

$$\mathbf{Q}_2\,\delta\mathbf{U} = \mathbf{Q}_2\left[\mathbf{G}_{j\max-\frac{1}{2}} - \frac{(\mathbf{F}_{j\max} - \mathbf{F}_{j\max-1})}{(x_{j\max} - x_{j\max-1})}\right] \qquad [31]$$

$$\mathbf{Q}_3\,\delta\mathbf{U} = \mathbf{Q}_3\left[\mathbf{G}_{j\max-\frac{1}{2}} - \frac{(\mathbf{F}_{j\max} - \mathbf{F}_{j\max-1})}{(x_{j\max} - x_{j\max-1})}\right] \qquad [32]$$

The inappropriate compatibility equation along the $\lambda = u - a$ characteristic is replaced by specifying the value of a function of the primitive variables ρ, u, and p at the node. The function of ρ, u, and p is linearized as:

$$\delta f = c_1 a^2\ \delta\rho + c_2 \rho a\ \delta u + c_3\ \delta p \qquad [33]$$

Equations 31, 32, and 33 can be combined into the following general form:

$$\delta \mathbf{U} = \Delta \mathbf{U} + \begin{bmatrix} 1 \\ u - a \\ \frac{u^2}{2} - ua + \frac{a^2}{(\gamma - 1)} \end{bmatrix} \frac{(\delta f - \Delta f)}{a^2 (c_1 - c_2 + c_3)} \qquad [34]$$

where Δf is calculated from $\Delta \mathbf{U}$ by:

$$\Delta f = c_1 a^2\ \Delta\rho + c_2 \rho a\ \Delta u + c_3\ \Delta p \qquad [35]$$

The method can be easily tailored to a variety of exit boundary conditions as long as $c_1 - c_2 + c_3 \neq 0$.

Specifying static pressure at the exit means $\delta f = \delta p$ and $\Delta f = \Delta p$ in time with $c_1 = c_2 = 0$, $c_3 = 1$, and $c_1 - c_2 + c_3 = 1$. Specifying Mach number (Mn) at the exit results in $\delta f = \delta Mn$ and $\Delta f = \Delta Mn$ in time with:

$$c_1 - c_2 + c_3 = \frac{Mn(1 - \gamma)}{2\rho a^2} - \frac{1}{\rho a^2} \qquad [36]$$

The calculated $\delta \mathbf{U}$ represent the change in the conservative variables to the new time step.

Implicit 1-D Algorithm

The following implicit algorithm development follows from Equation 16 above to solve the one-dimensional form of the Euler equations written in conservative form on a fixed grid. Equation 16 is a finite difference representation of the three compatibility

relations between grid points j and j+1 with the eigenrows ($\mathbf{Q}$) evaluated over the interval by applying Roe averaging.

Define $\mathbf{I}_D^i$ as a square matrix with ones on the i^{th} diagonal and zeros elsewhere. Multiplying Equation 16 by $\mathbf{Q}^{-1}\mathbf{I}_D^i$ gives:

$$\mathbf{I}^i_{j+\frac{1}{2}}\left(\frac{\Delta \mathbf{U}}{\Delta t}\right)_{j+\frac{1}{2}} = \mathbf{I}^i_{j+\frac{1}{2}}\left[\mathbf{G}^{n+1}_{j+\frac{1}{2}} - \frac{(\mathbf{F}_{j+1} - \mathbf{F}_j)}{(x_{j+1} - x_j)}\right] \qquad [37]$$

with:

$$\mathbf{I}^i_{j+\frac{1}{2}} = \mathbf{Q}^{-1}\mathbf{I}^i_D\mathbf{Q} \qquad [38]$$

Note that since $\mathbf{I}^1_{j+\frac{1}{2}} + \mathbf{I}^2_{j+\frac{1}{2}} + \mathbf{I}^3_{j+\frac{1}{2}} = \mathbf{I}$, the identity matrix, summing Equation 25 over i gives:

$$\sum_{i=1}^{3}\mathbf{I}^i_{j+\frac{1}{2}}\left(\frac{\Delta \mathbf{U}}{\Delta t}\right)^i_{j+\frac{1}{2}} = \left(\frac{\Delta \mathbf{U}}{\Delta t}\right)_{j+\frac{1}{2}} = \left[\mathbf{G}^{n+1}_{j+\frac{1}{2}} - \frac{(\mathbf{F}_{j+1} - \mathbf{F}_j)}{(x_{j+1} - x_j)}\right] \qquad [39]$$

For the explicit method, the $\mathbf{I}^i_{j+\frac{1}{2}}\left(\frac{\Delta \mathbf{U}}{\Delta t}\right)^i_{j+\frac{1}{2}}$ terms were shifted in the direction of the characteristics to either the j^{th} or $(j+1)^{th}$ node. In the implicit algorithm, this shift is extrapolated to points outside of the interval [j,j+1]. The axial location of the shift denoted by * in the following figure and is different for each eigenvalue:

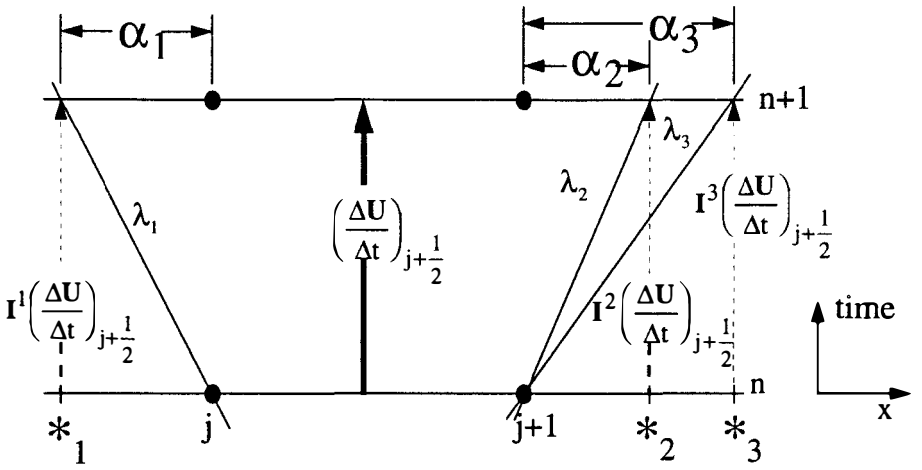

Time Derivative Split to Adjacent nodes by Implicit Characteristic Based Split Flux Difference Scheme

The location of * is to the right of the $(j+1)^{th}$ node if $\lambda_i > 0$ and to the left of the j^{th} node if $\lambda_i < 0$. Therefore, we set

$$\mathbf{I}^i_{j+\frac{1}{2}}\left(\frac{\Delta \mathbf{U}}{\Delta t}\right)^i_* = \mathbf{I}^i_{j+\frac{1}{2}}\left(\frac{\Delta \mathbf{U}}{\Delta t}\right)_{j+\frac{1}{2}} \qquad [40]$$

Substituting Equation 40 into Equation 37 gives:

$$\mathbf{I}^i_{j+\frac{1}{2}}\left(\frac{\Delta \mathbf{U}}{\Delta t}\right)^i_* = \mathbf{I}^i_{j+\frac{1}{2}}\left[\mathbf{G}^{n+1}_{j+\frac{1}{2}} - \frac{(\mathbf{F}_{j+1} - \mathbf{F}_j)}{(x_{j+1} - x_j)}\right] \qquad [41]$$

which is the implicit equivalent of Equation 18 and 19 of the explicit numerical solver development. The axial location of * represents where the j^{th} characteristic crosses the (n+1) time level when passing through the appropriate x^n_j or x^n_{j+1} node point. The non-dimensional axial distance between the * and node j or j+1 is given by

$$\alpha_i = \frac{\left(x_* - x_j\right)}{\left(x_{j+1} - x_j\right)} = \frac{\lambda_i \Delta t}{\Delta x} \quad ; \quad \lambda_i < 0 \qquad [42]$$

and

$$\alpha_i = \frac{\left(x_* - x_{j+1}\right)}{\left(x_{j+1} - x_j\right)} = \frac{\lambda_i \Delta t}{\Delta x} \quad ; \quad \lambda_i > 0 \qquad [43]$$

The $\left(\frac{\Delta U}{\Delta t}\right)_*^i$ terms in Equation 41 are replaced by the following extrapolations:

$$\left(\frac{\Delta U}{\Delta t}\right)_*^i = \left(1 - \alpha_i\right)\left(\frac{\Delta U}{\Delta t}\right)_j + \alpha_i \left(\frac{\Delta U}{\Delta t}\right)_{j+1} \quad ; \quad \lambda_i < 0 \qquad [44]$$

$$\left(\frac{\Delta U}{\Delta t}\right)_*^i = \left(1 + \alpha_i\right)\left(\frac{\Delta U}{\Delta t}\right)_{j+1} - \alpha_i \left(\frac{\Delta U}{\Delta t}\right)_j \quad ; \quad \lambda_i > 0 \qquad [45]$$

Characteristics are introduced into the extrapolations by substituting Equations 42 and 43 into Equations 44 and 45, respectively, giving:

$$\left(\frac{\Delta U}{\Delta t}\right)_*^i = \left(1 - \frac{\lambda_i \Delta t}{\Delta x}\right)\left(\frac{\Delta U}{\Delta t}\right)_j + \frac{\lambda_i \Delta t}{\Delta x}\left(\frac{\Delta U}{\Delta t}\right)_{j+1} \quad ; \quad \lambda_i < 0 \qquad [46]$$

$$\left(\frac{\Delta U}{\Delta t}\right)_*^i = \left(1 + \frac{\lambda_i \Delta t}{\Delta x}\right)\left(\frac{\Delta U}{\Delta t}\right)_{j+1} - \frac{\lambda_i \Delta t}{\Delta x}\left(\frac{\Delta U}{\Delta t}\right)_j \quad ; \quad \lambda_i > 0 \qquad [47]$$

Given the following matrix identity:

$$\lambda_i \mathbf{I}_i = \mathbf{I}_i \mathbf{A} \qquad [48]$$

substituting Equations 46 and 47 into the left hand side of Equation 41 gives:

$$\mathbf{I}^i_{j+\frac{1}{2}}\left(\frac{\Delta U}{\Delta t}\right)_*^i = \mathbf{I}^i_{j+\frac{1}{2}}\left(\mathrm{I} - \frac{\mathbf{A}\Delta t}{\Delta x}\right)\left(\frac{\Delta U}{\Delta t}\right)_j + \frac{\mathbf{A}\Delta t}{\Delta x}\left(\frac{\Delta U}{\Delta t}\right)_{j+1} \; ; \; \lambda_i < 0 \qquad [49]$$

$$\mathbf{I}^{i}_{j+\frac{1}{2}}\left(\frac{\Delta \mathbf{U}}{\Delta t}\right)^{i}_{*} = \mathbf{I}^{i}_{j+\frac{1}{2}}\left(\mathbf{I}+\frac{\mathbf{A}\Delta t}{\Delta x}\right)\left(\frac{\Delta \mathbf{U}}{\Delta t}\right)_{j+1} - \frac{\mathbf{A}\Delta t}{\Delta x}\left(\frac{\Delta \mathbf{U}}{\Delta t}\right)_{j} \quad ; \quad \lambda_i > 0 \qquad [50]$$

The source terms in Equation 41 are at the n+1 time interval and are linearized by the following truncated Taylor Series:

$$\mathbf{G}^{n+1} = \mathbf{G}^{n} + \left(\frac{\partial \mathbf{G}}{\partial \mathbf{U}_j}\right)^{n}_{j+\frac{1}{2}} \Delta \mathbf{U}_j + \left(\frac{\partial \mathbf{G}}{\partial \mathbf{U}_{j+1}}\right)^{n}_{j+\frac{1}{2}} \Delta \mathbf{U}_j \qquad [51]$$

The right hand side of Equation 41 expanded by Equation 51 becomes:

$$\begin{aligned}\mathbf{I}^{i}_{j+\frac{1}{2}}\left[\mathbf{G}^{n+1}_{j+\frac{1}{2}} - \frac{(\mathbf{F}_{j+1}-\mathbf{F}_j)}{(x_{j+1}-x_j)}\right] &= \mathbf{I}^{i}_{j+\frac{1}{2}}\left\{\left[\mathbf{G}^{n}_{j+\frac{1}{2}} - \frac{(\mathbf{F}_{j+1}-\mathbf{F}_j)}{(x_{j+1}-x_j)}\right]_{j+1}\right\} + \\ &\mathbf{I}^{i}_{j+\frac{1}{2}}\left\{\left(\frac{\Delta t \partial \mathbf{G}}{\partial \mathbf{U}_j}\right)^{n}_{j+\frac{1}{2}}\left(\frac{\Delta \mathbf{U}}{\Delta t}\right)_j + \left(\frac{\Delta t \partial \mathbf{G}}{\partial \mathbf{U}_{j+1}}\right)^{n}_{j+\frac{1}{2}}\left(\frac{\Delta \mathbf{U}}{\Delta t}\right)_{j+1}\right\}\end{aligned} \qquad [52]$$

Substituting Equation 49 and 50 and 52 into Equation 41 and summing over the negative characteristics (left shift) produces:

$$\begin{aligned}&\mathbf{I}^{-}_{j+\frac{1}{2}}\left\{\left(\mathbf{I}-\left(\frac{\Delta t \mathbf{A}}{\Delta x}\right)_{j+\frac{1}{2}}\right)\left(\frac{\Delta \mathbf{U}}{\Delta t}\right)_j + \left(\frac{\Delta t \mathbf{A}}{\Delta x}\right)_{j+\frac{1}{2}}\left(\frac{\Delta \mathbf{U}}{\Delta t}\right)_{j+1}\right\} + \\ &\mathbf{I}^{-}_{j+\frac{1}{2}}\left\{-\left(\frac{\Delta t \partial \mathbf{G}}{\partial \mathbf{U}_j}\right)^{n}_{j+\frac{1}{2}}\left(\frac{\Delta \mathbf{U}}{\Delta t}\right)_j - \left(\frac{\Delta t \partial \mathbf{G}}{\partial \mathbf{U}_{j+1}}\right)^{n}_{j+\frac{1}{2}}\left(\frac{\Delta \mathbf{U}}{\Delta t}\right)_{j+1}\right\} \\ &= \mathbf{I}^{-}_{j+\frac{1}{2}}\left[\mathbf{G}^{n}_{j+\frac{1}{2}} - \frac{(\mathbf{F}_{j+1}-\mathbf{F}_j)}{(x_{j+1}-x_j)}\right]\end{aligned} \qquad [53]$$

and summing over the positive characteristics (right shift) gives:

$$\mathbf{I}^{+}_{j+\frac{1}{2}}\left\{\left(\mathbf{I}+\left(\frac{\Delta t\mathbf{A}}{\Delta x}\right)_{j+\frac{1}{2}}\right)\left(\frac{\Delta \mathbf{U}}{\Delta t}\right)_{j+1}-\left(\frac{\Delta t\mathbf{A}}{\Delta x}\right)_{j+\frac{1}{2}}\left(\frac{\Delta \mathbf{U}}{\Delta t}\right)_{j}\right\}+$$

$$\mathbf{I}^{+}_{j+\frac{1}{2}}\left\{-\left(\frac{\Delta t\partial \mathbf{G}}{\partial \mathbf{U}_j}\right)^{n}_{j+\frac{1}{2}}\left(\frac{\Delta \mathbf{U}}{\Delta t}\right)_{j}-\left(\frac{\Delta t\partial \mathbf{G}}{\partial \mathbf{U}_{j+1}}\right)^{n}_{j+\frac{1}{2}}\left(\frac{\Delta \mathbf{U}}{\Delta t}\right)_{j+1}\right\} \qquad [54]$$

$$=\mathbf{I}^{+}_{j+\frac{1}{2}}\left[\mathbf{G}^{n}_{j+\frac{1}{2}}-\frac{(\mathbf{F}_{j+1}-\mathbf{F}_{j})}{(x_{j+1}-x_{j})}\right]$$

Equation 53 and 54 can be simplified by changing notation using the following definitions:

$$\mathbf{I}^{-}_{j+\frac{1}{2}}\left(\frac{\Delta t\mathbf{A}}{\Delta x}\right)_{j+\frac{1}{2}}=\left(\frac{\Delta t\mathbf{A}}{\Delta x}\right)^{-}_{j+\frac{1}{2}} \qquad [55]$$

$$\mathbf{I}^{+}_{j+\frac{1}{2}}\left(\frac{\Delta t\mathbf{A}}{\Delta x}\right)_{j+\frac{1}{2}}=\left(\frac{\Delta t\mathbf{A}}{\Delta x}\right)^{+}_{j+\frac{1}{2}} \qquad [56]$$

$$\mathbf{I}^{-}_{j+\frac{1}{2}}\left(\frac{\Delta t\partial \mathbf{G}}{\partial \mathbf{U}_j}\right)^{n}_{j+\frac{1}{2}}=\left(\frac{\Delta t\partial \mathbf{G}}{\partial \mathbf{U}_j}\right)^{-}_{j+\frac{1}{2}} \qquad [57]$$

$$\mathbf{I}^{+}_{j+\frac{1}{2}}\left(\frac{\Delta t\partial \mathbf{G}}{\partial \mathbf{U}_j}\right)^{n}_{j+\frac{1}{2}}=\left(\frac{\Delta t\partial \mathbf{G}}{\partial \mathbf{U}_j}\right)^{+}_{j+\frac{1}{2}} \qquad [58]$$

The implicit equations at the j^{th} node are obtained by summing the right shifted ($\lambda_i > 0$) version of Equation 41 from the [j-1,j] interval and the left shifted ($\lambda_i < 0$) versions of Equation 41 from the [j,j+1] interval. Substituting in the notation from Equations 55 through 58 gives:

$$\left[-\left(\frac{\Delta t\mathbf{A}}{\Delta x}\right)^{+}_{j-\frac{1}{2}}-\left(\frac{\Delta t\partial \mathbf{G}}{\partial \mathbf{U}_{j-1}}\right)^{+}_{j-\frac{1}{2}}\right]\left(\frac{\Delta \mathbf{U}}{\Delta t}\right)_{j-1}+$$

$$\left[\mathbf{I}^{+}_{j-\frac{1}{2}}+\mathbf{I}^{-}_{j+\frac{1}{2}}+\left(\frac{\Delta t\mathbf{A}}{\Delta x}\right)^{+}_{j-\frac{1}{2}}-\left(\frac{\Delta t\mathbf{A}}{\Delta x}\right)^{-}_{j+\frac{1}{2}}-\left(\frac{\Delta t\partial \mathbf{G}}{\partial \mathbf{U}_{j}}\right)^{-}_{j+\frac{1}{2}}-\left(\frac{\Delta t\partial \mathbf{G}}{\partial \mathbf{U}_{j}}\right)^{+}_{j-\frac{1}{2}}\right]\left(\frac{\Delta \mathbf{U}}{\Delta t}\right)_{j}+ \qquad [59]$$

$$\left[\left(\frac{\Delta t\mathbf{A}}{\Delta x}\right)^{-}_{j+\frac{1}{2}}-\left(\frac{\Delta t\partial \mathbf{G}}{\partial \mathbf{U}_{j+1}}\right)^{-}_{j+\frac{1}{2}}\right]\left(\frac{\Delta \mathbf{U}}{\Delta t}\right)_{j+1}=$$

$$\mathbf{I}^{+}_{j-\frac{1}{2}}\left[\mathbf{G}_{j-\frac{1}{2}}-\frac{(\mathbf{F}_{j}-\mathbf{F}_{j-1})}{(x_{j}-x_{j-1})}\right]+\mathbf{I}^{-}_{j+\frac{1}{2}}\left[\mathbf{G}_{j+\frac{1}{2}}-\frac{(\mathbf{F}_{j+1}-\mathbf{F}_{j})}{(x_{j+1}-x_{j})}\right]$$

To be consistent with the Explicit algorithm the sum of $\mathbf{I}^{+}_{j-\frac{1}{2}}$ and $\mathbf{I}^{-}_{j+\frac{1}{2}}$ is set to the identity matrix $\mathbf{I}$, giving:

$$\left[-\left(\frac{\Delta t\mathbf{A}}{\Delta x}\right)^{+}_{j-\frac{1}{2}}-\left(\frac{\Delta t\partial \mathbf{G}}{\partial \mathbf{U}_{j-1}}\right)^{+}_{j-\frac{1}{2}}\right]\left(\frac{\Delta \mathbf{U}}{\Delta t}\right)_{j-1}+$$

$$\left[\mathbf{I}+\left(\frac{\Delta t\mathbf{A}}{\Delta x}\right)^{+}_{j-\frac{1}{2}}-\left(\frac{\Delta t\mathbf{A}}{\Delta x}\right)^{-}_{j+\frac{1}{2}}-\left(\frac{\Delta t\partial \mathbf{G}}{\partial \mathbf{U}_{j}}\right)^{-}_{j+\frac{1}{2}}-\left(\frac{\Delta t\partial \mathbf{G}}{\partial \mathbf{U}_{j}}\right)^{+}_{j-\frac{1}{2}}\right]\left(\frac{\Delta \mathbf{U}}{\Delta t}\right)_{j}+ \qquad [60]$$

$$\left[\left(\frac{\Delta t\mathbf{A}}{\Delta x}\right)^{-}_{j+\frac{1}{2}}-\left(\frac{\Delta t\partial \mathbf{G}}{\partial \mathbf{U}_{j+1}}\right)^{-}_{j+\frac{1}{2}}\right]\left(\frac{\Delta \mathbf{U}}{\Delta t}\right)_{j+1}=$$

$$\mathbf{I}^{+}_{j-\frac{1}{2}}\left[\mathbf{G}_{j-\frac{1}{2}}-\frac{(\mathbf{F}_{j}-\mathbf{F}_{j-1})}{(x_{j}-x_{j-1})}\right]+\mathbf{I}^{-}_{j+\frac{1}{2}}\left[\mathbf{G}_{j+\frac{1}{2}}-\frac{(\mathbf{F}_{j+1}-\mathbf{F}_{j})}{(x_{j+1}-x_{j})}\right]$$

The above system of equations is solved by a block tri-diagonal matrix solver for the time derivatives at the nodes. A first-order Runge-Kutta integration scheme is then used to move the flow field solution to the next time step.

Boundary Conditions: Inlet: The inlet boundary condition is applied at the physical inlet of the grid and, as with the explicit numerical solver inlet boundary condition, is assumed to be subsonic. Boundary conditions are developed using characteristics through modifying the results of the interior algorithm on the first interval. Characteristic compatibility equations are obtained from the interior algorithm by pre-multiplying the implicit equations of the first interval (Equation 60 for the first node) by the eigenrows giving:

$$[\mathbf{Q}]\left\{\left[\mathbf{A}^{cof}\right]\left(\frac{\Delta \mathbf{U}}{\Delta t}\right)_0+\left[\mathbf{B}^{cof}\right]\left(\frac{\Delta \mathbf{U}}{\Delta t}\right)_1+\left[\mathbf{C}^{cof}\right]\left(\frac{\Delta \mathbf{U}}{\Delta t}\right)_2=\left[\mathbf{F}^{cof}\right]\right\} \qquad [61]$$

where the **A**, **B**, **C**, and **F** coefficient matrices are simply the terms in the square brackets in Equation 60, respectively.

The only applicable compatibility equation at the inlet is along the $\lambda = u - a$ characteristic. This compatibility equation transfers information from the interior to the inlet boundary. Therefore, only one row of the above system is calculated. The other two compatibility equations are inappropriate at the inlet boundary and are replaced by linearized gas dynamic relationships specifying the change in inlet total temperature and total pressure. The two equations to be linearized are given in Equations 27 and 28 above, and are repeated here for completeness:

$$\frac{a}{a_t} = \left[1 - \frac{(\gamma-1)}{2}\left(\frac{u}{a_t}\right)^2\right]^{\frac{1}{2}} \qquad [27]$$

$$\frac{P}{P_t} = \left[1 - \frac{(\gamma-1)}{2}\left(\frac{u}{a_t}\right)^2\right]^{\frac{\gamma}{\gamma-1}} \qquad [28]$$

These two relationships are linearized by using $a^2 = \frac{\gamma p}{\rho}$ and $p = (\gamma-1)\left[E - \frac{(\rho u)^2}{2\rho}\right]$ as in the explicit numerical solver inlet boundary condition derivation.

The following linearizations compliment the compatibility relations to complete the boundary condition equations:

$$\left[\frac{(\gamma-1)^2 u^2}{2} - T_t\right]\Delta\rho - \left[(\gamma-1)^2 u\right]\Delta(\rho u) + \left[\gamma(\gamma-1)\right]\Delta E = \rho\,\Delta T_t \qquad [62]$$

$$\left[\frac{(\gamma-3)u^2}{2}\right]\Delta\rho + \left[(2-\gamma)u\right]\Delta(\rho u) + \left[(\gamma-1)\right]\Delta E = p\frac{\Delta P_t}{P_t} + \frac{\rho u^2}{2}\frac{\Delta T_t}{T_t} \qquad [63]$$

The above linearizations contribute information to two rows of the **B** coefficient matrix and the **F** coefficient matrix. The corresponding rows of the **A** and **C** coefficient matrices are zeroed. An update in the inlet dependent variables can now be calculated from an iteration of the tri-diagonal matrix solver.

Exit: The exit boundary condition is applied at the physical exit of the grid and is assumed to be subsonic. Characteristic compatibility equations are used to pass

information from the interior algorithm to the exit boundary by pre-multiplying the implicit equations of the last interval by the eigenrows giving:

$$[Q]\left\{\left[\mathbf{A}^{cof}\right]\left(\frac{\Delta U}{\Delta t}\right)_{j\,max-1}+\left[\mathbf{B}^{cof}\right]\left(\frac{\Delta U}{\Delta t}\right)_{j\,max}+\left[\mathbf{C}^{cof}\right]\left(\frac{\Delta U}{\Delta t}\right)_{j\,max+1}=\left[\mathbf{F}^{cof}\right]\right\} \qquad [64]$$

Only the compatibility relations along the $\lambda = u$ and $\lambda = u + a$ characteristics are appropriate so only these two equations are calculated. The inappropriate compatibility equation along the $\lambda = u - a$ characteristic is replaced by a linearization of the gas dynamic relationship capable of specifying the exit boundary condition of static pressure or Mach number. If static pressure is specified, the following algebraic relationship is linearized:

$$p = (\gamma - 1)\left[E - \frac{(\rho u)^2}{2\rho}\right] \qquad [65]$$

producing:

$$\left[\frac{(\gamma-1)u^2}{2}\right]\Delta\rho - \left[(\gamma-1)u\right]\Delta(\rho u) + \left[(\gamma-1)\right](\gamma-1)\,\Delta E = \Delta p \qquad [66]$$

If Mach number (Mn) is specified, then the following relationship is linearized:

$$Mn = \frac{u}{a} \qquad [67]$$

with $a^2 = \frac{\gamma p}{\rho}$ and $p = (\gamma - 1)\left[E - \frac{(\rho u)^2}{2\rho}\right]$ to yield:

$$\left[-\frac{Mna^2}{2}\left(1+\frac{\gamma(\gamma-1)Mn^2}{2}\right)\right]\Delta\rho+\left[a\left(1+\frac{\gamma(\gamma-1)Mn^2}{2}\right)\right]\Delta(\rho u)-\left[\frac{\gamma(\gamma-1)Mn}{2}\right]\Delta E=\rho a^2\Delta Mn \qquad [68]$$

Either of the above linearizations are used to replace the inappropriate compatibility equation. The linearizations contribute information to a single row of the **B** and **F** matrices with the corresponding row of the **A** and **C** matrices zeroed . The exit conservative variables at the next time interval can now be obtained from an iteration of the tri-diagonal matrix solver.

VITA

Glenn Douglas Garrard was born in Hamilton County, Tennessee, on February 12, 1961. He attended Westwood Elementary and Junior High Schools in Manchester, Tennessee and graduated from Coffee County High School in May 1979. He entered Tennessee Technological University the fall of 1979, and in June 1983, he received a Bachelor of Science degree in Mechanical Engineering. Following graduation, he accepted employment with Sverdrup Technology, Inc. at the Arnold Engineering Development Center. He began taking graduate courses while working in September, 1983 at the University of Tennessee Space Institute, and graduated with a Master of Science degree in Mechanical Engineering in May 1990. He continued taking course work for a doctorate at the University of Tennessee Space Institute while continuing to work full time with Sverdrup Technology, Inc. In August 1992, he was the recipient of the Resident Graduate Study Program Scholarship, which permitted him to attend school full time for one year while still receiving salary and benefits from Sverdrup Technology, Inc. He graduated with a Doctor of Philosophy in Mechanical Engineering in August 1995.

Mr. Garrard is a member of the American Society of Mechanical Engineers and a senior member of the American Institute of Aeronautics and Astronautics. He is a member of the First Presbyterian Church in Manchester, Tennessee, and is an Eagle Scout. He and his wife, the former Angelia Gail Vaughn of Manchester, Tennessee, have one son, Justin Matthew Garrard, and one daughter, Rachel Marie Garrard.